CYRIC

ANNUAL REPORT

1996

(January 1996 - December 1996)

CYCLOTRON AND RADIOISOTOPE CENTER
TOHOKU UNIVERSITY

ЧЕРНЫЕ ТЕОРЕТИЧЕСКИЕ ОСНОВЫ

ТЕОРИЯ ЦЕПЕЙ

Учебник

Рекомендовано Министерством образования Российской Федерации в качестве учебника для студентов высших учебных заведений

PREFACE

In this seventeenth issue of the CYRIC Annual Report, we summarize the activities for research and development and results of training for radioisotope safe-treatment at Cyclotron and Radioisotope Center, Tohoku University during the calendar year 1996.

In 1996 research programs in various fields such as nuclear physics, nuclear chemistry, solid state physics and element analyses by PIXE and activation were carried out, and radioisotopes were produced for use in engineering, biology and medicine. At the same time several facility improvements have been carried out. A total of 2560 hours of the cyclotron beam was delivered for the scheduled researches, while 100 hours for research and development for the accelerator and related facilities. It should be noted here that a two weeks long unscheduled shut-down occurred in this year due to the break down of the RF power supply device, while unscheduled shut-down so far experienced by the last year was limited to a few percents of the total beam time used. In almost 75% of the beam time, protons were accelerated for nuclear physics and short-lived radioisotopes for medical and other studies, in 10% deuteron beams for the same purposes, while in 9% ^{4}He beams for material and solid state physics. Heavier ions such as ^{13}C and ^{15}N have been accelerated as well for some limited works.

Among the various research programs, studies with PIXE technique have been continuously carried out by using electro-static accelerator, installed at FNL (Fast Neutron Laboratory) in Graduate School of Technology, Tohoku University, under the scientific tie up between CYRIC and FNL. Indeed, more than six groups are running under this project using a total of its 250 hours beam-time in the last year.

During 1996, 511 of staff members and students of Tohoku University were trained at this Center in the beginner's course of safe handling of radiation and radioisotopes, while 219 staff members and students in the "x-ray course". In addition, a new course of safe handling of radiation from a SOR (Synchrotron Orbital Radiation) has been opened, and 36 . of staff members and students of Tohoku University were trained.

International work shop SATIF3 (The 3rd. Shielding Aspects of Accelerator, Targets and Irradiation Facilities) chaired by Prof. Takashi Nakamura will be held at Sendai on coming May 12 and 13th with 50 participants in which 30 scientists from foreign countries.

On July 23-29, 1997, The 3rd. Japan China joint Nuclear Physics Symposium is scheduled to be held in Sendai, Ogatsu, and Niigata hosted by CYRIC and Laboratory of

Nuclear Science, Tohoku University, and Niigata University chaired by Profs. Hikonojo Orihara and Luo Yixiao.

In the next school year, the 20th anniversary of the founding of CYRIC is coming after the 10th one in 1987. In the last decad, results of research and education were fruitful indeed. Accumuration of published paper (written in English with referee) based on the studies with facilities and equipments of CYRIC increased from 144 to 417 pieces, while that of doctor's thesis from 37 to 92 volumes. It shoud be noted that five international symposiums have hosted by CYRIC in this period, suggesting that world wide interest is focussed on the activities of this institute.

It has been of crucial importance to replace the cyclotron by a new one with higher specifications to maintain the present activities in CYRI higher specifications to maintain the present activities in CYRIC and its further development in force coming decade. We are planning and requiring the budget to replace the present K=50 MeV AVF cyclotron with K=130 MeV AVF cyclotron equipped with high-intensity negative ion-source together with ECR heavy-ion and polarized-ion sources.

We are very grateful to Tohoku University and to the Ministry of Education, Science, Sports and Culture for their continuous support.

January 1997

Hikonojo ORIHARA

Director
Cyclotron and Radioisotope Center
Tohoku University

EDITORS:

Hikonojo	*ORIHARA*
Manabu	*FUJIOKA*
Tatsuo	*IDO*
Takashi	*NAKAMURA*
Masatoshi	*ITOH*

WORD PROCESSED BY

Yu-ko YAMASHITA

CONTENTS

I. PYSICS AND TECHNOLOGY

II. CHEMISTRY

III. Medicine (Basic)

IV. MEDICINE (Clinical)

V. HEALTH PHYSICS

I. PHYSICS AND TECHNOLOGY

I. 1. Measurements of the Total Reaction Cross Section in ^{12}C, ^{13}C, ^{14}N, ^{15}N, ^{16}O + ^{28}Si Systems

Ishiyama H., Yamaya T., Yamazaki A., Tojima J., Katoh M., Kuzumaki T., Yahata H., Kotajima K., Suzuki K.*, Fujioka M.**, and Shinozuka T.***

Department of Physics, Tohoku University
*Department of Nuclear Engineering, Tohoku University **
*Cyclotron and Radioisotope Center, Tohoku University ***

A model independent determination of the total reaction cross sections has been experimentally made using the sum-of-differences method[3] in ^{12}C, ^{13}C, ^{14}N, ^{15}N, ^{16}O + ^{28}Si elastic scattering. The measurements of the total reaction cross section σ_R address a problem of deep significance to studies of nuclear reaction mechanism, since it contains information about all the possible channels of a scattering system. For example, the absorption term of the optical model potential (OMP) is quite sensitive to σ_R. The real part of OMP can be calculated using microscopic method with realistic nucleon-nucleon interaction data. However, other experimental data which are sensitive only to the imaginary part of the potential have hardly ever been found. Therefore, one of the fundamentally important experiments in nuclear physics is an accurate determination of total reaction cross sections.

Recently, Ostowski et al[4,5] have measured elastic cross sections in the forward angular range with the smallest angle of θ_{lab}=1.6° in the ^{12}C+^{12}C scattering at E/A=1-2 MeV, and they determined the total reaction cross sections model-independently. Elastic Cross sections of ^{12}C, ^{15}N, ^{16}O + ^{28}Si have been measured at the energies E/A = 4-5 MeV[6] in the forward angular range up to 1.2°. However, the measurements in such a limited angle range are not enough for the purpose to deduce the highly precise total reaction cross sections or the nuclear amplitudes at θ=0°.

In the present work, the measurements of elastic differential cross sections were extended to the forward angular region up to 0.6° in the scattering systems, ^{12}C, ^{13}C, ^{14}N, ^{15}N and ^{16}O on ^{28}Si. The result of the precise experiments showed undoubted oscillations and undulating envelope shape in the sum-of-differences cross sections(SOD), as shown in Fig. 1.

For the measurements at extremely forward angles(θ =0.6°-4.0°), a trapezoidal scattering chamber was designed and installed at the down stream of a large scattering chamber. The distance between the target position and a defining slit of the detector system was 1592mm. The detector system consists of two 25μm totally depleted silicon detectors

and a 240 μm position-sensitive silicon detector. The telescope was mounted by a thin tantalum plate with three slit apertures of 0.4×2 mm^2 in front of the ΔE detectors. Each slit aperture defined a solid angle of 3.1×10^{-7}sr. and a differential angle of $\Delta\theta=0.014°$ assuming a point beam spot on the target. The accuracy of angle setting was 5×10^{-4} degree. Four solid-state detectors were symmetrically situated with respect to the beam axis, to monitor the deflection of the beam intensity distribution in the beam spot. These monitor detectors were symmetrically placed on a circle with a small corn angle of $\theta_{lab}=1.1°$with the incident beam axis. This monitor system was movable on the scattering plane and an accuracy of absolute scattering angles was 0.02°. The absolute scattering angles was determined by measuring the symmetry of the slight small deflective patterns on the Rutherford scattering yields with the beam axis. The precision of the absolute scattering angle is ±0.001°. The beam was doubly collimated to a spot of diameter less than 0.4mm on the target. The target was a self-supporting natural Si metal of 180μg/cm^2 thickness.

The contributions from the target contaminations have to be taken into account in order to keep the resulting error small. We found a contaminant material of about 3.7×10^{-3}% in the Si target, which is estimated to have a mass number near A=180; it may be Au, from the elastically scattered energy spectra at the large angles.

As the physical effects for the elastic scattering data at very forward angles, the multiple scattering, the electron screening and the vacuum polarization should be considered. The effects of the first and second terms were negligible for the data at angles larger than 0.2° at least. However, the effect of the third term was taken into account for the data. The calculation of the vacuum polarization was done using the first order approximation to the equation proposed by Uehling[7]. The finite size effect of nuclei for the vacuum polarization has been calculated by Roesel et al[8]. The results show that the finite size effect is clearly sensitive to muonic atoms but can be neglected in heavy-ion scattering.

The sum-of-differences cross sections were calculated using the measured angular distribution. The resulting function $\sigma_{SOD}(\theta_0)$ were renormalyzed so that the median of the upper and lower envelopes of $\sigma_{SOD}(\theta_0)$ became a horizontal line. These $\sigma_{SOD}(\theta_0)$ functions exhibit a certain oscillation at small angles. The diffraction pattern at forward angles can be described by a Bessel function $J_0(L_g\sin\theta)$ with L_g being an angular momentum near the grazing angular momentum[9]. The $\sigma_{SOD}(\theta_0)$ obtained from data are compared in Fig.1 with the $J_0(L_g\sin\theta)$ function calculated with glory angular momenta of L_g = 30, 30, 40, 40 and 35 for ^{12}C, ^{13}C, ^{14}N, ^{15}N and ^{16}O projectile nuclei, respectively. In table 1, the values of the total reaction cross sections σ_R are listed together with the $f_N(0)$ and L_g. The uncertainty of total reaction cross sections obtained is within 5% except for ^{15}N projectile. In the case of ^{15}N projectile, the accuracy of the σ_R is about 11%. This large uncertainty may results from the measurement of σ_{SOD} in the angular range which is not sufficiently small to obtain the constant amplitude of oscillating σ_{SOD} function.

In Table 1, the total reaction cross sections obtained from the SOD method are compared with the results from the optical model potential analyses[10]. The total reaction cross sections from the OMP analyses are in good agreement with the results by SOD method.

References

1) Holdeman J. and Theler R., Phys. Rev. Lett. **14** (1965) 81.
2) Marty C., Z. Phys. A309 (1983) 261; Z. Phys. **A322** (1985) 499.
3) Barrette J. and Alamanos N., Phy. Lett. 153B (1985) 203; Nucl. Phys. **A441** (1985) 733.
4) Ostrowski A. et al., Phys. Lett. **B232** (1989) 46.
5) Ostrowski A. et al., Phys. Rev. **C44** (1991) 2082.
6) Yamaya T. et al., Proc. of 3rd-IN2P3-RIKEN Symposium on Heavy Ion Collision, Kawagoe, Saitama, Oct. 1994. p23-33.
7) Ueling E., Phys. Rev. **48** (1935) 55.
8) Rosel F. and Trautman D., Nucl. Phys. **A292** (1955) 523.
9) Ueda M, and Takigawa D., Nucl. Phys. **A598** (1996) 273.
10) Yamaya T. et al., Phys. Rev. **C37** (1988) 2585.

Table. 1. Results from the SOD analyses. k is the wave number, η is the Sommerfeld parameter; σ_R from SOD is the total reaction cross section from the SOD method, and σ_R from the OMP is the one from the OMP analyses.

Projectile	^{12}C	^{13}C	^{14}N	^{15}N	^{16}O
E_{lab}[MeV]	65	60	84	85	75
k[fm^{-1}]	4.28	4.17	5.00	5.08	4.83
η	5.68	6.16	6.30	6.26	8.14
σ_R from SOD [mb]	1490 ± 50	2090 ± 80	1970 ± 90	1600 ± 180	1600 ± 70
$\lvert f_N(0) \rvert$ [fm]	10 ± 2	21 ± 4	46 ± 14	48 ± 20	35 ± 5
σ_R from OMP[mb]	1630	2011	1901	1623	1519

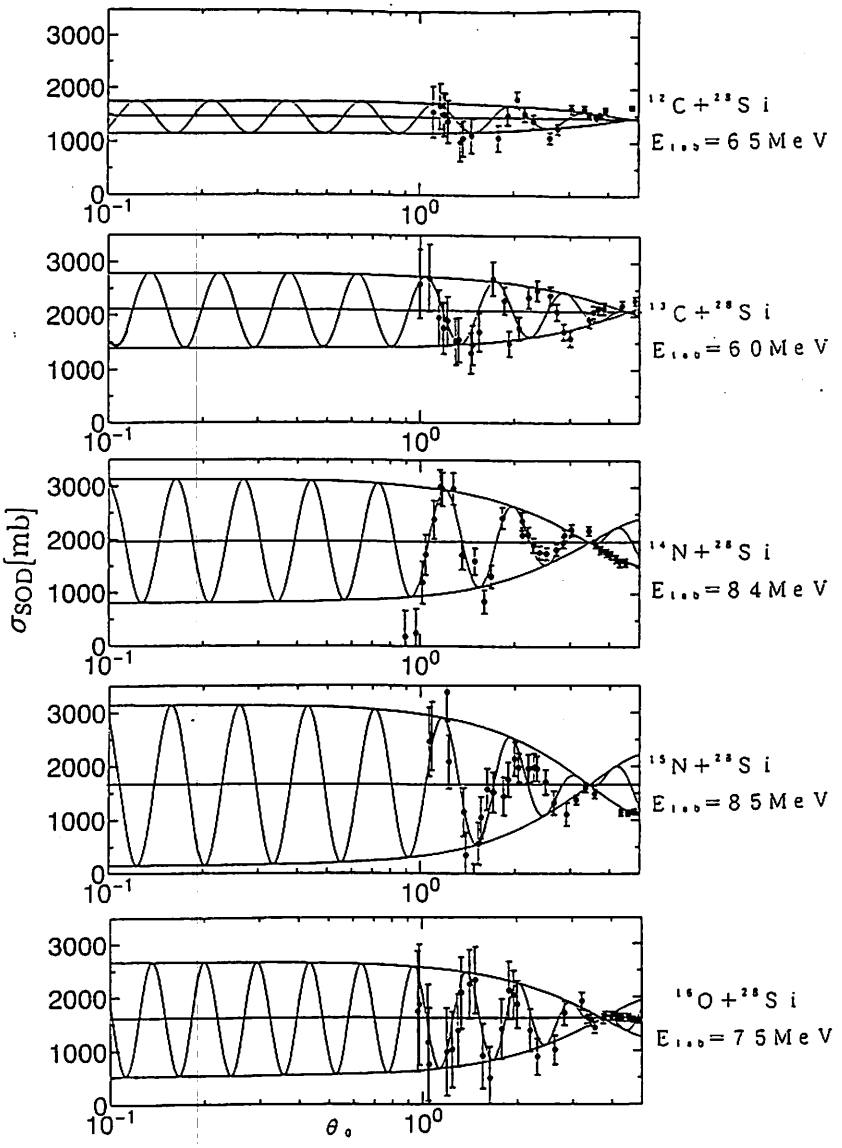

Fig. 1. The Sum-of-differences cross sections $\sigma_{SOD}(\theta_0)$ obtained from the present data. Solid curves are the results of the χ^2 fit. The holizontal lines give the total reaction cross sections σ_R as obtained from χ^2 fit.

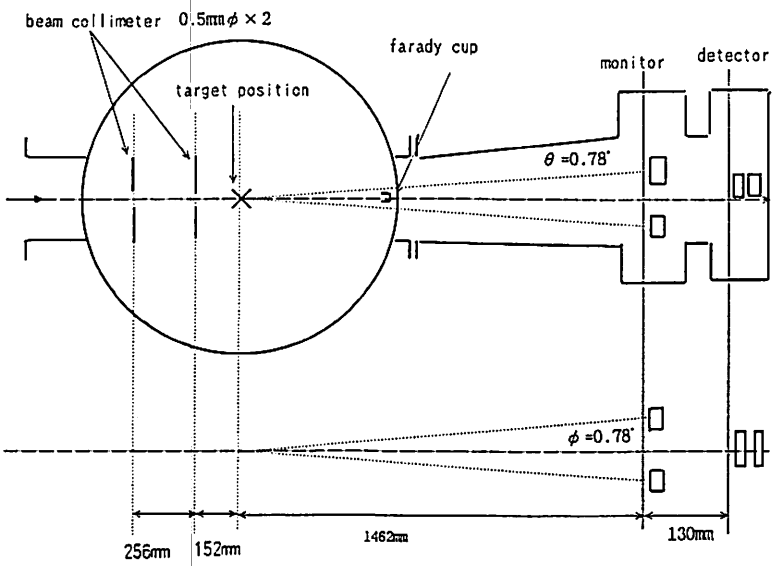

Fig. 2. Trapezoidal scattering chamber for the measurments at exteremely forward angles.

I. 2. The ^{54,56}Fe(d,n)^{55,57}Co Reactions at E_d=25MeV and Single-Particle Energies of Nuclei from A = 48 to 60

Aizawa T., Nakagawa T., Fujii Y., Hino T., Matsunaga M., Orihara H., Terakawa A.*, Itoh K.*, Yun C.C.*, Teramoto Y.*, Yamamoto A.*, Matsumura N.*, Kawami K.*, Suzuki H.*, Abe K.**, Ishii K.**, Tohei T.***, Suehiro T.***, and Ohnuma H.*****

Department of Physics, Tohoku University
*Cyclotron and Radioisotope Center, Tohoku University**
*Department of Nuclear Engineering, Tohoku University***
*Tohoku Institute of Technology****
*Chiba Institute of Technology*****

In nuclear shell-model, Z or N = 20-28 nuclei are expected to have simpler configurations in the ground state wave function, because of large energy gaps between orbits above and below $1f_{7/2}$ and itself. From this point of view, the spectroscopic studies for Sc and Cu isotopes have been done through (d,n) reactions with the Ca (Z = 20) and Ni (Z = 28) isotope targets, so far[1-3].

The (d,n) reaction at higher incident energy is likely to make a one-proton state as target nucleus + one proton. From spectroscopic factors derived as a ratio of experimental differential cross section to one calculated with distored wave Born approximation (DWBA),we can get information for a target nucleus, such as proton occupation probability and single-particle energies of shell-model orbits. Therefore, the (d,n) reaction plays an important role in the nuclear spectroscopic study.

Our spectroscopic study for ^{41}Sc has shown that proton or neutron holes exist in the doubly closed shell and ^{40}Ca does not behave as an complete 'inert core'[1]. Further, it has become clear that, from the results of ^{40,42,44}Ca experiments, as neutron increases, the core becomes more active[1]. This implies that the change of neutron number causes the change of proton single-particle energies, and then the proton transition probability from one shell to the other shell changes with the neutron number. On the other hand,the ^{48}Ca nucleus has turned out to be more hard inert core in comparison with ^{40}Ca[2].

As mentioned above, internal state for a nucleus cannot be described by the simple shell model because of the change of the proton single-particle energies with neutron number, even if the nucleus has the same proton number. Therefore, it is a very interesting problem how much the proton occupation probabilities and energy gaps between each shell-model orbit of $1f_{7/2}$ shell nuclei are. This time, based on above systematic results, a spectroscopic study has been done by the (d,n) reactions on ^{54,56}Fe (Z = 26) nuclei at E_d=25MeV.

The experiment was accomplished at CYRIC using AVF cyclotron and 44m time of flight facility[4,5]. The ^{54,56}Fe targets consisted of self-supporting foils with 2.6 and 3.4 mg/cm^2 thicknesses and 97.6 and 99.9% isotopical enrichments, respectively. Angular distributions of the differential cross section were measured between 0° and 70° at laboratory angles. Excitation energy spectra at θ_L=19° are shown in Figs. 1 and 2. Energy resolutions for the ground states were 200-230 keV. The angular distributions were measured for the states in excitation energy range up to 10 MeV.

DWBA calculations were done using the code DWUCK4[6,7]. Finite range and nonlocality corrections were applied to these calculations and the method of Vincent & Fortune[8] was used to do DWBA calculations for unbound states. Taking into account of deuteron break-up effect, the adiabatic approximation by Jonson and Soper[9] was used for optical model potential parameters in the incident channel. In this treatment, the potential parameters for a proton and neutron were taken from the systematics of Becchetti and Greenlees[10] and Carlson et al.[11] , respectively. The potential parameters of Carlson et al. were also used for the outgoing neutron. Typical differential cross sections for the ^{54,56}Fe(d,n)^{55,57}Co reactions are shown in Figs. 3 and 4.

Obtained spectroscopic factors for ^{55,57}Co are shown in Tables 1 and 2, respectively. The spectroscopic factors for ^{55}Co are almost the same strength as those have converged from the results of previous (d,n) and (^{3}He,d) experiments. In the case of ^{57}Co, these spectroscopic factors are slightly larger than the values derived in the past. However, the present results for ^{57}Co would be reliable, because of such similar measrement and analysis as in ^{55}Co.

The sums of the spectroscopic factors for each orbit are shown in Figs. 5 and 6. In the figure, the dotted lines show the simple shell-model limits and the solid lines show the derived values in the present work. Those for the $1f_{7/2}$ and 2p orbits reach the sum rule limits, so almost all strenghs for these orbits are considered to be observed. The strenghs for the $1f_{5/2}$ states are slightly smaller than the shell-model limits. This may imply that there exist weak peaks below 10 MeV, which have not been observed in the present measurement, or strengths distribute also in the excitation energy region above 10 MeV. The strenghs for the $1g_{9/2}$ and $2d_{5/2}$ orbits are much smaller than the sum-rule limits. These results are supposed from single particle energies in independent particle model, because those states are considered to lie mainly in the energy region above 10MeV.

Figure 7 shows the relative single particle energies for the ^{48}Ca, ^{54,56}Fe and ^{58,60}Ni. The spectroscopic factors obtained from the present (d,n) reactions were renormalized with the spectroscopic factors from previous pick-up reactions, ^{48}Ca, ^{54,56}Fe and ^{58,60}Ni (d,^{3}He)[12-15]. It is shown that with increasing mass number A, the energy gap between the $1f_{7/2}$ and 2s-1d shells becomes smaller and the one between the $1f_{7/2}$ and $1f_{5/2}$-2p shells becomes larger, except in the case of ^{54}Fe, in which it becomes close to the 2s-1d shells.

In conclusion, we have observed many proton-single-particle states for the ^{55,57}Co nuclei by the (d,n) reaction at E_d=25MeV in the excitation energy region up to 10 MeV and assigned the transfer momentum l for each state. The obtained spectroscopic factors are considered to be reliable, because they are almost similar to those derived from previous stripping experiments in ^{55}Co and satisfy the sum-rule predicted from the simple shell-model. The proton-single-particle energies calculated from the results of the stripping and pick-up reactions show a clear A-dependence, except ^{54}Fe.

References

1) Mori S., Phys. M. thesis, Tohoku University 1988.
2) Hino T., Phys. M. thesis, Tohoku University 1995.
3) Inomata T., Phys. M. thesis, Tohoku University 1992.
4) Orihara H. and Murakami T., Nucl. Instrum. and Meth. **188** (1981) 15.
5) Orihara H. et al., Nucl. Instrum. and Meth. **A257** (1987) 189.
6) Kunz P.D., a DWBA code. Univ. Colorado, unpublished.
7) Comfort J. R., Extended version for the program DWUCK4, unpublished.
8) Vincent C. M. and Fortune H. T., Phys. Rev. **C2** (1970) 782.
9) Johnson R.C. and Soper P. J. R., Phys. Rev. **C1** (1970) 976.
10) Becchetti F. D. and Greenlees G. W., Phys. Rev. **182** (1969) 1190.
11) Carlson J. D. et al., Nucl. Phys. **A249** (1979) 15.
12) Banks S. M. et al., Nucl. Phys. **A437** (1985) 381.
13) Puttaswamy N. G. et al., Nucl. Phys. **A401** (1983) 269.
14) Reiner K., Nucl. Phys. **A472** (1987) 1.
15) Mairle G., Nucl. Phys. **A543** (1992) 558.
16) Fortier S. et al., Nucl. Phys. **A288** (1977) 82.
17) Banu H. et al., Nucl. Phys. **A307** (1978) 106.

Table 1. Experimental spectroscopic factors for ^{55}Co.

	Present work $E = 25$MeV				^{54}Fe(^{3}He,d)^{55}Co S.Fortier et al. $E = 25$MeV [5]			
No.	Ex	l	j^π	$(2j+1)C^2S$	Ex	l	j^π	$(2j+1)C^2S$
1	0.00	3	$7/2^-$	1.98	0.000	3	$7/2^-$	1.68
2	2.17	1	$3/2^-$	1.28	2.165	1	$3/2^-$	1.20
3	2.56	1	$3/2^-$	0.91	2.565	1	$3/2^-$	0.80
4	2.93	1	$1/2^-$	0.36	2.935	1	$1/2^-$	0.29
5	3.30	1+3	$1/2^-+5/2^-$	0.50+2.05	3.302	3	$5/2^-$	2.31
					3.323	1	$1/2^-$	0.40
6	3.63	1	$3/2^-$	0.18	3.642	1	$3/2^-$	0.17
7	3.86	1+(3)	$(1/2^-+5/2^-)$	0.05+0.07	3.704	1	$(1/2^-)(3/2^-)$	0.01
			$(3/2^-+5/2^-)$	0.05+0.07	3.858			
		1+(4)	$(1/2^-+9/2^+)$	0.05+0.06	3.952	1	$(1/2^-)(3/2^-)$	0.02
			$(3/2^-+9/2^+)$	0.05+0.06				
8	4.17	1+3	$1/2^-+5/2^-$	0.31+0.87	4.164	1	$1/2^-$	0.27
					4.177	3	$5/2^-$	0.81
9	4.72	1	$3/2^-$	0.98	4.726	1	$3/2^-$	0.45
					4.752	1	$3/2^-$	0.37
10	5.17	1	$1/2^-$	0.46	5.172	1	$1/2^-$	0.32
11	5.52	1	$1/2^-$	0.17	5.550	1	$(1/2^-)(3/2^-)$	0.16
			$3/2^-$	0.17				
12	5.75	3	$5/2^-$	1.28	5.749	3	$5/2^-$	1.45
13	6.06	4	$9/2^+$	2.35	6.066	4	$9/2^+$	2.77
14	6.33	1+(2)	$3/2^-+(5/2^+)$	0.14+0.05	6.263	3	$(5/2^-)$	0.08
		1+(3)	$3/2^-+(5/2^-)$	0.19+0.08	6.326	1	$3/2^-$	0.08
					6.368	2	$5/2^+$	0.04
15	6.64	4	$9/2^+$	0.23	6.600	4	$(9/2^+)$	0.19
					6.673	3	$(5/2^-)$	0.07
16	6.85	1+3	$3/2^-+5/2^-$	0.16+0.27	6.830	1	$3/2^-$	0.09
					6.896	3	$5/2^-$	0.15
					6.916	3	$5/2^-$	0.30
17	7.09	4	$9/2^+$	0.44	7.110	4	$9/2^+$	0.61
18	7.28	1+4	$3/2^-+9/2^+$	0.45+0.08	7.239	4	$(9/2^+)$	0.10
					7.275	1	$3/2^-$	0.13
19	7.60	2+3	$3/2^++5/2^-$	0.06+0.11	7.576	2	$(3/2^+)$	0.02
					7.624	2	$3/2^+$	0.05
					7.654	3	$5/2^-$	0.07
20	7.89	2	$5/2^+$	0.13	7.888	2	$(5/2^+)$	0.10
					7.966	2	$5/2^+$	0.12
21	8.13	2	$5/2^+$	0.33	8.132	2	$5/2^+$	0.88
22	8.45	4	$9/2^+$	2.43	8.465	4	$9/2^+$	1.90
23	8.71	2+4	$5/2^++9/2^+$	0.04+0.21				
24	8.81	3	$5/2^-$	0.31	8.814	3	$5/2^-$	0.34
25	9.13	2	$5/2^+$	0.71	9.125	2	$5/2^+$	0.23
26	9.47	1+4	$(1/2^-)+9/2^+$	0.22+0.10				
			$(3/2^-)+9/2^+$	0.23+0.10				
27	9.73	2+4	$(5/2^+)+9/2^+$	0.11+0.07				
28	9.92							
29	10.36							
30	10.79							
31	11.19							
32	11.61							
33	12.04							
34	12.49							

Table 2. Experimental spectroscopic factors for ^{57}Co.

	Present work E = 25MeV				^{56}Fe(^{3}He,d)^{57}Co H.Banu et al. E = 18MeV [10]			
No.	Ex	l	j^{π}	$(2j+1)C^2S$	Ex	l	j^{π}	$(2j+1)C^2S$
1	0.00	3	$7/2^-$	2.25	0.000	3	$7/2^-$	1.50
2	1.40	1+1		2.34	1.376	1	$3/2^-$	1.29
					1.501	1	$1/2^-$	0.49
3	1.73	1	$3/2^-$	0.36	1.758	1	$3/2^-$	0.23
4	2.13	3	$5/2^-$	2.22	2.134	3	$5/2^-$	0.98
5	2.33	3	$7/2^-$	0.26	2.314	3	$7/2^-$	0.35
6	2.88	1	$3/2^-$	0.25	2.878	1	$3/2^-$	0.21
7	3.33	1+3	$3/2^- + 5/2^-$	0.81+1.00	3.177	3	$5/2^-$	0.31
					3.267	3	$(5/2^-)$	0.46
							$(7/2^-)$	0.71
					3.355	1	$(1/2^-)$	0.30
							$(3/2^-)$	0.39
					3.459	1	$(1/2^-)$	0.26
							$(3/2^-)$	0.35
8	3.94	1+3	$(1/2^-) + 5/2^-$	0.10+0.07	3.923	1	$(1/2^-)$	0.03
			$(3/2^-) + 5/2^-$	0.10+0.07			$(3/2^-)$	0.04
					4.001	(1)	$(1/2^-)$	0.05
							$(3/2^-)$	0.06
9	4.25	3	$(5/2^-)$	0.81	4.253	3	$(5/2^-)$	0.20
			$(7/2^-)$	0.51			$(7/2^-)$	0.31
10	4.62	2+4	$5/2^+ + 9/2^+$	0.44+1.68	4.590	4	$9/2^+$	2.60
					4.677	(1)	$(1/2^-)$	0.26
							$(3/2^-)$	0.33
11	5.12							
12	5.44							
13	5.71							
14	6.03	1	$(1/2^-)$	0.13				
			$(3/2^-)$	0.13				
15	6.21	1	$(1/2^-)$	0.15				
			$(3/2^-)$	0.15				
16	6.47							
17	6.78	3	$(5/2^-)$	0.48				
			$(7/2^-)$	0.31				
		4	$(9/2^+)$	0.56				
18	7.27	1	$(1/2^-)$	0.45	7.271	1		0.34
			$(3/2^-)$	0.43				0.31
19	7.43	3	$(5/2^-)$	0.83	7.434	3		0.52
			$(7/2^-)$	0.55				0.75
20	7.69	1	$(1/2^-)$	0.25				
			$(3/2^-)$	0.25				
21	8.01	1	$(1/2^-)$	0.16				
			$(3/2^-)$	0.16				
22	8.30							
23	8.53	1	$(1/2^-)$	0.38				
			$(3/2^-)$	0.38				
24	8.78							
25	9.11	1	$(1/2^-)$	0.29				
			$(3/2^-)$	0.29				
26	9.37							
27	9.69	(1)+4	$(1/2^-) + 9/2^+$	0.31+1.03				
			$(3/2^-) + 9/2^+$	0.31+1.03				
		(2)+4	$(5/2^+) + 9/2^+$	0.18+0.90				
28	9.91	1	$(1/2^-)$	0.27				
			$(3/2^-)$	0.27				

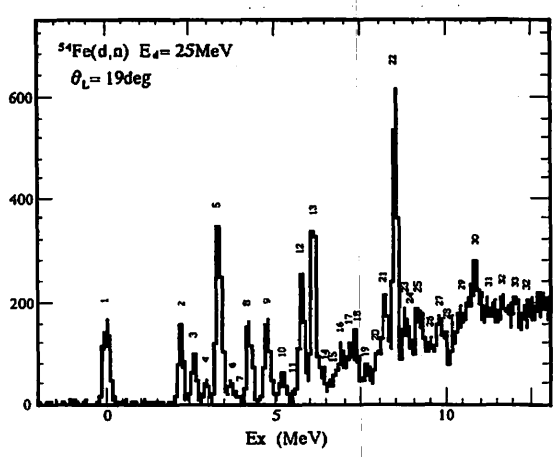

Fig. 1. A typical neutron energy spectrum in the ^{54}Fe(d,n)^{55}Co reaction at E_d = 25MeV.

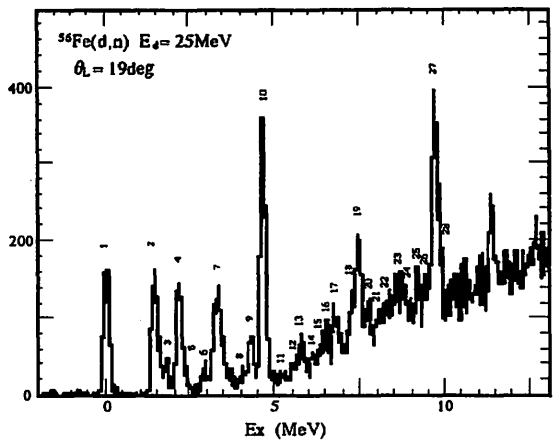

Fig. 2. A typical neutron energy spectrum in the ^{56}Fe(d,n)^{57}Co reaction at E_d = 25MeV.

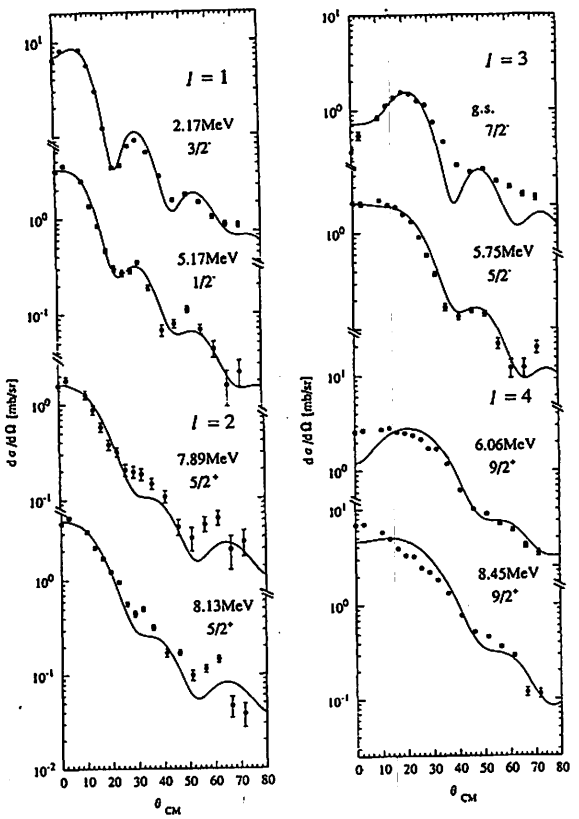

Fig. 3. Typical differential cross sections for the ℓ = 1-4 transitions in the ^{54}Fe(d,n)^{55}Co reaction.

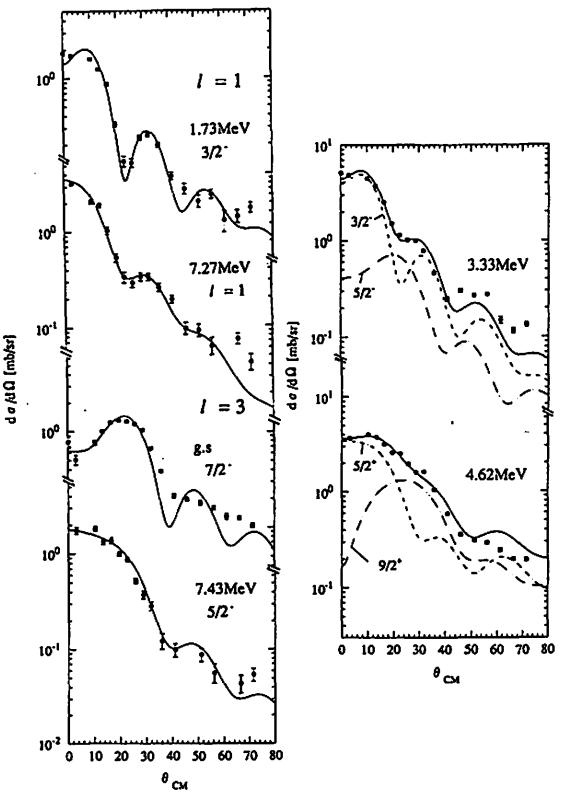

Fig.4. Typical differential cross sections for the transitions in the ^{56}Fe(d,n)^{57}Co reaction.

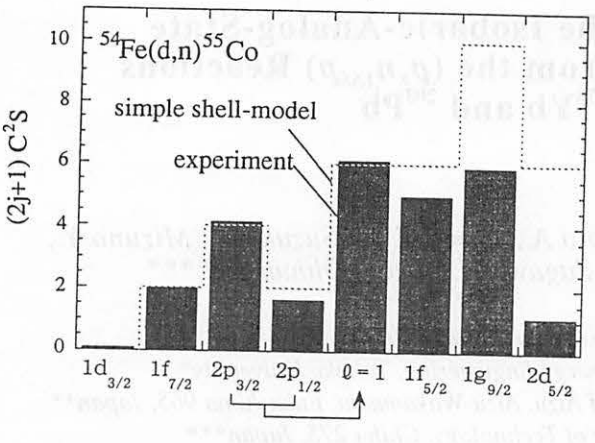

Fig. 5. Summed spectroscopic factors of ^{55}Co for each ℓ.

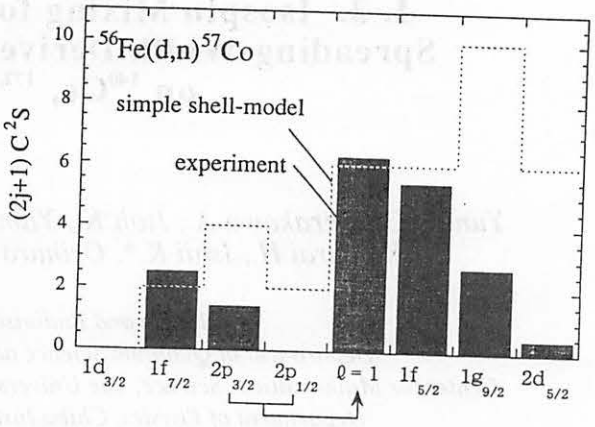

Fig. 6. Summed spectroscopic factors of ^{57}Co for each ℓ.

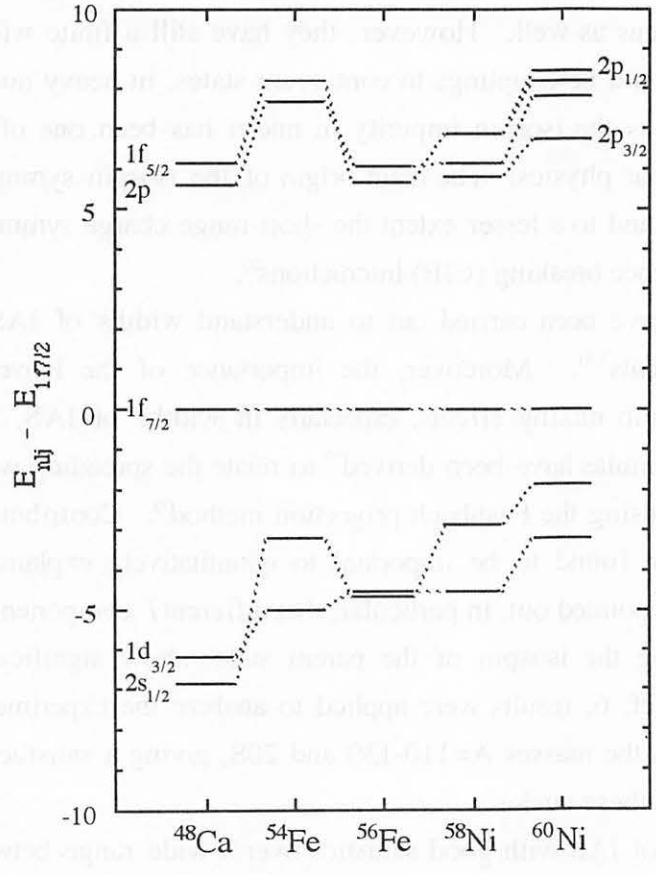

Fig. 7. Single-particle energies obtained from analyses of (d,n) and (d,^{3}He) experiments for ^{48}Ca, ^{54,56}Fe and ^{56,58}Ni. Each energy is measured from $E_{1f7/2}$.

I. 3. Isospin Mixing for the Isobaric-Analog-State Spreading-Width Derived from the $(p,n_{IAS}p)$ Reactions on ^{140}Ce, ^{172,174,176}Yb and ^{208}Pb

Yun C. C., Terakawa A., Itoh K., Yamamoto A., Kawami K., Suzuki H., Mizuno Y., Kamurai H., Ishii K., Orihara H., Sagawa H.**, and Ohnuma H.****

Cyclotron and Radioisotope Center, Tohoku University
*Department of Quantum Science and Energy Engineering, Tohoku University**
*Center for Mathematical Science, The University of Aizu, Aizu-Wakamatsu, Fukushima 965, Japan***
*Department of Physics, Chiba Institute of Technology, Chiba 275, Japan****

The idea of isospin was proposed by Heisenberg more than 60 years ago as a dynamical symmetry in physics, and was used successfully to explain structures of light nuclei. The most spectacular evidence of the isospin symmetry in heavy nuclei is the discovery of isobaric analog states (IAS) [1]. An IAS has indeed a narrow width manifesting the charge symmetry in a heavy nucleus as well. However, they have still a finite widths leading to a speculation that there should be couplings to continuum states, in heavy nuclei, through isospin violating forces. Thus the isospin impurity in nuclei has been one of the long-standing open problems in nuclear physics. The main origin of the isospin symmetry breaking is the Coulomb interaction, and to a lesser extent the short-range charge symmetry breaking (CSB) and charge independence breaking (CIB) interactions[2].

Several theoretical studies have been carried out to understand widths of IAS in relation with Coulomb matrix elements[3,4]. Moreover, the importance of the isovector monopole strength in various Coulomb mixing effects, especially in widths of IAS, was discussed[5]. Very recently explicit formulas have been derived[6] to relate the spreading width of IAS with the isospin impurity by using the Feshbach projection method[7]. Contributions from isovector monopole states were found to be important to quantitatively explain the experimental spreading width. It was pointed out, in particular, that different T-components in the T+1, T, and T-1 family, T being the isospin of the parent state, show significantly different strong A-dependence. In Ref. 6, results were applied to analyze the experimental data of limited number of nuclei with the masses A=110-130 and 208, giving a satisfactory description of the spreading widths of these nuclei.

Thus systematic decay data of IAS with good statistics over a wide range between A=130 and 208 nuclei have been strongly awaited for in order to obtain the A-dependence of spreading width, and to make clear the role of the T-component: i. e. the dynamics of isospin

symmetry breaking. Proton decay widths for IAS provide a good candidate to explore isospin mixing in nuclei. Studies of the decay properties for giant resonances following charge-exchange reactions are limited to a few cases. Especially for the $(p,n_{IAS}p)$ reaction, no reliable data has been reported due to its experimental difficulties encountered in measuring neutrons and decay protons with sufficient efficiency and with reasonable energy resolution.

Recently the study of isospin symmetry has become again a popular subject of nuclear structure, especially due to the development of experimental facilities for charge exchange reactions and those for radioactive beams. High resolution (p,n) measurements at low energy[8,9] following detection of decaying protons provide good place to investigate isospin properties of nuclei, compared to those at intermediate energy, because of the strong energy dependence of the effective interaction $V_\tau/V_{\sigma\tau}$. In this report, the experimental results for proton emission decay of IAS in ^{140}Pr, ^{172,174,176}Lu, and ^{208}Bi excited by (p,n) reactions at E_p = 35 MeV on ^{140}Ce, ^{172,174,176}Yb, and ^{208}Pb are presented. Deduced spreading widths, together with their A-dependence, are compared with theoretical predictions.

The experiment was performed using a 35 MeV proton beams from the AVF cyclotron, and neutron time of flight facilities[10,11] at CYRIC, Tohoku University. The targets used were self-supporting foil of ^{140}Ce in natural abundance and those of isotopically-enriched ytterbium isotopes and ^{208}Pb. Neutrons were detected with four neutron detectors containing the NE213 liquid scintillator located at the flight length of 12m. The size of each detector was 20.5 cm in diameter and 5 cm in length along the neutron-flight direction. The effective solid angle for the neutron detection was 0.53 msr. Decay protons were detected in coincidence with neutrons using a telescope of Si surface-barrier type detectors mounted at the distance of 8 cm from the target, and at θ_p = 135 degrees relative to the beam direction. The telescope consisted of ΔE (250μm thick), E (1000μm thick) and a veto counter, all with 100 mm^2 active surface area. The veto detector was used to reject energetic protons scattered at backward angles. The solid angle for the proton detection was 15.6 msr.

Figure 1 shows a schematic illustration for excitation of IAS in the (p,n) reaction followed by direct proton decay into residual neutron hole states. A sample neutron spectrum taken at E_p = 35 MeV for the first step in Fig. 1 is shown in Fig. 2. Over all energy resolutions for neutrons is 450 keV. High resolution experiments have been carried out as separate runs to obtain the total width of IAS. A typical resolution in this case is 27 keV for the ^{12}C$(p,n)^{12}$N reaction at E_p = 25 MeV by using a longer flight path of 44 m[12]. Decay proton spectra for the ^{140}Ce, ^{172,174,176}Yb, and ^{208}Pb targets are displayed in Fig. 3.

The total width Γ of IAS is expressed as a sum of the escape width $\Gamma^\uparrow$ and the spreading width $\Gamma^\downarrow$ as

$$\Gamma = \Gamma^\uparrow + \Gamma^\downarrow . \qquad (1)$$

The proton emission from the IAS is isotropic since IAS is 0^+. The branching ratio of the

proton decay is obtained with the singles and coincidence double differential cross sections

$$\frac{\Gamma_p^{\uparrow}}{\Gamma} = \frac{\Sigma\Gamma_{pi}^{\uparrow}}{\Gamma} \quad , \tag{2}$$

where

$$\Gamma_{pi}^{\uparrow} = \int \frac{d^2\sigma_{pi}}{d\Omega_n d\Omega_p} d\Omega_p = 4\pi \frac{d^2\sigma_{pi}}{d\Omega_n d\Omega_p}, \text{ and } \Gamma = \frac{d\sigma}{d\Omega_n} \quad . \tag{3}$$

The spreading widths $\Gamma^{\downarrow}$ thus obtained for the $(p,n_{IAS}p)$ reactions on ^{140}Ce, ^{172,174,176}Yb and ^{208}Pb are listed in Table 1 together with the theoretical predictions described later.

The isospin mixing amplitude in the parent nucleus can be obtained by coupling to isovector monpole states (IVM) with the isospin T+1 through the isospin violating force V_{IV}

$$\alpha_{\pi,M}^{T+1} = -\frac{1}{\Delta E_{M\pi}} \left\langle M;T+1,T \middle| V_{IV} \middle| T,T \right\rangle \tag{4}$$

where $\Delta E_{M\pi} = E_M^{T+1} - E_\pi$ is the energy difference between the IVM and the parent state. The spreading width of IAS is related with the isospin mixing amplitude $\alpha_{\pi,M}^{T+1}$ as

$$\Gamma_A^{\downarrow} = \Gamma_M \left(\alpha_{\pi M}^{T+1}\right)^2 \frac{T+1}{T} \left\{ \left(\frac{2T-1}{2T+1}\right) \frac{1}{(\Delta E_M^{T-1})^2} + \frac{(T-1)^2}{T+1} \frac{1}{(\Delta E_M^{T})^2} + \frac{4T^2}{(2T+1)(T+1)} \frac{1}{(\Delta E_M^{T+1})^2} \right\} (\Delta E_{M\pi})^2 \tag{5}$$

where Γ_M is the width of IVM at the energy of IAS, and the energy of IVM with T' in the daughter nucleus is given by

$$\Delta E_M^{T'} = \hbar\omega + \frac{V_1}{A} \vec{t} \cdot \vec{T}_C \tag{6}$$

Here, the excitation energy of IVM $\hbar\omega$ is given by $\hbar\omega = 170 / A^{1/3}$ MeV. V_1 is the strength of the Lane potential and $\vec{t} = 1$ is the isospin of IVM. The isospin mixing probability is estimated by using the sum rule approach to be

$$\left(\alpha_{\pi,M}^{T+1}\right)^2 = \frac{1}{T+1} P_{IM} \tag{7}$$

with

$$P_{IM} = Z^2 A^{2/3} \times 6.8 \times 10^{-7} \quad . \tag{8}$$

These formulas (7) and (8) give similar values to the isospin mixing probabilities calculated by microscopic mean field approaches. The formula (5) can be rewritten with more explicit isospin dependence as

$$\Gamma_A^{\downarrow} = \Gamma_M(E_A) P_{IM} \frac{1}{T}$$

$$\left\{ \left(\frac{2T-1}{2T+1}\right) \frac{1}{[1-(V_1/A\hbar\omega)(T+1)]^2} + \frac{(T-1)^2}{T+1} \frac{1}{[1-(V_1/A\hbar\omega)^2]} + \frac{4T^2}{(2T+1)(T+1)} \frac{1}{[1+(V_1/A\hbar\omega)^2 T]^2} \right\} \tag{9}$$

Notice that in this formula of the coupling to the IVM the second term with $T' = T$ has the dominant contribution.

The experimental spreading widths are compared with theoretical predictions in Fig. 4. The off-shell width $\Gamma_M(E_A)$ in Eq. (9) originates from the Feshbach projection method and there is no way to access experimentally. However, it was shown by theoretical study that the reasonable value for Γ_M should be in the range (500-700) keV[5]. The upper and lower curves in Fig. 4 are spreading widths corresponding to Γ_M of 500 and 700 keV, calculated by Eq. (9) for nuclei ranging A=134 (T=11) though 208 (T=22) using P_{IM} from Eq. (8) and V_1=100 MeV. The middle curve in Fig. 4 is for $\Gamma_M(E_A)$ = 625 keV, which was obtained by fitting the five experimental points by taking the off-shell width as a free parameter.

As seen in Fig. 4, the mass number dependence of $\Gamma_A^{\downarrow}$, is consistent with the calculated curves. Among the three terms in Eq. (9), corresponding respectively to $T' = T + 1$, $T' = T$, and $T' = T + 1$ contributions, the second term plays a dominant role. Almost 80% of the total magnitudes come from this term with increasing importance as the mass number increases, while the other terms become less important with mass number. These features are different from other theoretical models in the literature, where the first term due to the coupling to the IVM with $T' = T-1$ is the dominant term. It is obvious that the first and third terms have different isospin dependence and cannot reproduce the experimentally observed increase of the width as a function of isospin or mass number.

The quantitative agreement between the theory and the experiment also justifies the magnitudes of the isospin impurity P_{IM} represented by Eq. (8) within the experimental accuracy. The empirical values P_{IM} given in Table 1 are close to the microscopic predictions, although they are about 2 times larger than the hydrodynamical prediction[13].

To summarize, the experimental data of the width $\Gamma_A^{\downarrow}$ obtained by the $(p,n_{IAS}p)$ reaction have been reported for the first time in the mass region A = 140-208. These experimental widths are compared with the calculated values. The increasing width with the mass number is attributed to the isospin mixing contribution of the $T' = T$ component of the isovector monopole resonance. The off-shell width $\Gamma_M(E_A)$ at IAS is estimated to be 625 ± 60 keV. The empirical probabilities of isospin impurity show a good agreement with the values obtained from the microscopic models, but a factor 2 larger than the hydrodynamical prediction.

References

1) Anderson J. D. And Wong C., Phys. Rev. Lett. **7** (1961) 250; **8** (1962) 442; Anderson J. D. Wong C. and McClure J. W., Phys. Rev. **126** (1962) 2170.
2) Van Kolck U., Friar J. L. and Goldman T., Phys. Lett. **B371** (1996) 169.
3) Auerbach N., Hufner J., Kerman A. K., and Shakin C. M., Rev. Mod. Phys. **44** (1972) 48.
4) Auerback A. N., Phys. Rep. **98** (1983) 273.
5) Auerback A. N., Nucl. Phys. **A182** (1972) 247.
6) Suzuki T., Sagawa H. And Còlo G., Phys. Rev. **54**(1996) 2954.
7) Feshbach N., Annu. Rev. Nucl. Sci. **8**(1958)44; Ann. Rev. (N. Y.) **19** (1962) 287.
8) Orihara H., Ogawa K., Murakami T. et al., Nucl. Phys. **A403** (1983) 317.
9) Jon G. C., Orihara H., Niizeki T. et al., Phys. Rev. C **56** (1997) 900.
10) Orihara H. and Murakami T., Nucl. Instrum. Methods **181** (1981) 15.
11) Orihara H. et al., Nucl. Instrum. Methods **A257** (1987) 189.
12) Bohr A. and Mottelson B. R., *Nuclear Structure* (Benjamin, New York, 1969), Vol. I.

Table 1. Isospin impurities calculated by using the formulae (8) and (9). A P_{IM} is deduced by using Γ_M = 626 keV.

	Theory		Experiment			
	P_{IM}	$\left(\alpha_{\pi M}^{T+1}\right)^2$ (%)	E_x of IAS (MeV)	Γ (keV)	$\Gamma^{\downarrow}$ (keV)	P_{IM}(Exp.)
^{140}Ce-^{140}Pr	0.0617	0.47	11.04	46 ± 6	35 ± 6	0.053 ± 0.009
^{172}Yb-^{172}Lu	0.103	0.61	13.73	97 ± 10	70 ± 12	0.106 ± 0.018
^{174}Yb-^{174}Lu	0.104	0.58	14.80	96 ± 10	72 ± 10	0.109 ± 0.015
^{176}Yb-^{176}Lu	0.105	0.55	16.03	100 ± 15	74 ± 15	0.111 ± 0.023
^{208}Pb-^{208}Bi	0.161	0.70	15.17	232 ± 6	107 ± 17	0.161 ± 0.026

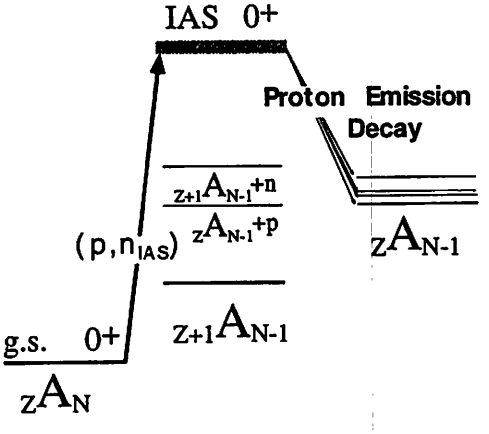

Fig. 1. Diagrams of the (p,n_{IAS} p) reaction.

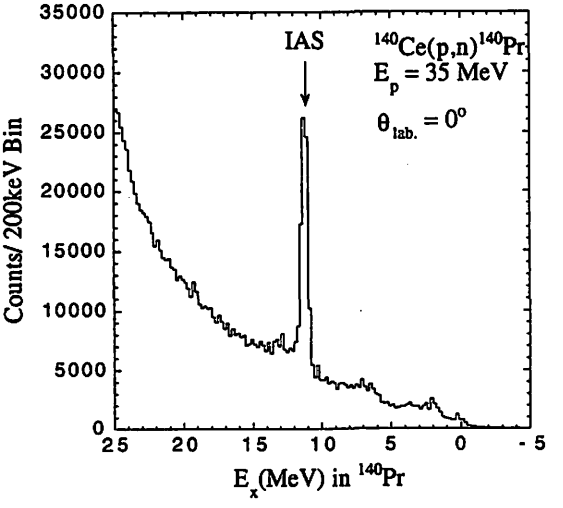

Fig. 2. Inclusive neutron spectrum of the ^{140}Ce(p,n)^{140}Pr reaction at 35 MeV.

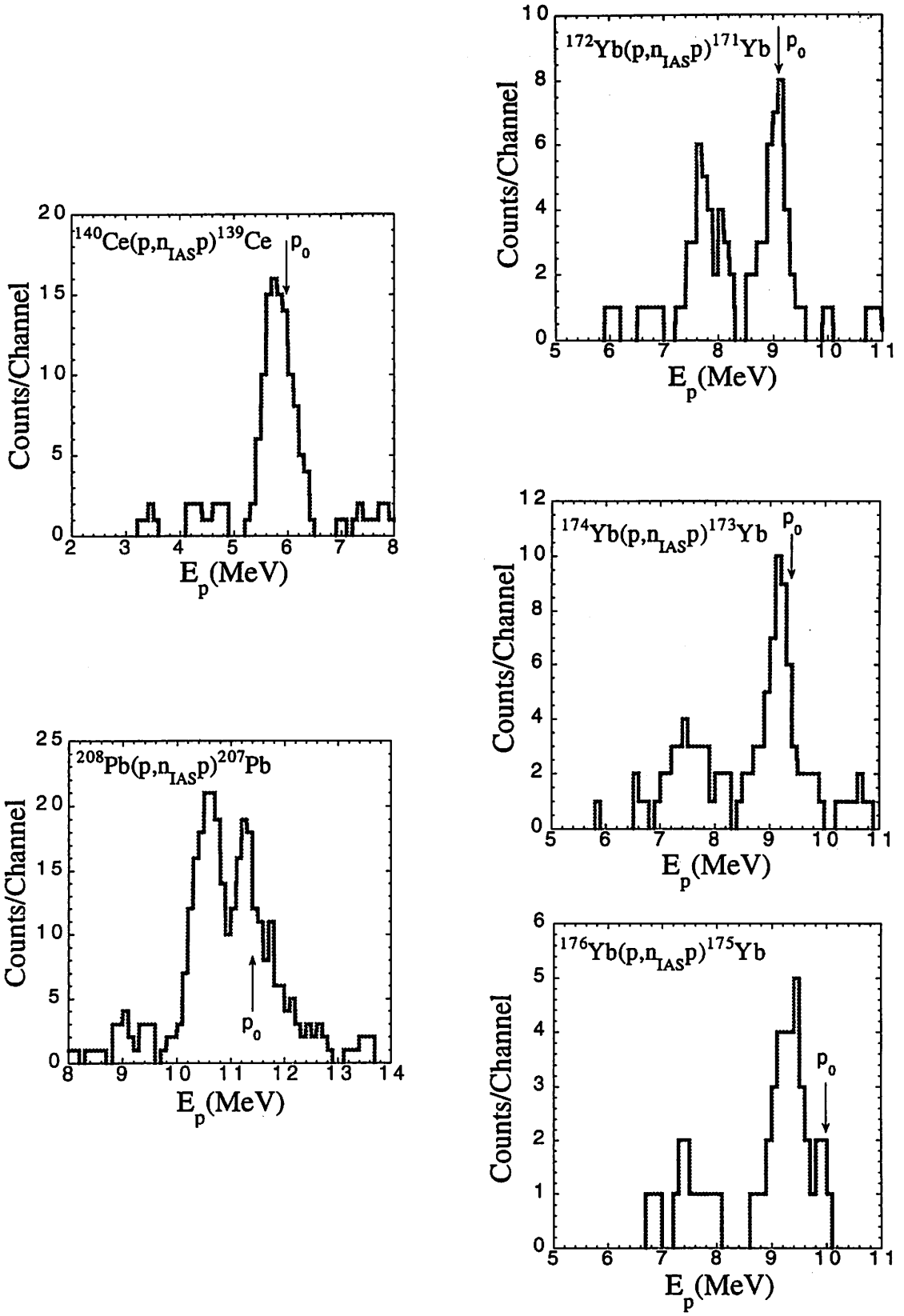

Fig. 3. Energy spectrum of the protons from the IAS into the low-lying neutron-hole states.

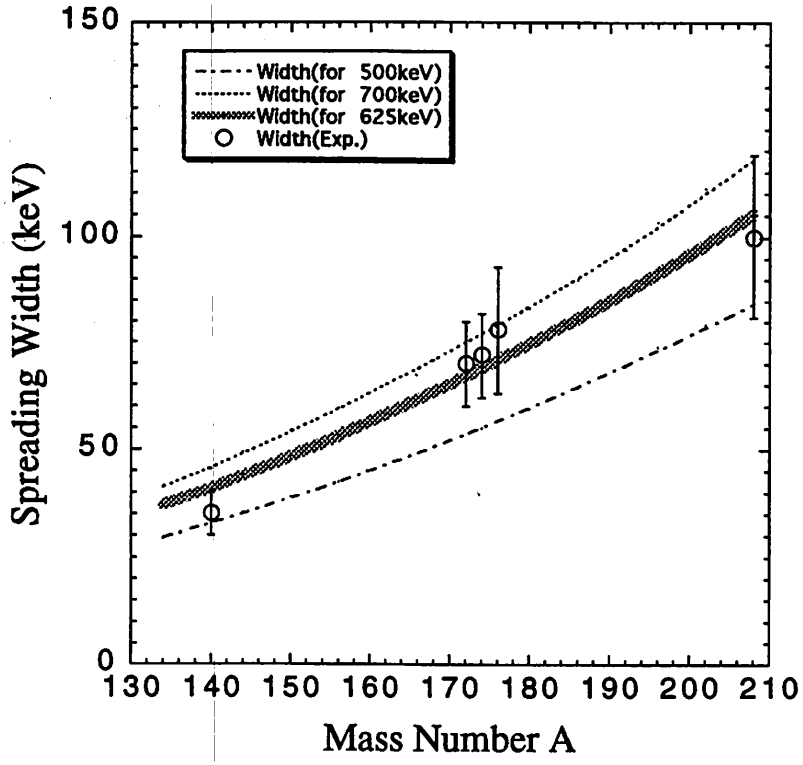

Fg. 4. Experimental and theoretical mass number dependences of spreading width $\Gamma_A^{\downarrow}$. Three lines denote eye guides for the results of theoretical culculation by Eq. (6) with the off-shell energies of 500, 626 and 700 keV for nuclei described in the text.

I. 4. Measurement of the g-factor of the 163 keV 3^+ State of ^{66}Ga

Kouda T., Fujita M., Sekiguchi K., Tanigaki M., Shinozuka T.*, Kawamura N.** and Fujioka M.**

Department of Physics, Tohoku University
*Cyclotron and Radioisotope Center, Tohoku University**
*Department of Technology, Aomori University***

The nuclear g-factor of the 163 keV 3^+ state of ^{66}Ga was measured by the TIPAD method.

The excited states were populated by the reaction ^{63}Cu(α, n)^{66}Ga at E_α = 12 MeV and 16 MeV. A natural Cu target of 4.2mg/cm^2 thickness was used. This target was placed in an external magnetic field of 11.8 kG applied perpendicularly to the beam-detector plane. Angular distributions of γ-rays were measured by a HPGe detector with an active volume of 21 cm^3 at seven angles between 64° and 130° with respect to the beam direction. Another HPGe detector with an active volume of 5 cm^3 placed at 270° was used as a monitor for normalizing the γ-rays yields for different angles. The angular distributions were measured for both fields up- and down-ward directions. The half-lives of the 163 keV and 1464 keV isometric states were remeasured to improve the accuracy of the previously reported values (163 keV, $T_{1/2}$ = 13 ± 5ns[1] and 1464 keV, $T_{1/2}$ = 57.3 ± 1.2ns[2]). The γ-rays were detected by a 21cm^3 HPGe detector and timed with respect to the alpha-beam bursts by using standard time-to-amplitude converter (TAC). The time resolution (σ) of this planar type HPGe detector was 1.9ns at 511 keV annihilation γ-ray. In the pulsed-beam measurements we used pulses with a repetition time of 220ns by using the S-chopper.

Angular distribution perturbed by the magnetic field is given by

$$W(\theta, \pm B_{\text{eff}}) = b_0 + \sum_{\lambda=\text{even}} \frac{b_\lambda}{\sqrt{1+(\lambda\omega_L\tau)^2}} \cos\{\lambda(\theta \mp \Delta\theta_\lambda)\},$$

where $\Delta\theta_\lambda = \frac{1}{\lambda}\tan^{-1}(\lambda\omega_L\tau)$ is the rotation of angular distribution, ω_L and τ are the Larmor-precession angular velocity and the life time of the level, respectively. Since $b_4 \approx 0$, only the terms with λ = 0 and 2 were taken into the consideration in this analysis. The g-factors is

obtained from the relation

$$g = -\frac{\hbar\omega_L}{\mu_N B_{eff}},$$

where B_{eff} is the effective magnetic field at the site of the nucleus. In this experiment, the effective magnetic field is equal to the external magnetic field because the residual gallium nuclei were implanted in copper.

In this analysis, we referred to a level scheme of ^{66}Ga presented by Morand et al[1]. The 1464 keV isometric state was also populated in this experiment. Therefore the rotation of angular distribution pattern for 96 keV γ-rays deexciting the 163 kev state is influenced by a γ-feeding from the 1464 keV state. Because if an isometric state is populated by reaction, Larmor precession of gallium nucleus starts at the same time, and the angular distribution pattern has already been rotating when the states of lower regions are formed as a result of decay of an isometric state. The values obtained for $\Delta\theta_2$ for the 96 keV γ-rays are $-10.3 \pm 1.8(^\circ)$ at $E_\alpha = 12$ MeV, and $-13.2 \pm 1.6(^\circ)$ at 16 MeV, respectively. This dependence of $\Delta\theta_2$ on E_α is due to the population of the 1464 keV state which is different at $E_\alpha = 12$ MeV and 16 MeV. Such an influence of the 1464 keV state on the 163 keV state can be removed by a two-components fitting of angular distribution ; one of the two components corresponds to a direct feeding of the 163 keV state by the nuclear reaction (A), and the other to an indirect feeding via the 1464 keV state (B). For the case (A) we have

$$W_A(\theta, \pm B_{eff}) = b_0 + \frac{b_2}{\sqrt{1+\tan^2(2\Delta\theta_2^A)}}\cos\{2(\theta \mp \Delta\theta_2^A)\}.$$

On the other hand for the case (B), the rotation of angular distribution for the 96 keV γ-rays is a sum of the rotation for the 163 keV state and that for the 1464 keV state. We have for the 96 keV γ-rays

$$W_B(\theta, \pm B_{eff}) = b_0 + \frac{b_2}{\sqrt{1+\tan^2(2\Delta\theta_2^B)}}\cos\{2(\theta \mp \Delta\theta_2^B)\},$$

where $\tan(2\Delta\theta_2^B) = \tan(2\Delta\theta_2^A) + \tan(2\Delta\theta_2^C)$ and $\Delta\theta_2^C$ is the rotation for the 114 keV γ-rays deexciting the 1464 keV state. The value obtained for $\Delta\theta_2^C$ is $-20.9 \pm 2.0(^\circ)$ in this experiment. The angular distribution (W_f) which is actually observed for the 96 keV γ-rays is a composition of W_A and W_B.

$$W_f(\theta, \pm B_{eff}) = W_A(\theta, \pm B_{eff}) + mW_B(\theta, \pm B_{eff}),$$

where m is the intensity ratio of (A) to (B). From the peak area of γ-ray energy spectrum, m is estimated to be 0.084 at E_α = 12 MeV and 0.274 at E_α = 16 MeV, respectively. The

intensity ratio of the two components (m) and the rotation angle for the 114 keV γ-rays ($\Delta\theta_2^C$) were taken as fixed in the fitting. The results of two-components fitting are presented in figures 1 and 2. The letters A and B in the figure indicate angular distributions W_A and W_B, respectively. Two straight lines are drawn at the positions of $90°+\Delta\theta_2^A$ and $90°-\Delta\theta_2^A$. The values obtained for $\Delta\theta_2^A$ are $-9.5\pm1.9(°)$ at E_α = 12 MeV, and $-10.9\pm1.8(°)$ at E_α = 16 MeV, respectively. These values agree within the experimental error. This means that the influence of 1464 keV isometric state on the 163 keV isometric state has been successfully removed. The weighted avarage of these values is $-10.3\pm1.8(°)$. From this value we get

$$\omega_L\tau = -0.186 \pm 0.036(\text{rad}).$$

The TAC spectrum was taken in coincidence with an energy window around the peak of interest. Background contributions were removed by subtracting spectra taken with energy windows just above and below the peak. Fig. 3 is a least-squares fit to the data for the 96 keV γ-rays, assuming two-components decay curve, obtained by folding the fitting function with the prompt line shape. The half life of the 1464 keV state was taken from the measurement for the 114 keV γ-rays. The prompt curves were obtained by using a ^{22}Na source selecting the respective gates of pulse height. The result for the half-lives of the 1464 keV and the 163 keV state are 39 ± 2ns and 4.2 ± 0.2ns, respectively.

The experimental values of $\omega_L\tau = -0.186 \pm 0.036(\text{rad})$, together with the half-life of $T_{1/2}$=4.2 ± 0.2ns and the effective magnetic field of B_{eff} = 11.8(4)kG lead to the g-factor of the 163 keV state,

$$g = +0.546(11).$$

For a doubly odd nucleus the g-factor is given by the Lande's formula

$$g = \frac{1}{2}(g_p + g_n) + (g_p - g_n)\frac{J_p(J_p+1) - J_n(J_n+1)}{2J(J+1)},$$

where J is the total angular momentum of the state of interest, g_p and g_n are the g-factors of the protons and neutrons, J_p and J_n are the angular momenta of the protons and neutrons, respectively. Filevich et al.[2] and Badica et al.[3] indicate that a better agreement with experiment is obtained when experimental values of the corresponding states in the neighbouring odd-A nuclei, instead of the Schmidt values, are used for g_p and g_n. The measured g-factor for the 163 keV state of ^{66}Ga is close to the value calculated by the above formula, +0.578, assuming the $[\pi(p_{3/2})^{-1}, \nu(f_{5/2})^3_{3/2}]_{3+}$ configuration by using experimental values for g_p and g_n. This configuration is the most likely one within the shell model.

References

1) Morand C. et al., Nuclear Physics **A308** (1978) 103-124.
2) Filevich A. et al., Nuclear Physics **A295** (1978) 513-524.
3) Badica T. et al., Hyperfine Interactions **36** (1987) 171-174.

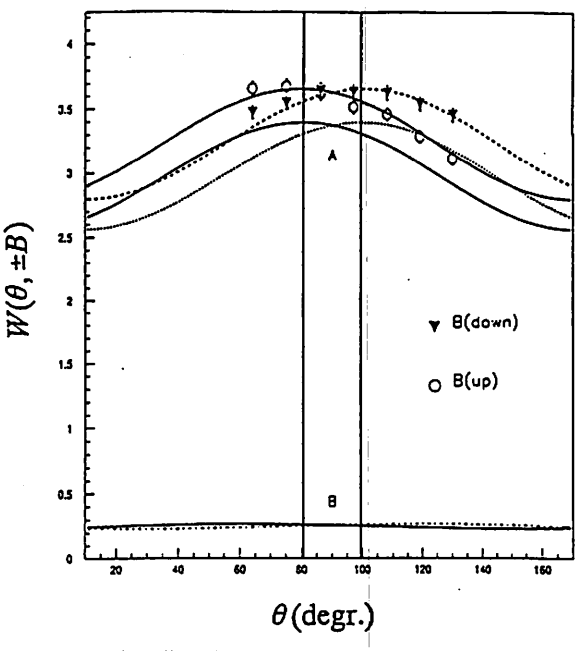

Fig. 1. Angular distribution for the 96 keV γ -rays at E_α = 12 MeV.

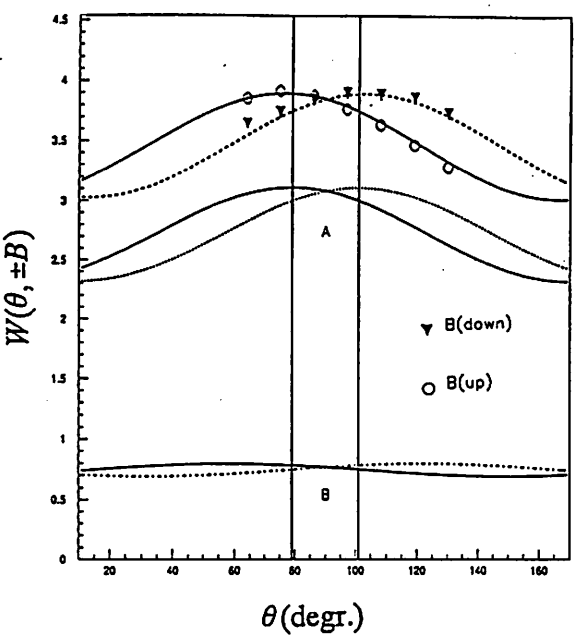

Fig. 2. Angular distribution for the 96 keV γ -rays at E_α = 16 MeV.

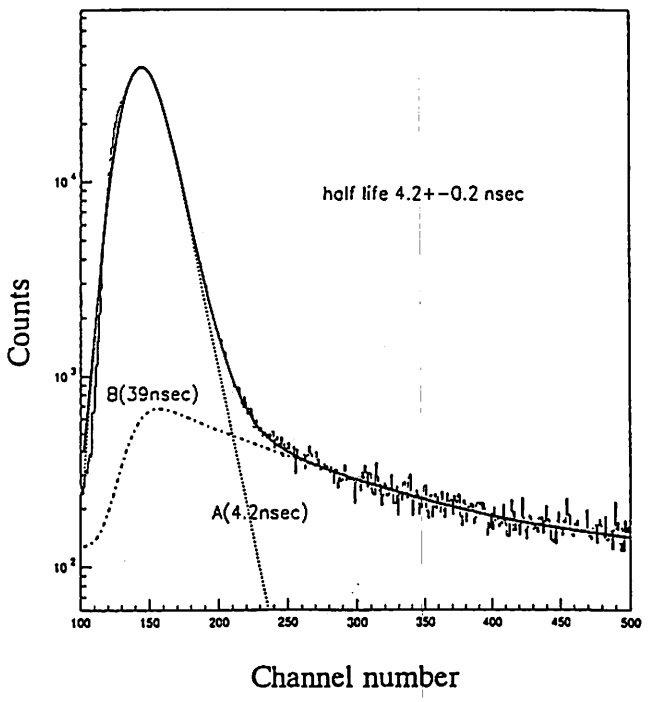

Fig. 3. TAC spectrum for the 96 keV γ -rays.

I. 5. Total Width of the Isobaric-Analog-State by the (*p*,*n*) Reactions on ^{140}Ce, ^{172,174,176}Yb and ^{208}Pb

Terakawa A., Yun C. C., Itoh K., Yamamoto A., Kawami K., Suzuki H., Mizuno Y., Kamurai H., Ishii K., and Orihara H.*

Cyclotron and Radioisotope Center, Tohoku University
*Department of Quantum Science and Energy Engineering, Tohoku University**

Existence of an isobaric analog state (IAS) has been considered to be one of the evidences of isospin symmetry in nuclei, since its discovery by the charge exchange (p,n) reaction[1]. At the same time, it has been found that an IAS has finite level width of several hundred keV in heavier nuclei, though it is narrow enough comparing to other kinds of giant resonance. The width of an IAS should primarily to attributed to that for particle decay in heavier nuclei, where the excitation energy of the IAS is sufficiently higher than that of binding energy of particles. However, it has been found that there are remaining width after subtraction of this escape width from the total width measured, while in lighter nuclei, where all particle decay channels are closed, an IAS has still a finite level width. The spreading width of an IAS is considered to be due to mixing to near-by lying T_o-1, 0^+ state for the cases of lighter nuclei[2], while, for the heavier nuclei, it is due to mixing to high-lying isovector monopole state through Coulomb mixing effects[3]. Thus, discussion on the width of IAS leads to the study of isospin mixing through Coulomb interaction[4], though other less effective short-range charge symmetry breaking (CSB) and charge independence breaking (CIB) interactions[5] have been investigated as well.

The total width Γ of an IAS is expressed as a sum of the escape width $\Gamma^{\uparrow}$ and the spreading width $\Gamma^{\downarrow}$ as:

$$\Gamma = \Gamma^{\uparrow} + \Gamma^{\downarrow} \quad (1)$$

Since the IAS is excited via the $L = 0$ transition, the proton emission from the IAS may be assumed to be isotropic. The branching ratio of the proton decay is obtained with the singles and coincidence double differential cross sections :

$$\frac{\Gamma_p^{\uparrow}}{\Gamma} = \frac{\Sigma\Gamma_{pi}^{\uparrow}}{\Gamma}, \quad (2)$$

where

$$\Gamma_{pi}^{\uparrow} = \int \frac{d^2\sigma_{pi}}{d\Omega_n d\Omega_p} d\Omega_p = 4\pi \frac{d^2\sigma_{pi}}{d\Omega_n d\Omega_p}, \text{ and } \Gamma = \frac{d\sigma}{d\Omega_n} \quad (3)$$

As such, the precise measurement of the total width of the IAS is of crucial importance[6] for

determination of the spreading width along with that for the escape width by decay experiment. In this report, we discuss the experimental results of the (p,n) reactions on ^{12}C, ^{140}Ce, ^{172,174,176}Yb, and ^{208}Pb targets taken by means of the high resolution low-energy time of flight technique.

The experiment was performed using a 25 MeV proton beams from the AVF cyclotron, and neutron time of flight facilities[7,8] at CYRIC, Tohoku University. The targets used were self-supporting foil of ^{12}C and ^{140}Ce in natural abundances and those of isotopically-enriched ytterbium isotopes and ^{208}Pb. The prepared targets were thin enough so as to lessen energy spread due to energy losses of incident protons. Their thicknesses were, 0.5, 1.8, 3.36, 4.11, 3.39 and 9.7 mg/cm^2, for ^{12}C, ^{140}Ce, ^{172,174,176}Yb, and ^{208}Pb targets, respectively. Neutrons were detected with 12- neutron detectors containing the NE213 liquid scintillator located at the flight length of 44 m.

Figures 1 through 6 illustrate the neutron excitation energy spectrum for the (p,n) reactions on ^{12}C, ^{140}Ce, ^{172,174,176}Yb, and ^{208}Pb leading to the ground and first excited (E_x = 2.190 MeV) states in ^{12}N, where no level width of the residual states are encountered, and to the IAS in ^{140}Pr, ^{172,174,176}Lu, and ^{208}Bi, where the final state has specific level width to be presently determined. Lines in the figures denote peak-fitting results, calculated by *The Voigt Profile* which has been used in spectroscopy when a given line shape is neither a Gaussian nor Lorentzian but rather is a combolution of the two[9].

Energy spread for observed neutron spectrum is, thus, partly due to following experimental conditions:

1) Resolving time of detector and electronics ΔT_d (measured to be 0.42 nsec by detecting cosmic μ-ons passing though near-by lying detectors)
2) Thickness of detector ΔT_d (ΔL = 5cm, corresponding to the ambiguity of flight pass length of neutron and gamma rays)
3) Ambiguity of detection solid angle $\Delta\theta_{Lab.} = 0.6°$ (kinematical effect)
4) Energy spread of beam $\Delta T_{\Delta Ebeam}$ ($\Delta E/E$ = 1/1200)
5) Time spread of beam bunch Δt_b
6) Beam energy losses in the target.

Among these, the most significant but difficult to estimate contribution is 5) time spread of beam bunch. Fortunately, we have another data. That is the time spread of γ-flash which contains ambiguities 1), 2) and 5), the last one being minor contributions.

Experimental conditions are listed in Table 1. The values of each contribution are listed in order to give the measure for experimental energy spread to detect a mono-energetic neutron. For the (p,n) reaction leading to the ground and first-excited states in ^{12}N, reasonable comparisons are given in Table 2. On the other hand, those for heavier nuclei, Γ_{IAS} is obtained from the observed width($\Delta E_{IASpeak}$) by removing the effect of experimental energy spread($\Delta E_{exp.}$). Another example to justify the present analysis is the case of the

width($\Delta E_{IASpeak}$ =220±30 keV) of the IAS in ^{208}Bi, for which the IAS level width has been previously reported to be 232 keV by Melzer et al[10].

We have successfully determined the level widths of the IAS observed by the (p,n) reactions in ^{140}Pr, ^{172,174,176}Lu, and ^{208}Bi by means of the high resolution TOF neutron detection, and measurement of γ-flash. These results, justified by the measurement for the ^{12}C(p,$n_{o \text{ and } 1}$)^{12}N reaction, and comparison with previous report for the ^{208}Pb(p,n_{IAS})^{208}Bi result, are ready to be used to determine the spreading width of the IAS, along with the data of corresponding escape width data.

References

1) Anderson J. D. and Wong C., Phys. Rev. Lett. **7** (1961) 250; **8** (1962) 442; Anderson J. D. Wong C. and McClure J. W., Phys. Rev. **126** (1962) 2170.
2) Orihara H., Ogawa K., Murakami T. et al., Nucl. Phys. **A403** (1983) 317.
3) Auerback A. N., Nucl. Phys. **A182** (1972) 247.
4) Suzuki T., Sagawa H. And Còlo G., Phys. Rev. **54** (1996) 2954.
5) Auerbach N., Hufner J., Kerman A. K., and Shakin C. M., Rev. Mod. Phys. **44** (1972) 48.
6) Auerback A. N., Phys. Rep. **98** (1983) 273.
7) Van Kolck U., Friar J. L. and Goldman T., Phys. Lett. **B371** (1996) 169.
8) Yun C. C. et al., See report in this issue.
9) Orihara H. and Murakami T., Nucl. Instrum. Methods **181** (1981) 15.
10) Orihara H. et al., Nucl. Instrum. Methods **A257** (1987) 189.
11) Hutchinson L., Igor Technical Notes 1991, *#026: The Voigt Profile.*
12) Melzer R. et al., Nucl. Phys. **A432** (1985) 363.

Table 1. Experimental conditions for determination of the width of IAS by the (p,n) reaction at E_p = 20 MeV.

Target Nucleus	Residual Nucleus	E_x. of IAS (MeV)	Target Thickness (mg/cm^2)	E_n (lab.) (MeV)	V_n (lab.) (cm/nsec)
^{12}C	^{12}N(g.s.)		0.5	6.353	3.468
^{12}C	^{12}N(1st.)		0.5	5.393	3.197
^{140}Ce	^{141}Pr	11.04	1.80	9.760	4.288
^{172}Yb	^{172}Lu	13.73	3.36	7.934	3.870
^{172}Yb	^{174}Lu	14.80	4.11	8.009	3.888
^{176}Yb	^{176}Lu	16.03	3.39	8.056	3.900
^{208}Pb	^{208}Bi	15.17	9.70	6.130	3.408

Table 2. Various uncertainties contributing to the energy spread for neutrons leading to IAS with a flight path of 43.25m. Also listed are estimated energy spread for IAS peaks($\Delta E_{exp.}$), observed width of IAS peaks($\Delta E_{IASpeak}$), and resultant intrinsic IAS width(Γ_{IAS}).

Residual Nucleus	ΔT_L (nsec)	$\Delta T_{\Delta Ebeam}$ (nsec)	$\Delta T_{\Delta Etarget}$ (nsec)	$\Delta T_{beam(\gamma\text{-flash})}$ (nsec)	ΔT_{Total} (nsec)	$\Delta E_{exp.}$ (keV)	$\Delta E_{IASpeak}$ (keV)	Γ_{IAS} (keV)
^{12}N(g.s.)	1.442	2.045	0.932	1.845	3.246	33	35±4	
^{12}N(1st.)	1.564	2.614	1.192	1.845	3.755	30	27±3	
^{140}Pr	1.17	1.10	0.99	1.41	2.36	45	73±3	46±2
^{172}Lu	1.292	1.467	2.603	1.648	3.649	52	120±18	97±15
^{174}Lu	1.286	0.670*	1.204*	1.303	2.354*	73	135±13	96±10
^{176}Lu	1.282	1.434	2.334	1.337	3.306	48	120±18	100±16
^{208}Bi	1.47	2.20	9.43	1.54	9.91	95	254±40	220±30

* values for the neutron flight path of 20 m instead of 43.25 m.
In order to obtain ΔT_{Total}, all vatues are written in time by using the following relation:

$$\Delta E(\text{MeV}) = \frac{2 \times \Delta T(\text{n sec})}{72.3 \times \text{L(m)}} E^{3/2}(\text{MeV})$$

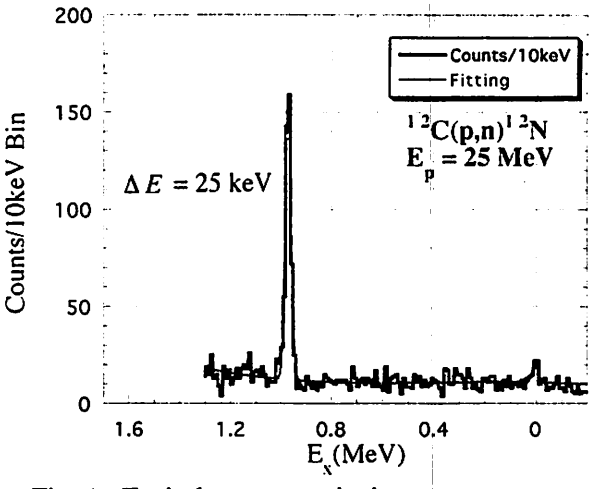

Fig. 1. Typical neutron excitation energy spectrum of the ^{12}C(p,n)^{12}N reaction at Ep = 25 MeV, taken at 0° with a flight path of 43.25m. See text for peak-fitting.

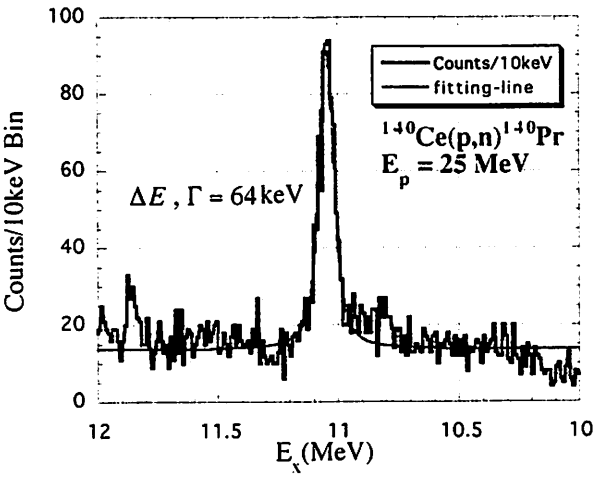

Fig. 2. Same as Fig. 1 but for the ^{140}Ce(p,n)^{140}Pr reaction at Ep = 25 MeV.

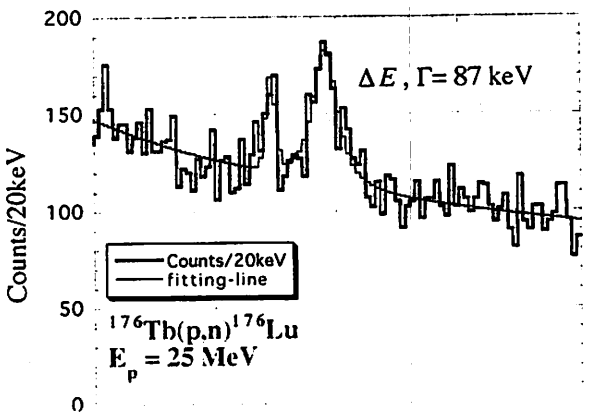

Fig. 3. Same as Fig. 1 but for the ^{176}Yb(p,n)^{176}Lu reaction at Ep = 25 MeV.

I. 6. Energy Depandence of Isomeric Yield Ratios of Fission Products in ^{232}Th + p System

Goto S., Kaji D., Kudo H., Fujita M., Shinozuka T.* and Fujioka M.**

Department of Chemistry, Faculty of Science, Niigata University, Niigata Japan
*Cyclotron and Radioisotope Center, Tohoku University**

In nuclear fission process, the angular momentum of fission fragment provides much information about the saddle point configuration and/or the state shortly after the scission point configuration. Because an isomeric yield ratio which is defined as the yield ratio of a high spin isomer to that of low spin one, σ_h/σ_l, reflects directly the angular momentum, the isomeric yield ratio has been examined precisely in the present work.

Until now, isomeric yield ratios have been measured in a wide mass range for the system of 24 MeV proton-induced fission of ^{238}U[1] and ^{232}Th. In the present work, the isomeric yield ratio of ^{135}Xe in proton-induced fission of ^{232}Th was measured by the use of IGISOL in the proton energy range of 13 to 26 MeV. The determination of fission products was made by a gamma-ray spectrometry. The obtained radioactvities were converted to independent yields by correcting the amount of the feeding from parent nuclides, if any.

The obtained isomeric yield ratio of ^{135}Xe is shown in Fig. 1(a) as a function of the proton energy. It is found that the isomeric yield ratio increases with the proton energy. The same tendency has been found in other fragment masses and in other systems. In order to see the correlation of the isomeric yield ratio with the charge dispersion, the charge distribution of A=135 is determined. The result is shown in Fig. 1(b), where the fractional yield of ^{135}Xe is shown. It is found that the fractional yield increases with the proton energy except in the case of E_p=13 MeV. This indicates that the charge dispersion of fission fragments relates to the isomeric yield ratios. In the system of 13 MeV proton energy, despite of the relatively larger fractional yield, the isomeric yield ratio is smaller. The detailed analysis is now in progress.

Reference

1) Tanikawa M., et al., Z. Phys. **A347** (1993) 53.

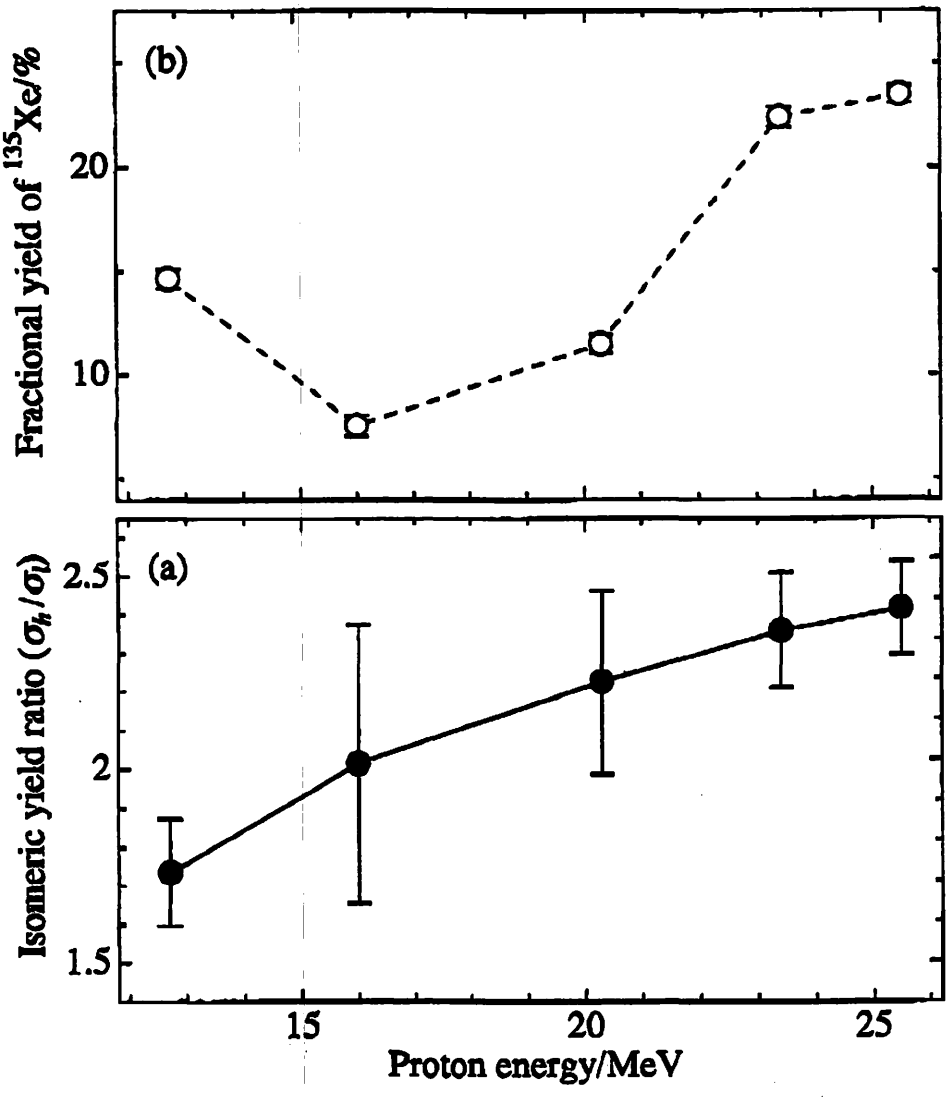

Fig. 1. A plot of isomeric yield ratios (a) and fractional yields (b) of ^{135}Xe against the proton energy in system of proton-induced fission of ^{232}Th.

I. 7. A Proposal for a High-Efficiency Mini Crystal Ring for Perturbed γ-γ (θ) Measurements at an IGISOL

Fujioka M., Shinozuka T., Tanigaki M., Honma T. and Wada M.***

Cyclotron and Radioisotope Center, Tohoku University
*NIRS, Chiba**
*Institute for Nuclear Study, University of Tokyo, Tokyo 188, Japan***

As an on-line separator an IGISOL has its characteristic features, by which many short-lived nuclie have been found and/or studied. One of the serious weak points of an IGISOL, however, is that the mass-separated beam therefrom is not so strong, typically ~10 atoms/s.

We have been engaged in the measurement of nuclear g-factors using perturbed γ (θ) in-beam, where we realized a difficulty arising from the existence of "higher isomers"[1]. In order to avoid this γ - $\gamma(\theta)$angular correlation instead of γ (θ)-angular distribution should be measured.

For doing such a measurement using short-lived isotopes made by our IGISOL we are proposing to contruct a high-efficiency apparatus consisting of as many as possible small γ - detectors of CdZnTe, 10×10×3 mm^3 encircling the source like a "ring". The purturbation field will be applied by a compact permanent- magnet circuit with variable polarity[2], the field intensity being designed to be ±2 T ; see Fig. 1.

References

1) Kouda T., Measurement of the g-factors of low-lying states of ^{66}Ga§ Master's thesis, 1997, Tohoku University.
2) Honma T. et al., NIM **A361** (1995) 13.

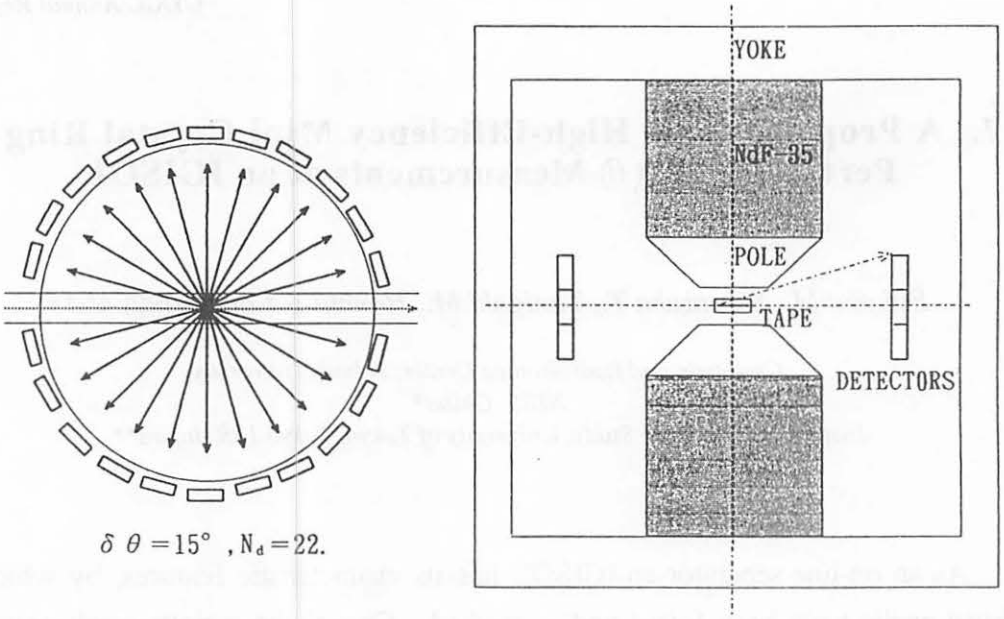

Fig. 1. A conceptual design of a high-efficiency mini crytal ring.

I. 8. Oxidation of Fe Studied by PAC and Mössbauer Spectroscopy

Hanada, R

Institute for Materials Research, Tohoku University

Introduction

Although Fe is one of the most technologically important materials, it is well known that it deteriorates during in use in an ambient atmosphere unless properly coated. This is due to the oxidation of Fe or steels by oxygen in the atmosphere. Also Fe oxides are utilized to fabricate electronics devices as storage media because of their unique magnetic properties. So the studies of Fe oxidation process or the properties of the oxcides are one important subject in materials science as well as in solid state physics.

In the present experiment, PAC as well as Mössbauer spectroscopy (CEMS) were performed to study the oxidation process of pure Fe or the magnetic properties of the resulting oxcides.

Experimental

PAC: The PAC probe ^{111}In was implanted to an Fe specimen at the energy of 40keV to the activity of several 10μCi. The specimen was annealed in an UHV at 400C to anneal out the damages due to the implantation. Subsequently, an oxidation procedure (500C×30min, 5×10^{-1} Torr air. Treatment I) was given to the specimen. After measuring the PAC spectrum, the specimen was given two annealing treatments(500C× 30min, 10^{-7} Torr UHV, Treatment II: an additional 6 hrs at 500C in UHV,Treatment III: and 30min at 600C in UHV,Treatment IV) for further PAC spectroscopies. As will be shown later, these annealing tveutments mentsin a vacuum are crucial to obtain a good PAC spectrum for the present Fe oxides using ^{111}In as the probe. The PAC spectroscopy was performed at RT in a three detectors mode with and without a vertical magnetic field.

CEMS: Almost the same oxidation treatments were given to an Fe foil (^{57}Fe enriched)for CEMS. The purpose of CEMS is to identify the species of oxides formed during the treatments. The use of the enriched foil is to obtain a high S/N ratio spectrum within a reasonably short time.

Results and Discussion

Fig.1 shows the results of the PAC spectrum measurements for Fe given the treatments described above. After the Treatment I, the spectrum shows a precession pattern with a very small amplitude (comparable with that in pure Fe). However, the amplitude becomes quite large after the treatment II and grows further after the Treatment III or IV. Since the period of the precession is 36 ns for the null external magnetic field(H=0) measurement and about 3 times longer than that in pure Fe (11.2ns), ^{111}In should be in an oxide phase and not in Fe host. The precession period becomes half upon the application of the vertical magnetic field and so the coupling of ^{111}In in the oxide is magnetic and not quadrupolar. This effect of the external magnetic field is in accord with a theoretical study[1] and also with the experimental results in Ni[2].

In order to examine what kind of oxides are formed after each treatments, CEMS were performed for Fe given the same treatments as the PAC specimen. Fig. 2 shows the results and reveals that γ Fe_2O_3 (mag-hematite) is formed after the Treatment I and Fe_3O_4 (magnetite) after Treatment II. These identifications are confirmed by (1) additional MS on Fe_2O_3 or Fe_3O_4 powders obtained as chemicals in the present and (2) other MS results on Fe oxides[3].

So we can conclude that the amplitude of PAC spectrum is quite large in Fe_3O_4 but not in Fe_2O_3. Since the amplitude of the PAC precession pattern stays constant up to 350ns and shows no dumping at RT, the frequency (or similarly, the magnitude of the hyperfine field) has only one value in Fe_3O_4 for ^{111}In. This shows a discrepancy from the result of CEMS since it shows that there are two magnetically different sites (Fe_3O_4-I and -II as shown in Fig.2) for ^{57}Fe. So the possibilities are: (1) different from the ^{57}Fe probe ,only one site is occupied by the ^{111}In probe or (2) both sites are occupied by ^{111}In but with exactly the same magnitude of the hyperfine field. Here we assume that the ^{111}In ions occupy the same sites with Fe ions and not that of O ions. Further experiments are now in progress to solve the apparent discrepancy between CEMS and PAC results.

In a previous paper where a result of an attempt to prepare a ^{111}In-Fe specimen by a diffusion method has been reported[4], a precession pattern with the period of 1/3 of that in Fe was found in a specimen annealed for several 10hrs in H_2. This has been interpreted by the present author as due to ^{111}In adsorbed on the surface. In the present light of oxidation experiments, however, the result should be interpreted as that an oxide layer was formed even in the H_2 treatment thus giving rise to the 1/3 precession pattern.

Acknowledgements

The author is indebted to prof. S. Nasu, Osaka University, for his permission to use his Mössbauer spectrum fitting program.

This work was supported by a Grant-in Aid for Scientific Research in Priority Area from the Ministry of Education, Science and Culture of Japan.

References

1) Frauenfelder H. and Steffen R.M. et al: *in α, β, γ Ray Spectroscopy II*, ed by K.Siegbahn North-Holland (1968).
2) Hanada R.:CYRIC Annual Report-1994 (1995) 44.
3) Simmons G. W. and Leidheiser H. Jr.: *in Application of Mössbauer Spectroscopy II* ed by Cohen R. L., Academic Press (1976).
4) Hanada R.: CYRIC Annual Report-1994 (1995) 49.

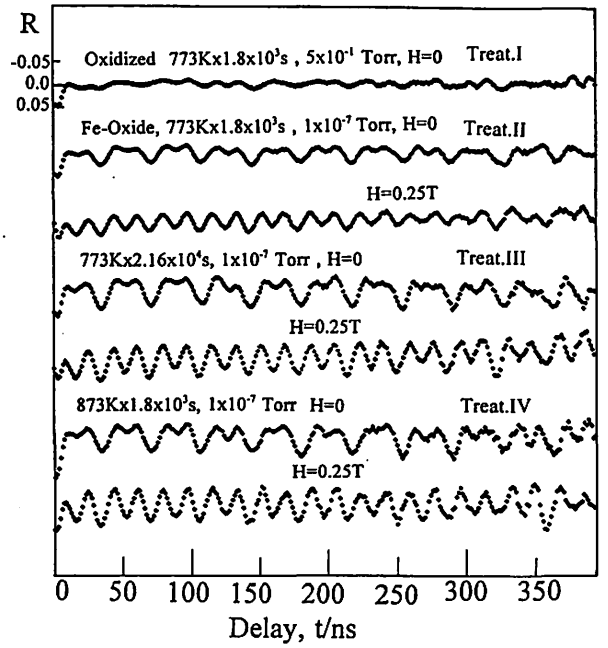

Fig. 1. PAC spectra for Fe during the oxidation treatments.

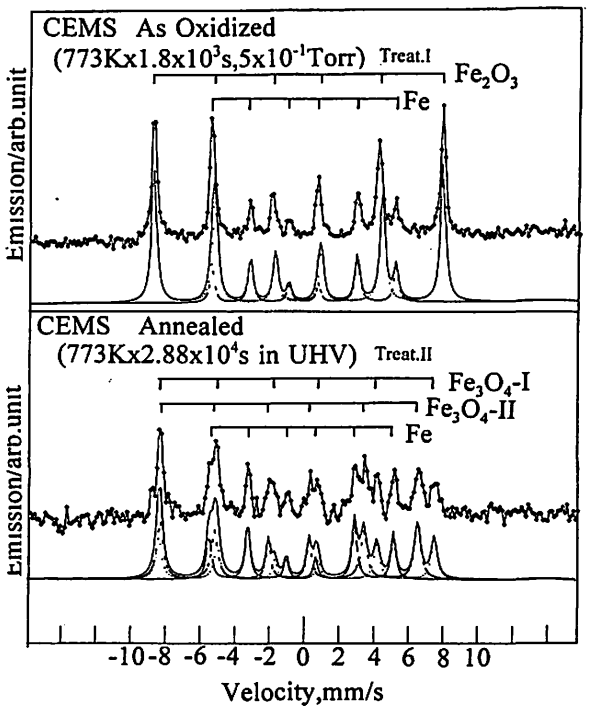

Fig. 2. CEMS spectra for Fe during the oxidation treatments. Data (symbols) and calculated (lower lines).

I. 9. PAC Study of Phosphorus Implanted Si

Hanada, R

Institute for Materials Research, Tohoku University

Introduction

Phosphorous (P) is a Va element and so acts as a doner in IVa Si by donating one electron to the lattice. So P is implanted or diffused to Si to fabricate n-type part in electronic devices. Since the system Si-P is a binary alloy, the solubility of P in Si must be known to perform most appropriate P doping.

In the present the dose of P is varied to control the local concentration and how the PAC signals depend on it is examined. This result is compared with the reported results of the P solubility in Si[1, 2].

Experimental

5×20×0.5mm^3 Si specimens were cut from a wafer (n-type low resistivity, (100) surface) supplied by NILACO. P was implanted to them with the doses between 4×10^{14} and 5×10^{16}/cm^2 at 30keV. The local maximum concentration was estimated as in Table I by the measured dose and TRIM calculations[3]. After the annealing at 600 C for 30min to remove the damage and amorphouszation by the implantation, ^{111}In was implanted to them at RT with the energy at 40keV. The PAC spectrum was measured at RT after the annealing between 700 C and 1000 C in a vacuum.

Result

Fig.1 summarizes the results of the present experiment where ^{111}In PAC spectra for Si implanted with P to various doses are shown. Although annealing was performed between 600C and 1000C, the spectrum is almost the same for the specimens where the P dose is below 5×10^{15}/cm^2. Here, a simple precession pattern with the period 35ns is present for all specimens showing a simple ^{111}In-P pair is formed, which shows a good agreement with a reported result for P implanted Si[4]. Namely P is soluble as an isolated impurity in Si lattice up to this dose(concentration).

On the contrary, for the highest dose (4×10^{16}/cm^2), the spectrum is almost featureless showing P is not in a form of an isolated impurity. For this dose, the local P concentration (10^{22}/cm^3) exceeds the P solubility limit at 1000C in Si (10^{21}/cm^3). So most of

P are in a form of precipitates and hence if ^{111}In probes are incorporated in them, no unique EFG will not be present thus giving no well defined precession pattern.

The spectrum for the intermediate dose(10^{16}/cm^2) is an interesting case since it has some complex pattern different from the simple ones for the low dose cases. For this dose, P seems to be present in a form somewhere between an isolated impurity and precipitates. Namely, part of P is likely to be present as dimers or trimers for this concentration. Further analysis of the spectrum is in progress to examine the possibility.

The comparison of the present results with the known P-Si phase diagram shows that the agreement between them is only qualitative. The ambiguities in the present P concentration estimation (the P dose measurement, the conversion of the dose to the local P concentration by TRIM, the concentration distribution of the implanted P, et cet) are responsible for it. Also the Si-P phase diagram which used for comparison was the one determined in an earlier days of semiconductors industry[1] and hence may need some modifications for the recent Si crystals, which are being fabricated to almost defects free state, as has been suggested in ref. 2.

Acknowledgement

This work is supported by a Grant-in-Aid for Scientific Research for Priority Area from the Ministry of Education, Science and Culture of Japan.

References

1) Trumbore F. A.: Bell.Syst.Tech.J, **39** (1960) 205.
2) Shimura F., *Semiconductors Silicon Crystal Technology*, Academic Press (1989), also Maruzen (1993).
3) Hanada R.: CYRIC Annual Report **1994** (1995) 39.
4) Wichert Th.: *Hyperfine Interactio of Defects in Semiconductors*, ed by Langouche G. Elsevier (1992).

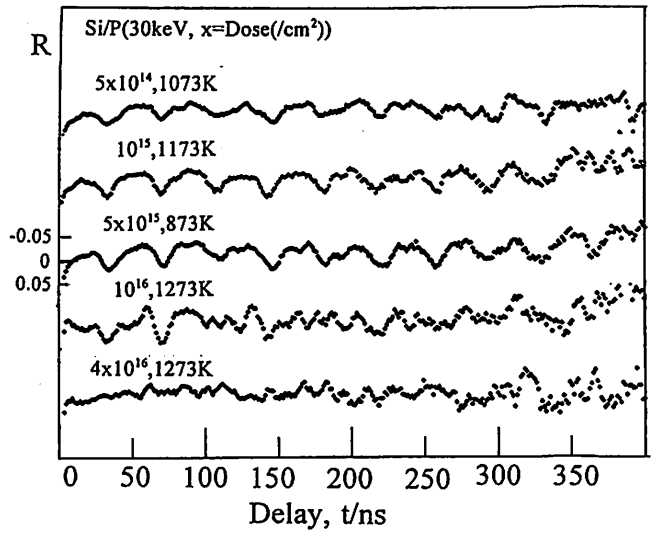

Fig.1 PAC spectra for Si implanted by P(phosphour) to various doses.

I. 10. Mössbauer Spectroscopy of Impurities Implanted Fe

Hanada, R

Institute for Materials Research, Tohoku University

Introduction

Mössbauer spectroscopy, especially CEMS (Conversion Electron Mössbauer Spectroscopy), is a good technique to study the properties of materials which are implanted with impurities ions in the energy range of several 10 keV. This is because that the range of conversion electrons and that of implanted ions overlap quite well and so only the part of the specimen disturbed by the implantation can be selectively studied. In a previous report by the present author[1], CEMS results were reported for Fe implanted by several kind of ions(N_2 ,CO, Ag, In). In these experiments, the dose has been limited below $2\times10^{17}/cm^2$ and so the effect of the implantation has been observed only faintly. In the present study, the doses have been increased up to $2\times10^{18}/cm^2$ to reveal the implantation effect more clearly, of which results are reported in the followings.

Experimental

^{57}Fe enriched Fe foils ($1\times1cm^2\times1.3\mu m$) were implanted by several ions (N_2, CO, D_2, ^{115}In) at the energy of 40keV to a dose of $1\text{-}2\times10^{18}/cm^2$ using ISOL at CYRIC. The use of the molecular ions is just for to shorten the implantation duration since the highest beam currents are obtained for them. Since the binding energies for these molecular ions are much smaller than the implantation energy, it is expected they split into two atomistic ions with about half of the implantation energy when they hit the surface of the target foil. Fig.1 shows TRIM results for the ions distribution with the assumption on the ion energies together with the range of CEMS electrons for ^{57}Co(^{57}Fe). Fig.1 shows the intermediate AMU ions as C,N,O are most appropriate for CEMS. Heavy ions as In are implanted too shallow for CEMS. D ions are implanted in the range of CEMS (3000 A) but too deep for the active CEMS range(540 A). Moreover D(H) is highly mobile in Fe at RT and so they may form bubbles during implantation at RT to lower the number of ^{57}Fe probes affected by D(H). The CEMS results in the followings will show that these expectations are indeed correct.

The CEMS was performed by a back scattering detector with a ^{57}Co/Rh source as He-isobuthane gas as the counting gas. CXMS (Ar-isobuthane counting gas) and a conventional transmission MS were also performed for comparison.

Result and Discussion

Fig. 2 shows results of CEMS for 4 different ions (^{115}In, N_2 ,CO and D_2) implanted to a dose of $10^{18}/cm^2$. For N_2 and CO ions, a remarkable implantation effects are observed. Namely for N_2 implantation, a large paramagnetic line takes place at v=0/mm. For CO, a new sextet ranging from -4mm/s to 4mm/s takes place together with the well known Fe sextet (-6 to 6mm/s). The positions of these implantation induced lines are exactly the same with those reported in ref. 1) for lower doses though the magnitude was much smaller and observed there only as small bulges. On the contrary in Fig.2 for In or D_2 implantation cases, almost no effect is observed and only Fe sextet is present.

The results for CO and N_2 implanted Fe were analyzed by a fitting program to give the hyperfine parameters as in Table I. Comparison of the results with others for C alloyed steels[2] or synthesized Fe nitride[3] reveals that Fe_3C(cementite) is formed in the present CO implanted Fe and an ε-nitride for N_2 implantation. So far no isolated C or N atom has been observed in the present implantation cases. This is an interesting result since C or N is almost immobile at RT and should distribute as a random solid solution after the implantation to give at least partly a magnetic sextet affected by C or N observed in alloyed steels. This may suggest that the high temperature and pressure caused by the implanted ions control the structure of the impurities implanted Fe as have been a proposed by several theoretical studies[4,5]. Further investigation is now in progress for N_2 implantation case for higher doses with annealing study.

So far no oxygen effect has been observed in the CO implanted specimen. If O is implanted to a high dose as in the present, an oxide should be formed as the cases of N or C. Most of Fe oxides are ferrimagnetic and the hyperfine fields for ^{57}Fe in them have been known to be much higher than that of pure Fe.(see a separate paper on Fe oxides in this volume). No such higher components are found in the present CO implanted specimens. So the lack of the oxygen component in CO implanted Fe remains as an issue to be solved.

Fig.3 shows a result of measurements for CO or N_2 implanted Fe by CEMS and CXMS spectroscopies. The result shows CEMS is most appropriate to study the implanted layer. The CXMS mode reveals the implantation effect only faintly and the transmission mode gives only the pure Fe sextet and no implantation effect even in the present case of the much thinner specimen(1.3μm) than the conventional(25μm).

Acknowledgements

The author is indebted to Prof. S.Nasu, Osaka University, for the permission to use his Mössbauer spectrum fitting program.

This work is supported by a Grant-in-Aid for Scientific Research in Priority Area from the Ministry of Education, Science and Culture of Japan.

References

1) Hanada R.: CYRIC Annual Report-**1995** (1996) 46.
2) Fujita F. E.: in *Mössbauer Spectroscopy*, ed by Gonser G. Springer Verlag (1975).
3) Ron M.: in Applications of Mössbauer Spectroscopy.
4) Rauschenbach B. et al :phys.stat.sol.(a) **80** (1983) 471.
5) Carter C.: Radiation Effects Letters, **50** (1980) 147.

Table 1

Impl.Ion Partial	1-6 sep/mm/s(F) or position(P)	Hyp.Field/T	RelativePop	Species
CO No.1 (F)	10.657		1.00	pure Fe
No.2 (F)	6.47	20	0.25	Fe_3C
N_2 No.1 (F)	10.657	33	1.00	pure Fe
No.2 (P)	- 0.37	-	1.02	ε nitride

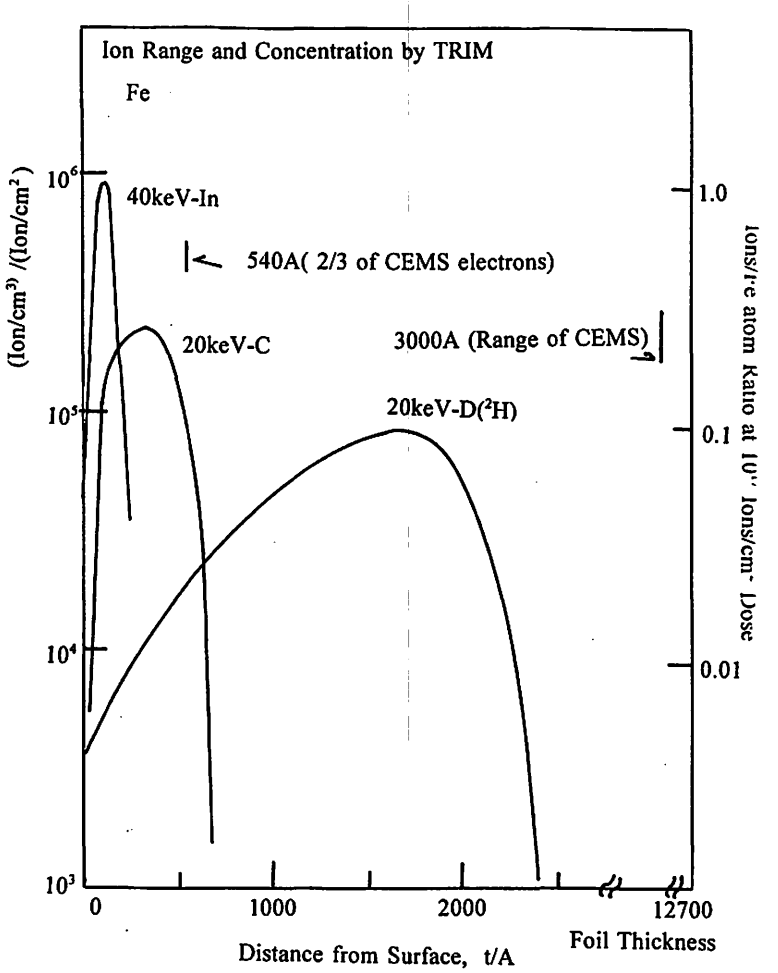

Fig. 1 Ions distribution calculated by TRIM.

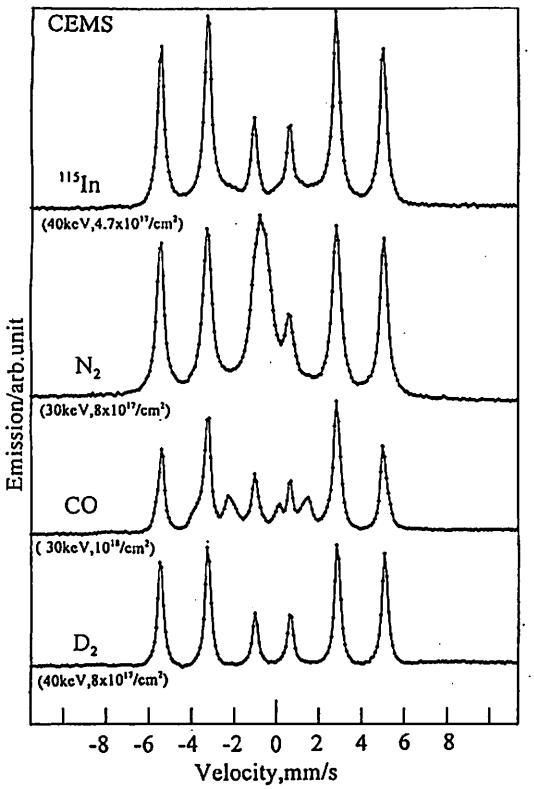

Fig. 2 CEMS spectra for Fe implanted by Ions ^{115}In(Indium), N_2(nitrogen molecule), CO(carbon monoxide) and D_2(deuterium) with the energy and the dose indicated.

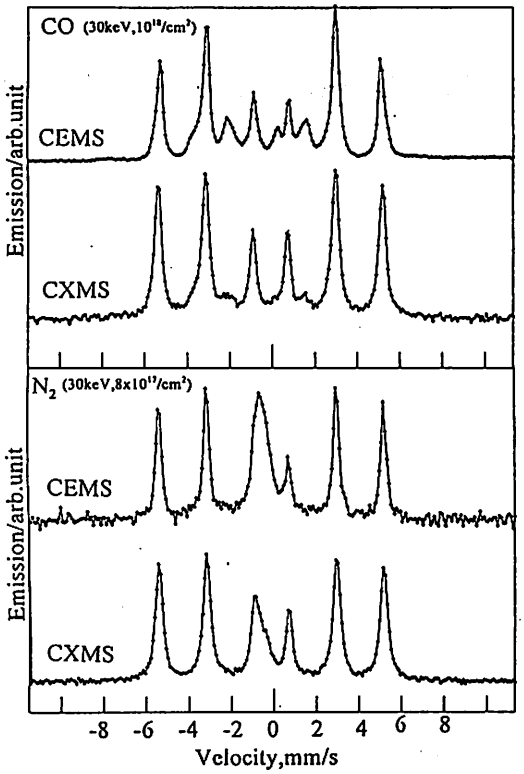

Fig. 3 Comparison of CEMS and CXMS spectroscopy for CO or N_2 Implanted Fe. The transmission mode for the same specimens shows only pure Fe sextet.

I. 11. Crystallization of Fe-based Metallic Glasses by Mössbauer Spectroscopy

Hanada, R

Institute for Materials Research, Tohoku University

Introduction

Metallic glasses (or amorphous alloys) have been one of the recent subjects in materials science because of their novel physical properties and of their technological applications. In the present, their crystallization processes have been studied by a Mössbauer spectroscopy.

The purposes of the experiments are three fold. Namely, to examine (1) how the non crystalline metallic glass state is reflected in the Mössbauer spectrum. (2) how the spectrum changes into that of the crystalline state upon annealing. (3) how the alloying elements distribute among several phases formed after the crystallization.

Experimental

5 different metallic glasses were obtained from NILACO, of which compositions are given as in Table 1 by the supplier. They are Fe based alloys with Si and B as the alloying elements (2605S2 and 2605S3A) with some modification with Ni and Mo (2826MB) or Co (2605CO) or C (2605SC). $2\times2cm^2$ foils with 25μ m thickness were cut from the original sheets and Mössbauer spectra were measured in the as received state as well as after the isochronal annealing (30min) in a vacuum (10^{-7}Torr) at temperatures between 400C and 1000C. The spectroscopy was in a transmission mode with ^{57}Co/Rh source. The spectra were analyzed by a program from Wissel Gmbh to obtain the hyperfine field distribution.

Results and Discussion

Fig.1 shows an example of the present spectroscopy for 2605S2($Fe_{78}B_{13}Si_9$), one of the simplest alloys studied in the present. In the as received state, the spectrum is a magnetic sextet with a smaller hyperfine field magnitude than that of the crystalline pure Fe and also with a broad distribution of the hyperfine filed. This shows Fe atoms in the metallic glass are in a ferromagnetic environment though Fe atoms experience a broad and continuous internal field distribution. This is a typical result for a metallic glass and proves that the obtained specimens are really in a metallic glass in the as received state. The specimen stays to be a

metallic glass state up to 670K (400C), though several new components start to develop at 770K (500C) and they tends to grow up to 1073K (800C). This trend is observed more clearly in Fig.2 where the hyperfine field distributions are shown. In the as received state or after 670K annealing, the hyperfine field shows a distorted Gaussian distribution with the center at H_{MG} with a half width $+\Delta H_f$ or $-\Delta H_f$. Here $+\Delta H_f$ and $-\Delta H_f$ are distinguished since the distribution is usually asymmetric for the alloys investigated. Namely, the field distributes more widely in the lower side than the higher. ($|-\Delta H_f| > |+|\Delta H_f|$). After the annealing at 770K, part of the continuous hyperfine field distribution changes into a discrete one. Here a part of metallic glass transforms to a crystal state. After the annealing at 770K and above, the field distribution develops into 4 well defined peaks at 33, 31, 28 and 24T. Here we label them as H_0, H_1, H_2 and H_{PPT} respectively, as shown in Fig. 2 after the 1270K annealing. Since each H_n has a unique magnitude with the width comparable with that of pure Fe in the crystalline state, we may conclude that they correspond to Fe atoms in different crystalline states. Namely, the metallic glass starts to transform into crystalline states at 770K and the crystallization is completed at 880K. Further annealing at higher temperatures causes redistribution of alloying elements among several phases as suggested by the relative magnitude change in H_n's population above 880K, which will be discussed later.

The trend described above was found to be in common for all 5 different metallic glasses investigated in the present and summarized in Table I. The alloy containing Co (2605CO) shows a lower crystallization temperature (670K) than others.

Next, we discuss the nature of H_n 's in Fig. 2. The magnitude of H_0 is almost the same with that of pure Fe. So we may conclude H_0 corresponds to Fe in a crystalline state with no impurities around it. The magnitude of H_1 is comparable with that of the 1st satellite in Fe-Si alloys (30.7T) and H_2 is for the 2nd satellite(27.8T) and these have been interpreted as due to Fe atoms with 1 and 2 Si atoms in the 1st neighbor site (8 for bcc Fe lattice) respectively[1]. So we may conclude that the alloy crystallizes into an Fe-Si alloy as the host with precipitates to give H_{PPT}, corresponding to a metallic compound of Fe, B and Si.

This interpretation is reasonable since Si is quite soluble in Fe host while B is insoluble and so the alloy tends to achieve the thermodynamical equilibrium state for B and a part of Si to form a compound once the alloy is relieved from the metallic glass state.

The relative change among H_0,H_1 and H_2 population above 880K is due to the Si concentration decrease in the Fe host with the compound growth. As well known in Fe-Si alloys studies, the H_1 or H_2 populations decrease with the Si concentration decrease in the host according to a binomial distribution.

This picture of the phase separation observed in the Fe-B-Si alloys can be extended to other alloys containing Ni,Mo and Co studied in the present. First, these elements are all soluble in Fe as in the case of Si. So upon the crystallization they form a complete solid solution as the host. Ferromagnetic elements Ni and Co have been known to give satellites at

higher positions than H_0 and a paramagnetic element Mo at the lower side. The examination of the spectrum after the crystallization indeed reveals this trend. Namely, 2826 MB (Mo and Ni) shows a broad H_0 due to Mo (a lower field side) and Ni (a higher field side). 2605 CO (Co) shows a higher H_0 than that of pure Fe due to Co in the host. The H_{PPT}'s show almost the same value for all alloys showing it is determined mainly by Si and B and additional elements (Ni, Co, Mo) contribution is only minor if they are incorporated in the precipitates.

Since the hyperfine distribution has been determined in the present Mössbauer study, it is interesting to examine how it will be reflected in the PAC spectroscopy for the metallic glass. The result of the experiment will be reported in a separate paper in this volume.

Adding to this spectroscopic observation, all metallic glasses were found to become extremely brittle after the crystallization and easily be powdered upon handling. So care must be taken in cases they are activated by particles irradiations or by activity implantation and then crystallized.

Acknowledgement

This work is supported by a Grant-in-Aid for Scientific Research in Priority Area from the Ministry of Education, Science and Culture of Japan.

Reference

1) Kobayashi M.: A Masters Thesis, Dept. Materials Science, Tohoku Univ.(1989).

Table 1. Summary of the Mössbauer Spectroscopy on Metallic Glasses.

No. Alloys	Composition/at%	H_{MG}/T	$+\Delta H_c$/T	$-\Delta H_c$/T	Cryst.Temp./K
0 2826MB	$Fe_{40}Ni_{38}Mo_4B_{18}$	23	3	6	6
1 2605S2	$Fe_{78}B_{13}Si_9$	26	4	6	6
2 2605S3A	$Fe_{78}B_{16}Si_6$	23	4	8	8
3 2605CO	$Fe_{67}Co_{18}B_{14}Si_1$	28	4	4	4
4 2605SC	$Fe_{81}B_{13.5}Si_{3.5}C_2$	25	4	4	4

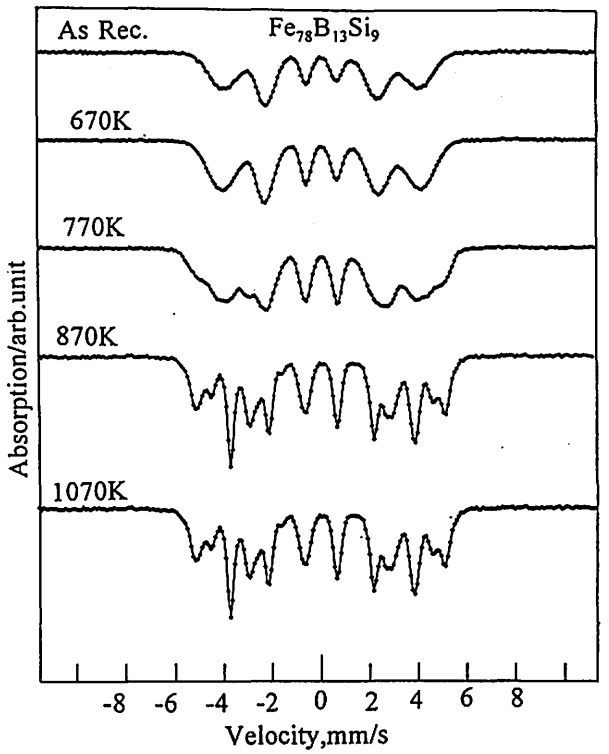

Fig.1 Transmission Mössbauer spectra for a metallic glass $Fe_{78}B_{13}Si_9$ during annealing between RT and 1000C.

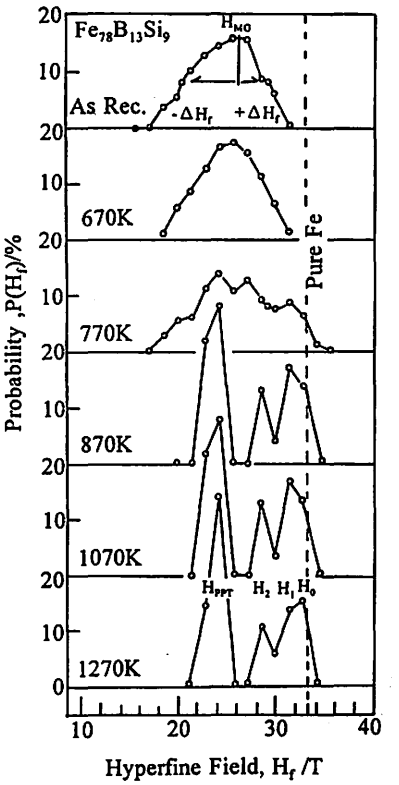

Fig.2 Hyperfine field distributions obtained from Fig.1.

I. 12. PAC Study of Metallic Glass

Hanada, R

Institute for Materials Research, Tohoku University

Introduction

Several Fe based metallic glasses have been studied by Mössbauer spectroscopy (MS) to determinethe distribution in the hyperfine field in both metallic glass and crystallized states.(in this volume). This paper reports a result of a PAC spectroscopy in one of the metallic glasses to examine how the distribution is reflected in the spectrum.

Experimental

One of metallic glasses with the simplest composition 2605S2 ($Fe_{78}B_{13}Si_9$) was implanted with ^{111}In at the energy of 50 keV at RT. A PAC spectroscopy was performed at RT using ^{111}In as the probe in the as implanted state or after annealing below 400C without a magnetic field.

Result

Fig.1 shows the result of the PAC spectroscopy for the metallic glass (bottom two) as well as for pure Fe (top). As reported in the MS result on the same alloy, this alloy is a metallic glass below 400C and crystallized above 500 C. So the two spectra for the alloy in Fig.1 are for the metallic glass state and not after the crystallization. The 300 C annealing is to anneal out possible damage due to the ^{111}In implantation though the spectrum after it is almost the same with that right after the implantation. So no damage effect was observed in the present below 300 C.

The spectrum for the metallic glass shows a dumped precession pattern near the delay time 0 and almost flat up to the delay time t=100 ns both in the as implanted state or after 300 C annealing. This is in contrast to pure Fe where the precession pattern keeps taking place for longer delay time of 100 ns without any dumping.

This dumping is a characteristics of the PAC spectrum in a metallic glass. Namely, ^{111}In nuclei in a metallic glass experience a distribution of the hyperfine field and hence precess with a angular frequency that have a distribution as the hyperfine field. In the γ-γ correlation measurement as PAC for a magnetic interaction, the time spectrum is best described as a simple cosine function as $\cos(2\omega t)$. So in a metallic glass, the PAC spectrum

consists of an overlap of the cosine waves with a distribution in ω. This overlap of the cosine wave causes the dumping as shown in Fig.1 for the metallic glass. As shown in a MS study for the alloy (in this volume), the distribution is not so large and the half width of it is only 20% of the average value. This small distribution is high enough to cause the fast dumping as in Fig.1. This will be shown more quantitatively later.

The period of the precession pattern is 13.3 ns for the metallic glass which is s larger than that for pure Fe.(11.2 ns) This shows the magnitude of the average hyperfine field at the ^{111}In nucleus in the metallic glass is smaller (84%) than that of pure Fe. The hyperfine parameters determined in the present for ^{111}In is summarized in Table 1 together with for ^{57}Fe from MS on the same alloy.

Discussion

The above observation can be quantitatively analyzed as follows. The hyperfine field distribution may be approximated as a Gaussian as eq.(1),

$$P(H) = A \exp\left(-\ln 2(H - H_0)^2 / \Delta H^2\right), \quad (1)$$

where H_0 is the average field, ΔH is the half width of the distribution and A is a constant. The correlation function is best described as eq (2) for Fe or Fe based alloys,

$$W(t, H) = B \cdot \cos(2\omega(H)t), \quad (2)$$

where the angular frequency ω is given as eq.(3) for a magnetic interaction and B is a constant.

$$\omega(H) = g\mu_N H / \hbar, \quad (3)$$

where g, μ_N and $\hbar$ have usual meanings. So the correlation function D(t) for the spin ensemble in a distribution of the hyperfine field as in a metallic glass is given as eq.(4)

$$D(t) = \int P(H)W(t, H)dH \quad (4)$$

The eq.(4) was calculated to give Fig.2 where $\Delta H/H_0$ was taken as a parameter between 0 and 50%.

The comparison of the calculated result with the experimental results in Fig.1 reveals that $\Delta H/H_0$=25 % gives a best fit in that the amplitude is observed as finite at $\omega t/\pi$=3 but not at =4 as in the experimental result. This value shows a good agreement for that obtained in an independent MS result using ^{57}Fe probe on the same alloy in the metallic glass state as given in Table 1.

The present calculated results for a magnetic interaction show a good agreement for a similar calculation for a quadrupole interaction case where 20 % distribution in EFG causes a

high dumping in the PAC spectrum[1]. So if one obtains a PAC spectrum without a high dumping in a "metallic glass", one should suspect the specimen has been crystallized by warming up during previous treatments as pile irradiation et cet for the probe introduction.

Acknowledgement

This work is supported by a Grant-in-Aid for Scientific Research in a Priority Area from the Ministry of Education, Science and Culture of Japan.

Reference

1) Frauenfelder, H and Steffen R. M.:Angular Distribution of Nuclear Radiation:in α, β *and* γ *ray Spectroscopy Vol. II* ed. by Siegbahn K. pub. by North Holland (1968).

Table 1. Hyperfine Parameters for a Metallic Glass 2605S2($Fe_{78}B_{13}Si_9$)

Probe	Method	H_0/T	ΔH/T	$\Delta H/H_0$/%
^{111}In	PAC	28	7	25
^{57}Fe	MS	26	5(+4,-6)	20(15,-23)*

* For ^{57}Fe the distribution has been found not symmetric.
(see a paper for MS on metallic glasses in this volume)

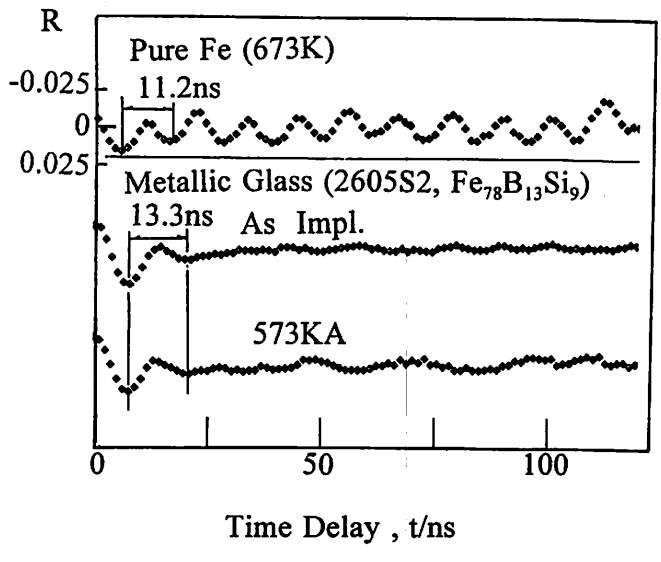

Fig. 1. ^{111}In PAC spectra for a metallic glass 2605S2($Fe_{78}B_{13}Si_9$) .(bottom two) For comparison a spectrum for Fe is shown (top) Temperatures indicated are the annealing temperature (30min) after the implantation.

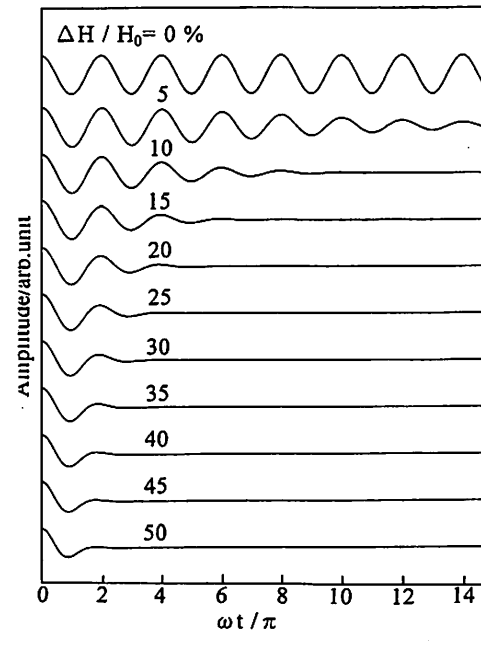

Fig. 2. Calculated PAC spectrum for a probe in a Gaussian distribution of a hyperfine field.

I. 13. CEMS of Fe Implanted by Nitrogen to a High Dose

Hanada, R

Institute for Materials Research, Tohoku University

Introduction

Nitrogen (N) in Fe has been a subject of Mossbauer Spectroscopy study since the first discovery of the satellites due to interstitially dissolved N[1)] in Fe martensite. Also many Fe-N alloys or Fe-nitride phases have been studied by MS and the results have been summarized in ref.(2). Also with practical application in mind, N has been implanted to many kind of steels to harden the surface to improve the wear resistance or other physical properties[3-10)].

In a report in this volume, CEMS for Fe implanted by N_2 to a dose of $8\times10^{17}/cm^2$ was reported together with the results for other ions. There, a paramagnetic emission line near v=0 mm/s has been observed with pure Fe sextet and ascribed to a nitride. Since a report on synthesized nitride[2)] has shown that the nitride transforms to a ferromagnetic phase with the increasing N concentration, it is expected that the paramagnetic nitride found in the implanted Fe also transforms to a ferromagnetic phase if the N implantation dose is increased. This paper reports the result of the experiment together with an annealing study. Also in the present, the results were analyzed by a method different from the conventional fitting procedure. Namely, the hyperfine field distribution was determined by a program from Wissel Gmbh. This approach has an advantage to extract hidden components from the experimental spectrum.

Experimental

The experimental procedure is the same with those reported in a paper for CEMS for Fe implanted by various ions in this volume. The method of the analysis is the same with those reported in a paper for metallic glasses in this volume.

Result

Fig.1 shows the CEMS spectra for Fe implanted with N_2 to a dose of $2\times10^{18}/cm^2$ at the energy of 40 keV. Different from the case for $8\times10^{17}/cm^2$, here, we see ferromagnetic components in the as implanted state as well as during annealing up to 800 C. Fig.2 shows the field distribution extracted from the spectra in Fig.1.

In order to perform the interpretation easier , we start with the results in Fig.1 and 2 after the highest annealing temperature, 800 C. Here, we see only pure Fe sextet in Fig.1, which is revealed in Fig.2 as a prominent peak at 33 T, the well known hyperfine field of pure Fe. The finite width of the peak (±0.5 T) is due to a limited experimental spectrum resolution, which should be a delta function if the spectrim measurement is done ideally.

Returning to the as implanted state, we see two prominent peaks in Fig.2 at 19 T (associated by 23 T peak) and 33 T. Except for these 2 peaks, there observed 3 smaller ones at 5,12 and 14 T.

The peaks except for the 33 T peak should be related to the implantation of N. As will be shown later, the 19 T (and 23 T) component is due to a nitride formed by the implantation. From the population of them, about 2/3 of Fe are in a form of the nitride.

The populations of other components are relatively low though they are reproducibly present in Fig.2 below 400C. Possibilities for them are (1) nitride of which structures are different from that for 19 T peak or (2) damages due to N implantation.

After the annealing at 500 C, the 19 T peak shift to 21 T and also 33 T peak splits into 2. This shows some structure change has taken place at 500 C. After the annealing at 600 C, the 33 T peak grows with decays of 19 T peak and others. This shows N is diffusing out of Fe at 600 C and almost completely out of the specimen at 800 C leaving only pure Fe matrix.

Discussion

Fig.3 summarizes experimental results by MS on Fe with N implanted or alloyed together with the present. Here, the hyperfine fields determined from MS spectra are plotted against the N doses just for convenience. The parts of null dose in Fig.3 correspond to the ones where N is added as an alloying element or to synthesized nitrides and not by implantation. The points with the null hyperfine field correspond to the cases where a paramagnetic component is observed.

Despite of the wide varieties of the experimental procedures (implantation energy, dose measurement, analysis, specimens used (pure, C steels, martensite et cet)), the values of hyperfine field related to N in Fe show a good agreement among the workers as well as in the present. Namely, the ones at 33T(pure Fe), 19-23T(nitride), 10T and 0T(the paramagnetic line). The components with 10 T(±4 T) are observed only in ref.(4) and in the present. The species of the 19T component in the implanted specimens are difficult to conclude on the basis of the magnitude of the hyperfine field only. As shown in Fig.3, several nitride(ε-, γ-) are proposed for the components on N alloyed or synthesized nitride where both MS and/or a structure analysis have been performed.

The present method of MS spectrum analysis, the determination of field distribution, seems to work well not only for the metallic glasses but also for the cases where unique

hyperfine fields are present as in the present case. As shown Fig.3 the values determined by fitting procedures by others(especially ref.(4)) show a good agreement with the present ones.

Acknowledgement

This work is supported by Grant in Aid for scientific Research in Priority Area from the ministry of Education, Science and Culture of Japan.

References

1) Gielen P. M. and Kaplow R.: Acta Met.**15** (1967) 49.
2) Ron.M.: *Application of Mössbauer Spectroscopy II* ed by Cohen R. L. Academic Press (1976).
3) Prinpici G. et al: J. Materials Science Letters **15** (1980) 2665.
4) Frattini R. et al :J. Materials Science **17** (1982) 1683.
5) dos Santos C. A. et al: Appl. Phys.Lett. **41** (1982) 237.
6) Raushenbach B. et al : Phys. Stat. Sol.(a) **80** (1983) 211.
7) Eickel et al : Phys. Stat. Sol. **39** (1970) 121.
8) Carbucicchio M. etal: J. App. Phys. **52** (1981) 4589.
9) DeCristofaro N. and Kaplow R.:Met. Trans. **8A** (1977) 35.
10) Ramous E. et al :This Solid Films **102** (1983) 97.

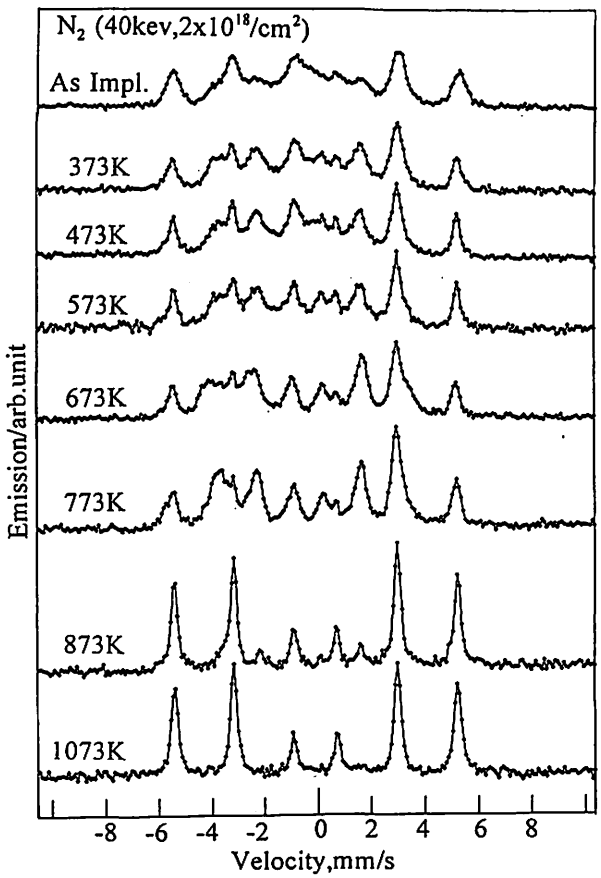

Fig.1 CEMS for Fe implanted by N2 during isochronal annealing (30min) in a vacuum.

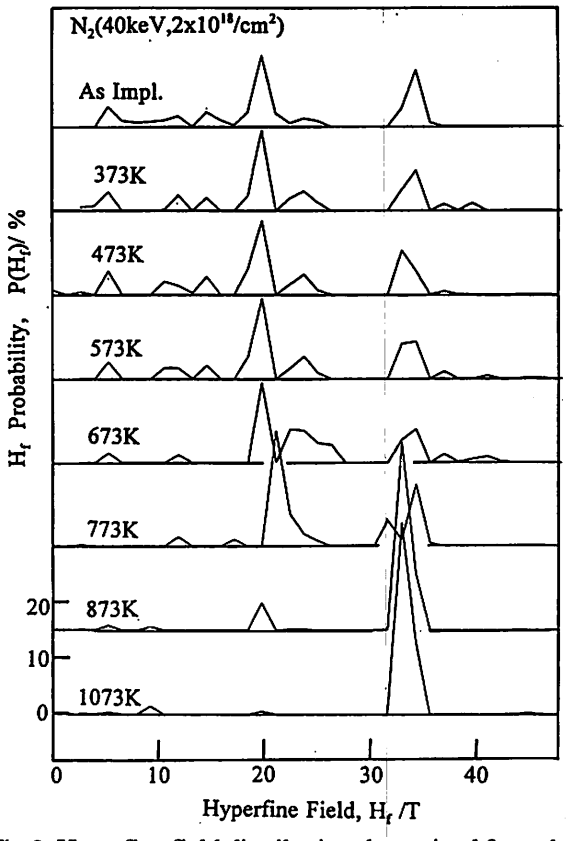

Fig.2 Hyperfine field distribution determined from the spectra in Fig.1

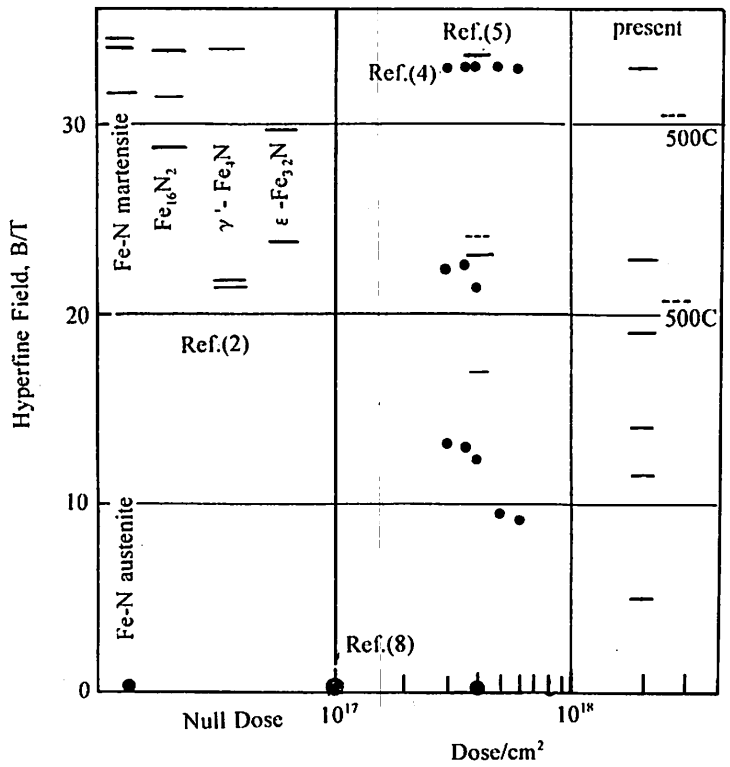

Fig.3 Summary of hyperfine field in Fe-N systems, alloyed, synthesized and implanted.

I. 14. Helium Implantation Effects on Mechanical Properties of SiCf/SiC Composites

*Hasegawa A., Saito M., Abe K. and Jones R. H.**

Department of Quantum Science and Energy Engineering, Tohoku University,
*Pacific Northwest National Laboratory, P.O.Box 999, Richland, WA99352, U.S.A.**

Introduction

SiC fiber reinforced SiC composite has been proposed for structural materials for fusion application because of its low induced activation by 14MeV neutron irradiation and high temperature strength. In a fusion reactor environment, helium will be produced at the rate of about 1500-2000appm He/(MW•a•m^2) in SiC by transmutation reactions and displacement damage will be 10-15dpa/(MW•a•m^2), depending on the details of the blanket structure and on neutron spectrum[1]. The He/dpa ratio of SiC will be higher than that of other candidate alloys such as vanadium and ferritic steels. Since He may accelerate swelling and creep, and precipitate on interfaces such as grain boundaries and fiber/matrix interfaces, mismatch and interface debonding between fiber and matrix may occur in SiC composite under fusion reactor conditions. The strength of fiber/matrix interface will have a direct influence on the fracture strength and toughness of composites, therefore behavior of He gas atom and evaluation of He effect on mechanical properties of SiC/SiC composite will be important for its application to structural materials of fusion reactor. In this work, we will present preliminary results of He effects on mechanical properties of SiC/SiC composite using He implantation methods by accelerators.

Specimens

Previous research has shown that post irradiation behavior of SiC fiber was influenced by its impurity such as oxygen and its microstructure. In the case of Nicalon fibers, irradiation effects on density change and tensile strength were influenced by its oxygen contents[2,3]. We also reported about microstructural stability of Nicalon fibers after neutron irradiation (43dpa at 1040C in EBR-II)[4]. The results showed that grain growth was observed in Nicalon-CG fiber, which was commercial grade and contained large amount of oxygen (11.7wt%[5]), however, microstructural change was not observed in Hi-Nicalon fiber, which was cured by electron irradiation and oxygen level was relatively low (0.5wt%)[5]. The result showed that lower oxygen and more crystalline SiC fibers such as Hi-Nicalon and Nicalon type-S may be appropriate SiC fiber for fusion application. In this work, we studied

about He effects on two types of 2D-SiCf/SiC composites using SiC weaves made of Hi-Nicalon fiber. Specimen code names are JSS01 and USSD01 respectively. Both JSS01 and USSD01 were fabricated by chemical vapor infiltration(CVI) method. The JSS01 is a Japanese reference material of SiC/SiC composite fabricated by Ube Industries Ltd. The details of fabrication and its strength at room temperature and higher temperature is presented elsewhere[6]. The USSD01 was fabricated by Dupont in U.S.A. and its mechanical properties are reported elsewhere[7]. Major difference of the specimen was thickness of carbon coating on SiC fibers. The thickness of carbon coating of JSS01 is approximately 100nm and that of USSD01 was 1.2μm.

Because relatively large volume was required to evaluate bending strength, high energy He ion implantation were used to prepare He implanted bend bars. Specimen size of bend bar was 4mm width, 1mm thickness and 18mm length. The numbers of 2D woven SiC cloth in the bend bar were 3 in JPSS01 and 4 in USSD01.

Helium implantation and post implantation test results

Experimental procedure for 36MeV He implantation and bending test

Helium implantation was carried out using a cyclotron of Tohoku University. The accelerated energy of He ion was 36MeV and the projected range in SiC was 470μm which was calculated by TRIM code. To obtain uniform He depth distribution, tandem type degrader wheels were used. Total amount of implanted helium concentration calculated by its irradiated fluence was 150 -170 appm. Displacement damage in the He implanted area was approximately 0.08dpa using E_d=45eV. Implantation temperature was 400-800C depending on the specimen. He implanted area was a central part of a bend bar where the maximum tensile stress was loaded during bend test.

Three-point bending test was carried out at room temperature before/after He implantation. The span length was 14mm and the cross head speed was 0.2mm/min. After the bending test, fractography observation was carried out by SEM.

Results of bending test

Fig.1 shows stress-deflection curves of He implanted and unimplanted JSS01 and USSD01. Stress level of first matrix cracking (FMC) in both composites was in the range of 100 to 150MPa and He implantation effect was not clearly seen in the FMC behavior. After FMC, stress-deflection curve and maximum bending strength of JSS01 had wide scatter and He implantation effects was not clearly seen. On the other hand, a decrease of the maximum bend strength was observed in He implanted USSD01. Inclination of stress-deflection curve after FMC decrease by He implantation. This effect may be attributed to He effects on fiber pull-out behavior during bending test of USSD01.

Fig.2 shows SEM results of unimplanted specimen after bending test. Upper side

of these pictures were tensile-stress-loaded side. Helium was injected in this side. Small crack and fine debonding crack between fiber/matrix was observed in USSD01, but large crack and large delaminated surface was observed in JSS01. The difference of bending behavior between the two composites may be attributed to fiber/matrix interface strength which was influenced by thickness of carbon coating on the fibers. In order to clarify the carbon coating and He effect on the fracture behavior, fractographic analysis of He implanted specimens is in progress.

Acknowledgements

The authors are grateful to Prof. A. Kohyama, Kyoto University, for preparation of JSS01 composites, and to Dr. T. Yano, Tokyo Institute of Technology, for his help of bending test and staffs of cycrotron of Tohoku University for their accelerator operation.

References

1) Snead L. L., Jones R. H., Kohyama A. and Fenici P., J. Nucle. Mater., **233-237** (1996) 26-36.
2) Youngblood G. E., Senor D. L. and Hollenberg G. W., Fusion Materials Semiannual Progress Report for Period ending March 31,1995, U.S. DOE-/ER-0313/18.
3) Snead L. L., Osborne M. and More K. L., Mater J. Res., 10 (3), (1995) 736-747.
4) Hasegawa A., Youngblood G. E. and Jones R. H., J. Nucle. Mater., vol. **231** (1996) 245-248.
5) Ichikawa H., Okamura K. and Seguchi T., High-Temperature Ceramic-Matrix Composites II, Ceramic Transactions vol.. **58** (1995) 65-74.
6) M. Satou, Proc. of the 14 th Fusion Reactor Materials Forum Oct. 15-16, 1996, NIFS (Japan).
7) Youngblood G. E. et al. to be published.

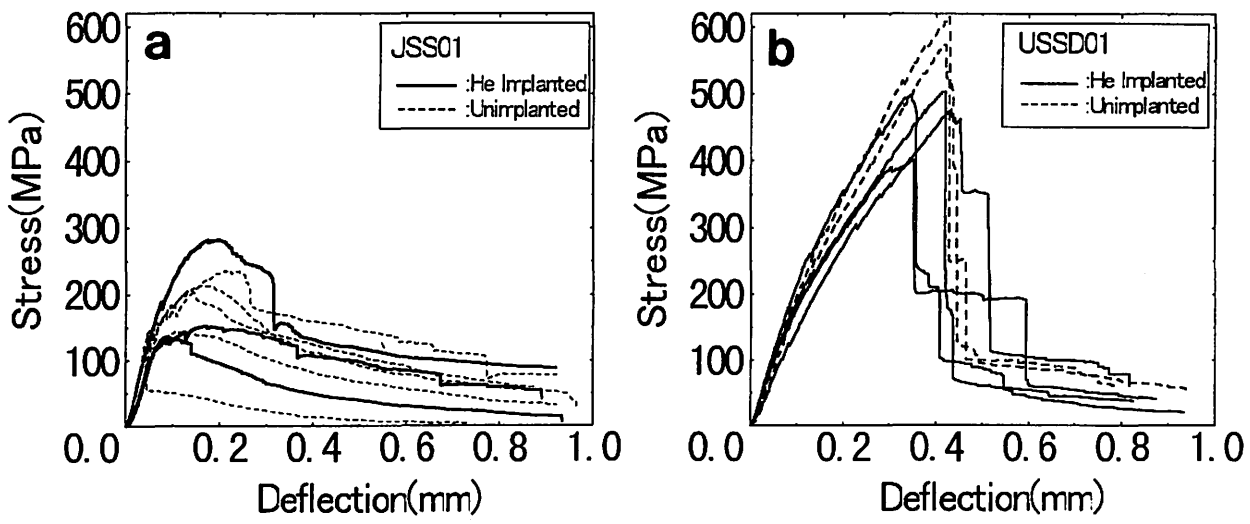

Fig. 1. Stress-deflection curves of SiC/SiC composites at room temperature. (a) JSS01, (b)USSD01.

of these plastics were tensile-stress-induced cracks. Attention was imported to this side. Small cracks and fine debonding crack between fibers/matrix was observed in [ISSN]QE. But large cracks and large debonded surface was observed in ISSN . The difference of bonding nature between the two composites may be attributed to fiber/matrix interface strength which was influenced by existence of carbon coating on the fibers. In order to clarify the carbon coating and its effect on the fracture behavior, fractographic analysis of the tensile specimens is in progress.

Acknowledgements

The authors are grateful to Prof. A. Kobayama, Kyoto University, for preparation of ISSN composites and to Dr. T. Yano, Tokyo Institute of Technology, for his help of bending test and supervision of Tadaki University for his technical cooperation.

References

1) Sawada T., ... K. H. ... and Tsuda P. J. Mode Mater., 2[2]-3[2]7 (1990) 2[-]7
2) Yamaguchi S. S. Sawada T. and Hollaway W. Tec. Materials Reinforced Progress
Polym. ... Mater. 3[1](2)(...) 2[0]-[2]9 (1[2]18)
3) Sawada T. ... Carbone H. and Yano K. ... J. Mat., [1](1995)-[2]9-2[2]
4) Hayama A., Yamaguchi C. and Inoue F. H. J. Mech. Mater., vol. 2[2] (19[-]), 2[2]-[2]6
5) Tanikawa H., Okamura K. and Sprecht J. ... Engineering Science-Mech. Comp. ...
... vol. 8[-] (1[2]9[2]) 6[-]-[2]
6) A. Sakai, Proc. of the ... Jenkins Greater Materials Forum (Jan. 1[-]-1[2], 19[2]6, [2]1[2]) (pp. to be published)

Fig. 1. Stress-deflection curves of ISSN composites at room temperature (ISSN, vol. ISSN).

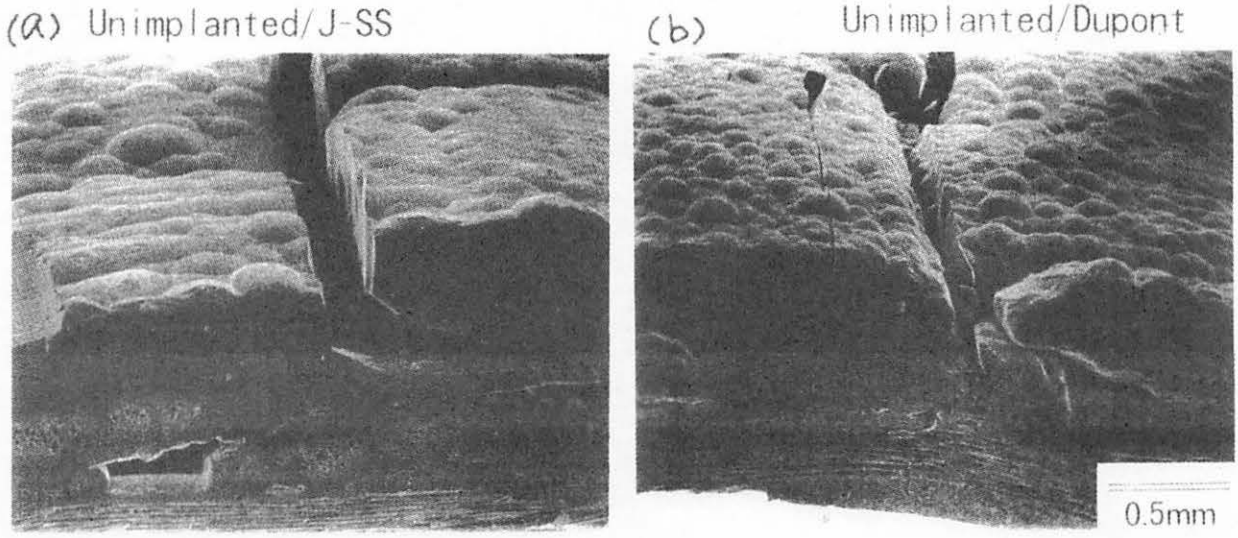

Fig. 2. SEM micrographs of bend tested SiC/SiC composites. (a) unimplanted JSS01, (b) unimplanted USSD01.

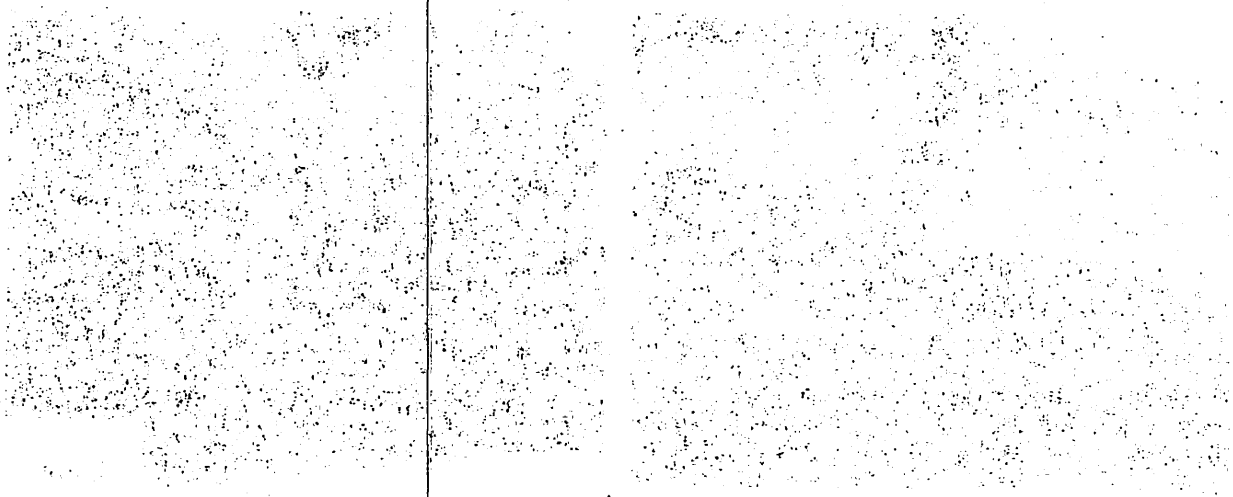

I. 15. Effect of Helium Implantation on Tensile Properties of V-Ti-Cr-Si Type Alloy

Satou M., Koide H., Hasegawa A. and Abe K.

Department of Quantum Science and Energy Engineering, Tohoku University

Introduction

Vanadium alloys are considered to be one of the candidate structural materials for fusion reactor[1]. Because they have several advantages, such as high-heat loading capability, good mechanical properties at high temperatures, low swelling under irradiation at high-neutron fluence, low induced radio-activity, good compatibility with liquid lithium. In fusion reactor environment, helium generation by (n,α) reaction is considered to be about 500appmHe for vanadium after 10MWy/m^2 operation. Helium may segregate to grain boundary and weaken the boundary. It is one of the important issue to understand the helium effects on the mechanical properties of the vanadium alloy. V-Ti-Cr-Si type alloys containing Al and Y were studied as proof-oxidation and irradiation resistant materials for fusion reactor applications[2]. Various techniques have been adopted to study helium effects on mechanical properties of the alloy[3]. In this paper, the results of implantation experiment introduced relatively high amount of helium compared to displacement damage are described in order to study the resistance against helium embrittlement of the alloy in relatively severe condition.

Experimental

The chemical composition of the V-5Ti-5Cr-1Si-Al-Y alloy is given in table 1. The preparation procedure of the alloy was described earlier[4]. Tensile specimens or disks for transmission electron microscopy were punched out from 0.25mm thick sheets. These specimens were annealed at 1100°C for 3.6ks in a vacuum of 5×10^{-3}Pa to obtain a fully recrystallized and grain size of about 20μm. The tensile specimen had a gauge section of 5mm long and 1.2mm wide. The disks had a diameter of 3mm. Helium ion of 36MeV was implanted by Tohoku University cyclotron accelerator using tandem-type energy degrader wheels. To obtain uniform helium distribution along the implanted direction, the energy degrader foil had 525 equivalent thickness. Total amount of helium in the specimen was evaluated about 50 appmHe with displacement of about 0.02 dpa. The helium ion beam was scanned by 1Hz in horizontally and 10 Hz in vertically. Specimens of 8 tensile and 14 disks were fix on water-cooled holder by indium solder, therefore, the specimen temperature during

implantation kept below melting point of the solder 156°C. Tensile tests were carried out at temperature ranging from room temperature to 850°C and at strain rates from 6.7×10^{-5} to 6.7×10^{-3}/s in a vacuum (less than 2×10^{-3}Pa) after implantation. Fracture mode was characterized by scanning electron microscopy. Microstructures of the specimens as-implanted condition or post-implanted annealing conditions (650 or 850°C for 3.6ks) were observed by transmission electron microscopy. Specimens of pure vanadium were also examined for comparison.

Results

Stress-strain curves

Both of helium-implanted and un-implanted conditions, serrated portion was observed in the curves of the alloy tested at 450 or at 650°C. In un-implanted pure-vanadium, serrated portion of the curve was observed in at 350 and at 450°C. After implantation, serrated portion was disappeared at 450°C. The serrated strain-stress curves were corresponding to dynamic strain aging, so impurity atom such as oxygen or nitrogen might be trapped by the defects by helium implantation.

Tensile properties

Results of yield stress, tensile strength and elongation of unimplanted and helium implanted specimens are shown in Fig. 1. Increase of yield stress is not observed in helium-implanted alloy except for 450°C testing. Increase of yield stress is observed in pure-vanadium. The level of the hardening is decrease with testing temperatures. Tensile strength of the implanted alloy is same as unimplanted alloy except for 650°C testing. The decrease of tensile strength at 650°C is corresponding to decrease of elongation. Tensile strength of unimplanted vanadium shows the maximum at 350°C, that is corresponding to dynamic strain aging. Helium implanted vanadium shows increase of strength at room temperature, decrease at 350 and 450°C. Total elongation of the helium implanted alloy decrease with temperature from 15% at room temperature to 6.2% at 650°C. At 850°C, elongation becomes to 16%. Total elongation of unimplanted vanadium is 40% at room temperature. At 350 or 450°C, elongation decreases to about 25%. Helium implanted vanadium shows decrease of elongation at room temperature. At higher temperature than 450°C, elongation is recovered.

Fractography

Fracture mode of unimplanted alloy was ductile at the testing temperature range. Helium implanted alloy tested at room temperature showed ductile mode. At higher temperature than 450°C, mixed fracture mode was observed. Intergranular fracture mode was only observed in small part. Segregation of helium atoms could decrease the grain boundary strength, so that intergranular mode was observed. In case of pure vanadium, reduction in area was large, almost 100%, even after helium implantation.

Microstructural observation

Microstructure of helium implanted alloy shows in Fig. 2. In as-implanted specimen, fine black dots are observed. After 650°C annealing, the size of the defects become large. Defects free zone was observed along grain boundaries, but no bubbles was observed. Dislocation loops of about 200nm diameter were observed in the specimen annealed at 850°C. Helium bubbles were observed both on grain boundary and in the matrix. The size of bubble on the grain boundary was larger than that in the matrix. Intergranular fracture was observed in the specimen tested at 450°C or higher. After testing at 850°C, helium bubbles were observed both in the grain boundary and in the matrix.

Dependence on strain rate of tensile properties

Yield stress at 450 or 850 °C did not varied with strain rate of the ranging from 6.7×10^{-5} to 6.7×10^{-3}/s. Tensile strength was increased with the strain rate increase. The increase was correspond to increase of uniform elongation with the strain rate. Total elongation of the specimen tested at 450°C decreased with the strain rate. It is possible that He atoms are swept to grain boundary by moving dislocations more effectively at low strain rate.

Discussion

At 450 °C, intergranular fracture mode was observed in V-5Ti-5Cr-Si-Al-Y alloy. It is possible that segregation of implanted helium caused the degradation of grain boundary strength. After 850°C annealing or deformation, helium bubbles were observed on grain boundary, however, no bubbles was observed in the specimen annealed at 650°C. These observations indicate that invisible helium atoms may affect grain boundary strength below 650 °C testing. Segregation of helium atom on grain boundary was larger at 850°C than at 650 or 450°C. Decrease of elongation was smaller at 850°C than at 650 or 450°C. Therefore, lower concentration of helium on grain boundary caused intergranular fracture at lower testing temperature. When intergranular fracture occurs, fracture stress of grain boundary must be smaller than that of matrix and at same time deformation stress must be larger than the grain boundary strength. At 850°C testing, grain boundary strength became weaken by helium atom, which could defused from matrix and swept by moving dislocation, however, deformation stress was too small to make fracture on grain boundary. On the other hand, at 450°C testing, helium concentration on grain boundary was small but deformation strength was larger than grain boundary strength, so that intergranular fracture mode was observed. The level of tensile strength of the alloy showed almost same at temperatures from 200 to 650°C. The testing temperature became higher, helium segregation on grain boundary became higher. Therefore, the specimen tested at 650°C showed the lowest elongation of them.

Summary

Effects of helium implantation of V-5Ti-5Cr-Si-Al-Y alloy were studied.

- Intergranular fracture mode was observed at 450, 650, 850°C testing after about 50appmHe implantation.
- Decrease of elongation was observed at all testing temperatures. The lowest elongation was observed in the specimen tested at 650°C.
- Helium bubbles were observed in grain boundary and matrix in the specimen tested at 850°C.
- Elongation became lower with the strain rate at ranging from 6.7×10^{-3} to 6.7×10^{-5}/s.
- Relationship between tensile strength and decrease of elongation was discussed.

References

1) Matsui H. Fukumoto K. Smith D. L., et al., J. Nucl. Mater. **233-237** (1996) 92.
2) Satou M., Abe K. and Kayano H., J. Nucl. Mater. **212-215** (1994) 794.
3) Satou M., Koide H.,Hasegawa A., et al., J. Nucl. Mater. **233-237** (1996) 447.
4) Satou M., Abe K. and Kayano H., J. Nucl. Mater. **179-181** (1991) 757.

Table1. Chemical analysis of vanadium alloy.

V	Ti	Cr	Si	Al	Y	C	O	N
Balance	4.79	4.01	0.85	0.95	0.77	0.0126	0.014	0.0054
	(5.0)	(5.0)	(1.0)	(1.0)	(1.0)			

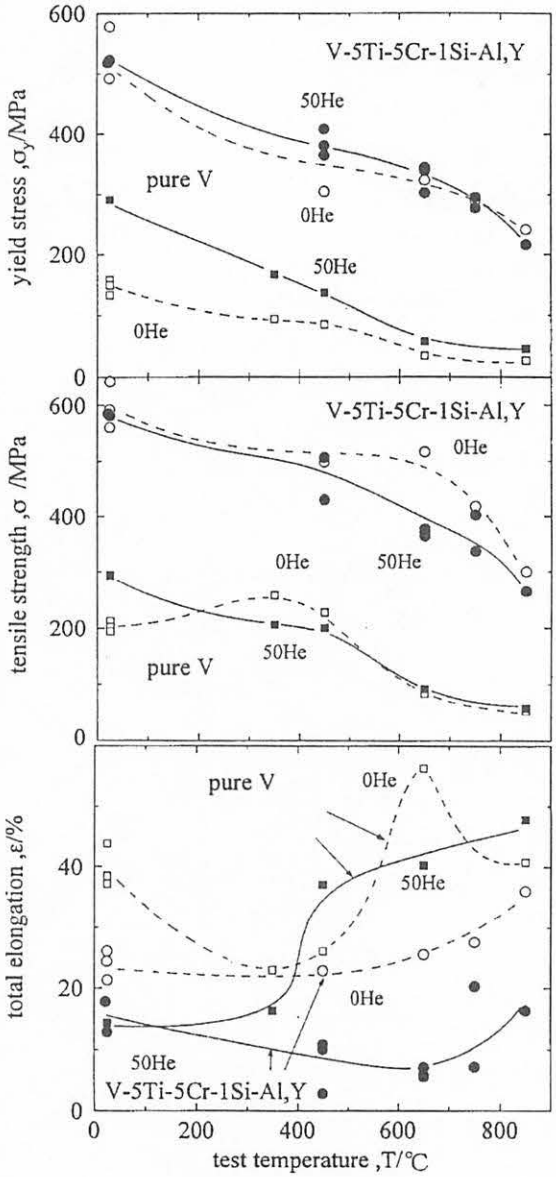

Fig. 1. Tensile properties of helium-implanted V-5Ti-5Cr-Si-Al-Y alloy and pure vanadium at temperatures from room temperature to 850°C.

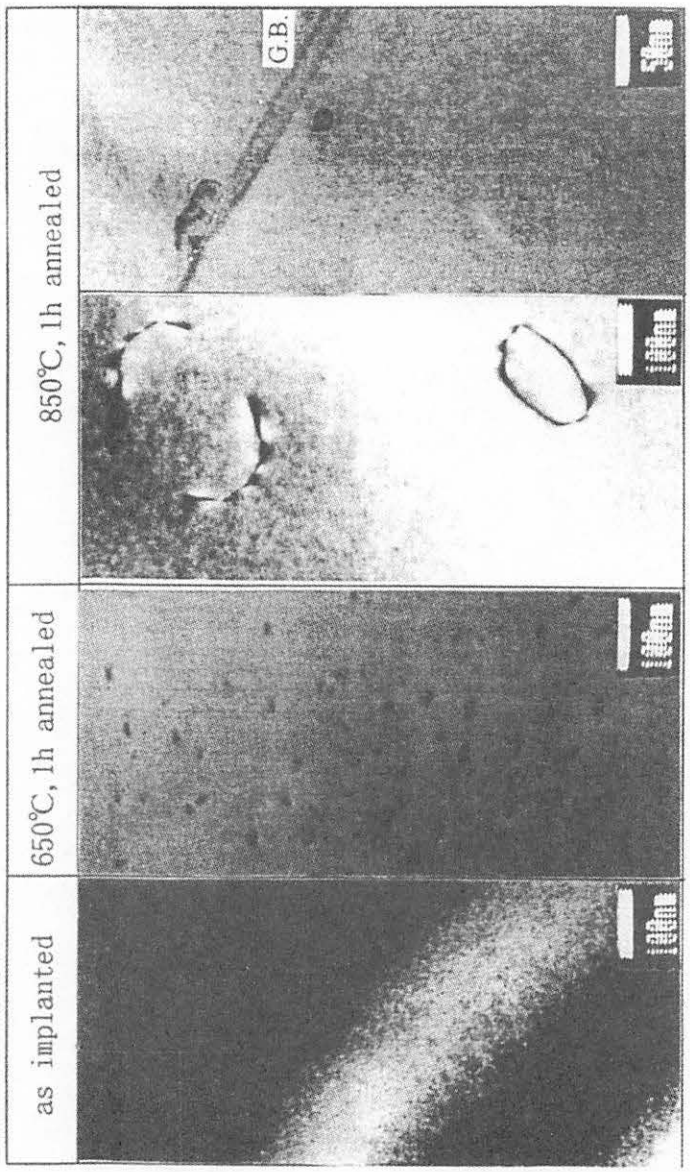

Fig. 2. Transmission electron microscopy of helium-implanted V-5Ti-5Cr-Si-Al-Y alloy as implanted and post-implanted annealing at 650 and 850°C.

I. 16. Calibration of Large Volume Neutron Detector

Toyofuku A., Kuzumaki T., Maeda K., Yahata H., Yamaya T., Maruyama K., and Ito S.***

Department of Physics, Graduate School of Science, Tohoku University
*Institute for Nuclear Study, Tokyo University**
*The Institute of Physical and Chemical Research(RIKEN)***

A large volume liquid-scintillator neutron detector has been developed. The scintillator container is made of an aluminum cylinder of 300mm in length and 200mm in diameter, viewed by a photomultiplier through a plastic light guide. The total volume of NE213 is 9.4ℓ It is intended to measure neutrons in an energy range from 1 MeV to several tens of MeV. We designed it to obtain the optimum power of n-γ discrimination by using a computer simulation. The response function was measured at TOF facilities of the Cyclotron and Radioisotope Center, Tohoku University. The neutrons which have continuous energy spectra have been provided by using a ^{9}Be(p, n) reaction at E_p=30 MeV. The neutron detector was placed at 12 meters far from the target. Neutrons were selected by the pulse shape discriminator method (PSD) and their energies were determined by TOF. Measured response functions were compared with calculations by using the computer code CECIL. The comparisons between the data and the simulations are shown in Fig. 1. At each neutron energy, their agreement was good enough to adopt the calculated result as the neutron detection efficiency. We deduced the neutron detection efficiency shown in Fig. 2.

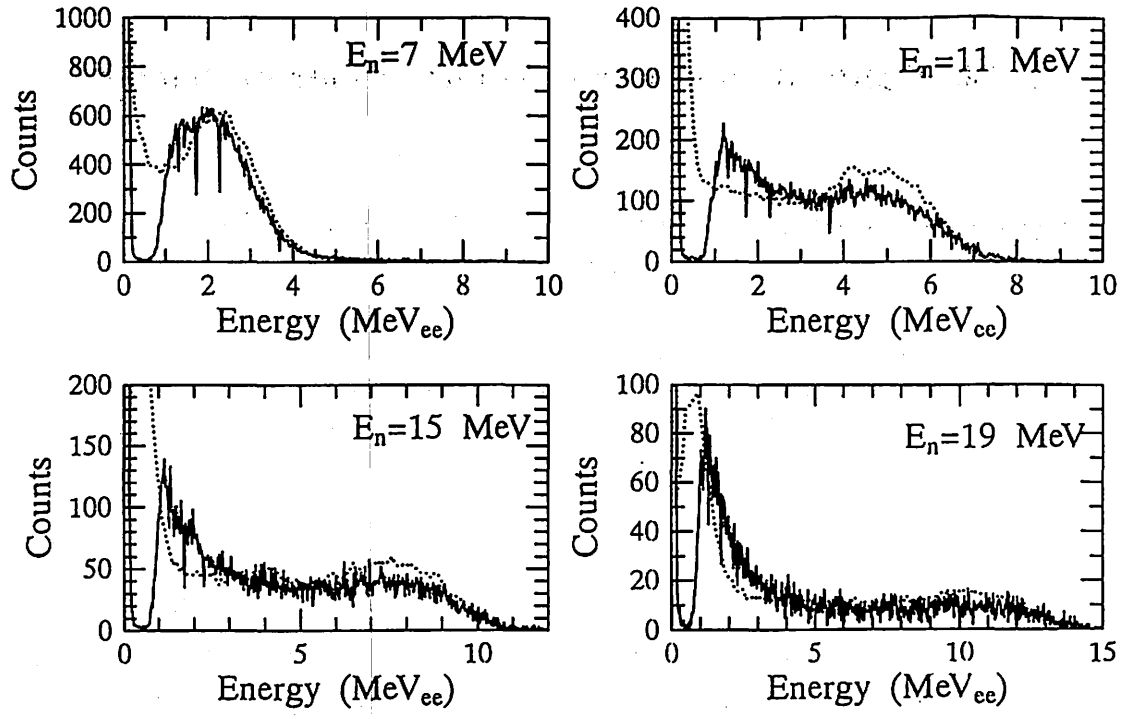

Fig. 1. Measured response functions (solid lines) are compared with simulation (dotted lines).

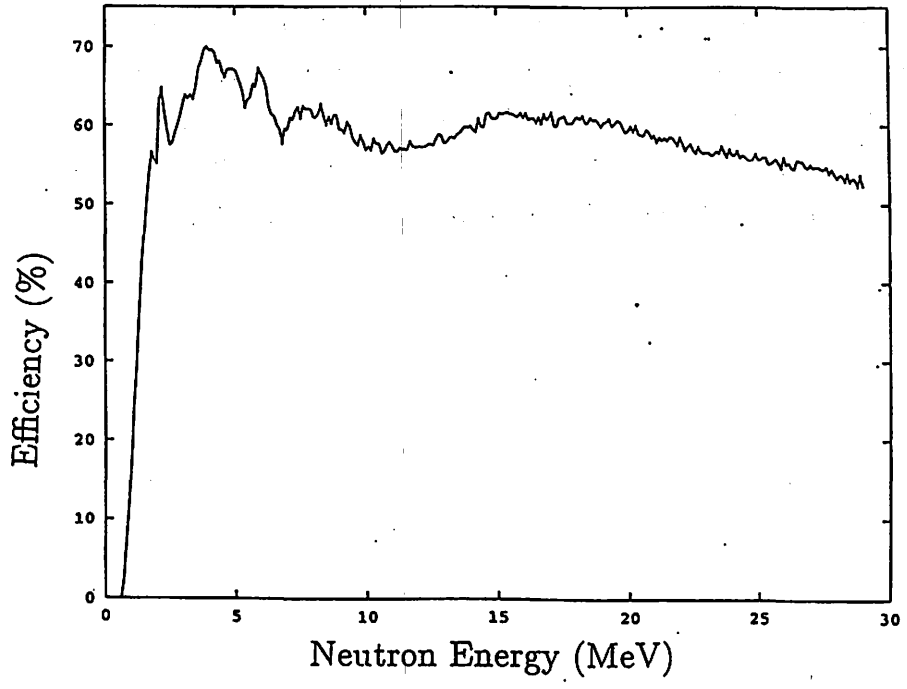

Fig. 2. Neutron detection efficiency. The threshold is 0.5 MeV_{ee}

I. 17. Attenuation of Neutron Flux by a Bismuth Absorber used for a Neutron Detector

Yoshida K., Kino K., Endo T., Saito T., Ueno H., Nakagawa T.**, Fujii Y.**, Aizawa T.**, Matsunaga M.**, Terakawa A.****

Laboratory of Nuclear Science, Tohoku University
*Department of Physics, Yamagata University**
*Department of Physics, Tohoku University***
*Cyclotron and Radioisotope Center, Tohoku University****

We have been used a bismuth absorber for a neutron detector to absorb scattered electrons and soft γ -rays from the target in (e, e'n) experiments. This absorber attenuates not only soft γ -rays but also the neutron flux. This attenuation was measured for the neutron energy below 8 MeV using the ^{252}Cf neutron source by Takakuwa et al.[2]. In this report we discuss the energy dependence of the attenuation of neutron flux by a bismuth absorber for the neutron energy above 8 MeV obtained by the TOF measurement of the neutron from the ^{9}Be(p, n)^{9}B reaction.

The experiment was carried out using the continuous neutron beam from the ^{9}Be(p, n)^{9}B reaction for an incident proton energy of 30 MeV at the Cyclotron Radioisotope Center. Neutrons emitted from the ^{9}Be target of 2.75 mm thickness were measured at $\theta_n = 35$ from the proton beam line. The neutron detector consisted of a cylindrical NE213 scintillator, 18 cm in diameter and 10 cm in depth, coupled to a Hamamatsu photomultiplier. The detector was placed at 10.5 m from the center of the scattering chamber and shielded by 15-20 cm thickness of lead. We placed the bismuth plate in front of the detector to absorb γ -rays from the target. Lead collimators were placed in front of the bismuth plate to restrict the acceptance of the neutron detector to particles from the direction of the target (Fig. 1). The attenuation rate was measured without and with the 2 cm, 4 cm, and 6 cm bismuth plates.

The n/ γ discrimination was achieved by the two-dimensional plot of ADC channels as a function of PSD timing and Charge Comparison method. In both methods, neutron events and γ events were clearly discriminated. Neutron energy distributions and the neutron attenuation factor obtained by the TOF measurement are shown in Fig. 2 and Fig. 3a-c. The neutron attenuation factor tends to get bigger in the low energy region. But there are no sudden changes or bumps and the factor keeps the constant value as a whole. The constant value of 0.3 in the energy range 5-10 MeV for the 4cm bismuth plate is in good agreement with the value deduced by Takakuwa et al. According to Takahisa et al.[3] γ -rays are well absorbed by the bismuth plate so that the counts of them decrease rapidly as the thickness of

the bismuth plate increases, while the neutron attenuation factor does not make the rapid change and keeps the value between 0.2 and 0.4. Therefore we can say that the bismuth plate is suitable for the γ absorber.

In summary, the energy dependence of the neutron attenuation factor by bismuth plates have been measured using continuous neutron beam from the ^{9}Be(p, n)^{9}B reaction at 30 MeV. Though the neutron attenuation factor for bismuth plates tends to be a little bit big at low neutron energy, it keeps roughly 30 % and there are no structures. So the bismuth plate is found to be suitable for absorption of γ -rays not only for the low neutron energy below 8 MeV but also above 8 MeV up to 25 MeV.

References

1) Suzuki S., Saito T., Takahisa T., et al., Nucl. Instrum. Methods **A314** (1992) 547.
2) Takakuwa C., M. thesis, Tohoku University (1990).
3) Takahisa K., D. thesis, Tohoku University (1991).

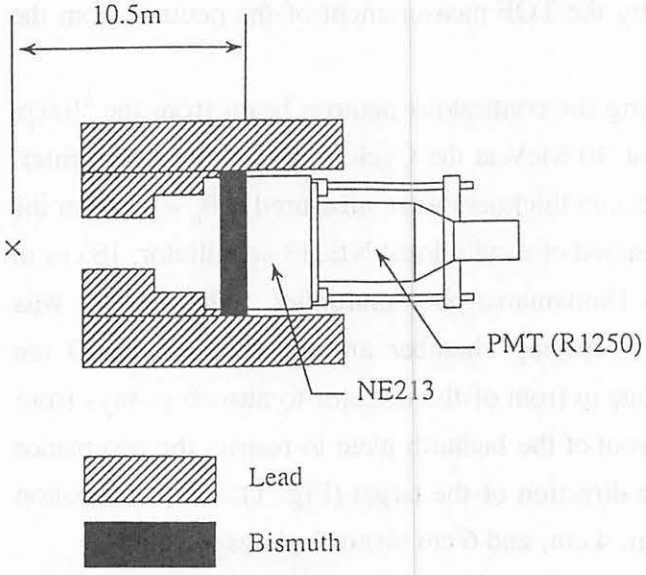

Fig. 1. Schematic view of the shield for the neutron detector. Cross shows the target position.

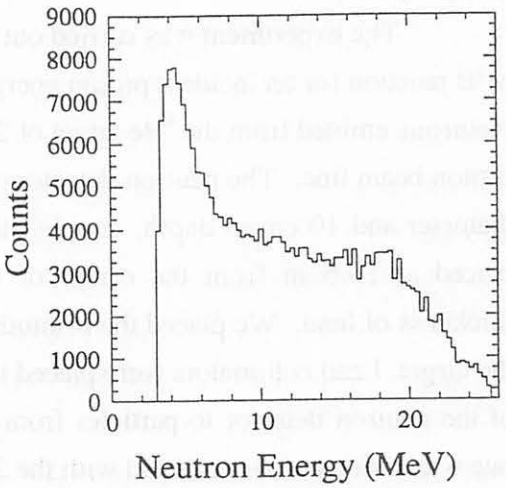

Fig. 2. Neutron energy spectrum without bismuth plate.

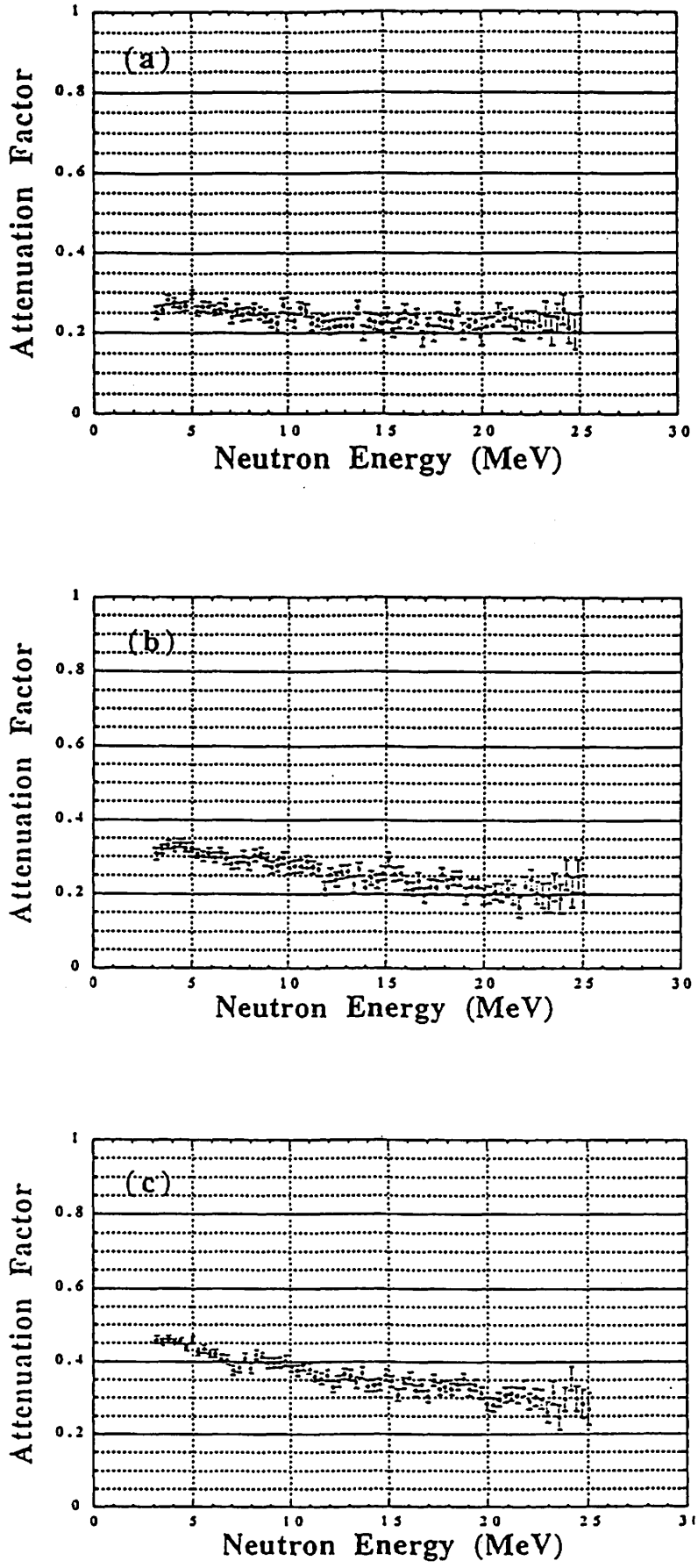

Fig. 3. The neutron attenuation factor for the (a) 2cm; (b) 4cm; (c) 6cm bismuth plates.

I. 18. R & D of Large GSO Scintillators for 10 MeV γ-rays

Takahashi T., Koshino K., Saito Y., Satoh S., Fujii Y., Sato Y., Endo T., Tamura H., Hashimoto O., Noumi H., and Tanida T***

Department of Physics, Tohoku University
*National Laboratory for High Energy Physics (KEK)**
*Department of Physics, University of Tokyo***

Detection of γ-ray from hypernucleus is one of the most important topics in Λ hypernuclear spectroscopy. Two directions are being pursued concerning to the γ detection. One is measurement of low energy γ-ray by germanium detectors. Spin-spin interactions between a Λ hyperon and a nucleon are to be investigated with the ultra-high energy resolution. The other is measurement of higher-energy γ-ray of about 10 MeV with high efficiency, requiring a small radiation length good scintillator. It aims to detect γ-ray transition between major shells of Λ hyperon in order to determine spin-orbit splitting of a Λ hyperon orbitals with better resolution than with magnetic spectrometers. GSO (Gd_2SiO_5:Ce)[1-3] is one of promising scintillators. It has following great advantages,

1. High Z and high density. Radiation length is 1.38 cm , about a half of NaI(Tl)'s.
2. Large light yield (20% of NaI(Tl)'s).
3. Small decay constant (60ns at 0.5mol% Ce concentration) for major component.

However it was not available large crystals because of the difficulty of the production. The advantages have not been confirmed for a large crystal.

The GSO with the Ce concentration of 0.5mol% whose size was 50 mm × 50 mm × 130 mm^L was used in following tests,

1. Energy resolution and their energy dependence.
2. Counting rate dependence of the resolution.
3. The response for 10 MeV γ-rays.

The energy resolution of 11.5% (FWHM) at 662 keV of ^{137}Cs source was obtained using 3" PMT (HAMAMATSU R1911-05MOD) directly attached to the crystal. Number of scintillation photons is measured by using ^{241}Am NaI(Tl) pulser (corresponding to 3.2 MeV γ). Assuming 40000 photons/MeV of NaI(Tl) and 20% quantum efficiency of PMT, about 3200 photons are estimated at 662 keV. This number explains the obtained energy resolution, although it is worse than reported value for a small crystal. Absorption of photons might be responsible for the energy resolution of a large GSO crystal. Measurement of absorption length are planned.

The 3" PMT cannot be used for the application, for example, array configuration of 3 x 3 or 4 x 4, since size of PMT is larger than the crystal. Therefore, data were also taken with 3/2" PMT (HAMAMATSU R580). The resolution of 18 % and about 1300 photon are obtained. The obtained number of photons is proportional to the area of the photo-cathode attached to the crystal. The energy dependence measured with ^{137}Cs and ^{22}Na (511, 662, 1275 keV) shows 1/sqrt(E) dependence in this energy range. Extrapolated to 10 MeV, the energy resolution of 0.5 MeV is expected. Tests with 10 MeV γ-ray are in progress.

References

1) Ishibashi H., Nucl. Instr. Meth. **A294** (1990) 271.
2) Melcher C. L. et al., IEEE Trans. Nucl. Sci. **37** (1990) 161.
3) Ishii M. and Kobayashi M., Prog. Crystal Growth and Charact. **23** (1992) 245.

I. 19. Using a Combination of Chelation by Dibenzyldithiocarbamate with Condensation into Dibenzylidene-D-Solbitol Gels for Heavy Metal Preconcentration on PIXE Analysis

*Yamazaki H., Tanaka M., Tsutsumi K., Ishii K., Iwasaki S., Matsuyama S., Inoue J., Murozono K., and Orihara H.**

*Department of Quantum Science and Energy Engineering, Tohoku University, Cyclotron and Radioisotope Center, Tohoku University**

Introduction

An interest in the chemical composition of different natural waters has increased very much due to greater awareness of the problem of pollution. Particle-induced X-ray emission (PIXE) has been used extensively for a variety of water samples[1-5]. PIXE is conveniently applied to the analysis of thin solid samples and offers a higher absolute sensitivity (nano-gram levels) than atomic absorption spectrophotometry. In addition, PIXE analysis allows simultaneous determination of the concentrations of the elements heavier than Mg. However, chemical treatment of water samples is especially suited for detection of the traces of heavy metals with respect to other representative metal ions in higher concentrations.

Sodium dibenzyldithiocarbamate (DBDTC) has been used to collect nano- and microgram amounts of various heavy metals as well as Se and As from aqueous samples having a wide range of acidity[6-10]. The attractive performance of DBDTC as a precipitant is due to the quite low solubility of its complexes with heavy metals: DBDTC anion strongly complexes with many transition metals in acidic solution (~pH 2)[11]. In precipitation, however, the use of carriers or the coprecipitation technique is important especially when the solubility of a chemical species formed in exceedingly dilute solutions is not low enough to prove the complete precipitation, or when the particle size of precipitates is too small to be collected on a filter. The metal-DBDTC complexes have affinity to hydrophobic polymer gels such as dibenzylidene-*D*-sorbitol (DBS), so the coagulation of the metal complexes with DBS gels makes the filtration easier regardless of the concentration of the complexes in aqueous samples.

In this paper, the enrichment procedure composed of two elemental reactions, *i.e.*, the formation of metal-dibenzyldithiocarbamate complex and the coagulation with dibenzylidene-*D*-sorbitol gels, was studied in conjunction with rapid preparation of thin target specimens of uniform composition for PIXE analysis.

Experimental

Reagents

Sodium salt of *N,N*-dibenzyldithiocarbamic acid (DBDTC) was obtained from Aldrich Chemical Company, Inc. A solution of the complexing agent consisting of 0.1% (w/v) of DBDTC in methanol was prepared immediately before use. Dibenzylidene-*D*-sorbitol (DBS), commercially called "Gelol D", was obtained from New Japan Chemical, Ltd. DBS is one kind of condensation polymers of *D*-glucitol and benzaldehyde, and easily dissolves into a polar solvent such as dimethylsulfoxide (DMSO). A 4% (w/v) of DBS solution in DMSO was used as a coagulant of DBDTC-metal complexes; this solution added to water samples sets to gelation when the samples are kept at neutral pH. All solid reagents (DBDTC, DBS) were checked for the purity with PIXE.

Humic acid (technical grade, Aldrich Chemical Company, Inc.) was purified by leaching it for 3 days with 0.1M (1M=1mol·dm^{-3}) HNO_3 to remove the heavy metal contaminants. The leached acid was washed with pure water (passed through a mixed ion-exchanger bed and distilled) for several times and dried at 180°C. A stock solution containing 200 μg/cm^3 of humic acid was prepared by dissolving 10mg of purified acid in 5 cm^3 of 2M Na_2CO_3 and then diluting the solution to 50 cm^3 with pure water. The stock solution was filtered by a nuclepore membrane (pore size, 0.2 μm in diameter) prior to use.

The standard solutions of Fe^{3+}, Co^{2+}, and Hg^{2+} in appropriate concentrations were used after serial dilution of the metal solutions of the certified concentrations (1.00 mg/cm^3). These heavy metals were used to represent the stability of metal-carbamate complexes decreasing in the order of Hg^{2+}>Pd^{2+}>Ag^{+}>Co^{2+}>Cu^{2+}>Ni^{2+}>Pb^{2+}>Cd^{2+}>Zn^{2+}>Fe^{3+}>Mn^{2+}[12]. All the other chemicals used were the highest purity grade obtained from Wako Pure Chemical Industries, Ltd.

Enrichment procedure

Into a 25 cm^3 of solution containing a heavy metal, a desired amount of the DBDTC solution was pipetted, and the solution was kept stirred for 5 min. After the pH of the solution was adjusted to around 5.2 with 1M acetate buffer solution, an appropriate volume of the DBS-DMSO solution was added to coagulate the metal-DBDTC complexes. The DBS gels thus formed were filtered under reduced pressure (~250 mmHg) on a nuclepore membrane of 0.2 μm pore. In the modified procedure, some amounts of zirconium nitrate were first added to the sample solutions. As zirconium is a rare element in natural surface waters, it is expected to work as an internal standard in PIXE analysis; but this attempt was not accomplished yet. After filtration, the sediment on the filter was washed with 9 cm^3 of pure water and dried at room temperature; the volume of washing water was based on the elimination of sodium ions from the sediments without any loss of heavy metals in question. The filtration and washing procedures required around 10 min; obviously the time may

change if a larger volume of sample solutions is processed in order to attain a higher enrichment factor. In the preliminary investigation, the filtrates were analyzed for heavy-metal concentrations by atomic absorption spectrophotometry. In PIXE measurement, the filter was mounted on a holder, which was screwed on a steel slide frame, for the direct irradiation.

Apparatus

In enrichment of sample solutions, we used a glass filter-holder (13 mm diameter and 50 cm^3 volume) which was equipped with a nuclepore membrane (10 μm thickness, 0.2 μm pore size and 3×10^8 pores/cm^2 pore density). An atomic absorption spectrophotometer (Nippon Jarrell-Ash, Model 311) was employed for measurements of metal concentrations in the filtrate.

In PIXE analysis, we used the system of vertical beam type in-air PIXE, called ViaPIXE, in 4.5-MV Dynamitron laboratory of Tohoku University. Details of the ViaPIXE was described in Reference 13. A-3MeV proton beam from the accelerator was passed through a graphite collimator of 3 mm in the inner diameter and impinged a target specimen in vertical direction. The yields of X-rays were measured by a Si(Li) detector which viewed the target position through a guide of ~5 mm diameter in the direction of 135 deg with respect to the vertical beam axis. An apparent beam current (2 nA) was measured through a wire connected to the stainless steel slide. Proportionality of the beam current vs X-ray yield was confirmed good, but the absolute value of the impinging beam current has remained uncertain.

Results and Discussion

Recommended enrichment procedure

PIXE analysis turns out to be simple in the case of very thin specimens with uniform thickness and homogeneous composition, so experimental studies were first carried out to minimize the amount of the chemicals used in enrichment of heavy metals in aqueous solutions.

Quantitative recovery of heavy metals is necessary for any preconcentration techniques. DBDTC is a singly charged anion in mild acidic solutions and shows lower affinity for trivalent iron ions than for divalent transition metals such as mercury and cobalt.11 The recovery of ferric ions with less ability of complex formation was investigated as a function of the amount of DBDTC added to the samples. Table 1 reveals that ferric ions in a 25 cm^3 of 1 ppm solution (0.45 μmole) are quantitatively recovered when DBDTC exists in a large excess to neutralize the charge of the metal ions. The large molar ratio of DBDTC to metal ion (7.6) is obviously sufficient to complex with other heavy metals having smaller charge and higher affinity to the complexing reagent. As shown in the first two rows in Table 1, the recovery does not decrease considerably even in the solutions containing DBDTC deficient to compensate the charges of ferric ions. This may indicate that the DBDTC-

deficient complexes are electrically neutralized by acetate anions in high concentration and adsorbed onto the hydrophobic surface of DBS gels due to an organic nature of the complexes.

In addition to quantitative collection of metals existing in solutions, rapid preparation of target specimens is desired for routine analysis of many water samples, such as in the case of environmental monitoring. Table 2 represents the effect of the collection with DBS on the filtration efficiency. The amount of DBS added to solutions did not appreciably affect the recovery and the filtration time when the cobalt-DBDTC complex exists in appreciable concentration. On the other hand, it took very long time to filtrate the solutions with very low concentration of the complexes. This may be ascribed to the instability of DBS gels; DBDTC anions in organic nature are aggregated in some extent to hydrophobic surface of DBS gels, which results in the repulsion of gel particles.

Zirconium ions were added to solutions in order to compensate the surface charge of DBS gels due to the adsorption of DBDTC anions. As shown in Table 3, the addition of 0.014 μmole zirconium reduced the filtration time to one third or less than the case without zirconium. This small amount of zirconium was enough to stabilize the gels formed in solutions regardless of the concentrations of DBS gels and metal-DBDTC complexes. Moreover, the last three rows in Table 3 indicate the necessity of both zirconium and DBS in order to maintain rapid filtration of samples having very low concentration of metal-DBDTC complex.

It can be concluded that the quantitative recovery and the rapid filtration are accomplished by the use of small amounts of DBS (0.4 mg) and zirconium ions (0.014 μmole); these small amounts of the chemicals used in enrichment are favorable to the preparation of thin targets for PIXE analysis. At this stage, however, it is rather difficult to give a proper explanation to the complexity of DBS-gel stability in aqueous solution.

Based on the findings described above, the optimum amount of the chemicals used in the preconcentration step is set as follows: 3.5 μmoles of DBDTC, 0.4 mg of DBS and 0.014 μmole of zirconium nitrate are added to 25 cm^3 samples. The recommended amounts of the chemicals is sufficient to collect up to 2 ppm of ferric ions in 25 cm^3 samples (0.90 μmole Fe^{3+}), as shown in Table 3. Under this condition of the chemicals, DBS gels containing metal-DBDTC complexes appeared to be mounted on the nuclepore filter of 0.2 μm pores in the form of a thin paste with uniform thickness irrespective of the concentration of the metal complexes in sample solutions. Moreover, the filtration time and the recovery were checked by increasing the volume of solution containing cobalt in 0.2 ppm in order to acquire information relating to the largest volume of sample solutions capable to be concentrated by the use of the recommended amounts of the chemicals. Aside from elongation of the filtration time, the recovery was proved to be quantitative up to a 200 cm^3 sample, indicating 8 times larger enrichment factor attainable in a solution with low metal concentrations. However, around one tenth of cobalt ions in a 250 cm^3 solution was lost, although the total amount of

the metals in the solution was less than the maximum amount of metal ions collectable under the given conditions of the chemicals. This may be ascribed to very low concentration of DBS incapable of forming stable gels.

Versatility of the enrichment procedure

The coexistence of Mg^{2+}, Ca^{2+} and humic acid in much higher concentrations (40 ppm) did not interfere with the recovery of 1 ppm Fe^{3+} ions. These findings indicate that dibenzyldithiocarbamic acid does not form chelates with any of alkaline earth metal ions and that transition metal ions interact much stronger with the carbamate anions than with the carboxyl groups in humic acids. Therefore, the enrichment procedure consisting of the formation of metal-DBDTC complexes and their coagulation with DBS gels is useful both for aqueous samples with high contents of alkaline earth metal ions, *e.g.* sea-waters and for solutions containing various amounts of humic substance, *e.g.* river-waters.

PIXE *analysis of target specimens*

The yields of characteristic X-rays (N) for a particular element is proportional to the concentration (C) by a coefficient (K) which is specific for each element (chemical precipitation mechanism, cross section, X-ray energy) and depends on the detector system (solid angle, detector efficiency): $N=KC\eta$, where η is a fluctuating factor related both to the surface density of heavy metal atoms and to the surface density of impinging protons; therefore η is related both to target preparation and to proton beam characteristics, and may have a random behavior in each target specimen and in each exposure.

In order to check the fluctuation due to the random behavior in target preparation, 3-MeV proton beam was incident repeatedly to different surface points of the identical target specimen, and several targets, which were prepared independently under the same condition, were analyzed with PIXE. Table 4 reveals that the yields of characteristic X-rays is nearly equal at the different location of impinging beam spot on the identical target; it can be concluded that regardless of the concentrations the heavy metals in solutions are collected in the form of sediment having uniform thickness and homogeneous composition. The results in this table also indicate almost constant feature of the impinging proton beams during short period of the experiment (at least one hour or more), although the yields of cobalt K_α X-rays are poorly proportional to the concentrations due to the failure of beam charge collection in the PIXE measurements. Table 5 shows the reproducibility of preparation of target specimens. As compared with the results in Table 4, a larger deviation in measured counts was observed on the targets prepared from solutions having the same concentration of metals. This large scatter may rise in random behavior in the whole enrichment step. The results in Table 5, however, indicate that the fluctuation in the whole chemical procedures seldom results in an analytical error above ±8 % independently of the concentration of heavy metals in sample

solutions.

Figure 1 shows the calibration curves for iron (A), cobalt (B) and mercury (C) in the PIXE analyses: the logarithm of counts in the characteristic X-ray peaks, which are normalized at 2 μC of the accumulated charge, is plotted as the ordinate and the logarithm of the metal concentrations in 25 cm^3 samples as the abscissa. The counts in the peak of zirconium *K*-shell X-ray were not accumulated with analytical precision under the present conditions in PIXE measurement owing to the small amount of coprecipitated zirconium (0.014 μmole) and its small ionization cross-section, so we abandoned the use of the zirconium peak counts as a standard for the yields of X-rays characteristic of other heavy metals. A good linear relationship was obtained in every case, indicating the determination of metal concentrations in a wide range by Via-PIXE. For the target specimens of Fe and Co solutions in 1 ppb and of Hg in 10 ppb, however, the statistical errors in the counts were larger than the scatter due to a random behavior in enrichment (< ±8%). In the case of determination of more dilute concentrations of these heavy metals, the precision becomes much worse in the PIXE analysis under the present condition: preconcentration of a 25 cm^3 sample, the geometoric setup of the target and detector, and irradiation by 2 nA proton beam for ~ 20 min (accumulated charge, 2 μC). As described in the preceding section, a trace of heavy metals in a 200 cm^3 solution can be quantitatively collected by the use of the selected amounts of the chemicals, aside from much longer time of the filtration (40 min). It can be concluded that the detection limits of heavy metals will be lowered around one order of magnitude using the present setup of the apparatuses in PIXE measurement; 0.1 ppb or less of Fe and Co, and 1ppb or less of Hg in solutions will be determined precisely. However, it is desired to attain lower detection limit in PIXE analysis especially for an analysis of water quality regarding mercury (< 0.5 ppb).

Conclusion

The useful enrichment procedure was obtained for heavy metals in a wide range of the concentrarions; the elementary processes are the complexation of metals with dibenzyl-dithiocarbamate ions and the coagulation of the complexes wit dibenzylidene-*D*-sorbitol gels due to a hydrophobic interaction. The gels formed in solution were stabilized by addition of small amount of zirconium ions and speedily collected on the nuclepore membrene of 0.2 μm pores by filtration under reduced pressure. The amounts of the chemicals used in the preconcent-ration step were optimized to make thin sediments on the filter. The uniformity in thickness and composition of the sediments leads to the good linear calibration curve for PIXE analysis in a wide range of metal concentrations (1 to 1000 ppb). In order to attain lower detection limit and higher accuracy in PIXE analysis, however, an additional experiment should be carried out on the enrichment procedure and the PIXE measurement; in the preconcentration step, a large bulk of sample solution should be speedily processed without any loss of heavy metals by the use of a filter having pores larger than 0.2 μm in

diameter and the sufficient amount of an internal standard element like zirconium should be coprecipitated, and in the PIXE measurements the geometrical arrangement of a detector and the device measuring the currents of impinging proton beam should be improved.

Acknowledgements

The authors are grateful to New Japan Chemical, Ltd. for a generous gift of dibenzylidene-*D*-sorbitol powder (Gelol-D).

References

1) Johansson E. M. and Akselsson K. R., Nucl. Instr. and Meth., **181** (1981) 221.
2) Tanaka S., Darzi M, and Winchester J. W., Environ. Sci. Technol., **15** (1981) 354.
3) Hansson H. C., Johanson E. M. and Ekholm A. K., Nucl. Instr. and Meth., **B3** (1984) 158.
4) Johansson E. M. and Johansson S. E., Nucl. Instr. and Meth., **B3** (1984) 154.
5) Aprilesi G., Cecchi R., Ghermandi G. et al., Nucl. Instr. and Meth., **B3**, (1984)172.
6) Martens R. I. and Githens R. E., Sr., Anal. Chem., **24** (1952) 991.
7) Hulanicki A., "Complexation Reactions of Dithiocarbamates," Talanta, **14** (1967) 1371.
8) Sastri V. S., Aspila K. I., and Chakrabarti C. L., Canad. J. Chem., **47** (1969) 2320.
9) Fukusawa T. and Yamane T., Anal. Chim. Acta, **84** (1976) 195.
10) Grieken R. V., Anal. Chim. Acta, **143** (1982) 3.
11) Linder H. R., Seltner H. D., and Schreiber B., Anal. Chem., **50** (1978) 896.
12) Minczewski J., Chwastowska J., and Dybczynski R., Separation and Preconcentration Methods in Inorganic Trace Analysis, (John Wiley & Sons, New York (1982), Chap. 5).
13) Iwasaki S., Ishii K., et al., Internat. J. PIXE, to be published (1996).

Table1. The effect of DBDTC amounts on the recovery of ferric ions

Fe (μ mole)	DBS (mg)	DBDTC (μ mole)	Recovery (%)
0.45	4.0	0.68	79±2
0.45	4.0	1.0	78±2
0.45	4.0	1.4	83±2
0.45	4.0	1.7	82±2
0.45	4.0	3.4	100±2

Solution : 1 ppm, 25cm^3.

Table2. The effect of an addition of DBS on the filtration of efficiency

Co (μ mole)	DBDTC (μ mole)	DBS (mg)	Recovery (%)	Filtration time (min)
0.42a	3.4	5.0	100±2	14
0.42	3.4	4.0	100±2	22
0.42	3.4	3.0	100±2	23
0.42	3.4	2.0	100±2	23
0.42	3.4	1.0	99±2	24
0.42	3.4	0.0	100±2	30
4.2×10^{-4}	3.4	0.8	-	>45

Solution volume : 25cm^3. a: 1 ppm, b: 0.001 ppm

Table3. The effect of zirconium amounts on the stability of DBS gels

Fe (μ mole)	Co (μ mole)	DBDTC (μ mole)	DBS (mg)	Zr (μ mole)	Recovery (%)	Filtration time (min)
0.090	-	3.4	2.0	0	100±20	25
0.090	-	3.5	2.0	0.014	99±20	7
0.090	-	3.6	2.0	0.027	95±20	4
0.090	-	3.8	2.0	0.055	100±20	6
0.18	-	3.5	0.4	0.014	95±8	10
0.18	-	3.5	0.0	0.014	100±8	11
0.67	-	3.5	2.0	0.014	100±5	9
0.90	-	3.5	2.0	0.014	100±4	10
1.3	-	3.5	2.0	0.014	85±2	11
-	0.42	3.5	0.4	0.014	97±5	5
-	0.42	3.5	0.0	0.014	99±5	5
-	4.2x10	3.5	0.4	0.014	99.9±1.8*	8
-	4.2×10^{-5}	3.5	0.4	0.014	99.7±1.8*	8
-	4.2×10^{-5}	3.4	2.0	0	-	>60
-	4.2×10^{-5}	3.5	0.4	0.014	-	6
-	4.2×10^{-5}	3.5	0.0	0.014	-	>60

Solution volume : 25cm^3. *: experiments with a radioactive tracer (60Co).

Table4. Fluctuation in the X-ray yield of the identical target

M etal amount (μmole)	Location	Yield (counts / 2 μC)
Co 0.42 μmole	A	38316±277 [1)]
	B	38347±160
	C	38796±153
Co 0.042 μmole	A	5188±72
	B	5433±70
	C	5272±73
Hg 0.012 μmole	A	601±24
	B	569±24

Location, A: the center of sample (13 mm diameter); B: the 4 mm left side of the center; C: the 4 mm right side of the center.

1) : statistical error (1 σ). Apparent beam current : 2nA.

Table5. Reproducibility of sample preparation

Metal amount (μmole)	Sample No.	Yield (counts / 2μC)
Co 0.42 μmole	No.1	48394±212[1)]
	No.2	47035±217
	No.3	50647±201
Co 0.042 μmole	No.1	4566±68
	No.2	5104±71
	No.3	5242±82
Co 0.0042 μmole	No.1	517±23
	No.2	582±24
Hg 0.012 μmole	No.1	569±23
	No.2	542±22
	No.3	498±21

1) : statistical error (1 σ). Apparent beam current : 2nA.

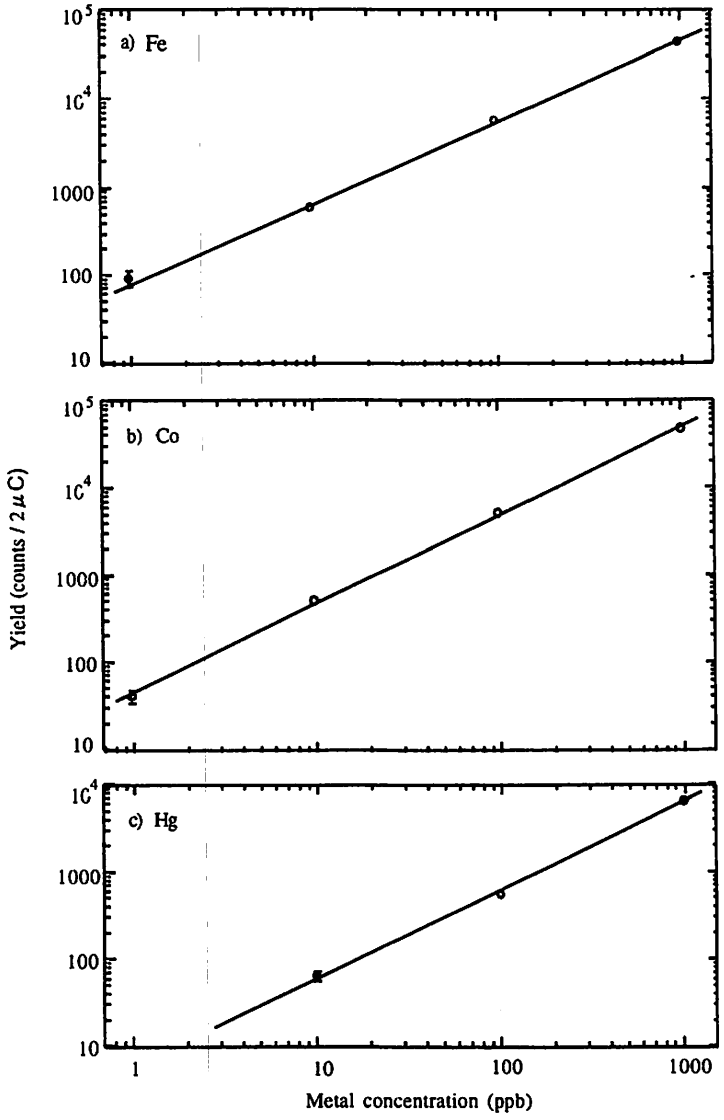

Fig1. Calibration curves in Via-PIXE analysis for heavy metals. The X-ray yields were normalized at 2 μ C of the accumulated charge(apparent beam current : 2nA).

I. 20. System of Pattern Analysis in PIXE Spectra

Murozono K., Iwasaki S., Inoue J., Ishii K., Kitamura M., Sera K., and Futatsugawa S.***

Department of Quantum Science and Energy Engineering, Tohoku University
*Cyclotron Research Center, Iwate Medical University**
*Nishina Memorial Cyclotron Center, Japan Radioisotope Association***

Introduction

We aim at industrial application of PIXE, e.g., environmental monitoring by analyzing aerosol samples, or hopefully, health diagnosis with biomedical samples such as blood serum. In these cases, we have to process a large number of samples of the same kind. Thus tasks in PIXE analysis such as spectra data analysis should be automatized. In recent years, a lot of computer software for analysis of PIXE spectra has been developed which is usually based on a least-squares fit to each peak[1]. However we have paid attention to distinctive features of a new method called pattern analysis method by Iwasaki, et al[2,3]. In the pattern analysis method, all peaks from an element are put together as a pattern. This treatment fairly reduces the difficulty in decomposition of overlapping peaks. Furthermore, the actual decomposition is only to multiply a matrix to measured spectra. Thus the results can be obtained immediately without any complicated tasks. They have tested the method in a few PIXE spectrum, such as from a stainless steel sample(type SUS316) and from a standard solution INTB1 sample in the previous papers. Based on these studies, we have developed a software system for PIXE spectra analysis and applied it to the spectra from some biomedical samples to test the proposed method.

Pattern Analysis Method

The principle of the pattern analysis method is briefly shown here. In this approach, a PIXE spectrum from a sample is considered as a linear superposition of some fundamental patterns named reference spectra: spectra of each single element in the sample and a continuum component of bremsstrahlung and gamma-rays. This assumption is reasonable when a sample is very thin. It can be written with vectors as

$$\boldsymbol{x} = y_1\boldsymbol{x}_1 + \ldots + y_m\boldsymbol{x}_m \qquad (1)$$

where vector $\boldsymbol{x}$ denotes the PIXE spectrum from the sample and $\boldsymbol{x}_1$ to $\boldsymbol{x}_m$ are the reference spectra. The number of reference spectra m is around 15 for typical biomedical samples.

Each element of these vectors is the count of respective channel of the pulse-height spectra. The factors y_1 to y_m denote relative concentrations of elements in the sample.

Now we assume the reference spectra are already known and we intend to obtain relative concentrations of elements $y = [y_1 \cdots y_m]^T$ from the measured spectrum $\tilde{x}$. If the relation (1) is valid for $\tilde{x}$, $\tilde{x}$ is expressed as

$$\tilde{x} = X y \tag{2}$$

where $X = [x_1, \ldots, x_m]$. The formal solution of equation (2) is given as

$$y = X^{-} \tilde{x} \tag{3}$$

where X^{-} is a generalized inverse matrix of X. Since X is not a square matrix, X^{-} is not unique. In addition, the measured spectrum $\tilde{x}$ is slightly different from x of equation (1) due to the statistical fluctuation during the measurement. That is rigorously, equation (3) has no solution or equivalently y of equation (3) is not the solution of equation (2). However it is known that favorable estimation $\hat{y}$ can be obtained if we apply the least-squares condition

$$\left\| \tilde{x} - X\hat{y} \right\|^2 = \min. \tag{4}$$

and some additional conditions[4]. In this case, X^{-} becomes the Moore-Penrose (MP) pseudo-inverse matrix of X, usually denoted as X^{+}. Thus $\hat{y}$ can be given as

$$\hat{y} = X^{+} \tilde{x}. \tag{5}$$

In this way, if reliable reference spectra were obtained beforehand, relative concentrations of elements in the sample are simply obtained by a matrix multiplication. In the next section, the software system for analysis of PIXE spectra based on the above principle will be described.

Software System

Schematic diagram of the software system is shown in figure 1. It has several modules used for the model calculation of reference spectra, for the computation of the MP pseudo-inverse matrix and for conducting the actual analysis, etc. The programs are tentatively written in a computation environment called MATLAB[1] because it provides simple handling of matrices and graphics.

In the pattern analysis method, it is a principal requisite that reliable reference spectra of all elements in a sample can be obtained. We adopted a model-calculation method to determine them. In this model-based approach, K X-ray peaks of elements with atomic number Z=11 to 60 and L X-ray peaks of elements with Z=31 to 92 observed in a given detector system are simulated as follows.

1. Relative intensities of X-rays are calculated using database values. Necessary databases have been created from recent literature values, i.e., K and L-shell ionization cross-sections[5], relative emission rates of K and L X-rays[6] and their energy values[7].
2. These intensities are adjusted to a given measurement condition by multiplying the detector efficiency and the X-ray transmission through the absorber placed in front of the X-ray detector, which is usually used to stop the incident of scattered protons from the samples.

   Detector efficiency ε of a Si(Li) detector, for example, is calculated by the equation

$$\varepsilon = \exp\left(\sum_{n=1}^{3} -\mu_i t_i\right)\left[1 - \exp\left(-\mu_{Si} t_{Si}\right)\right] \tag{6}$$

where t_{Si} is the silicon crystal thickness and μ_{Si} is the linear attenuation coefficient of silicon; t_i are the thickness of beryllium window, gold contact and silicon dead layer and μ_i are their respective linear attenuation coefficients. The absorber transmission T is calculated by

$$T = -\exp\left(-\mu t\right) \tag{7}$$

where t and μ are the thickness and the linear attenuation coefficient of the absorber, respectively.

3. Each X-ray line is folded by the response function of the given detector. At the present time, we adopted a simple Gaussian model with the width corresponding to the detector energy resolution for the peak profile function.

Here we can determine the matrix X from these reference spectra. Then its MP pseudo-inverse matrix X^+ is computed with a MATLAB function based on singular-value decomposition. The actual spectra analysis is conducted by multiplying the pseudo-inverse matrix by measured spectra. Since the same pseudoinverse matrix can be applied to a series of PIXE spectra from similar samples measured in the same condition, only lower part of figure 1 is required.

Test of the Method

To test the pattern analysis method, the software system was implemented in a personal computer for MCA data collection and applied to some PIXE spectra. Measurements of the PIXE spectra were conducted at Nishina Memorial Cyclotron Center(NMCC) of Japan Radioisotope Association, in Takizawa, Japan. Samples of blood serum, animal livers, etc. were prepared on 4-μm polypropylene films[8] and were bombarded by 2.9-MeV protons in the vacuum chamber for PIXE. Emitted X-rays were measured with two Si(Li) detectors located at 90° and 135° with respect to the beam direction. Several kinds of absorbers were used. Parameters in equations (6) and (7), such as the Si crystal thickness, have been determined with the methods developed by Sera et al[9].

Through the tests, the important knowledge was gained for the following three issues Section 4.1-4.3. In Section 4.4, we will show some results of the improved approach based on the new knowledge.

Model of Continuum Component

In the present method, the continuous spectra of Bremsstrahlung and gammarays are treated as a pattern composing PIXE spectra. We had adopted a PIXE spectrum from a backing foil as the reference spectra of continuum[2] because the continuum component is almost Secondary Electron Bremsstrahlung(SEB) from a backing foil when a sample is very thin. However this approach did not suit in some cases. Figure 2 shows an example of such cases; comparison of a part of a PIXE spectrum from a serum sample and from its backing foil polypropylene. Noticeable discrepancy can be seen in the higher energy side of the hump of Bremsstrahlung between the serum spectrum and the polypropylene spectrum. This is attributed to the Atomic Bremsstrahlung(AB) from elements in the sample[1]. In such cases, the discrepancy causes overestimation of concentrations of some elements. Then we adopted an approximation of the continuum component as shown in figure 3 tentatively: a combination of a polynomial curve and two exponential ones derived by least-squares fits. The polynomial curve describes the lower energy side of Bremsstrahlung, while the two exponential curves describes the higher energy side of Bremsstrahlung portion and gamma-ray Compton tail respectively.

Necessity of Pre-selection of Candidate Elements

As above, all necessary reference spectra can be determined. First we tried a naive approach. If the MP pseudo-inverse matrix was computed from the total set of reference spectra of all possible elements, the matrix may applicable whatever elements are there in the sample. However this approach was unsuccessful. Figure 4 shows a part of PIXE spectrum from a serum sample(dotted line) and the result of pattern analysis conducted with all reference spectra as the fitted curve(thick solid line). The result is also shown by the reference spectra with corresponding outputs(solid lines). It can be seen that our model expressed as equation (1) is no longer disregarded. It is interpreted as an ill-conditioned feature of the MP pseudoinverse approach. In order to satisfy the least-squares condition, reference spectra of various elements which are not actually present are used to describe the measured spectrum. Further, negative magnitude were derived as well.

To avoid this type of difficulty, it is necessary to limit reference spectra to those of elements likely to exist in the sample. In figure 5, the MP pseudo-inverse matrix was computed from reference spectra of 11 elements which were selected with both peak identification and a priori knowledge on the sample. The preselection is mathematically considered as a method of regulation of the above illposed problem.

Usefulness of Pinhole Absorbers

As discussed in the previous paper for the SUS316 case, overlaps of K_β of element Z and K_α of element Z+1, frequently seen in region Z=20 to 30, has not caused any serious problems in the pattern analysis method. In contrast, overlaps of L peaks of heavy elements and K peaks of light ones were found to be difficult in the present method. In figure 6, for example, negative magnitude was obtained for indium(internal standard). It can be explained by the overlap of indium L peaks and potassium K peaks.

In this case, since L peaks are major components of the reference spectra of indium, L/K X-ray intensity ratio is about 10^2, K peaks of the reference spectra are disregarded. Thus the independence of reference spectra of indium and potassium becomes very poor compared with the SUS316 case.

In the present study, we adopted use of pinhole absorbers placed in measurements to avoid this type of difficulty. Since pinhole absorbers selectively reduce intensities of low energy X-rays, relative intensities of K peaks of heavy element become comparable to that of L peaks. Thus the independence between reference spectra of heavy and light elements increases; as a result, this type of illconditioned situation is avoided. Figure 7 shows an example of a PIXE spectrum measured with a pinhole absorber(pierced 1000-μm Mylar film) and the result of pattern analysis. They are in good agreement including indium.

The transmission of pinhole absorber cannot be expressed as equation (7). Therefore we determined the transmissions of the absorber with the method developed by Sera et al.[9] In which the transmission curve of an absorber is derived by dividing two spectra measured with and without the absorber each other.

Analysis of Similar Spectra

Based on the studies above, the software system was applied to several other spectra. Figure 8 shows PIXE spectra from a bovine liver, two mouse liver and two rat liver samples measured with the pinhole absorber and the results of pattern analysis. These analyses were conducted with the same MP pseudo-inverse matrix: computed from reference spectra of the pre-selected 16 elements and a continuum component derived by fitting to the spectra from the bovine liver sample. Although there still can be seen slight differences between the measured and the fitted spectra, we can say that the results are reasonable at the present phase.

Summary

We have developed a software system for PIXE spectra analysis based on the pattern analysis method. The software system was applied to some PIXE spectra to test the present method. Through the tests, important knowledge was acquired and following notions were adopted to the system:

To obtain reasonable results, it is necessary to limit reference spectra to those of elements likely to exist in the sample. This approach requires peak identification and a priori knowledge on samples to analysts. However we do not think it to be a severe drawback in industrial PIXE. Because we can easily select elements by pre-processing some representative spectra before analyzing a large number of similar spectra. While analyzing the same kinds of samples, some of them may contain another elements. Such sample will be able to detect with supervision of the residuals between model-based and measured spectra.

Peak overlaps of K X-rays from light elements and L X-rays from heavy ones causes decrease of the independence between reference spectra. This problem was avoided by using suitable pinhole absorbers in measurements. Reduction of sensitivity due to the absorbers is small for Fe, Cu, Zn, etc. which are usually of interest in PIXE analysis of biomedical samples.

We also showed some examples of analysis with the present method. At present, the results are almost reasonable. In the above examples, the analysis took about only a second per a spectrum. This indicates that, the pattern analysis method will prove a promising method for processing a large number of samples.

In the next phase of the development of the software system, the following will be considered:

•More detailed model for the reference spectra of elements including peak tailing, plateau component and escape peak must be added instead of simple Gaussian. In addition, M-lines of heavy elements must be simulated as well.

•A theoretical approach for determination of the continuum component to eliminate uncertainty in the above curve fitting method.

References

1) Johansson S. A. E. and Campbell J. L., PIXE: A Novel Technique for Elemental Analysis(Wiley, Chichester, 1988).
2) Iwasaki S., Fukuda H., Yoshizaki K., Kitamura M. and Ishii K., International Journal of PIXE **4** (1994) 131.
3) Fukuda H., Iwasaki S., Yoshizaki K., Kitamura M. and Ishii K., KEK proceedings **95** (1995) 324.
4) Rao C. R. and S. K. Mitra., Generalized inverse of matrices and its applications(Wiley, New York, (1971) .
5) Cohen D. D. and Harrigan M., Atomic Data and Nuclear Data Tables **33** (1985) 121.
6) Scofield J. H., Atomic Data and Nuclear Data Tables**14** (1974) 121.
7) Storm E. and Israel H. I., Nuclear Data Tables **A7** (1970) 565.
8) Futatsugawa S., Hatakeyama S., Saitou Y. and Sera K., NMCC Annual Report **1** (1993) 70.
9) Sera K. and Futatsugawa S., Nuclear Instruments and Methods **B109** (1996) 99.
10) Sera K. and Futatsugawa S., International Journal of PIXE, in press.

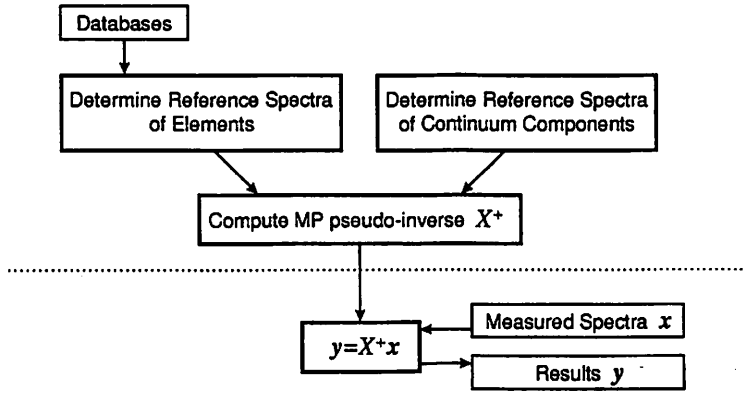

Figure 1. Schematic diagram of the software system. The programs were written in MATLAB.

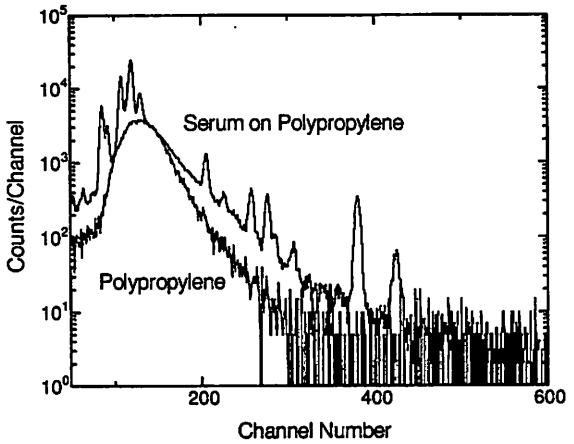

Figure 2. Part of PIXE spectra from a serum sample (upper line) and one from its backing foil polypropylene(lower line).

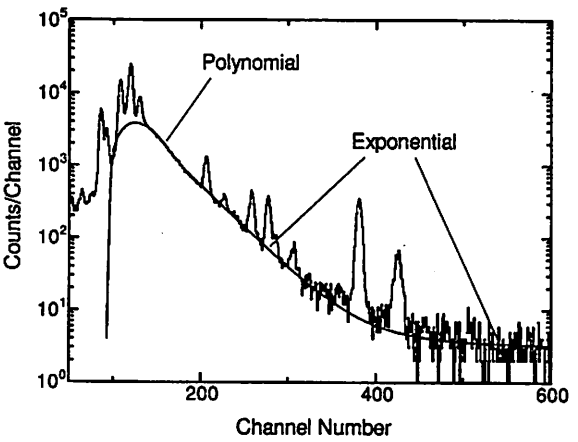

Figure 3. Part of PIXE spectra from a serum sample and an approximation of its continuum component.

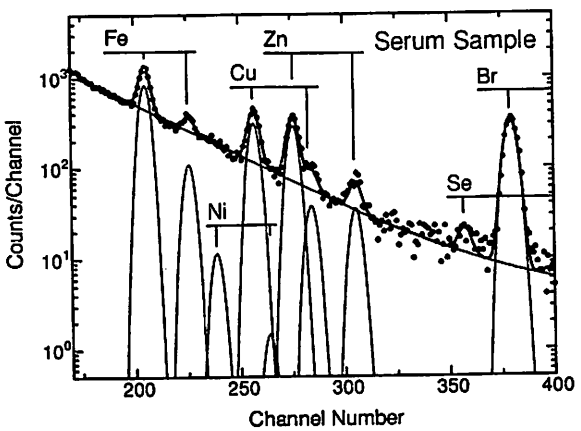

Figure 4. Part of PIXE spectrum from a serum sample (dotted line) and the result of pattern analysis conducted with all reference spectra as the fitted curve(thick solid line). Reference spectra are also shown(solid lines).

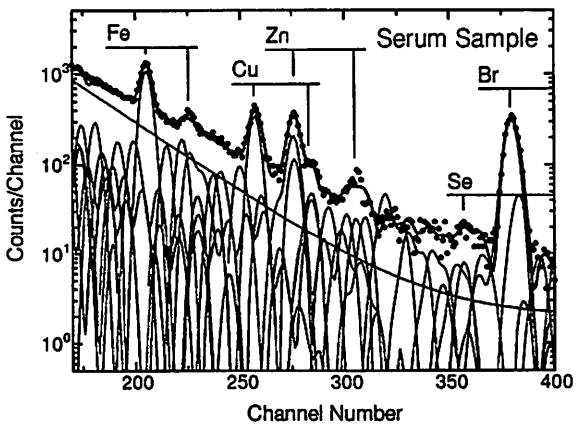

Figure 5. Part of PIXE spectrum from a serum sample and the result of pattern analysis conducted with reference spectra of pre-selected 11 elements: Cl, K, Ca, Fe, Ni, Cu, Zn, Se, Br, In and Pb. Each line corresponds to the same curve used in figure 4.

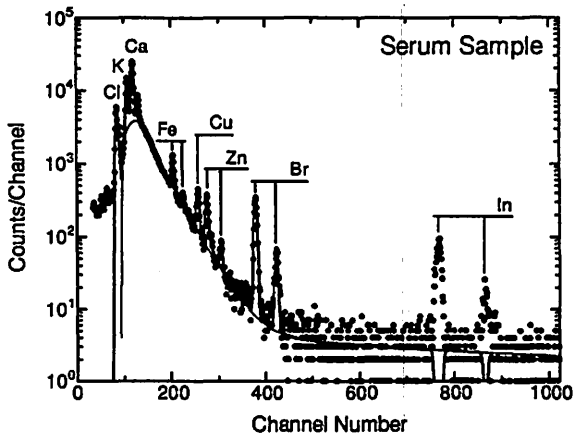

Figure 6. PIXE spectra from a serum sample measured with 300-mm Mylar absorber and the result of the pattern analysis.

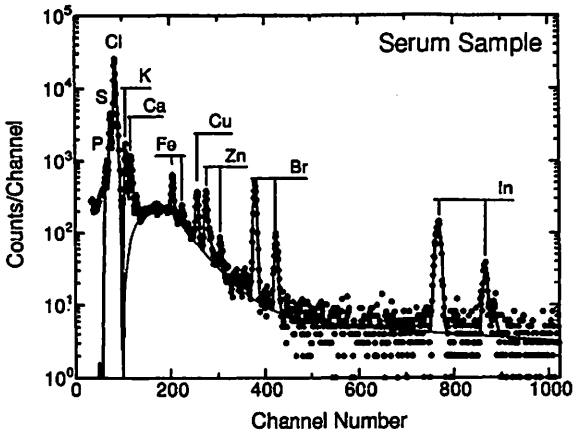

Figure 7. PIXE spectra from the same serum sample measured with the pinhole filter and the result of the pattern analysis.

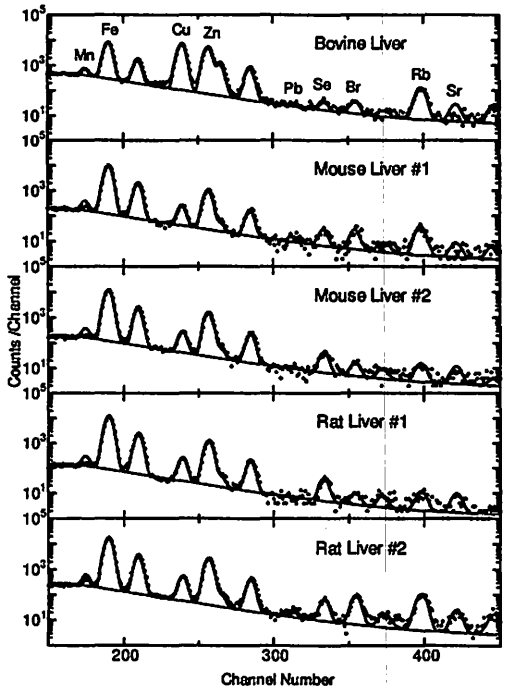

Figure 8. Part of PIXE spectra from a bovine liver, two mouse liver and two rat liver samples and the result of pattern analysis.

I. 21. Use of Si-PIN Photodiode X-Ray Detector for PIXE

Inoue J., Iwasaki S., Murozono K., Ishii K., and Matsuyama S.

Department of Quantum Science and Energy Engineering, Tohoku University

Introduction

Si-PIN Photodiode type detector (hereafter SPINP for short) is one of the X-ray detectors which have shown significant improvement in resolution recently. It is reported that the most advanced detector has a specification value of FWHM of 250 eV at 5.9 keV[1]. This value is worse only by 150 eV than the typical value of conventional Si(Li) detectors. The remarkable advantage of the detector is its high operability due to the Peltier (thermoelectric) cooler and low voltage bias. The detector with the cooler and its preamplifier are housed in a box of the size of 9.5×4.4×2.9t in cm. Disadvantage of this detector is still in the small size of crystal, both in area and thickness, especially the latter; this might cause the low detection efficiency for the higher energy X-rays. In this paper, basic characteristics of this detector and feasibility to PIXE, especially to bio-PIXE are investigated.

Basic Characteristics of Si-PIN Photodiode Detector

First, the basic characteristics of a SPINP detector (Model XR100T, Amptek, Inc.) have been studied using some radioactive X-ray sources, such as Fe-55, Sr-85, Cd-109 and Am-241. Related nuclear data for these sources were taken from the reference[2]. Energy resolution of the detector was derived as the FWHM value at each peak energy from the Gaussian peak fitting to the source spectra in the energy range from 4 to 26 keV. The relation between the resolution and X-ray energy was obtained by the least-squares method by assuming that FWHM of each peak was expressed by the quadratic sum of energy dependent and independent terms. The resultant curve shifts from that of an old Si(Li) detector by about 100 eV as shown in Fig.1. At 5.9 keV, the observed value of 249 eV is quite consistent with the nominal value of the specifications given by the detector manufacturer, and is about twice of that of the commercially available Si(Li) detectors with the maximum performance. Intrinsic efficiency of SPINP was calculated by assuming a simple slab geometry having the thicknesses of 300 μm with 0.025-mm beryllium window.

The calculated efficiency curve is compared with the measured data for Fe-55 and Cd-109 sources and also with measured data for a typical Si(Li) detector in Fig. 2. The observed data are consistent with the calculation. The calculated curve is almost the same

with that of the conventional detector below 10 keV because the Si(Li) detector has similar window structure, while the curve begins to decrease at 8 keV, and becomes a half of the maximum around 15 keV due to the insufficient thickness of SPINP. The energy 15 keV corresponds to the energy of characteristic K X-rays of the elements with atomic numbers around 40. Finally the efficiency value is only as low as a tenth of that of the Si(Li) detector above 20 keV.

Applicability to PIXE

Applicability of SPINP to PIXE has been studied in a condition of in-air PIXE in which we intend to use this type of detector in most cases. A SPINP detector was mounted in the assembly for the beam exit of ViaPIXE[3] (Vertical beam in-air PIXE system) of Dynamitron laboratory at Tohoku University[4]. Fig. 3 shows the beam exit assembly together with the SPINP detector having 6 inch extension rod.

As the first example, typical spectra of PIXE measured by both the SPINP detector (upper) and a Si(Li) detector (lower) for a layer of ZnCdS on aluminum foil are shown in Fig. 4. The ZnCdS scintillator has usually been used for the beam monitor at the sample position and for the purpose of the detector energy calibration in Via PIXE. In the lower channel regions of the spectra, peaks from several elements: aluminum, argon, iron, and zinc are clearly observable. The peaks of cadmium are also in the higher channel regions. The peak of argon is due to the excitation of argon in the beam path between the beam exit foil (Kapton foil ;12.5 μm) and sample position.

An inspection does not reveal significant difference, especially in the separability of each peak, between the spectra of both detectors, though the peak shape of the Si(Li) detector is sharper. While, one could notice the cadmium counts of an order of magnitude lower in the SPINP spectrum as mentioned before. Another feature of the spectrum by SPINP is that clear shoulder structure exists in the low energy side of the Zn Kα line peak. This type of structure was also found in the spectra from the radioactive sources, but the shape of the structure sometimes changed with time. This may be due to the insufficient charge collection in the detector, but further study is needed to prove this.

Fig. 5 shows the spectrum of a standard sample (SRM 1833) mounted on a Mylar foil measured with the SPINP detector. The peaks of titanium, iron, zinc, and lead can be clearly identified, whereas the peaks of sulfur, chlorine, argon, potassium, and calcium can hardly be separated. The interference is due to the strong argon peak. These peaks could be partially separated in the spectrum measured by the Si(Li) detector. The result of the spectrum decomposition by the pattern analysis method[5,6] is also shown in Fig. 5. The solid line represents the whole fit and the dotted lines indicate each single component including the background. The agreement between the experimental data and fitted ones is fairly good. The previous extensive simulation study has shown the feasibility of the pattern analysis

method to such bad resolution spectra for the SUS316 case[7].

In the case of the bio-samples, usually a known amount of yttrium, indium or silver is added as an internal standard for the determination of the absolute concentrations. These three elements have been chosen because these are usually not contained in bio-samples with a few exceptional cases. But, for SPINP, silver and indium might not be suitable because the efficiency for the K-lines of these elements is very low as mentioned above. In this case yttrium is preferable, if the yttrium is not contained or the amount of yttrium is negligible small in the sample.

Conclusions

The basic characteristics of a new Si-PIN photodiode detector were examined by a set of X-ray sources, and they were consistent with the catalogue data given by the manufacture. Feasibility of this detector to PIXE was also investigated in an actual condition of PIXE. In conclusion, this type of detector can be applied to PIXE from the view points of the efficiency and resolution, if they are interested in the common lower Z elements below about 40; K-X rays from these elements can be observed with almost the same efficiency as conventional Si(Li) detectors. It can be expected that rather poorer resolution of the detector does not introduce significant drawback in the spectrum analysis if we use the pattern analysis method.

According to the manual of the SPINP detector, the detector shows that the rise time of pulses varies with the location of the detection. This needs to use a longer shaping constant in the main amplifier than in the case of the conventional Si(Li) detector; a triangular fixed shaping time constant of about 12 μsec is used in the amplifier provided by the manufacturer to realize the highest resolution. If we use the detector in a high counting rate condition, this could cause deterioration of the detector performance. The counting rate effect on the performance remains to be uninvestigated.

References

1) Huber A. C., Pantazis J. A., Jordanov V., Nuclear Instruments and Methods in Physics Research **B99** (1995) 665.
2) Nuclear Data Standards For Nuclear Measurements (1991), NEANDC/INDC Nuclear Standard File.
3) Iwasaki S., Ishii K., Yoshizaki K. et al., Internat. J. PIXE **5** (1995) 163 .
4) Iwasaki S., Ishii K., Matsuyama S. et al., Internat.J. PIXE , in press.
5) Iwasaki S., Fukuda H., Yoshizaki K. et al., Internat. J. PIXE **4** (1994) 131 .
6) Murozono K., Iwasaki S., Inoue J. et al., Internat. J. PIXE , in press.
7) Yoshizaki K., Fukuda H., Iwasaki S., and Kitamura M., KEK Proceedings **95** (1995) 330.

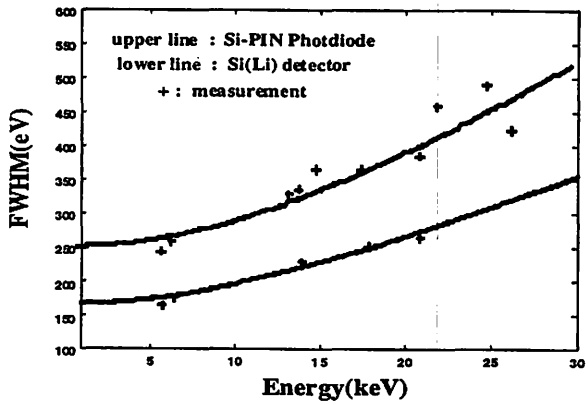

Fig. 1. The relation between the resolution and X-ray energy for a SPINP detector measured by using the X-ray sources compared with the data for a Si(Li) detector. The least squares fitting curves are also shown.

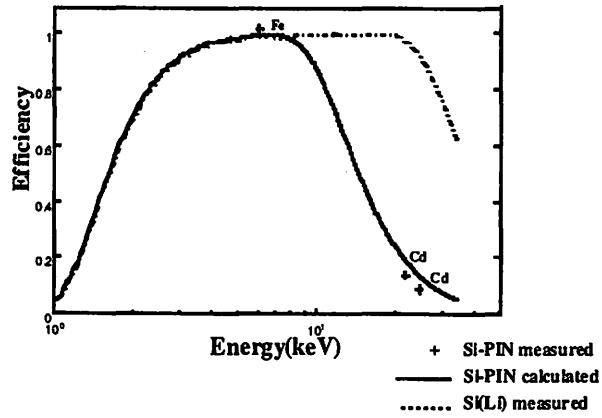

Fig. 2. The relation between the efficiency and X-ray energy calculated by a slab geometry for SPINP, compared with the experimental data using the X-ray sources and also the data for a Si(Li) detector.

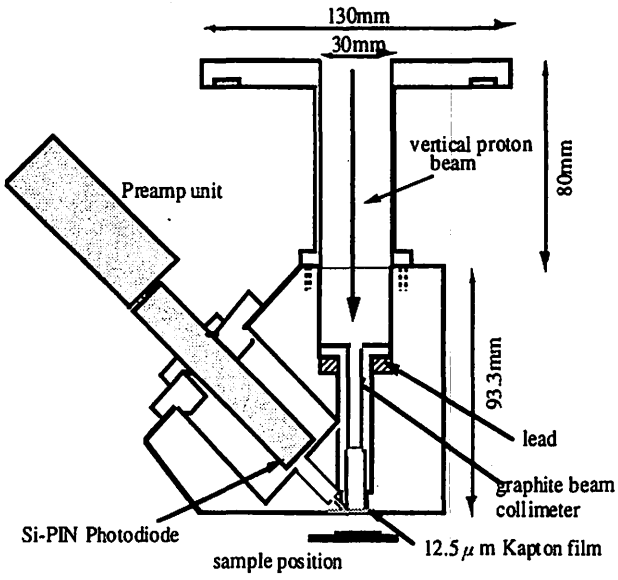

Fig. 3. The set up of the beam exit assembly together with the SPINP having 6 inch extension rod.

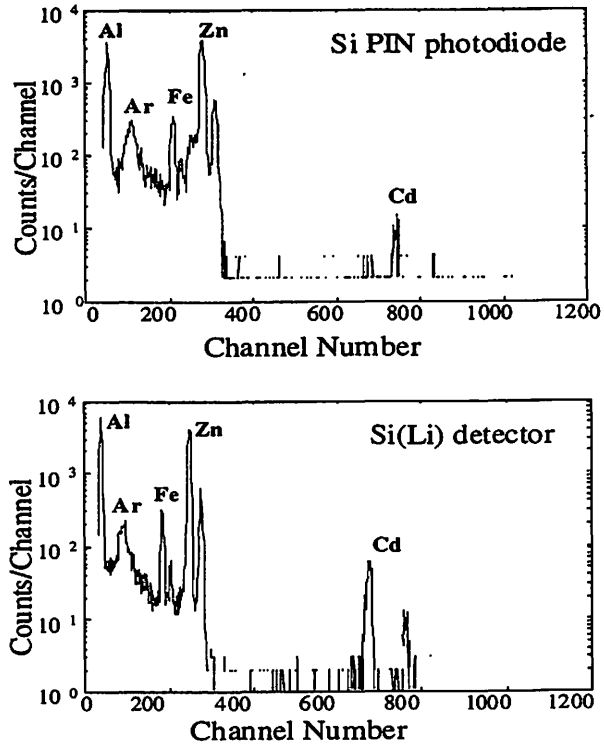

Fig. 4. Typical spectra of PIXE measured by both SPINP (upper) and Si(Li) detector (lower) for the same layer of ZnCdS on aluminum foil, respectively.

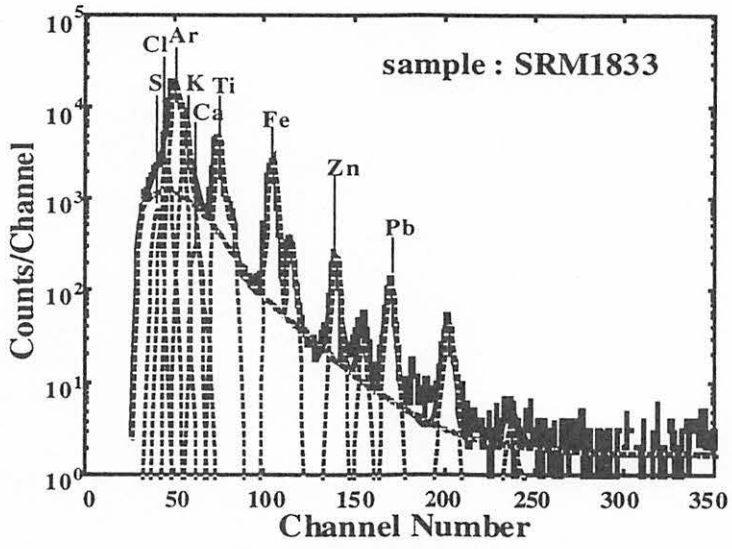

Fig. 5. A measured spectrum by SPINP for a bio-sample on Mylar backing. A result of decomposition by the pattern analysis method is also shown.

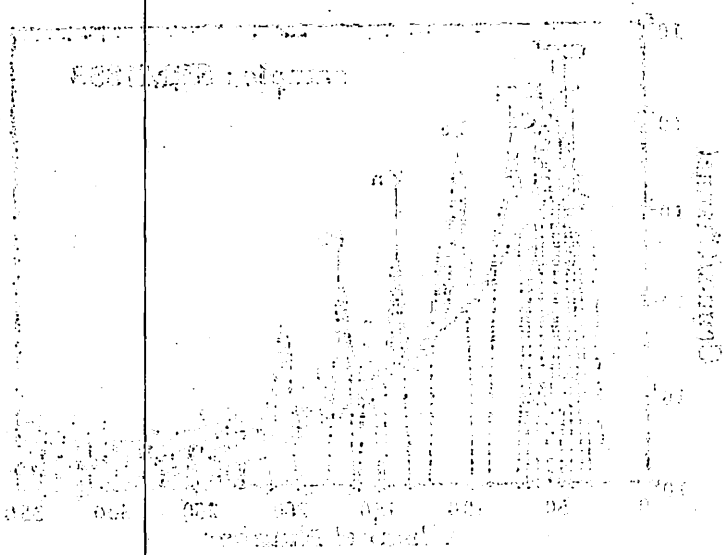

II. CHEMISTRY

II. 1. Preparation of Carrier Free ^{95m}Tc Tracer by a Sublimation Method

Sekine, T., Konishi, M., Kudo, H., Tagami, K. and Uchida, S. **

Department of Chemistry, Graduate School of Science, Tohoku University
*National Institute of Radiological Sciences **

Technetium-99, which is one of long-lived fission products formed with a comparatively high yield, has been released into the environment as a result of nuclear weapons tests and nuclear reprocessing [1]. Due to its long half life ($T_{1/2}$ = 2.111 × 10^5 y), the migration of ^{99}Tc has been attracting interest from the viewpoint of nuclear waste management as well. Inductively coupled plasma mass spectrometry (ICP-MS) is a powerful tool to determine ^{99}Tc with a high sensitivity (0.05 ppt) [2]. When ICP-MS is applied to the measurement of ^{99}Tc in environmental samples, careful chemical separation of technetium is necessary before analysis. For the chemical separation, ^{95m}Tc has been suggested as the best radioisotope to be used as a chemical yield monitor [3], because of its a suitable half life (61 d) and preferable γ-rays (204 keV, 582 keV). However, it is known that ICP-MS spectra of commercial ^{95m}Tc solutions show large background peaks at mass numbers of 97, 98 and 99 [4], arising from contamination with other technetium isotopes. Because of high sensitivity of ICP-MS, a high quality ^{95m}Tc tracer is strongly demanded. In this paper, we report preparation of a high quality ^{95m}Tc tracer by a sublimation method.

Technetium-95m was obtained by the ^{93}Nb(α,2n)^{95m}Tc reaction bombarding stacked niobium metal foils (Fuchikawa Kinzoku Co., Ltd., 99.9 %, 10 mm × 10 mm × 0.05 mm thick) with α particles (E_α = 40 MeV, 5 μA) from a 40 MV AVF cyclotron at the Cyclotron Radioisotope Center, Tohoku University. The irradiated foils were stored for a month to decay out short-lived radionuclides. The γ-ray spectrum of the irradiated target indicated the presence of ^{95m}Tc as a main product of the ^{93}Nb(α,2n)^{95m}Tc reaction. In addition, γ-ray peaks from ^{96}Tc (4.28 d) produced by the ^{93}Nb(α,n)^{96}Tc reaction and ^{92m}Nb (10.15 d) by the ^{93}Nb(α,αn)^{92m}Nb reaction were seen. The bombardment of niobium targets with α particles is of an advantage to give ^{95m}Tc mainly without other long-lived technetium isotopes such as ^{97}Tc, ^{98}Tc and ^{99}Tc, which are produced via (p,xn) reactions or (d,xn) reactions of natural molybdenum. Therefore, the contamination with other isotopes in the ^{95m}Tc tracer can be avoided by the use of (α,xn) reactions of niobium.

Excitation functions of ^{93}Nb(α,2n)^{95m}Tc, ^{93}Nb(α,n)^{96}Tc, and ^{93}Nb(α,αn)^{92m}Nb are shown in Fig.1, as a function of the average energy of α-particles in each target foil. The

results agreed with those reported by N. Ramamoorthy *et al.* [5]. Thick target yields at the end of bombardment were determined as 2.1 μCi/μAh for ^{95m}Tc, 71 μCi/μAh for ^{96}Tc, and 1.5 μCi/μAh for ^{92m}Nb, respectively.

Separation of ^{95m}Tc from the niobium targets was carried out based on the difference in volatility of oxides. The melting point of technetium oxide (Tc_2O_7) is 119.5 °C and the boiling point is 310.6 °C , showing much higher volatility than niobium oxide (Nb_2O_5) which is not volatile even at 1000 °C. The conversion of the chemical form from metal to oxide was achieved by heating the targets at 1100 °C. The samples were placed in a quartz tube in a home-made electric furnace (Fig.2). Under an oxygen gas flow (50cc/min), technetium oxide was formed and gradually sublimated as shown in Fig.3, in which γ-ray dose rate outside the quartz tube was monitored with an NaI(Tl) scintillation detector. The γ-ray dose rate considerably decreased within 50 min and became a constant in 2 h. The distribution of radioactivity along the quartz tube after the sublimation, measured with a Ge semiconductor detector equipped with 4 k MCA, showed quantitative deposition of ^{95m}Tc at a prescribed point in the tube out of the electric furnace (Fig.4), while a macroscopic amount of Nb_2O_5 together with the radioactivity of ^{92m}Nb was at the original place. The technetium oxide deposited on the inner wall of the quartz tube was easily removed by washing with a small amount of water, giving a pertechnetate solution.

An aliquot of this solution was subjected to ICP-MS (Yokogawa, PMS-2000) to examine the contamination in the mass region between 93 and 104. The results are shown in Fig.5 together with that for a commercial ^{95m}Tc solution. The mass spectrum of the commercial ^{95m}Tc showed the intense peaks at mass numbers 97, 98 and 99, due to the contamination of other technetium isotopes. According to the data sheet accompanying the ^{95m}Tc solution [1], the ^{95m}Tc was produced by the ^{96}Mo(p,2n)^{95m}Tc reaction, suggesting the co-production of ^{97}Tc, ^{98}Tc, and ^{99}Tc from other molybdenum stable isotopes. In contrast to the commercial one, the spectrum of our ^{95m}Tc solution could not be distinguished with that of water, as background, which was used for dissolution of the ^{95m}Tc. Although a macroscopic amount of niobium was heated in the sublimation process, no contamination with niobium was found. The detection limit of the ICP-MS was given as 0.02 ppt from background counts which was determined separately by measuring ^{99}Tc solutions with different concentrations.

Advantages of the present preparation method are as follows.

1) The contamination with other technetium isotopes can be avoided by the use of the ^{93}Nb(α,2n)^{95m}Tc reaction.
2) The separation of ^{95m}Tc from niobium targets is sufficient even by a simple treatment.

The measurement of ^{99}Tc by ICP-MS is seriously interfered by the presence of ruthenium which has a stable isotope at mass number 99. Due to a high sensitivity of ICP-MS, a trace amount of ruthenium, ppt level, in chemical reagents might be enough to be

taken into account. The sublimation method is superior to normal wet chemical separation methods, because no chemicals are necessary for the separation while wet chemical methods need some reagents which may contaminate a ^{95m}Tc tracer solution.

This tracer is suitable for ICP-MS and will be practically used to determine the concentration of ^{99}Tc in environmental samples.

References

1) Desmet, G., Myttenaere, C., " Technetium in the Environment ", Elsevier Applied Science, New York, 1986.
2) Tagami K., Doctor Thesis, Kyoto University (1997).
3) Nicholson S., Sanders T. W., Blaine L. M., Sci. Total Environ., **130/131** (1993) 275.
4) Tagami K., Uchida S., Appl. Radiat. Isot., **47** (1996) 1057.
5) Ramamoorthy N., Das M. K., Sarkar B. R., *et al.*, J. Radioanal. Nucl. Chem., Articles, **98** (1986) 121.

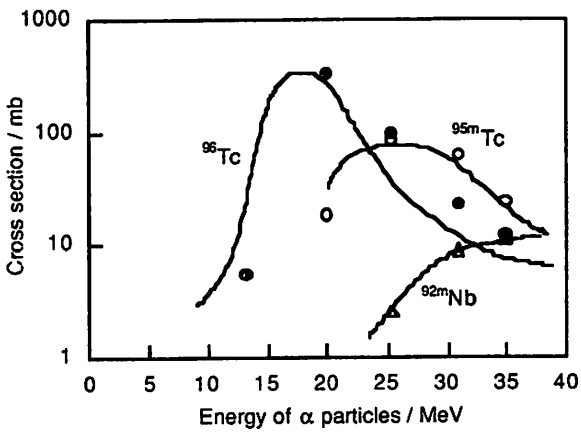

Fig. 1 Excitation functions of the ^{93}Nb(α,2n)^{95m}Tc, ^{93}Nb(α,n)^{96}Tc and ^{93}Nb(α, α n)^{92m}Nb reactions as a function of average energy of α particles in each Nb foil. The solid lines show the excitation functions reported in ref. 5.

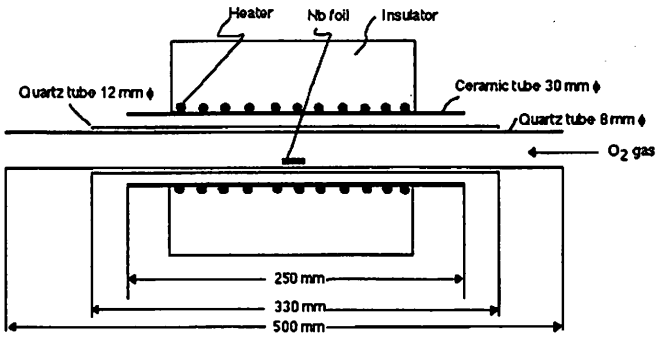

Fig. 2 The schematic figure of the electric furnace used in this study.

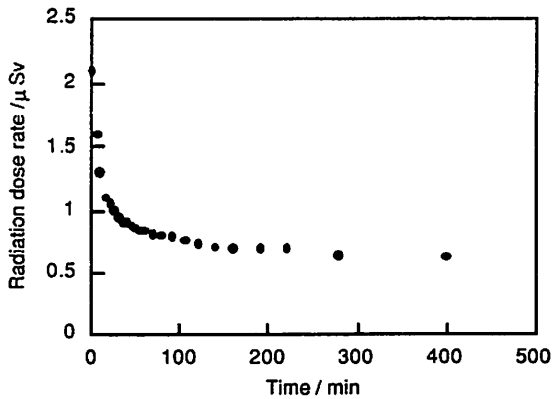

Fig. 3 γ-ray dose rate change during sublimation outside the electric furnace at the sample position against heating time

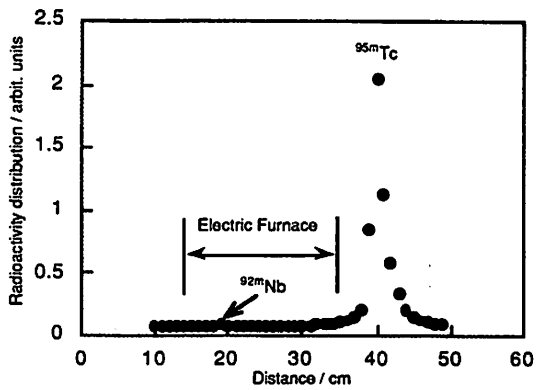

Fig. 4 The radioactivity distribution along a quartz tube after the sublimation.

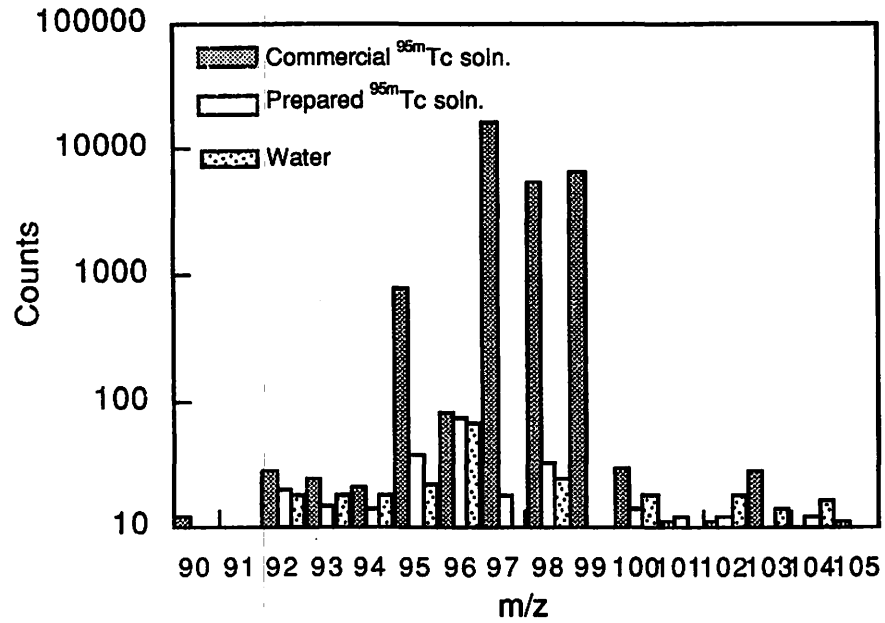

Fig. 5 ICP-MS spectra for the ^{95m}Tc tracer solutions prepared, the water used, and the commercial ^{95m}Tc solutions.

III. BIOLOGY AND MEDICINE (Basic)

III. 1. Characteristics of $^{45}Ca^{2+}$ Release Induced by Quinolidomicin A_1, a 60-membered Macrolide from Skeletal Muscle Sarcoplasmic Reticulum

Ohkura M., Miyashita Y., Kakubari M., Hayakawa Y., Seto H.*, and Ohizumi Y*

Department of Pharmaceutical Molecular Biology, Faculty of Pharmaceutical Sciences, Tohoku University
*Institute of Molecular and Cellular Biosciences, The University of Tokyo**

Quinolidomicin A_1, isolated from an actinomycete *Micromonospora* sp., is a 60-membered macrolide having cytotoxic effects on P388 murine leukemia cells[1]. In the course of our survey of natural products having Ca^{2+} releasing activity in the heavy fraction of skeletal muscle SR (HSR), we have found that quinolidomicin A_1 powerfully induces Ca^{2+} release from HSR but induces only slightly from the light fraction of SR (LSR), having novel pharmacological properties. Present study reports that quinolidomicin A_1-induced Ca^{2+} release from HSR is consisted of two components, which are both sensitive and insensitive to blockers of Ca^{2+} release channels, and that the former component is associated with the ryanodine receptor.

Quinolidomicin A_1 was isolated from an actinomycete *Micromonospora* sp. as described previously[2]. Ryanodine was purchased from S.B. Penick (New York, NY). Procaine was from Sigma (St. Louis, MO). $^{45}CaCl_2$ (0.70 Ci/mmol) and [^{3}H]ryanodine (60 Ci/mmol) were from Du-Pont New England Nuclear (Boston, MA). All other chemicals were of analytical grade.

Results

Quinolidomicin A_1-induced Ca^{2+} release was studied in $^{45}Ca^{2+}$ release experiments. Fig. 1 shows the time course change in $^{45}Ca^{2+}$ content in HSR (A) and LSR (B) after adding quinolidomicin A_1, caffeine or A23187. A23187 markedly induced $^{45}Ca^{2+}$ leak both from HSR and LSR. The $^{45}Ca^{2+}$ releasing activity of quinolidomicin A_1 or caffeine was significant in HSR, whereas this was only slightly observed in LSR. Fig. 2 shows the concentration-response curves for quinolidomicin A_1 and caffeine in $^{45}Ca^{2+}$ release. $^{45}Ca^{2+}$ release was accelerated by quinolidomicin A_1 in a concentration-dependent manner. The EC_{50} values of quinolidomicin A_1 and caffeine were approximately 20 μM and 2 mM, respectively, indicating that quinolidomicin A_1 is 100 times more potent than caffeine. Thirty μM quinolidomicin A_1

and 1 mM caffeine potentiated $^{45}Ca^{2+}$ release from HSR with bell-shaped profile of Ca^{2+} dependence, however both the patterns were different from each other. The affinity of Ca^{2+} for the channels increased in the presence of caffeine (the EC_{50} values of Ca^{2+} for $^{45}Ca^{2+}$ release in the absence and presence of 1 mM caffeine were approximately 300 and 30 nM, respectively), however this was not affected by quinolidomicin A_1. Interestingly, $^{45}Ca^{2+}$ release induced by 30 μM quinolidomicin A_1 was only partially inhibited by blockers of Ca^{2+} release channels such as Mg^{2+}, procaine and ruthenium red at 10 mM, 10 mM and 10 μM, respectively.

The interrelations between the Ca^{2+} releasing activities of quinolidomicin A_1 and caffeine were examined by measuring $^{45}Ca^{2+}$ release from HSR at pCa 8. At this Ca^{2+} concentration, the maximum response of $^{45}Ca^{2+}$ release induced by the single addition of quinolidomicin A_1 or caffeine was low enough, therefore it is appropriate to observe the synergism in $^{45}Ca^{2+}$ release between the two agents. The maximum response of $^{45}Ca^{2+}$ release induced by 300 μM quinolidomicin A_1 was significantly ($p < 0.01$) increased by the additional application of 30 mM caffeine, indicating that quinolidomicin A_1 induces Ca^{2+} release by affecting a site different from that of caffeine.

[^{3}H]Ryanodine binding to HSR was examined in the presence or absence of quinolidomicin A_1. Quinolidomicin A_1 remarkably enhanced [^{3}H]ryanodine binding to HSR in a concentration-dependent manner. Fig. 3 shows a saturation curve (A) and a corresponding Scatchard plot (B) of [^{3}H]ryanodine binding in the presence or absence of 100 μM quinolidomicin A_1. The K_D value was decreased from 47.1 to 37.4 nM by adding quinolidomicin A_1, while the B_{max} value was unaffected.

Discussion

In the present study, we found that quinolidomicin A_1 potentiated $^{45}Ca^{2+}$ release from HSR at concentrations higher than 3 μM with EC_{50} = 20 μM. Ca^{2+} releasing potency of quinolidomicin A_1 was approximately 100-fold higher than that of caffeine. Quinolidomicin A_1 did not show the Ca^{2+} ionophoretic activity even at a high concentration of 300 μM, using the two-phase partition system and SR membranes.

The Ca^{2+} dependency of quinolidomicin A_1-induced $^{45}Ca^{2+}$ release from HSR had a bell-shaped profile, but its pattern was different from that of caffeine. The affinity of Ca^{2+} for the channels increased in the presence of caffeine, whereas this was not changed by quinolidomicin A_1. As reported previously[4], the maximum response of $^{45}Ca^{2+}$ release to MBED did not increase further in the presence of caffeine, indicating that the binding site of MBED was the same as that of caffeine. In contrast, quinolidomicin A_1 further enhanced the maximum response in the presence of caffeine. These observations suggest that quinolidomicin A_1 acts on a different site from that of caffeine.

[^{3}H]Ryanodine was reported to bind to its receptor in an open state[1]. Quinolidomicin A_1 significantly potentiated [^{3}H]ryanodine binding to HSR in a concentration-dependent manner. Therefore Ca^{2+} release from HSR induced by quinolidomicin A_1 has been shown to at least partially associate with the ryanodine receptor. Scatchard analysis of [^{3}H]ryanodine binding revealed that quinolidomicin A_1 decreased K_D without affecting B_{max}, probably suggesting that it makes easy to open the ryanodine receptor. Mg^{2+} (10 mM), procaine (10 mM) and ruthenium red (10 μM) have been reported to nearly abolish the Ca^{2+} release mediated through the ryanodine receptor[1]. The $^{45}Ca^{2+}$ mobilizing effect of quinolidomicin A_1 was only partially blocked by these inhibitors at concentrations described above. On the basis of these data, it is suggested that there are three possibilities, i.e., quinolidomicin A_1 induces $^{45}Ca^{2+}$ release through (1) the ryanodine receptor and novel Ca^{2+} release channels, (2) the ryanodine receptor with changed gating characteristics or (3) the ryanodine receptor with partly modulated sensitivity to the only blockers tested.

In summary, it has been demonstrated that quinolidomicin A_1 induces Ca^{2+} release from HSR with at least two components, which are consisted of both sensitive and insensitive to the blockers of Ca^{2+} release. Quinolidomicin A_1 may be a useful pharmacological tool to elucidate the molecular mechanisms of Ca^{2+} release in skeletal muscle HSR.

References

1) McPherson P. S. and Campbell K. P. J., Biol. Chem. **268** (1993) 13765.
2) Endo M., Tanaka M. and Ogawa,Y. Nature **228** (1970) 34.
3) Inui M., Saito A. and Fleischer S., J. Biol. Chem. **262** (1987) 1740.
4) Seino A., Kobayashi M., Kobayashi J. et al., J. Pharmacol. Exp. Ther. **256** (1991) 861.

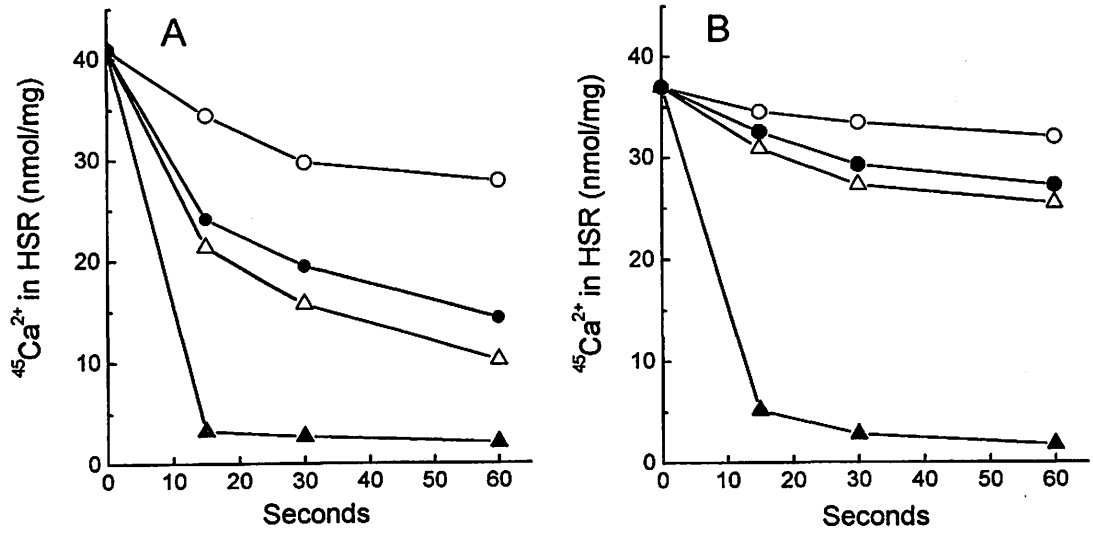

Fig. 1. Stimulatory effects of quinolidomicin A_1 and caffeine on $^{45}Ca^{2+}$ release from skeletal muscle HSR. The $^{45}Ca^{2+}$ content in HSR (A) or LSR (B) vesicles was measured at 0°C by the Millipore filtration. In A; ○, control; ●, 30 mM quinolidomicin A_1; ▲, 3 mM caffeine; ■, 10 μM A23187. In B; ○, control; ●, 300 μM quinolidomicin A_1; ▲, 30 mM caffeine; ■, 10 μM A23187.

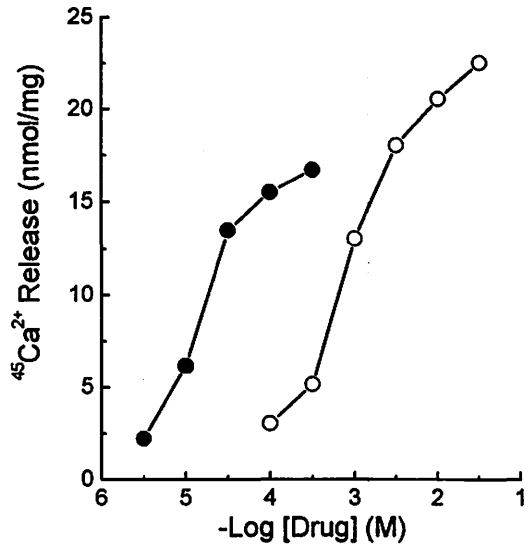

Fig. 2. Concentration-dependent acceleration of $^{45}Ca^{2+}$ release from HSR by quinolidomicin A_1 and caffeine. $^{45}Ca^{2+}$ release was measured at pCa 7. Experimental protocols were the same as those described in Fig. 1. O, caffeine; ●, quinolidomicin A_1.

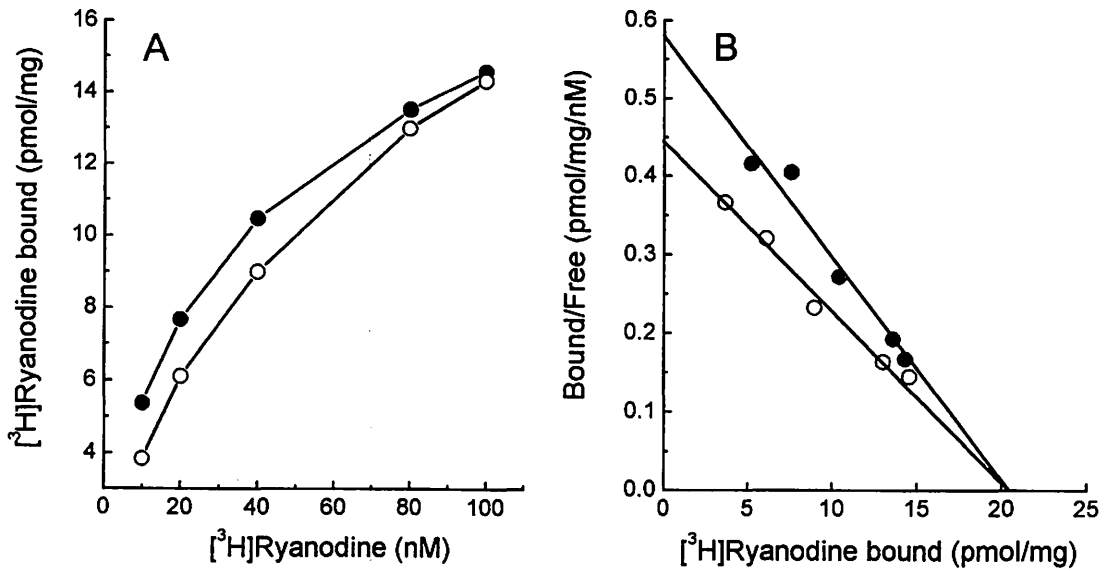

Fig. 3. Saturation curve (A) and Scatchard plot (B) of [^{3}H]ryanodine binding to HSR. HSR was incubated with 10-100 nM [^{3}H]ryanodine for 2 h at 37°C in the presence or absence of 100 μM quinolidomicin A_1. O, control; ●, 100 μM quinolidomicin A_1.

III. 2. Effects of Proton Beam on Mouse Fetuses

*Sato S., Yajima. A and Orihara. H**

Department of Obstetrics and Gynecology, Tohoku University School of Medicine
*Cyclotron and Radioisotope Center, Tohoku University**

Introduction

Experiments using radiation have been used as a means to investigate the general principles of the mechanism of endogenous anomalies, and few problems including the critical point of teratogenesis, dose-effect relationship in teratogenesis, and changes in the sensitivity to radiation injury with the fetal age have been clarified[1-3]. However, in γ ray and neutron ray irradiation as well as conventional irradiation such as X-ray irradiation by extracorporeal methods, even local abdominal irradiation of the dams has meant systemic exposure of embryos and fetuses.

The purposes of this study were to evaluate effects of proton rays on fetuses by exposing fetuses locally by the use of proton rays with a characteristic dosimetric profile called Bragg curve and examining their body weight, number of viable fetuses, and external anomalies and to establish a new approach of experimental teratology to congenital anomalies.

Materials and Methods

The animals were male and female C3H/He mice 8-12 weeks after birth (Funabashi Farm). They were maintained in a temperature-and humidity-controlled animal room with ad libitum intake of food and water. They were mated by mixing at a male-female ratio of 1:2, and the day on which the vaginal plug was observed was defined as day 0. The females were immobilized on a fixing board designed by the authors and irradiated with proton rays on days 10, 11, and 12 of pregnancy.

Protons were accelerated with the AVF type cyclotron at Tohoku University. The mechanism of beam control and the experimental set up are as shown in Fig. 1[4,5]. Protons accelerated and transported from the main chamber of the cyclotron (38 MeV) were converged on a quartz plate, transported again with minimum energy loss, and led into the atmosphere through Mylar foil (beam diameter 20 cm). Also, to measure proton induced photon, a plastic scintillator was placed near the proton transporting pipe, and the dose was measured with a parallel plate ionization chamber.

Fig. 2 shows a proton dosimetric curve at 38 MeV. The dose rate varied slightly among days of measurement but was adjusted to 5-6 rad/sec. The position of Bragg peak was adjusted at 9.15 mm on the acryl plate, and the peak/plateau ratio was about 4.3.

By a preliminary study, the location of the uterus in pregnant mice was determined, the acryl plate was adjusted so that Bragg peak would occur at 4.5-5.0 mm in the bodies of mice, and the proton beam was collimated with an acryl plate 15 mm in thickness with a hole 4 cm in diameter in the center. Four mice were fixed gently not to suppress respiration on an acryl plate 10 mm in thickness with holes 3 cm in diameter at the abdominal regions at intervals of about 7 cm, and irradiation was made by driving the acryl plate with a motor by remote control from the operation room under TV monitoring.

X-ray irradiation was made under the following conditions: Tube current 20 mA, tube potential 250 kV, filter 0.3 mm Cu+1 mm Al, focus-mouse distance 50 cm, irradiation field 13×13 cm, and dose rate 128.2 R/sec. Pregnant mice immobilized similarly to the irradiated mice but not irradiated were regarded as a treated control (TC) group, and those that were not restrained or irradiated were regarded as an untreated control (UC) group.

Animals were exposed to 70 rad, 130 rad, and 200 rad proton beams and 130 R X-ray under the above conditions, and animals in these groups as well as TC and UC groups were given Cesarean section on day 18 of pregnancy. The fetuses were taken out, the number of implantations, positions and numbers of living and dead embryos and fetuses, and estimated age of dead fetuses were recorded. The fetuses were examined for external anomalies, weighed, and fixed with 10% formalin and 95% alcohol.

The dose of the proton beam was expressed as the absorbed dose (rad) at the plateau, and the dose of the X-ray was expressed as the surface irradiation dose (R).

Results

First, the 130 rad proton group, 130 R X-ray group, TC group and UC group were compared. The percentage of living fetuses relative to the number of implantations was significantly greater in the TC group than in the 130 R X-ray group ($p<0.01$) and in TC group than in the 130 rad proton group ($p<0.005$)(Table 1). The mean body weight was significantly greater in the UC group than in the TC group, in the TC group than in the 130 R X-ray group, in the TC group than in the 130 rad proton group, and in the 130 R X-ray group than in the 130 rad proton group ($p<0.0001$, Table 2). Next, the frequency of anomalies was significantly higher in the 130 R X-ray group than in the TC group, in the 130 rad proton group than in the TC group, and in the 130 rad proton group than in the 130 R X-ray group ($p<0.001$, Table 3).

Among the proton irradiated groups, the percentage of living fetuses was not markedly different between the 70 rad and 130 rad groups (52.7% and 46.3%, respectively) but was markedly lower in the 200 rad group (27.3%). The mean body weight was not markedly different in the 70 rad group (0.86 ± 0.20g) as compared with the X-ray irradiation

group but was significantly smaller in the 130 rad and 200 rad groups. The percentage of fetuses with external anomalies was high in the 70 rad and 130 rad groups (83.3% and 90.3%, respectively), but anomalies of the same types were severer in the 130 rad group. Table 4 summarizes these results.

Fig. 3 shows external anomalies that were observed in the 130 rad proton group (on day 11 of pregnancy). They are considered to clearly represent the effects of Bragg peak and to be characteristic of local irradiation. External anomalies caused by Bragg peak, e.g. microphthalmia (Mo), cleft palate (Cp), micrognathia (Mg), micromelia (Mm) of the fore and hind limbs, oligodactylia (Od), and short tail (St), are observed on the right side of the fetus.

Discussion

Radiation may cause congenital anomalies by affecting genes and chromosomes or by affecting embryos and fetuses after fertilization. In humans, radiation has been confirmed in actual cases to cause developmental disturbance by embryonic exposure. Also, X-rays are used widely in experimental research of teratology for clarification of general principles of the mechanism of exogenous teratogenesis. Works by Russel and Rugh et al.[1-3] are well-known in this field.

However, these studies have been conducted primarily using X-rays and γ-rays as the source, and teratogenicity of other types of radiation is considered to be largely unknown. Among factors that modify radiation-induced teratogenesis, the type and energy of radiation indicated by differences in LET, which represents effects of the dose rate and split irradiation and the kind and physical characteristics of radiation, are the most important radiobiological parameters, there have been very few studies on the LET effect on teratogenesis of mammalian embryos. Systematic research particularly including quantitative analysis is considered to be needed[6-7].

Tables 5 and 6 summarize the results of irradiation of pregnant animals with neutron beams, which have been evaluated relatively frequently among rays other than X-rays[6-15]. Biological effects of neutron beams appear to be modified by differences in the generator and the energy level.

Moreover, proton beams are different from neutron beams, which show deep dose distribution similar to that of X-rays, and exhibit high LET values and unique dose distribution in irradiated materials. As shown in Fig. 2, the entrance dose is low, a relatively flat plateau zone continues, and the dose increases rapidly near the end of the range, forming a portion called Bragg peak. The range of proton beams is proportionate to the initial energy, and was about 9.85 mm in the 38 MeV beam used in this study. This unique dose distribution observed in particles in general shows "changes in the number of ions generated in the tracks of particles" called Bragg curve, and it indicates that most of the radiation energy of a particle beam is absorbed near the end of the range when it passes through tissues[16,17].

Proton beams are considered to have more complex teratogenic effects than electromagnetic radiation such as X-rays and γ-rays, because they are corpuscular radiation, and they have excellent dose localization. Radiobiological effects (RBE) of proton beams have been evaluated in cells in culture, but this problem has not been approached from the viewpoint of experimental teratology [16-18].

We prepared regional anomalies by irradiating pregnant animals with a 38 MeV proton beam with a range not penetrating the uterus and generally succeeded in establishing a new experimental model of congenital anomalies. By using the anomaly model obtained by this method, we intend to perform quantitative analyses concerning interesting problems such as the mechanisms of tissue injury and repair in the period of development of the cerebral pallium, which is reported to be after day 11 of pregnancy in mice, estimation of LD_{50} by local irradiation, and calculation of the RBE value in the Bragg peak area.

Closing Remarks

1) We attempted to produce a new experimental anomaly model by 38 MeV proton beam (corpuscular beam) irradiation using the AVF type cyclotron at Tohoku University.
2) External anomalies were observed frequently in the animals exposed to 70 rad proton beam and 130 rad proton beam (83.3% and 90.3%, respectively).
3) The external anomalies were characteristically local malformations (multiple malformations) occurring near Bragg peak.

References

1) Kameyama Y., Radiation. Scientific Lectures at the 17th. Conference of the Japanese Association of Medical Sciences, 934-946, 1967.
2) Kameyama Y. Igakunoayumi, 103: 919-926, 1977.
3) Murakami U. Prenatal Medicine, ed. Murakami U., Baba K., Suzuki M., 12-20, Kanehara Shuppan, Tokyo, 1976.
4) Sasaki T., Ohta Y., Sakka M., et al., CYRIC annual report 1980, 212-215.
5) Sato S., Takabayashi T., Suzuki M., et al., CYRIC annual report 1981, 251-255.
6) Sato S. and Yajima S.:Congenital Anomalies. 23: 95-100, 1983.
7) Translated under the supervision of General Research Institution of Radiology: Developmental Abnormalities Caused by Intrauterine Irradiation: Sources of Radiation and their Effects (Report of the United Nations Scientific Committee, 1977), 761-840, ISU, Tokyo, 1978.
8) Tabuchi A, Acta. Obst. Gynaec. Jpn. 16: 561-569, 1964.
9) Cairnie A. B., Grahn O., Raybum H. B., et al:Teratology, 10: 133-140, 1974.
10) Deguchi H., Hiroshima J. Med. Sci., 23: 127-147, 1977.

11) Di Majo V., Ballardin E., Metalli P., Radiat. Res., 87: 145-158, 1981.
12) Friedberg W. , Hanneman G. D., Faulkner D. N., Int. J. Rad. Biol., 24: 549-560, 1973.
13) Nakagawa S., Fujiwara T., Hori I., et al., Hiroshima J. Obstet. Gynecol., 3: 431-434, 1964.
14) Okaki N., Inoue A., Ikeda T., Congenital Anomalies, 6: 182-183, 1966.
15) Okamoto K., Ikeda T., Sato Y., et al., Hiroshima J. Med. Sci., 21: 101-114, 1972.
16) Ohara H., Science, 23: 53-57, 1980.
17) Kawachi K., Nippon Acta. Radiol., 37: 876-885, 1977.
18) Raju M. R., Amols H. I., Bain E. et al., Brit. J. Radiol., 51: 712-719, 1979.
19) Murakami U. Prenatal Medicine, ed. Murakami U., Baba K., Suzuki M., 563-612, Kanehara Shuppan, Tokyo, 1976.

Table 1. Comparison of the number of living fetuses.

Group	No.of litters	No. of implantations	Living fetuses	Living/implantations(%)
Proton 130 rad	7	67	31	46.3
X ray 130 R	14	123	66	53.7
Treated Control	10	90	63	70.0
Untreated Control	10	86	69	80.2

* P<0.01 ** <0.005

Table 2. Comparison of mean body weight.

Group	No.of litters	Living fetuses	Body weight(M±SD)
Proton 130 rad	7	31 (4.4)	0.71±0.16
X ray 130 R	14	66 (4.7)	0.85±0.13
Treated Control	10	63 (6.3)	1.08±0.15
Untreated Control	10	69 (6.9)	1.22±0.19

* P<0.0001

Table 3. Comparison of percentages of fetuses with anomalies.

Group		Living fetuses	Malformed fetuses	Malformed/Living (%)
Proton	130 rad	31	28	90.3
X ray	130 R	39	15	38.5
Treated	Control	63	1	1.6
Untreated	Control	69	2	2.9

* $P<0.001$

Table 4. Experinmental Study of Proton irradiation on C_3H/He Mice.

Group	No.of litters	No. of implantations	Living fetuses	Prenatal deaths	(%) Living/Imp.	Malformed fetuses(%)	Body weight (M±SD)
Proton (70)	10	91	48(4.8)*	43	52.7	40 (83.3)	0.86±0.20
Proton (130)	7	67	31(4.4)	36	46.3	28 (90.3)	0.71±0.16
Proton (200)	5	44	12(2.4)	32	27.3	5 (41.7)	0.60±0.17
Xray (130)	14	123	66(4.7)	57	53.7	18 (27.3)	0.85±0.13
T.C.	10	90	63(6.3)	27	70.0	1 (1.6)	1.08±0.15
U.C.	10	86	69(6.9)	17	80.2	2 (2.9)	1.22±0.19

* parenthesis shows the number of living fetuses per a mouse.

Table 5. Studies of neutron beam irradiation in pregnant animals.

Authors	Animals	Generator	Energy of neutron beam
Tabuchi (1964)	Mouse	d-T generator	14.1 MeV
Nakagawa et al. (1964)	Mouse	d-T generator	14.1 MeV
Okamoto et al. (1966)	Rat	d-T generator	14.1 MeV
Okamoto et al. (1972)	Rat	d-T generator	14.1 MeV
Friedberg et al. (1973)	Mouse	reactor	1.2 MeV
Cairnie et al. (1974)	Mouse	reactor	0.8 MeV
Deguchi (1977)	Mouse	d-T generator	14.1 MeV
Majo et al. (1981)	Mouse	reactor	0.4 MeV

Table 6. Summary congenital caused by their biological effects.

1. By a d-T generator (14.1 MeV)

   a. Frequent occurrence of tail anomalies (90 rad, days 10-12 of pregnancy)

   b. RBE; 1.5-2.5 (intrauterine death, injury of embryos)

   c. Frequent occurrence of anomalies in the heart and great vessels (92.7%, 130 rad, day 8 of pregnancy)

   d. Critical period of CNS abnormalities not different from that for X-rays (100 rad, days 4-11 of pregnancy)

2. By a reactor

   a. RBE; About 4.5 (Absorbed or dead embryos, early after implantation, 1.2 MeV)

   b. RBE; About 3 (Specific limb abnormalities, day 11 of pregnancy, 0.8 MeV)

   c. No qualitative differences in teratogenesis compared with X-rays (days 3-11 of pregnancy, 0.8 MeV)

   d. RBE; 3.2±0.8 in weight loss, 2.4 in major malformations (day 7.5 of pregnancy, 0.4 MeV).

Table 7. Biological effects of proton beam.

Materials	Parameters	Proton bean energy	RBE	References
Mouse	LD50/30days	340 MeV	1	Tobias et al (1954)
	LD50/6	730	1.2	Ashikawa et al (1964)
	LD50/30	730	0.8	Ashikawa et al (1964)
Apical cells	Abnormal metaphase	170	0.7	Larsson & Kihlman (1960)
Skin	Acute cutaneous reaction	185	1	Falkmer et al (1960)
Mouse	LD50/30	157	0.77±0.1	Bonet Maury et al (1960)
Mouse (body weight)	Body weight changes	460	1.75±0.23	Wapshaw & Oldfield (1960)
Mouse (spleen)	Spleen weight	460	2.08±0.07	Wapshaw & Oldfield (1960)
Culture cell (liver cancer)	Cell death rate	160	1.0±0.1	Robertson et al (1975)
Culture cell (V79)	Cell death rate	160	1.2	Raju et al (1975)
Mouse	Acute cutaneous reaction	160	1.2	Raju & Carpenter (1977)
Culture cell (V79)	Cell death rate	160	1.2	Hall et al (1978)
Mouse	Intestinal crypts	160	1.2	Tepper et al (1977)
Culture cell (Mouse)	Cell death rate	126-730	0.82±0.26	Ueno & Grigoviev (1960)
Culture cell (Mouse)	Cell death rate	90	0.75	Wainson et al (1972)
Culture cell (Mouse)	Cell death rate	90	1.84±0.15	Wainson et al (1972)
Culture cell	Cell death rate	8,12,31	1.0~1.5	Bettega et al (1979)
Culture cell	Cell death rate	70	1.1~1.3	Ohara et al (1979)

(from Raju, 1979)

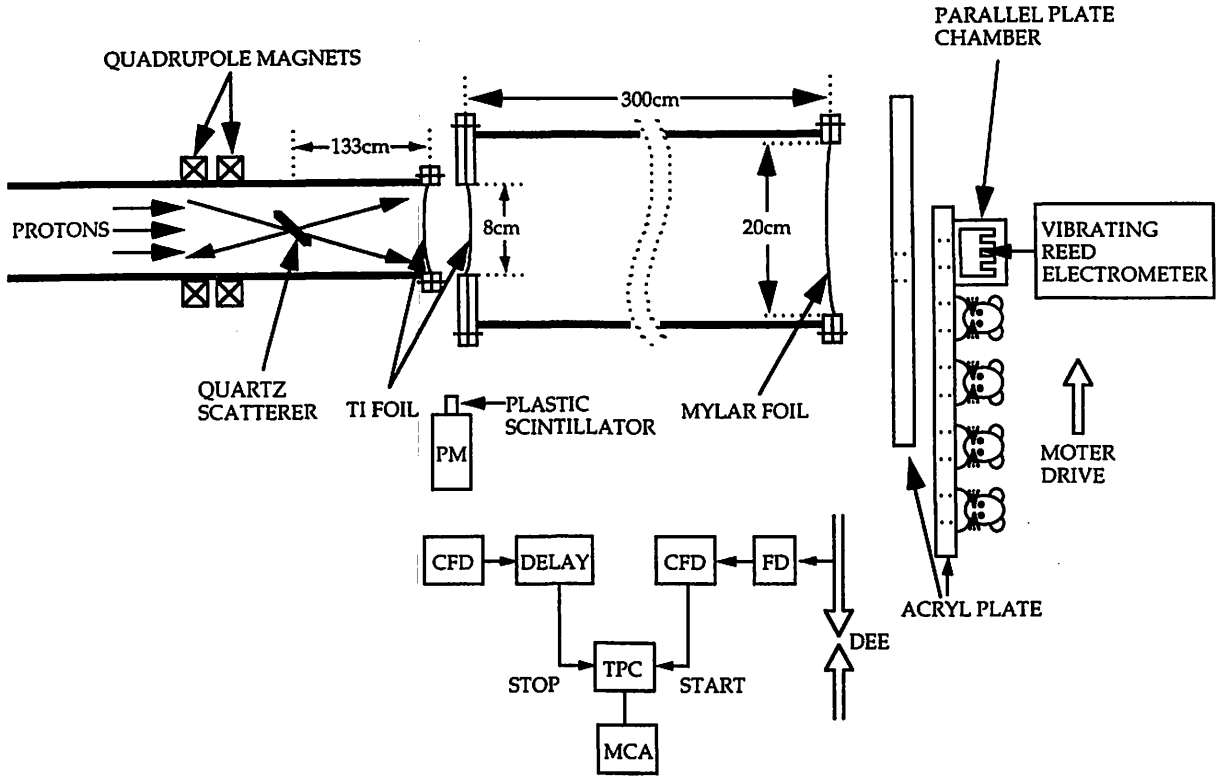

PM; photomultiplier, CFD; constant fraction discriminator,
FD; frequency divider, TPC; time to pulse converter, MCA; multi-channel analyzer.

Fig. 1 Experimental setup of this research.

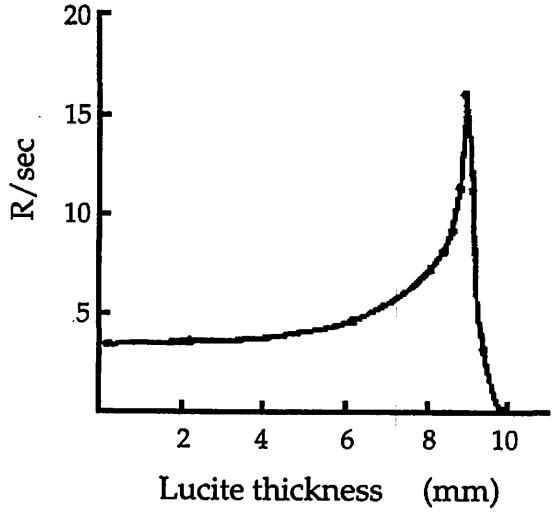

Fig. 2 Bragg curves of 38 MeV Protons.

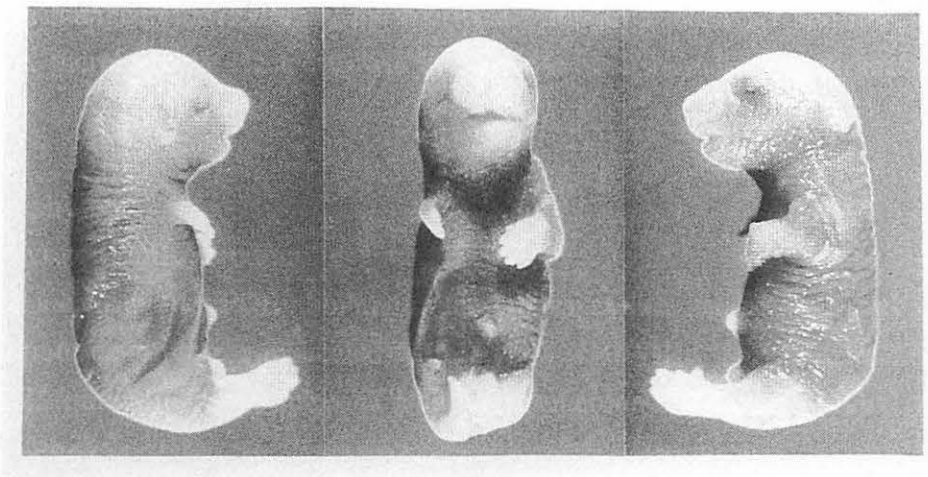

Fig. 3. External anomalies observed in the proton beam.

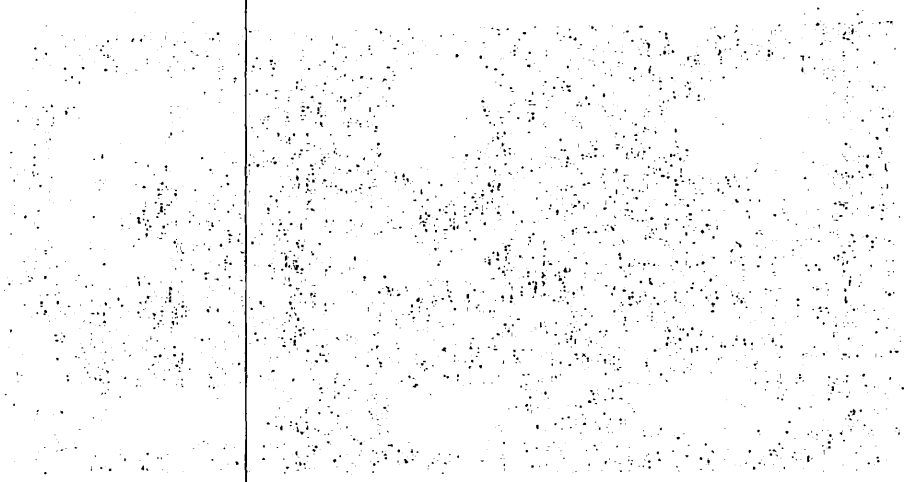

III. 3. Role of Nitric Oxide Synthase on Age-related Changes in Second Messenger Systems and Calcium Channels in Rats

Araki T., Kato H., Oshima Y., Fujiwara T.**, and Itoyama Y.*

Department of Neurology, Tohoku University School of Medicine
*Department of Pharmacognosy, Faculty of Pharmaceutical Sciences, Tohoku University**
*Cyclotron and Radioisotope Center, Tohoku University***

Introduction

Nitric oxide (NO) is an intracellular and short-lasting second messenger molecule that is synthesized from L-arginine in several tissues by a reaction catalyzed by NO synthases[1-2]. In brain, NO has been proposed to be implicated in many physiological, pathological and biochemical conditions, such as learning and memory, synaptic plasticity and neurotoxicity[3-4]. Recent evidence suggests that NO is deleterious and may be a mediator of neurotoxicity during cerebral brain damage[5-6]. However, some reports have demonstrated that NO is beneficial to the ischemic brain[7]. Therefore, the role of NO in the mechanisms of cerebral ischemia remains to be clearly defined.

On the other hand, conflicting results regarding the possible role of NO are also apparent in brain neurotransmission. Depending on the experimental conditions used, the effects of NO are either an increase[8-9] or a decrease[3,10] in neurotransmission. Thus, the role of NO in brain neurotransmission is still unclear.

Therefore, in order to examine the role of NO as a second messenger, we investigated the effect of NO inhibitor, N^G-nitro-L-arginine methyl ester (L-NAME), on age-related changes in second messenger receptor systems and calcium channels in rats using in vitro autoradiography.

Materials and Methods

Animals

Male Fischer 344 rats, 6 months (adult) and 24 months (aged) of age, were used throughout the experiments. Animals were killed by decapitation under a light ether. The brains were removed quickly, frozen in powdered dry ice, and stored at -80°C until assay. Sagittal sections 12 μm in thickness were cut on a cryostat and thaw-mounted onto gelatin-coated slides. Adjacent brain sections were stained with Cresyl violet. The animals were divided into three groups; (1) 6-month-old group (n=6); (2) vehicle- treated 24-month-old group (n=7); (3) N^G-nitro-L-arginine methyl ester (L-NAME, Sigma)-treated 24-month-old

group (n=6). L-NAME (5mg/kg) or vehicle (distilled water) were adiministered ip once a day for 4 weeks before decapitation.

We initially planned to study low (5 mg/kg) and high (20 and 50 mg/kg) doses of L-NAME. However, we observed that the rats treated with high doses of L-NAME developed cardiac arrhyhmias with a change in the rhythm of the heartbeat , abnormal behavior and loss in weight. In this study, therefore, we elected to use a low dose of L-NAME for chronic treatment.

Quantitative autoradiography

[^{3}H]Phorbol 12,13-dibutyrate (PDBu) binding

Autoradiographic localization of PDBu binding in the brain was detected as described previously[11]. Briefly, brain sections were incubated with 2.5 nM [^{3}H]PDBu (New England Nuclear, spec. act. 20.7 Ci/mmol) in 50 mM Tris-HCl buffer (containing 100 mM NaCl and 1 mM $CaCl_2$ for 60 min at 25°C.

[^{3}H]Forskolin binding

Autoradiographic distribution of forskolin binding was performed as described previously[12]. Briefly, brain sections were incubated with 10 nM [^{3}H]forskolin (New England Nuclear, spec. act. 33.0 Ci/mmol) in 50 mM Tris-HCl buffer (pH 7.7) containing 100 mM NaCl and 5 mM $MgCl_2$ for 10 min at 25°C.

[^{3}H]Rolipram (Calcium/calmodulin-independent cyclic-AMP selective phosphodiesterase inhibitor) binding

Autoradiographic distribution of calcium-calmodulin-independent cyclic-AMP PDE sites was detected, as described previously[12]. Briefly, brain sections were incubated with 5 nM [^{3}H]rolipram (Amersham, spec. act. 60 Ci/mmol) in 150 mM phosphate buffer (pH 7.4) containing 2 mM $MgCl_2$ and 100 μM ditiothreitol for 60 min at 20°C.

[^{3}H]PN200-110 (Voltage-dependent L-type calcium channel blocker) binding

Autoradiographic distribution of PN200-110 binding was detected as described previously[13]. Briefly, brain sections were incubated with 0.1 nM [^{3}H]PN200-110 (New England Nuclear, spec. act. 71.5 Ci/mmol) in 70 mM Tris-HCl buffer (pH 7.4) for 60 min at room temperature.

Data analysis

The above sections were rapidly dried under a cold air stream and were exposed to Hyperfilm-[^{3}H] (Amersham) for 2-5 weeks in X-ray cassettes with a set of [^{3}H]microscales (Amersham). The optical density of the brain areas was measured with a computer-assisted

image analyzer, as described previously[14]. The relationship between the optical density and radioactivity was obtained with reference to the [^{3}H]microscales co-exposed with the brain sections. Values were expressed as the mean ±S.D. Statistical comparisons were made using an analysis of variance (ANOVA) followed by Dunnett's multiple comparison test.

Results

The effect of L-NAME on these bindings in the aged rat brain is summarized in Tables 1-4.

[^{3}H]PDBu binding

In adult (6-month-old) rats, [^{3}H]PDBu binding was greatest in the molecular layer of cerebellum, hippocampus and neocortex. The striatum, substantia nigra and thalamus also exhibited a relatively high [^{3}H]PDBu binding. Other regions had a low density of [^{3}H]PDBu binding. In vehicle-treated aged (24-month-old) rats, no significant change of [^{3}H]PDBu binding was observed in the brain, as compared with the adult animals. Chronic treatment with L-NAME also showed no significant change in the brain of aged rats.

[^{3}H]Forskolin binding

In adult rats, the highest of [^{3}H]forskolin binding was observed in the striatum, followed by the hilus of the hippocampus, the molecular layer of the cerebellum, hippocampal CA3 sector and substantia nigra. Other regions showed a relatively low [^{3}H]forskolin binding. In vehicle-treated aged rats, a marked reduction in [^{3}H]forskolin binding was found in the striatum, hippocampal CA3 sector, dentate gyrus, hilus, thalamus, substantia nigra and molecular layer of the cerebellum, as compared with the adult animals. In contrast, chronic treatment with L-NAME showed a significant decline in [^{3}H]forskolin binding in the frontal cortex, striatum and hippocampal CA1 sector of aged rats, as compared with vehicle-treated aged animals.

[^{3}H]Rolipram binding

In adult rats, [^{3}H]rolipram binding was greatest in the hippocampus, especially the hippocampal CA1 sector. The striatum, substantia nigra, frontal cortex, parietal cortex and thalamus also had a relatively high [^{3}H]rolipram binding. Other regions exhibited a low density of [^{3}H]rolipram binding. In vehicle-treated aged rats, no significant change in [^{3}H]rolipram binding was observed in the brain, as compared with the adult animals. Chronic treatment with L-NAME also showed no significant change in [^{3}H]rolipram binding in the brain of aged rats, as compared with vehicle-treated aged animals.

[^{3}H]PN200-110 binding

In adult rats, [^{3}H]PN200-110 binding was greatest in the dentate gyrus and hippocampal CA3 sector. The hippocampal CA1 sector, frontal cortex, parietal cortex and thalamus also had a relatively high density of [^{3}H]PN200-110 binding. Other regions exhibited a low [^{3}H]PN200-110 binding. In vehicle-treated aged rats, no significant change was observed in the brain, as compared with the adult animals. Chronic treatment with L-NAME also showed no significant alteration in [^{3}H]PN200-110 binding in the brain of aged rats, as compared with vehicle-treated aged animals.

Discussion

NO is synthesized as a product of the enzyme NO synthase (NOS). NOS exists in at least two major isoforms[15]. The inducible NOS (iNOS) is not regulated by calcium concentration but is regulated transcriptionally, and is primarily expressed in astrocytes, microglia and inflammatory cells[2,16]. In contrast, there are two distinct constitutive calcium-dependent NOS (cNOS) isoforms, i.e. neuronal NOS(nNOS) form in neurons and endothelial NOS (eNOS) from in pyramidal cells and endothelial cells[17]. NOS is known to be abundant in brain tissue[15,18].

Recent attention has been focused the role of NO as a retrograde intracellular messenger mediating cell-to-cell interactions in the brain including the cell-mediated immune system, cerebral smooth muscle relaxation, inhibition of platelet aggregation, learning and synaptic plasticity[4,19]. A number of experimental studies have also demonstrated that NO and NO donors can enhance the basal release of neurotransmitters in the mammalian brain, including dopamine, norepinephrine, glutamate, acetylcholine and GABA[8,20-22]. These observations are great interest in regard to the role of NO in the central nervous system as an intracellular messenger.

An interesting study has reported that purified brain NOS was stoichiometrically phosphorylated by cAMP-dependent protein kinase, protein kinase C, and calcium/calmodulin-dependent protein kinase, with each kinase phosphorylating a different serine site on NOS[23]. On the other hand, cytokines such as interleukin-1, tumor necrosis factor a and g-interferon have been shown to induce NOS in a huge variety of different cell types including macrophages, endothelial cells and astroglia[24]. Recently, Durieu-Trautmann et al[25] have demonstrated that the cytokine-stimulated NO production in brain endothelial cells is potentiated by cyclic AMP. It has also been reported that cyclic AMP can enhance NO formation caused by calcium release from internal stores in neuronal cell line[26]. However, so far little is still known for the role of NO on intracellular second messenger systems in the brain. Thus NO may play some role in modulation of second messenger systems including adenylate cyclase system. Therefore, we focused on adenylyl cyclase, PKC, calcium/calmodulin-independent cyclic-AMP PDE and voltage-dependent L-type calcium

channels and investigated the effects of L-NAME against age-related changes in these bindings in the rat brain, using in vitro autoradiography.

In the present study, [^{3}H]forskolin binding showed a marked reduction in the striatum, hippocampal CA1 sector, hippocampal CA3 sector, dentate gyrus, hilus, thalamus, substantia nigra and cerebellum of aged rats. However, [^{3}H]rolipram binding exhibited a significant reduction only in the striatum and cerebellum of aged animals. In contrast, no conspicuous changes in [^{3}H]PDBu and [^{3}H]PN200-100 binding was observed in the aged rat brains. These findings suggest that adenylyl cyclase is more susceptible to aging processes than PKC, calcium/calmodulin-independent cyclic-AMP PDE and calcium channels. On the other hand, chronic L-NAME treatment showed no significant changes in [^{3}H]PDBu, [^{3}H]rolipram and [^{3}H]PN200-110 binding in the aged rat brains. However, this treatment caused a significant reduction in [^{3}H]forskolin binding in the frontal cortex, striatum and hippocampal CA1 sector of aged rats. Thus, chronic L-NAME treatment produced a significant reduction in [^{3}H]forskolin binding in any several brain areas of aged rats. The reason for this phenomenon is presently unclear. However, a recent study has reported that both cyclic AMP and NO production in vascular smooth muscle cells are enhanced in the presence of forskolin, as an activator of adenylyl cyclase[27]. Furthermore, Hernádez et al[28] have suggested that NOS is a potential substrate for cyclic-AMP dependent protein kinase and that forskolin may act at this point. From these observations, therefore, our findings suggest that NO may play a key role in the regulation of adenylyl cyclase system during aging processes. However, at least three major isoforms of NOS have been identified. Therefore, it is necessary to investigate the role and regional pattern of each isoform of NOS for the further understanding of age-related changes in the brain using in vitro autoradiography.

References

1) Ignarrro L. J., Annu. Rev. Pharmacol. Toxicol. **30** (1990) 535.
2) Dawson T. M. and Snyder S. H., J. Neurosci. **14** (1994) 5147.
3) Daniel H., Hermart, N., Jailard, D. et al., Eur. J. Neuosci. **5** (1993) 1079.
4) Bredt D. S. and Snyder S. H., Annu. Rev. Biochem. **63** (1994) 175.
5) Pelligrino D. A., J. Neurosurg. Anesthesiol. **5** (1993) 221.
6) Iadecola C., Pelligrino D. A., Moskowitz, M. A. et al., J. Cereb. Blood Flow Metab.**14** (1994) 175.
7) Kuluz J. W., Prado R. J., Dietrich W. D.et al., Stroke **24** (1993) 2023.
8) Zhu X. -Z. and Luo L. -G., J. Neurochem. **59** (1992) 932.
9) Meffert M. K., Premack B. A., Schulman H., Neuron **12** (1994) 1235.
10) Boulton C. L., Irving A. J., Southam, E. et al., Eur. J. Neurosci. **6** (1994) 1528.
11) Araki T., Kato H., Fujiwara T. et al., Brain Res. **704** (1995) 227.
12) Araki T., Kato H. and Kogure, K., Brain Res. Bull. **28** (1992) 843.
13) Araki T., Kato H. and Kogure, K., J. Neurol. Sci. **106** (1991) 206.
14) Araki T., Kato H., Kanai Y. et al., J. Neural Transm. **97** (1994) 135.
15) Marletta M. A., Cell **78** (1994) 927.
16) Nathan C., FASEB J. **6** (1992) 3051.
17) Moncada S., Palmer R. M. and Higgs E. A., Phatmacol. Rev. **43** (1991) 109.
18) Kidd E. J., Michel A. D. and Humphrey P. P. A., Neuropharmacology **34** (1995) 63.

19) Shibuki K. and Okada D., Nature **349** (1991) 326.
20) Prast H. and Philippu A., Eur. J. Pharmacol. **216** (1992) 139.
21) Lonart G., Wang J. and Johanson K. M., Eur. J. Pharmacol. **220** (1992) 271.
22) Lonart, G. and Johanson K.M., J. Neurochem. **63** (1994) 2108.
23) Bredt D.S., Ferris C. D. and Snyder S.H., J. Biol. Chem. **267** (1992) 10976.
24) Nathan C. and Xie Q.W., Cell **78** (1994) 915.
25) Durieu-Trautmann O., Federici C., Creminon C. et al., J. Cell. Physiol. **155** (1993) 104.
26) Reiser G., Eur. J. Pharmacol. **227** (1992) 89.
27) Scott-Burden T., Elizondo E., Ge T. et al., Mol. Pharmacol. **46** (1994) 274.
28) Hernádez F., Alexander S. P. H. and Kendall D.A., J. Neurochem. **62** (1994)2212.

Table 1. The effect of L-NAME on [^{3}H]PDBu binding in aged rat brain

	6-month-old	24-month-old	
Regions		Vehicle	L-NAME
Frontal cortex	762±71	781±98	785±124
Parietal cortex	895±249	754±104	729±93
Striatum	622±49	659±82	653±119
Hippocampus			
CA1 sector	1091±226	956±125	954±104
CA3 sector	894±80	919±82	899±141
Dentate gyrus	896±56	962±133	972±122
Thalamus	501±26	513±85	552±69
Substantia nigra	662±112	598±165	736±139
Cerebellum			
Molecular layer	1259±90	1322±162	1254±78
Granule cell layer	483±58	473±59	461±46

Optical density was converted to fmol/mg tissue. Each value was expressed as means ± S.D. The values for the 6-month-old- and L-NAME-treated animals were not significantly from the vehicle-treated 24-month-old group (Dunnett's multiple comparison test).

Table 2. The effect of L-NAME on [^{3}H]forskolin binding in aged rat brain

	6-month-old	24-month-old	
Regions		Vehicle	L-NAME
Frontal cortex	56±6	49±8	37±7*
Parietal cortex	62±11	55±9	44±8
Striatum	255±17**	196±16	171±20*
Hippocampus			
CA1 sector	33±7	38±5	23±11*
CA3 sector	73±13*	58±7	53±6
Dentate gyrus	80±7**	67±9	57±11
Hilus	183±31*	146±30	142±16
Thalamus	47±7*	35±10	30±8
Substantia nigra	118±19**	91±11	94±11
Cerebellum			
Molecular layer	161±11**	138±4	129±9
Average	78±10**	62±6	53±6

Optical density was converted to fmol/mg tissue. Each value was expressed as means ± S.D. *$p<0.05$, **$p<0.01$ vs. vehicle-treated 24-month-old group (Dunnett's multiple comparison test).

Table 3. The effect of L-NAME on [^{3}H]rolipram binding in aged rat brain

Regions	6-month-old	24-month-old	
		Vehicle	L-NAME
Frontal cortex	102±19	83±15	91±8
Parietal cortex	85±14	94±8	88±9
Striatum	74±8	66±12	77±3
Hippocampus			
CA1 sector	127±15	128±11	145±26
CA3 sector	123±12	109±20	133±27
Dentate gyrus	89±18	74±8	84±13
Thalamus	87±12*	73±8	83±10
Substantia nigra	43±9	38±4	43±6
Cerebellum			
Molecular layer	91±21	78±10	83±22
Granule cell layer	62±11*	48±8	52±8

Optical density was converted to fmol/mg tissue. Each value was expressed as means ± S.D.
*$p<0.05$, **$p<0.01$ vs. vehicle-treated 24-month-old group (Dunnett's multiple comparison test).

Table 4. The effect of L-NAME on [^{3}H]PN200-110 binding in aged rat brain

Regions	6-month-old	24-month-old	
		Vehicle	L-NAME
Frontal cortex	9.1±2.0	7.0±1.7	7.5±1.0
Parietal cortex	10.3±2.4	8.2±2.4	7.4±1.0
Striatum	7.2±0.9	7.5±2.0	7.4±0.8
Hippocampus			
CA1 sector	9.8±1.9	8.5±2.6	7.2±0.7
CA3 sector	11.3±1.9	10.1±2.0	9.5±1.2
Dentate gyrus	16.6±3.3	16.1±3.1	13.5±1.4
Thalamus	8.8±1.5	8.7±1.9	8.3±2.3
Substantia nigra	2.2±0.9	1.2±1.0	1.8±0.7
Cerebellum	3.3±1.0	2.2±0.8	2.3±0.7

Optical density was converted to fmol/mg tissue. Each value was expressed as means ± S.D.
The values for the 6-month-old- and L-NAME-treated animals were not significantly from the vehicle-treated 24-month-old group (Dunnett's multiple comparison test).

III. 4. Effects of L-DOPA on Haloperidol-Induced Motor Deficits in Mice

Kobayashi T., Araki T., Itoyama Y.*, Ohta T., and Oshima Y.*

Department of Pharmacognosy, Faculty of Pharmaceutical Sciences, Tohoku University
*Department of Neurology, Tohoku University School of Medicine**

Introduction

The motor deficits are thought to be predominantly associated with the antagonistic action of the neuroleptics on dopamine receptors[1]. Haloperidol, a commonly used neuroleptic agent, belongs chemically to the class of butyrophenones and is well-known to cause motor impairments in humans. Therefore, motor-related side effects are commonly encountered in the treatment of schizophrenia with neuroleptics such as haloperidol.

The loss of dopamine input to the striatum from the substantia nigra is the major factor contributing to the clinical features of Parkinson's disease. This disorder is commonly characterized by symptoms of motor disturbances such as bradykinesia, rigidity, resting tremor and loss of postural reflexes. Therefore, the motor deficits produced in humans by neuroleptics, such as haloperidol and sulpiride, are considered to be model aspects of the movement disturbances found in Parkinson's disease[2-3].

L-3, 4-Dihydroxyphenylalanine (L-DOPA), the precursor of dopamine, is considered the most successful medication for the treatment of Parkinson's disease, although a progressive loss of the initial beneficial effect has been observed in a large proportion of parkinsonian patients after long-term therapy[4-5]. However, little is known for the effect of these drugs against neuroleptics-induced motor deficits. In the present study, therefore, we investigated the effects of L-DOPA on haloperidol-induced motor deficits in mice using both catalepsy and pole tests.

Materials and Methods

Experimental animals

Male ddy mice, 6 weeks old (30-36 g), were used in this study. The animals were housed in air-conditioned rooms at a room temperature of 22±1°C and under a 12-hr light-dark cycle with standard food and tap water available ad libitum.

Drugs

Haloperidol, L-DOPA and carbidopa were used in this study. Haloperidol (0.125, 0.25 and 0.5 mg/kg) was dissolved in 2 % gum arabic solution and was given subcutaneously (sc) in mice. L-DOPA (200 and 400 mg/kg) was dissolved in 0.5 % Tween 80 solution, and carbidopa (10 mg/kg) was dissolved in 2 % gum arabic solution. These drugs were injected intraperitoneally (ip) in animals.

Experimental procedures

Catalepsy test

In order to measure a cataleptic symptoms such as akinesia and rigidity, bar-test catalepsy was evaluated by placing both forepaws of the mouse over a horizontal bar (diameter: 0.2 cm), elevated 15 cm from floor. The time during which the animal maintained this position was recorded up. In preliminary study, the test was performed at immediately before (0 hr) and 0.5, 1, 2, 4, 7 and 24 hr after haloperidol treatment. For the evaluation of drugs, the test was performed at immediately before (0 hr) and 0.5, 1, 2 and 4 hr after haloperidol treatment.

Pole test

In order to measure the degree of bradykinesia, a typical symptom of parkinsonism, pole test was performed according to the method of Ogawa et al[6-7]. In brief, the mouse was placed head upward on the top of a rough-surfaced pole (8 mm in diameter and 50 cm in height) which was wrapped doubly with gauze to prevent slipping; the time until it turned completely downward (Tturn) and the time until it climbed down to the floor (TLA) were examined. In preliminary study, the test was performed at immediately before (0 hr) and 0.5, 1, 2, 4, 7 and 24 hr after haloperidol treatment. For the evaluation of drugs, the test was performed at immediately before (0 hr) and 0.5, 1, 2 and 4 hr after haloperidol treatment.

In both tests, L-DOPA was treated ip 60 min before haloperidol treatment in mice. Carbidoda was injected ip 10 min before the treatment with L-DOPA to block the metabolism of L-DOPA. Control mice received vehicle (0.5 % Tween 80 solution or 2 % gum arabic solution) at the same schedules before haloperidol treatment. In addition, vehicle-treated mice received 2% gum arabic solution without haloperidol in preliminary study.

Statistical analysis

Values were expressed as the means ±S. E. Statistical significance was made using an analysis of variance (ANOVA) followed by Williams multiple comparison test with two-side.

Results

Preliminary test

Haloperidol was examined for its potency to induce catalepsy in the horizontal bar test. Fig. 1 shows that haloperidol caused a significant and dose-dependent cataleptic effect in the range of 0.125-0.5 mg/kg. This cataleptic effect gradually developed from 0.5 hr after haloperidol injection and lasted more than 7 hr. After 24 hr, however, haloperidol-induced cataleptic effect was not observed in mice. In pole test, haloperidol caused a significant prolongation of Tturn and TLA in the range of 0.125-0.5 mg/kg as shown in Figs. 2 and 3. This effect was especially noted in higher dose of 0.5 mg/kg and developed gradually from 0.5 hr after haloperidol injection and lasting more than 7 hr. Twenty-four hr after haloperidol treatment, however, this effect was not significant in mice.

Effects of L-DOPA

Catalepsy test

Haloperidol at a dose of 0.125 mg/kg caused a significant cataleptic effect from 1 hr after its treatment. This effect lasted for at least 4 hr after haloperidol treatment as shown in Fig. 4. Co-pretreatment with L-DOPA (200 mg/kg) + carbidopa (10 mg/kg) had no effect on the catalepsy induced by haloperidol throughout the experiment. However, the haloperidol-induced catalepsy in mice was significantly reduced by co-administration with L-DOPA (400 mg/kg) + carbidopa (10 mg/kg). This therapeutic effect was noted at 1, 2 and 4 hr after haloperidol treatment (Fig. 4).

In addition, haloperidol at a higher dose of 0.5 mg/kg caused a severe cataleptic effect in mice. As shown in Fig. 5, co-pretreatment with L-DOPA (200 mg/kg) + carbidopa (10 mg/kg) showed no significant reduction on the catalepsy induced by haloperidol. However, the pretreatment with L-DOPA (400 mg/kg) + carbidopa (10 mg/kg) had a beneficial effect on the catalepsy 1 and 2 hr after haloperidol treatment. However, this effect was not found at 4 hr after haloperidol treatment.

Pole test

Haloperidol at a dose of 0.125 mg/kg caused a significant prolongation of Tturn and TLA from 0.5 hr after haloperidol treatment. The significant prolongation lasted at least 4 hr after haloperidol treatment. Co-pretreatment with L-DOPA + carbidopa dose-dependently reduced the prolongation of Tturn 1, 2 and 4 hr after haloperidol treatment. Furthermore, the pretreatment with L-DOPA + carbidopa significantly decreased the prolongation of TLA 0.5, 1 and 2 hr after haloperidol treatment in a dose-dependent manner. This effect was especially evident in Tturn test (Figs. 6 and 7).

Discussion

Following many years of clinical experience with neuroleptics, there is a extensive consensus on the merits and disadvantages of their use for the treatment of schizophrenia. The blockade of dopamine D_2 receptors, as the common activity of well-known neuroleptics, is held responsible for the marked control of positive symptoms such as delusions, hallucinations and thought disorders in schizophrenia, but at the same time for the frequent occurrence of extrapyramidal symptoms as a side effect. Thus neuroleptic-induced extrapyramidal symptoms are similar to motor deficits in Parkinson's disease. Therefore, the present study investigates whether anti-parkinsonian agents such as L-DOPA and bromocriptine are able to prevent neuroleptic-induced catalepsy (rigidity and akinesia) and bradykinesia, which are regarded as an animal model of Parkinson's disease[3,8].

Numerous studies have shown that various drugs, such as L-DOPA, agonists of dopamine receptors and antagonists of *N*-methyl-D-aspartate (NMDA) receptors, can attenuate catalepsy induced by neuroleptics such as haloperidol using the horizontal bar test[9-12]. The present study also showed that co-pretreatment with L-DOPA + carbidopa significantly reduced haloperidol-induced catalepsy. Furthermore, pretreatment with bromocriptine dose-dependently decreased haloperidol-induced catalepsy. The results, at least in part, are consistent with previous reports[9,11].

Interestingly, Ogawa et al.[6,7] reported that pole test may be of value in the screening of anti-parkinsonian agents. Several studies also suggested that pole test is a useful technique to measure motor disturbances including bradykinesia in 1-methyl-4-phenyl-1,2,3,6-tetrahydropyridine (MPTP)-treated mice which are well-known as a suitable model of parkinsonism[13,14]. Furthermore, Ogawa et al.[6,7] demonstrated that L-DOPA can prevent bradykinesia in MPTP-treated mice using pole test. However, little is known for the effect of pharmacological drugs against neuroleptic-induced motor disturbances using pole test. In the present study, pretreatment with L-DOPA + carbidopa decreased haloperidol-induced bradykinesia in a dose-dependent manner. These findings strongly indicate that pole test is of value in the screening of drugs on motor deficit in haloperidol-treated mice as well as MPTP-treated animals.

Of particular interest, in the present study, is that the effect of co-pretreatment with L-DOPA + carbidoba in pole test was more pronounced than that in catalepsy test. These observations seem to suggest that the pole test may be more excellent than catalepsy test for the screening of drugs against neuroleptic-induced motor deficits. The reason for this phenomenon is presently unclear. Therefore, it is necessary to investigate the precise biochemical mechanisms for the further understanding of our findings. In the present study, however, we speculate that pole test is a useful approach for diagnosis of motor disturbances caused by neuroleptics and evaluation of anti-parkinsonian drugs.

In conclusion, the present study demonstrates that co-treatment with L-DOPA + carbidopa can prevent haloperidol-induced motor deficits in mice. The beneficial effects were

confirmed by both catalepsy and pole tests. Therefore, our study also suggests that pole test as well as catalepsy test is of value in the evaluation of drugs against motor disturbances in neuroleptic-treated animals.

Acknowledgement

This work is supported in part by a Grant-in Aid for Scientific Research from the Ministry of Education, Science, Sports and Culture of Japan.

References

1) Peroutka S. L. and Snyder S. H. L., Am. J. Psychiatry **137** (1980) 1518.
2) Hornykiewicz O., Br. Med. Bull. **29** (1973) 172.
3) Sanberg P. R., Bunsey M. D., Giordano M. et al., Behav. Neurosci. **102** (1988) 748.
4) Kurlan R., Arch. Neurol. **45** (1988) 204.
5) Calne D. B., New Eng. J. Med. **32** (1993) 1021.
6) Ogawa N., Hirose Y., Ohara S. et al., Res. Comm. Chem. Pathol. Pharmacol. **50** (1985) 435.
7) Ogawa N., Mizukawa K., Hirose Y. et al., Eur. Neurol. **26** (1987) 16.
8) Papa S. M., Engber T. M., Boldry R.C. et al., Eur. J. Pharmacol. **232** (1993) 247.
9) Maj J., Kapturkiewicz Z. and Sarnek J., J. Pharm. Pharmacol. **24** (1972) 735.
10) Schmidt W. J. and Bubser M., Psychopharmacol. Biochem. Behav. **32** (1989) 621.
11) Wanibuchi F. and Usuda S., Psychopharmacol. **102** (1990) 339.
12) Kretschmer B. D., Zadow B., Volz T. L. et al., J. Neural. Transm. **87** (1992) 23.
13) Arai N., Misugi K., Goshima Y. et al., Brain Res. **515** (1990) 57.
14) Takahashi Y., Makino Y., Ohta S. et al., J. Neurochem. **57** (1991) 1940.

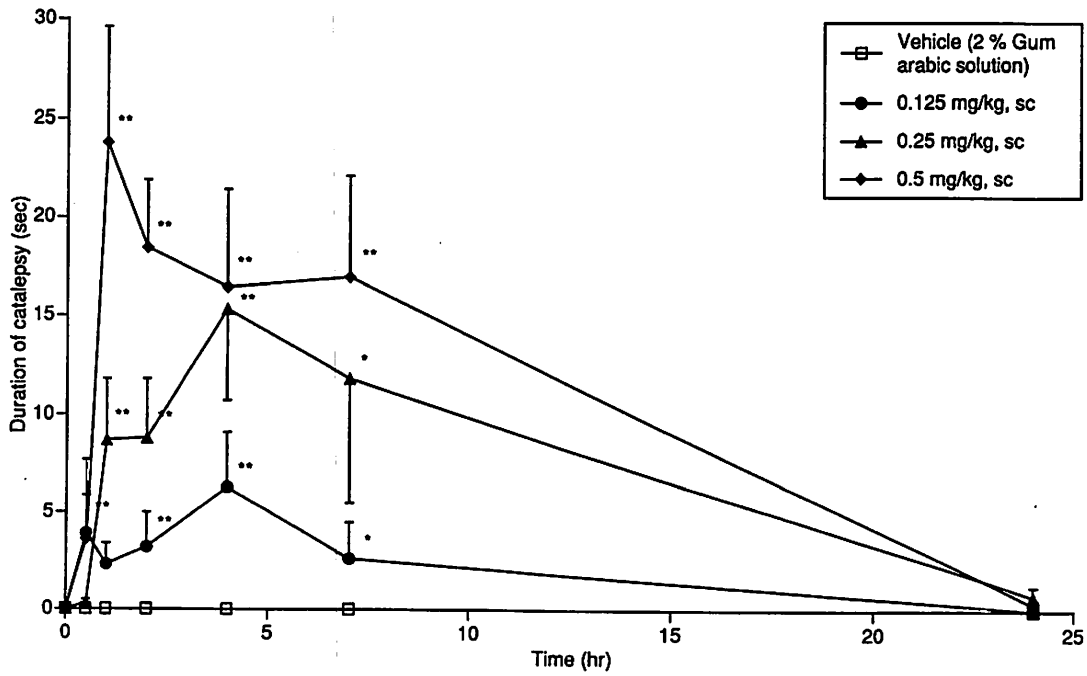

Fig. 1 Time course of the catalepsy induced by haloperidol in mice. Points show the means ± SEM of 6 - 9 mice. $^{*}p < 0.05$, $^{**}p < 0.01$ vs. the corresponding value in vehicle group (Williams multiple-range test).

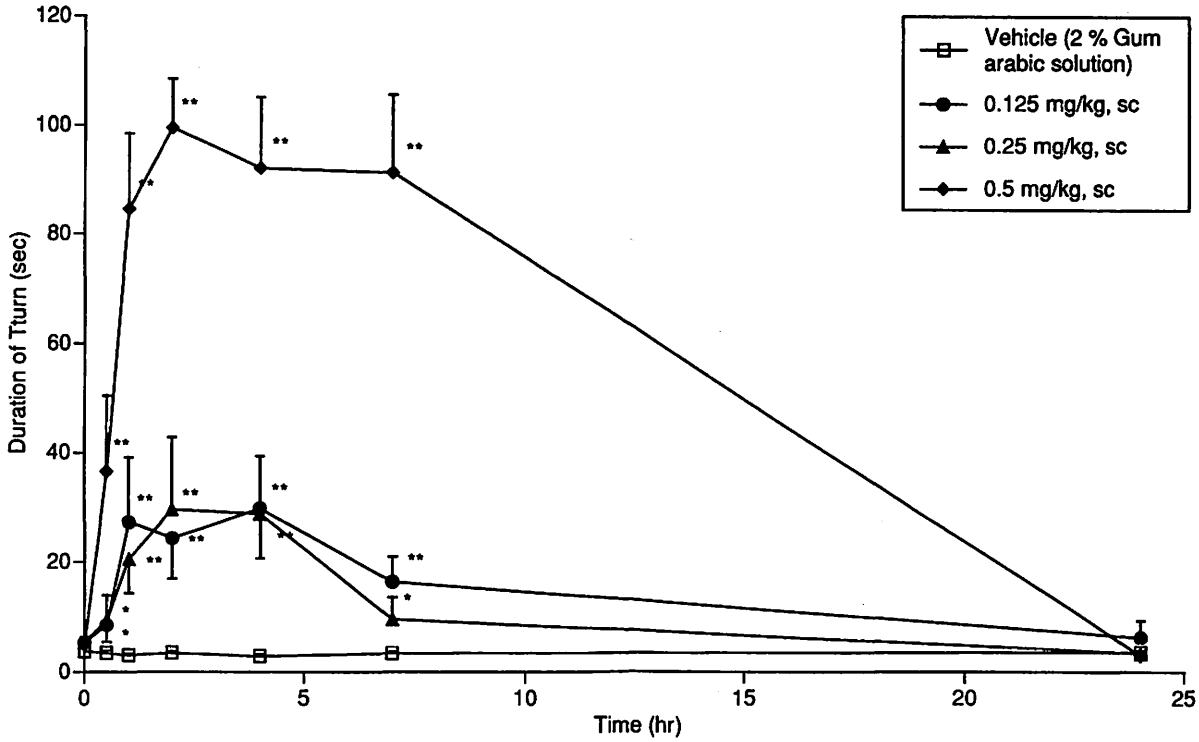

Fig. 2 Time course of values of the Tturn in haloperidol-treated mice. Points show the means ± SEM of 7 - 8 mice. $^{*}p < 0.05$, $^{**}p < 0.01$ vs. the corresponding value in vehicle group (Williams multiple-range test).

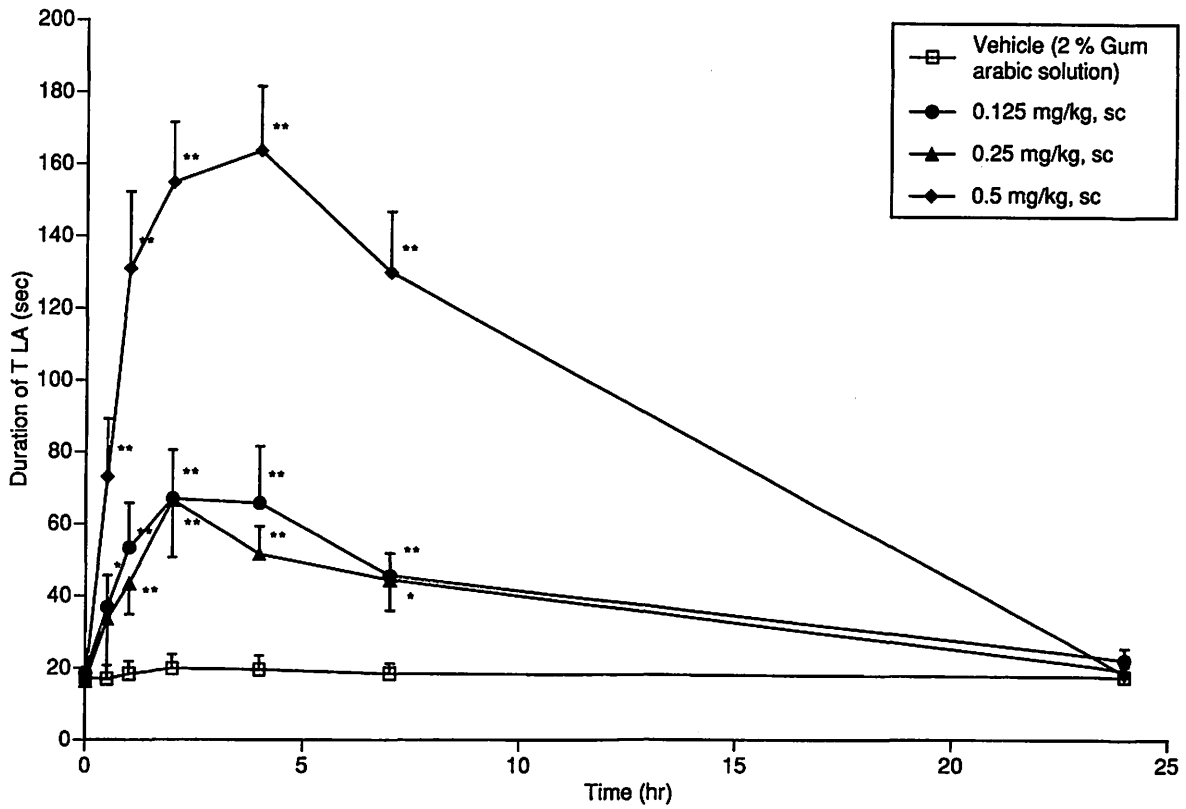

Fig. 3 Time course of values of the TLA in haloperidol-treated mice. Points show the means ± SEM of 7 - 8 mice. $^{*}p < 0.05$, $^{**}p < 0.01$ vs. the corresponding value in vehicle group (Williams multiple-range test).

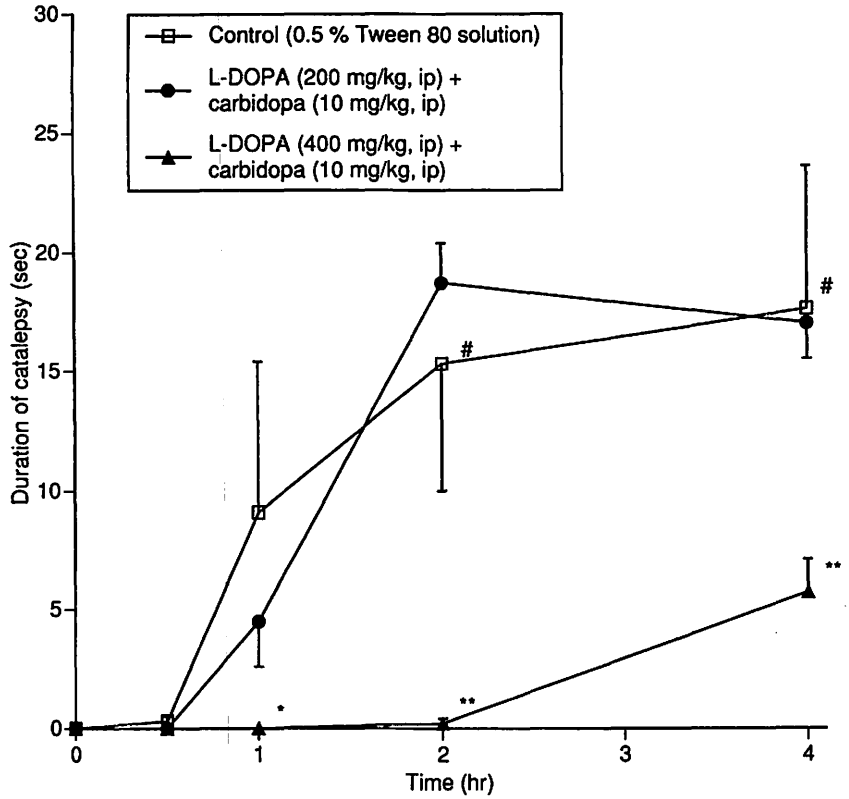

Fig. 4 Effect of L-DOPA + carbidopa on haloperidol (0.125 mg/kg, sc)-induced catalepsy in mice. Points show the means ± SEM of 6 - 8 mice. $*p < 0.05$, $**p < 0.01$ vs. the corresponding value in vehicle group and $\#p < 0.05$ vs. 0 hr in vehicle group (Williams multiple-range test).

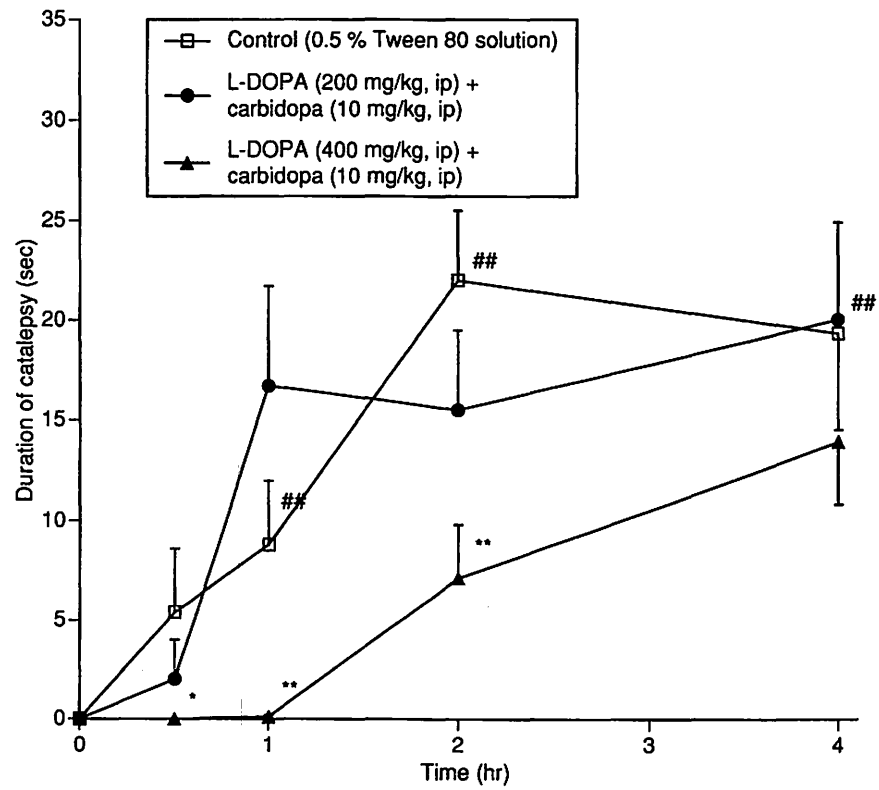

Fig. 5 Effect of L-DOPA + carbidopa on haloperidol (0.5 mg/kg, sc)-induced catalepsy in mice. Points show the means ± SEM of 6 - 8 mice. $*p < 0.05$, $**p < 0.01$ vs. the corresponding value in vehicle group and $\#\#p < 0.01$ vs. 0 hr in vehicle group (Williams multiple-range test).

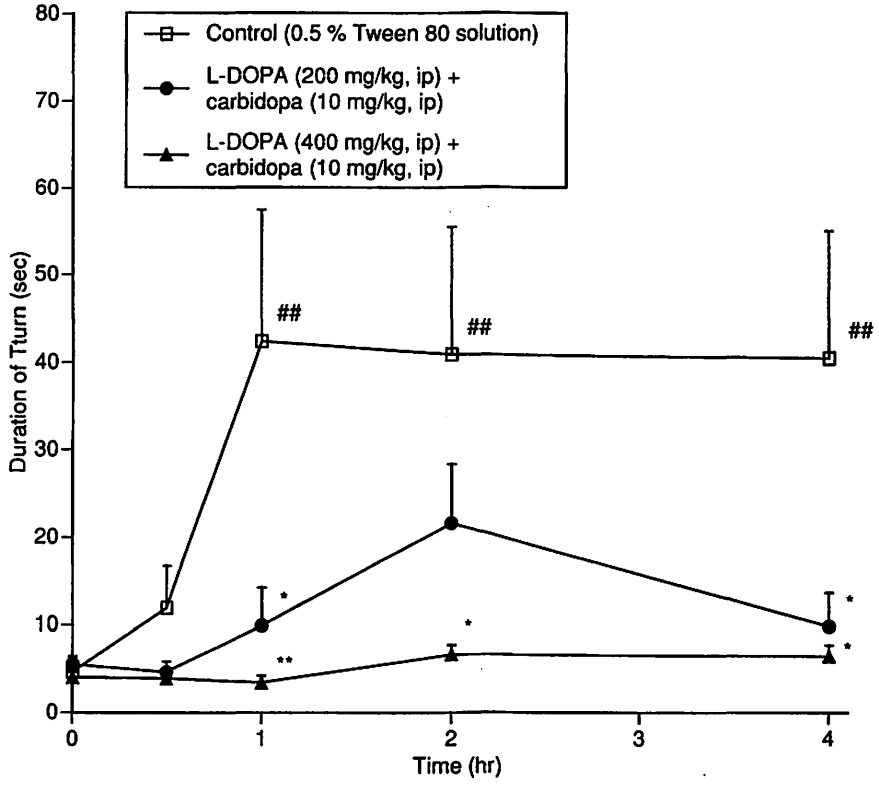

Fig. 6 Effect of L-DOPA + carbidopa on the Tturn in haloperidol (0.125 mg/kg, sc)-treated mice. Points show the means ± SEM of 7 - 8 mice. $*p < 0.05$, $**p < 0.01$ vs. the corresponding value in vehicle group and $\#\#p < 0.01$ vs. 0 hr in vehicle group (Williams multiple-range test).

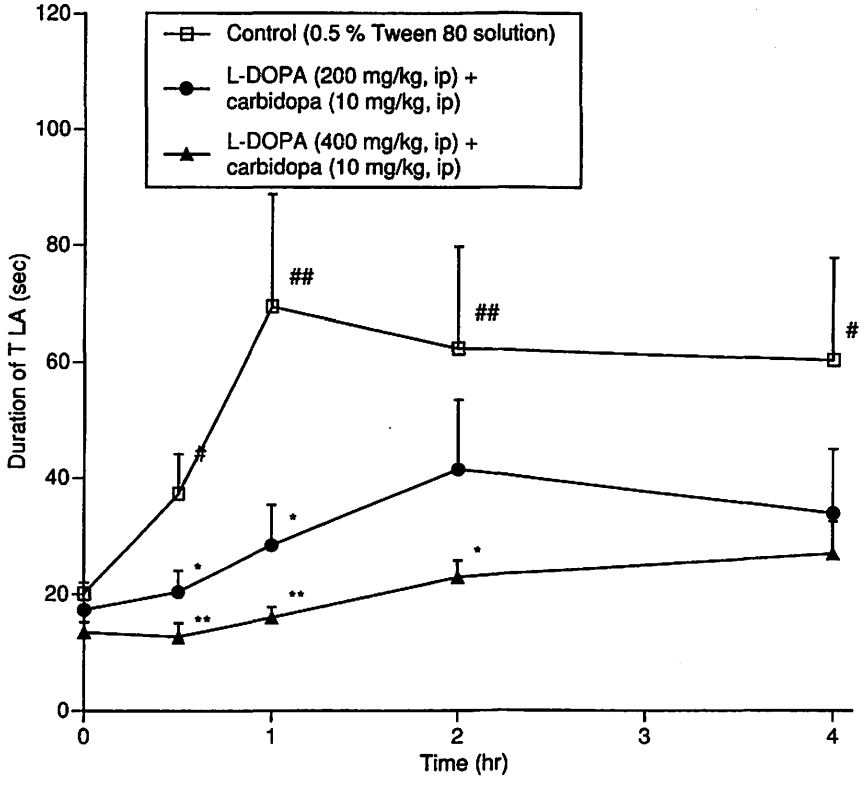

Fig. 7 Effect of L-DOPA + carbidopa on the TLA in haloperidol (0.125 mg/kg, sc)-treated mice. Points show the means ± SEM of 7 - 8 mice. $*p < 0.05$, $**p < 0.01$ vs. the corresponding value in vehicle group and $\#p < 0.05$, $\#\#p < 0.01$ vs. 0 hr in vehicle group (Williams multiple-range test).

III. 5. [^{18}F]fluorodiacylglycerol: The new radiopharmaceutical for PET imaging of intracellular signal transduction

Nagata S., Yamaguchi K., Takahashi T., Iwata R., Ido T.

Cyclotron and Radioisotope Center, Tohoku University

Introduction

Positron emission tomography (PET) has an advantage of studying the molecular actions. 2-Deoxy-2'-[^{18}F]fluoro-D-glucose[1] has made it to examine cellular metabolism in neurons. Further positron emitting ligands have assayed the binding capacity of many kinds of neurotransmitter receptors *in vivo*[2-4]. To give more appropriate information in neural systems, we have developed the fundamental concept for visualizing intracellular signal transduction in the brain using PET.

Diacylglycerol plays an important role in the neural function of postsynapses as a second messenger[5-10] produced from the phosphatidylinositide turnover (fast response) and the phosphatidylcholine or phosphatidylethanolamine (PE) turnover (slow response)[11,12]. For PET imaging of slow response which is concerned with memory or learning in a brain[13] and differentiation or proliferation in a cell[11,12,14-16], 1-(8-[^{18}F]fluorooctanoyl)-2-palmitoylglycerol ([^{18}F]FDAG) is a recently developed radiopharmaceutical under research on intracellular signal transduction. BBB permeability is generally an important factor for delivering a drug to the brain. Accordingly we have investigated the effects of solubilizers on BBB permeability of this labeled compound. Brain uptake was measured for several solubilizers (human serum albumin, Tween 20, Tween 80, positive charged liposome, weekly negative charged liposome, and negative charged liposome). Accumulation of the [^{18}F]FDAG in tumor was also investigated to apply as a radiopharmaceutical for cancer diagnosis.

Materials and Methods

The synthesis of [^{18}F]FDAG was carried out by esterification of 2-monopalmitoylglycerol with 8-[^{18}F]fluorooctanoyl chloride as previously report[17]. The mass spectra, NMR and HPLC of this material were identical to authentic material. Overall radiochemical yield was 21-34% (EOB), with radiochemical purity over 99% and total synthesis time was 122-141 min. Specific activity was 3.7-18.5 GBq/μmol (EOS).

The preparation of [^{18}F]FDAG encapsuled within liposome is shown in Fig. 1.

Yield was 80-85%, and preparative time was 19-26 min. Liposome size was 48-123 nm.

Seven-week old male Wistar rats were injected intravenously into the lateral tail vein with 1.85 MBq of [^{18}F]FDAG suspended with the solubilizers and killed by cervical spine dislocation 30 min later. Tissue samples were excised and weighed, and ^{18}F radioactivity was expressed as the differential absorption ratio (DAR).

Seven-week old male Wistar rats were injected into the lateral tail vein with 37 MBq of [^{18}F]FDAG suspended the solubilizers and killed 30 min later. The blood, liver, cerebral cortex and hippocampus were rapidly removed. Metabolites of [^{18}F]FDAG extracted according to the method of Folch[18] were analyzed on TLC plates (Merck) according to the method of Yamaguchi.

A three-week old Wistar rat was transplanted with 0.02 mL suspension of C6 glioma cells. The tracer experiment was performed three weeks after tumor transplantation. The rat bearing C6 glioma tumor was injected into the lateral tail vein with 37 MBq of the [^{18}F]FDAG encapsuled within the negative charged liposome and killed by decapitation 30 min later. The rapidly removed frozen brain was fixed on a mount and was sliced 20 μm thickness by cryotome. The sample was contacted to an imaging plate and the autoradiogram was reconstructed with a BASS 3000 system (Fuji film, Japan).

Results and Discussion

The results of [^{18}F]FDAG suspended with the solubilizers uptakes in various tissues of rats at 30 min after intravenous injection is shown in Fig. 2. The negative charged liposome containing [^{18}F]FDAG gave the highest uptake with DAR of 0.50±0.03 in the brain.

The metabolic distribution of [^{18}F]FDAG suspended the solubilizers in several tissues of rats at 30 min after intravenous injection is depicted in Fig. 3. [^{18}F]FDAG suspended with any solubilizer was mainly metabolized into PE in every tissue.

The radioautogram of the rat brain with C6 glioma at 30 min after intravenous injection is shown in Fig. 4. [^{18}F]FDAG accumulated in the C6 glioma 2.1-2.7 times higher than the contralateral region in the brain. However, this mechanism is not clear yet although cellular proliferation signal transduction might be suggested for this accumulation in tumor.

PE turnover has been reported to be promoted by some growth factors[11,12,14-16] and to control cellular proliferation or differentiation. We have found that the [^{18}F]FDAG encapsuled within the negative charged liposome was mainly metabolized into PE and accumulated in C6 glioma. This labeled compound is expected as a promising radiopharmaceutical for not only brain function studies but also cancer diagnosis and myocardial infarction prognosis.

References

1) Ido T., et al., J. Label. Compd. Radiopharm. **175** (1978) 14.
2) Comer D., et al., Nature **280** (1979) 329.
3) Wagner Jr. H. N., et al., Science **221** (1983) 1264.
4) Garnett E. S., Firnau G. and Nahmias C. Nature **305** (1983) 137.
5) West J. W., et al., Science **254** (1991) 866.
6) Nishizuka Y. Science **233** (1986) 305.
7) Takuwa Y., et al., J. Cereb. Blood Flow Metab. **13** (1993) 409.
8) Berry N. and Nishizuka Y. Eur. J. Biochem. **189** (1990) 205.
9) Nishizuka Y. Nature **308** (1984) 693.
10) Nishizuka Y. Nature **334** (1988) 661.
11) Wright T. M., et al., J. Biol. Chem. **263** (1988) 9374.
12) Ha K. S. and Exton J. H. J. Biol. Chem. **268** (1993) 10534.
13) Rusted J. M. and Warburton D. M. Psychopharmacol. **96** (1988) 145.
14) Kiss Z. and Anderson W. B. J. Biol. Chem. **264** (1989) 1483.
15) Kiss Z., Crilly K. S. and Anderson H. W. FEBS **336** (1993) 115.
16) Larrodera P., et al., Cell **61** (1990) 1113.
17) Takahashi T., et al., CYRIC Annual Report **1991** (1991) 119.
18) Folch J.,et al., J. Biol. Chem. **191** (1951) 833.

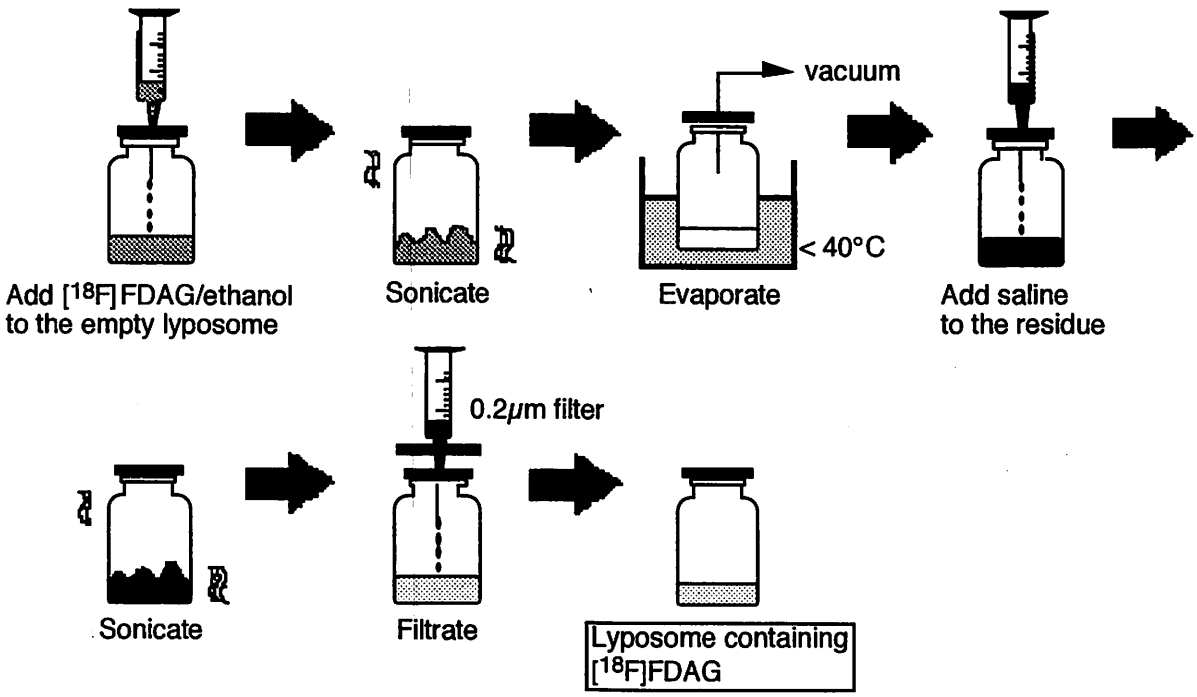

Fig. 1. Preparation of 1-(8-[^{18}F]fluorooctanoyl)-2-palmitoylglycerol encapsuled within liposome.

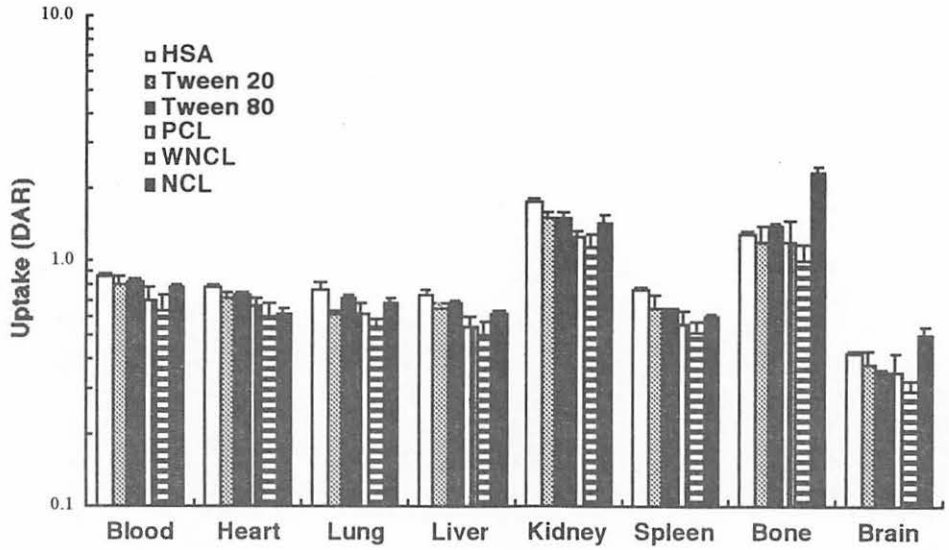

Fig. 2. Biodistribution of 1-(8-[^{18}F]fluorooctanoyl)-2-palmitoylglycerol suspended with several solubilizers in rats at 30 min after injection (i.v.). Values are means ± S.E. (n = 3).

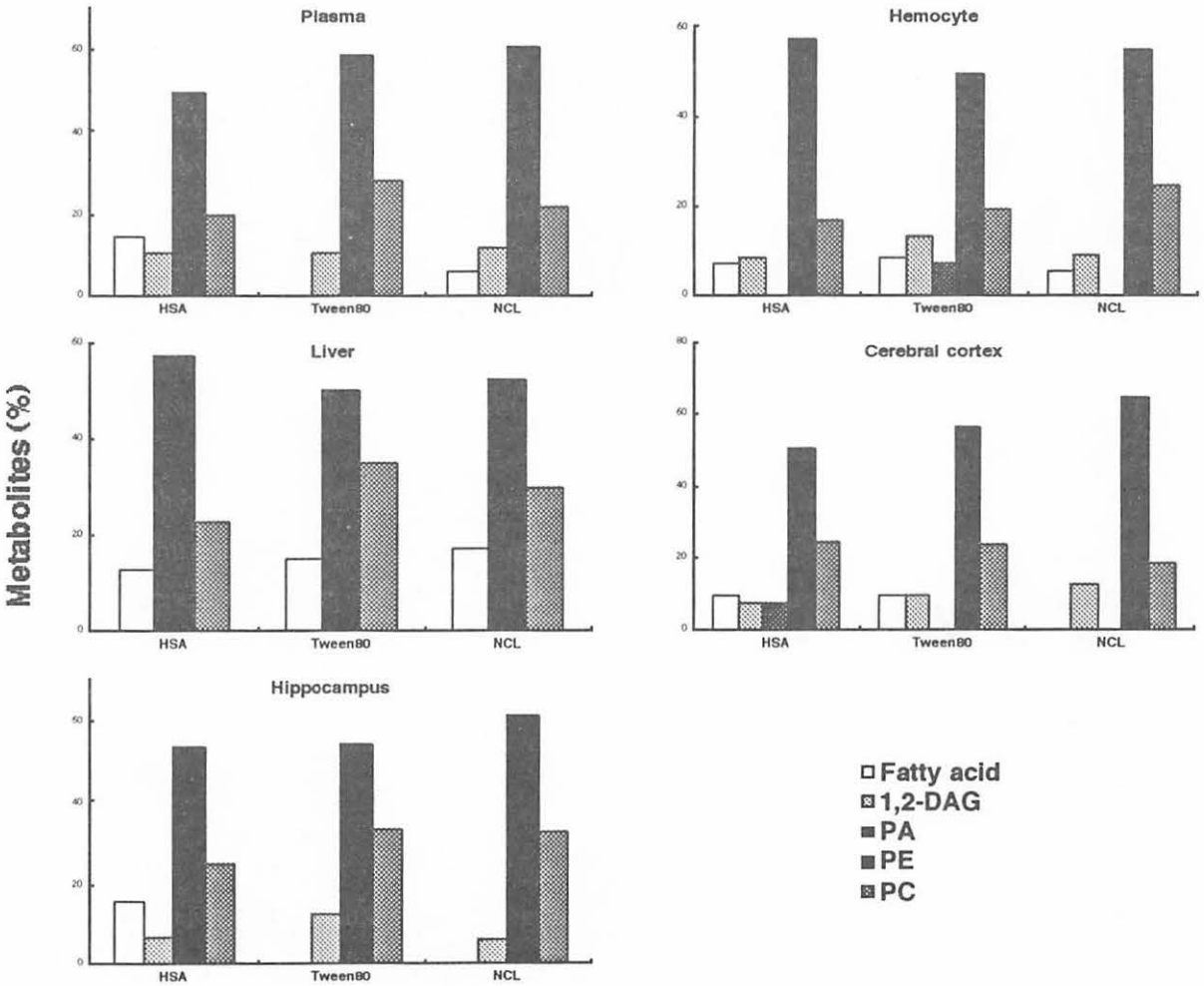

Fig. 3. Metabolic distribution of 1-(8-[^{18}F]fluorooctanoyl)-2-palmitoylglycerol suspended with several solubilizers in rats at 30 min after injection (i.v.).

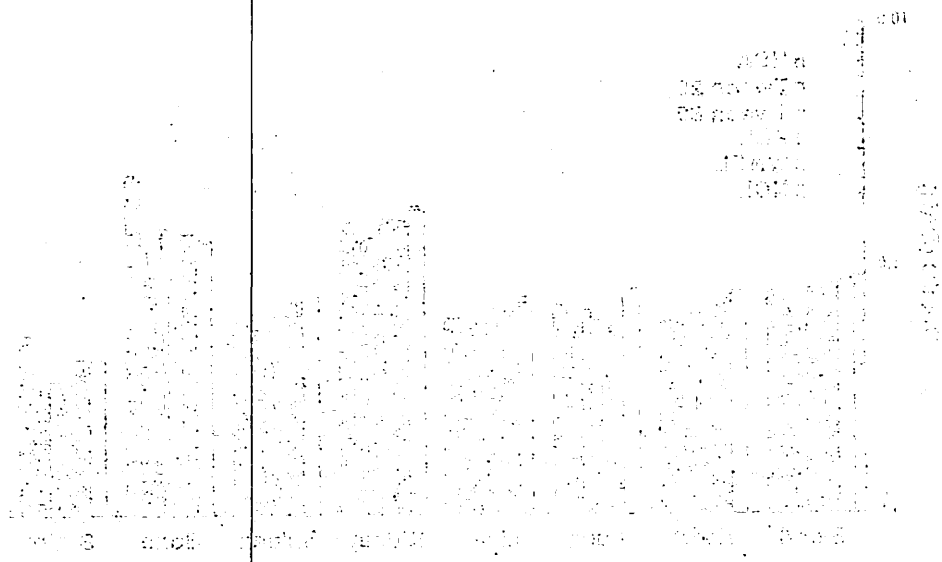

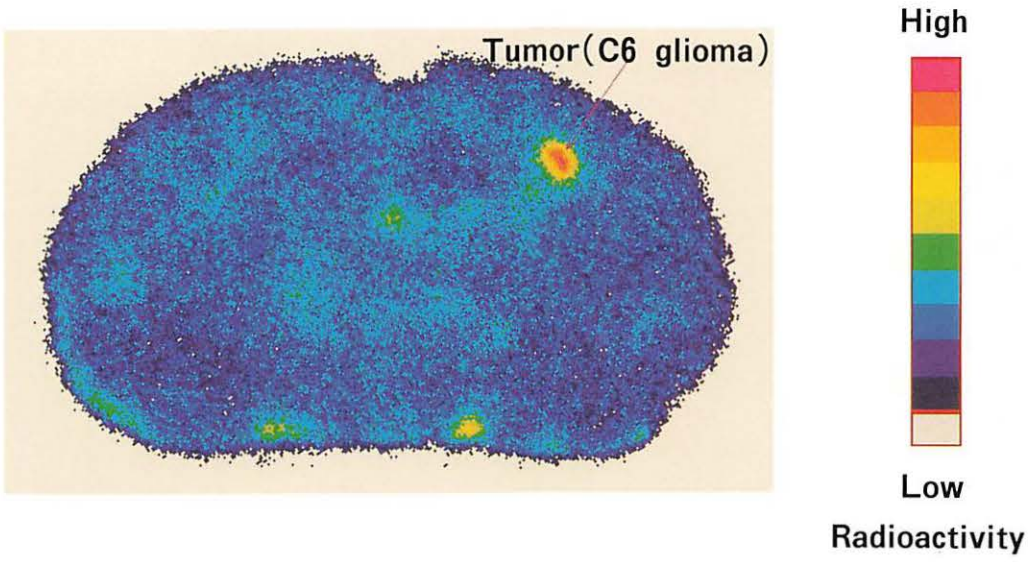

Fig. 4. Autoradiogram of the rat brain with C6 glioma at 30 min after injection (i.v.) of 1-(8-[^{18}F]fluorooctanoyl)-2-palmitoylglycerol.

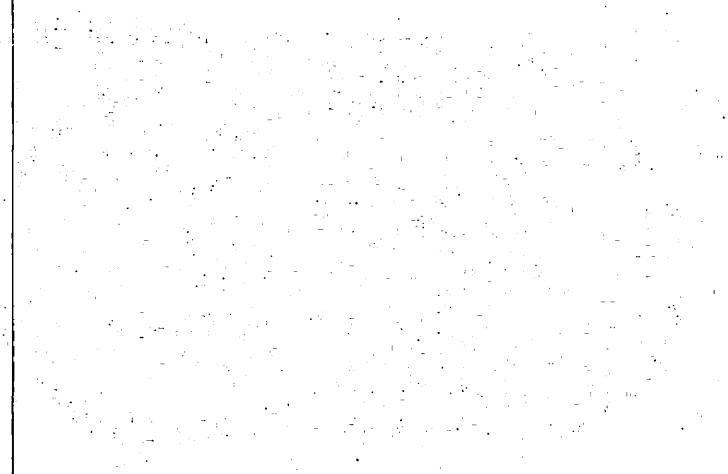

III. 6. Double Tracer Autoradiography Using ^{18}F-fluoromisonidazole

Kubota K., Tada M., Yamada S., Iwata R.***, Sato K.**, Fukuda H., and Ido T.****

Department of Nuclear Medicine and Radiology, Pharmacological Chemistry, Radioisotope Laboratory**, Institute of Development Aging and Cancer Cyclotron Radioisotope Center, Tohoku University****

Introduction

Misonidazole (MISO) and its derivatives have been used as markers of hypoxic tissues[1]. Because hypoxic cells in a tumor form the radiotherapy-resistant component, MISO has been examined as a radio-sensitizer in cancer radiotherapy[2]. Fluorine-18-labeled fluoromisonidazole (FMISO) has been developed[3] and its binding to hypoxic cells has been demonstrated mainly in *vitro* studies[4,5]. Preliminary PET studies of patients with cancer have shown positive imaging of various tumors[6-9], however, the definition of hypoxic tissues in PET images is still unclear. Also the correlation between FMISO uptake and other tumor imaging agent [^{11}C]Methionine (Met) and [^{18}F]Fluorodeoxyglucose (FDG) remain to be evaluated. In order to examine the correlation between intra-tumor distribution of FMISO, FDG and Met, we have performed double tracer macro-autoradiography study.

Materials and methods

The experimental protocol was approved by the Laboratory Animal Care and Use Committee of Tohoku University.

Fluorine-18 fluoromisonidazole (FMISO) was prepared in cyclotron radioisotope center according to the new one-pot synthesis method starting from [^{18}F]fluoride and (2R)-(-)-glycidyltosylate using v-vial, as reported previously[10]. The radiochemical yield was 20%, with a radiochemical purity of > 98%. The total synthesis time was about 80 min. L-[methyl-^{14}C]methionine (Met, specific activity 2.04 GBq/mmol) as a substitute for L-[methyl-^{11}C]methionine, 2deoxy-d-[1-^{14}C]glucose (2DG, specific activity 2.04 GBq/mmol) as substitutes for FDG, was purchased from commercial sources.

A mixture of 111 MBq of FMISO and either 740 kBq of Met or 2DG was injected into each of four rats bearing AH109A tumors, and sacrificed 2 hr later. The time for study after injection (2 hr) was determined in a series of time-course studies. The tumors were dissected and frozen for sectioning as previously described[11]. Briefly, several 5-10 μm thick sections were mounted on clean glass slides, air-dried and placed in direct contact with ARG films for 2 hr to produce FMISO images. Four days later, following the decay of ^{18}F, the same

sections were placed in contact with separate films for 7 days to produce Met. After developing the films, the sections on the slides were fixed, stained with hematoxylin and eosin, and examined under a microscope.

Results and Discussion

Figure 1 showed typical two pairs of double tracer macro ARG of AH109A tumor and each histology. Right panel is FMISO and Met. Left panel is FMISO and 2DG. In the right, high grain density areas with Met showed low grain density with FMISO. High grain density areas with FMISO showed low grain density with Met. There are small overlapping areas in the distribution of FMISO and Met. In the left panel, FMISO showed high grain density in the peripheral rim surrounding the necrosis. 2DG showed similar tendency, and more homogeneous distribution than that of the FMISO. Area of 2DG uptake is larger than that of FMISO. There is a large overlapping area in the distribution of FMISO and 2DG.

FMISO uptake seems to be a marker of hypoxic tissue. ARG of AH109A tumor showed a high FMISO uptake by cancer cells present in the rim surrounding the necrotic area. These cells were probably hypoxic but viable cancer cells. This distribution pattern is consistent with previous *in vivo* studies using [^{14}C]Misonidazole[1,12].

FDG(2DG) uptake is considered as a marker of viable tissues, including proliferating and non-proliferating cancer cells, as shown in *in vitro* [13] and *in vivo* studies[14]. It has been reported that FDG uptake by cancer cells, especially glucose transport, increases under *in vitro* hypoxic conditions[15]. However, in the intact animal, tissue hypoxia is likely to occur as a result of inadequate delivery of oxygen, i.e., reduced blood flow. The reduced blood flow must be associated with reduced delivery of the tracer to the tissue. The reduced delivery of glucose to the hypoxic tumor tissue *in vivo* is probably compensated by elevated tissue extraction which results in a relatively uniform net glucose uptake within a tumor tissue.

Hypoxia itself does not alter Met uptake by cancer cells *in vitro* [16]. However, tracer delivery seems to be an important factor for *in vivo* distribution of Met. Met distribution in tumor tissue is strongly dependent on blood flow as shown in a double tracer autoradiography study using Met and [^{18}F]fluoro-antipyrine[17]. Because of the flow-dependent distribution, Met distribution seems to parallel well-perfused, normoxic, and prolilferative tissue fractions. These characteristics of Met seems to explain the opposite distribution pattern of FMISO and Met.

Acknowledgement

The authors thank Mr. Sugawara for photography, and Roko Kubota, PhD for discussion. This study was supported by grants-in-aid (06454320, 08266205, 09470195) from the Ministry of Education, Science and Culture, Japan.

References

1) Chapman J. D., Franko A. J., Sharplin J., Br J Cancer **43** (1981) 546.
2) Hall E. J., Radiobiology for the radiologists, 4th ed. Philadelphia:JB Lippincott (1994).
3) Jerabek P. A., Patrick T. B., Kilbourn M. R., et al., Appl Radiat Isot **37** (1986) 599.
4) Jerabek P. A., Patrick T. B., Kilbourn M. R., et al., Appl Radiat Isot **37** (1986) 599.
5) Rasey J. S., Nelson N. J., Chin L, et al., Radiat Res **122** (1990) 301.
6) Rasey J. S., Koh W. J., Grierson JR, et al., Int J Radiat Oncol Biol Phys **17** (1989) 985.
7) Koh W. J., Rasey J. S., Evans M. L., et al., Int J Radiat Oncol Biol Phys **22** (1991) 199.
8) Valk P. E., Mathis C. A., Prados M. D., et al., J Nucl Med **33** (1992) 2133.
9) Yeh S. H., Liu R. S., Wu L. C., et al., Eur J Nucl Med **23** (1996) 1378.
10) Tada M., Iwata R., Sugiyama H., et al., J Labelled Compds Radiopharm **38** (1996) 771.
11) Kubota R., Yamada S., Kubota K., et al., J Nucl Med **33** (1992) 1972.
12) Blasberg R., Horowits M., Strong J., et al., Cancer Res **45** (1985) 1692.
13) Higashi K., Clavo A. C., Wahl R. L., J Nucl Med **34** (1993) 414.
14) Kubota R., Kubota K., Yamada S., et al., J Nucl Med **35** (1994) 1067.
15) Clavo A. C., Brown R. S., Wahl R. L. J Nucl Med **36** (1995) 1625.
16) Clavo A. C., Wahl R. L. J Nucl Med **37** (1996) 502.
17) Abe Y., Matsuzawa T. Y., Itoh M., et al., Eur J Nucl Med **14** (1988) 388.

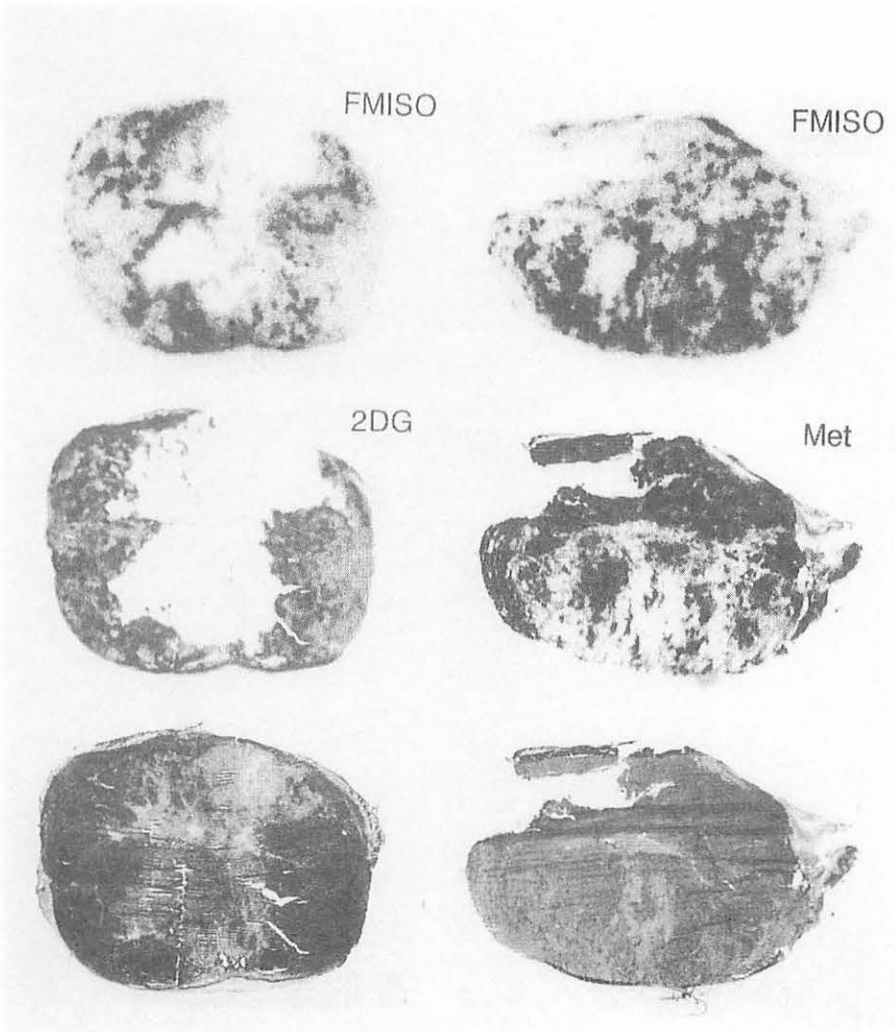

Fig. 1. Typical two pairs of double tracer macro ARG of AH109A tumor with histological sections stained with HE. *Right panel:* FMISO (top), Met (middle) and histology (bottom). *Left panel:* FMISO (top), 2DG (middle) and histology (bottom).

III. 7. ^{99m}Tc-MIBI and PET Tracers Uptake by MDR Tumor

*Kubota K., Yamada S., Fukuda H., and Ido T. **

Department of Nuclear Medicine and Radiology Institute for Development, Aging and Cancer, Tohoku University
*Cyclotoron and Radioisotope Center, Tohoku University**

Introduction

Cellular accumulation of ^{99m}Tc-methoxy isobutyl isonitrile (MIBI) has been shown to correlate with the level of P-glycoprotein (P-gp) expression[1]. P-gp is an energy-dependent membrane transporter protein that is responsible for the development of multi-drug resistance (MDR) of tumors to a broad spectrum of cytotoxic drugs. It has been shown that ^{99m}Tc MIBI is a Pgp transport substrate. Evaluation of Pgp function using ^{99m}Tc MIBI may open a new possibility for the prediction of efficacy of cancer chemotherapy.

Recently, positron emission tomography (PET) imaging of tumor using tracers of metabolic substrate, especially ^{18}Ffluorodeoxyglucose (FDG), has demonstrated excellent clinical usefulness in oncology. FDG uptake by tumor representing elevated glucose metabolism of malignant cell is correlated to the grade of malignancy, to the growth rate, and to the cell density. Other PET tracers for tumor imaging ^{11}C-methionine (Met), ^{11}Cthymidine (Thd) representing amino acid metabolism and nucleic acid metabolism respectively, have been more correlated to the proliferation of cancer cells. However, correlation of these metabolic tracers and the P-gp function has never been studied. In this study, FDG, Met, Thd and MIBI uptake were compared with the MDR tumor and the control tumor.

Materials and methods

Mouse leukemia cell P388 and vincristine-resistant subline P388VCR are kindly gifted from Japanese Foundation for Cancer Research. P388VCR is well known muti-drug-resistant subline[2]. Six-week old female CDF1 mice were implanted by subcutaneous injection with 0.1ml suspension of 10^7 P388 cells in the right thigh regions and P388VCR cells in the left thigh. These cell lines are used for tumor innoculation as ascites after i.p injection of fresh recovered frozen stocks. Tracer experiments were performed 9 days after tumors transplantation following 8 hr of fasting. A dose of 28 μCi of ^{18}Ffluorodeoxyglucose (FDG), 76 μCi of ^{99m}TcMIBI, 1.33 μCi of ^{14}C-L-methionine (Met), and 1.67 μCi of ^{3}H-thymidine (Thd) were mixed in 0.25ml of saline and injected intravenously into the lateral tail vein in each of 20 mice. FDG was synthesized at CYRIC, ^{99m}TcMIBI was obtained from Daiichi

Radioisotope Lab. LTD, Met and Thd were from Amersham International plc. The mice were sacrificed 5 (n=4), 30 (n=4), 60 (n=6), and 120 (n=6) min later. Tissue samples were excised and weighted and ^{18}F radioactivity was measured using an automated gamma-scintillation counter with the window of 450-600keV just after sampling. There was no spill over of ^{99m}Tc radioactivity to the window of ^{18}F. And 27hrs later, when ^{18}F was decayed to 0.003%, ^{99m}TcMIBI was measured with the window of 70-180keV. Contamination of ^{18}F radioactivity to ^{99m}Tc window at this time was less than 0.3%. One month later, after the decay of ^{99m}Tc, tissue samples were processed and radioactivity of ^{14}C and ^{3}H was measured with liquid scintillation counter as described previously.

Results and discussion

Figure 1 showed tumor uptake of ^{99m}TcMIBI by P388 and P388VCR tumors. P388VCR showed lower uptake and faster clearance of ^{99m}TcMIBI than that of P388. It suggested that ^{99m}TcMIBI is excreted rapidly through P-glycoprotein from solid tumors of P388VCR, while from P388 tumor of without P-gp, clearance of ^{99m}TcMIBI becomes slower. Figure 2 showed completely different results with PET tracers. FDG, Met, and Thd all showed higher uptake by P388VCR than that by P388. P388VCR tumors grew faster than the P388, and all these metabolic tracers seem to represent growth rate rather than the presence of P-gp. FDG uptake by both tumors became highest among these three metabolic tracers. Compared to the tumors uptake of these three metabolic tracers, tumor uptake of ^{99m}TcMIBI was very low. ^{99m}TcMIBI may be useful for the prediction of multi-drug resistance of tumor[3,4], while our data suggested that value of ^{99m}TcMIBI for the tumor detection seems to be very limited compared to these three metabolic tracers.

Acknowledgement

This study was supported by Grants-in-aid for cancer research (08266205) from the Ministry of Education, Science, Sports and Culture, Japan.

References

1) Piwinica-Worms D., Chiu M. L., Buding M., et al., Cancer Res. **53** (1993) 977.
2) Tsuruo T., Iida H., Tsukagoshi S., et al., Cancer Res. **41** (1981) 1967.
3) Moretti J. L., Caglar M., Duran-Cordobes M., et al., Eur J Nucl Med **22** (1995) 97.
4) Vecchio S. D., Ciarmiello, A., Potena M. I., et al., Eur J Nucl Med **24** (1997) 150.

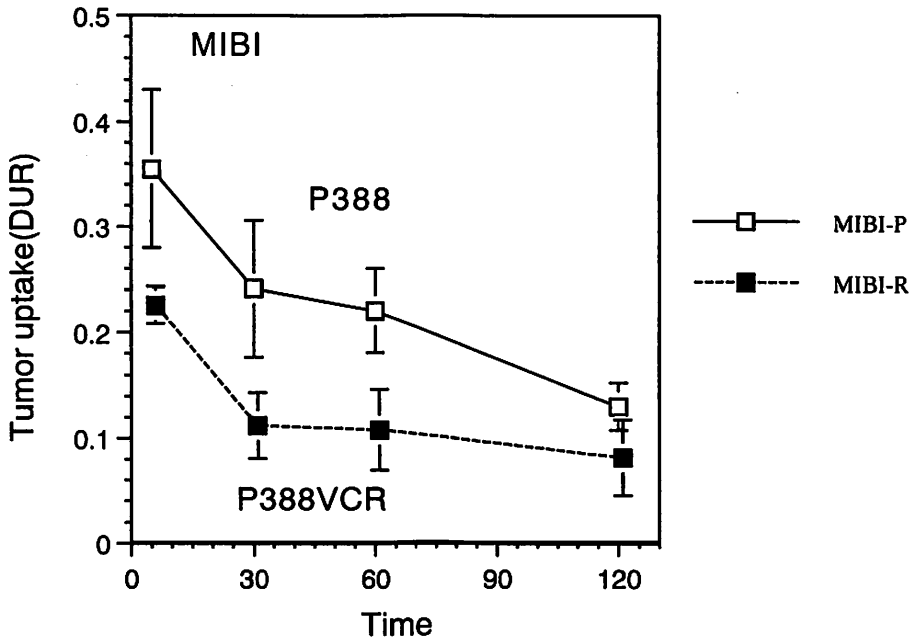

Fig. 1. Time course tumor uptake of ^{99m}TcMIBI. Tumor uptake was expressed as differential uptake ratio (DUR). P388VCR is P-gp positive multi drug resistant cell line. P388 is the control cell line.

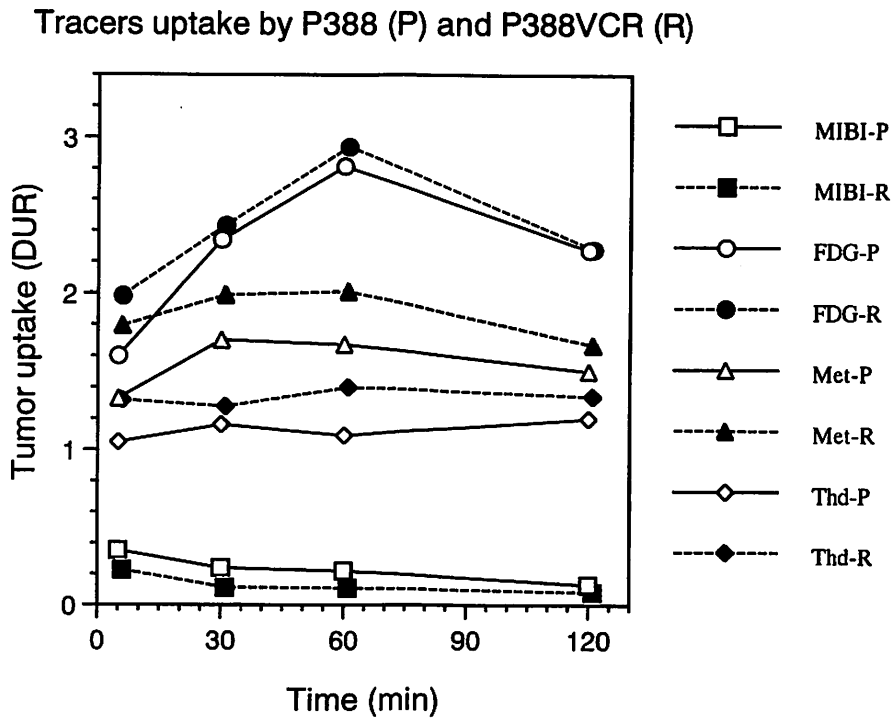

Fig. 2. Time course tumor uptake of FDG, Met, Thd, and ^{99m}TcMIBI. Note the difference of the scale of the ordinate from figure 1. P-gp positive multi drug resistant cell line P388VCR grew faster than that of P388.

III. 8. The Influence of General Anesthesia on Brain Distribution and Kinetics of [^{11}C]Methamphetamine in Monkey

Mizugaki M., Nakamura H., Hishinuma T., Tomioka Y., Ishiwata S., Ido T., Iwata R.*, Funaki Y.*, Itoh M.*, Higuti M.*, Okamura N.*, Fujiwara T.*, Sato M.**, Shindo K.** and Yoshida S.***

Department of Pharmaceutical Sciences, Tohoku University Hospital
*Cyclotron and Radioisotope Center,Tohoku University**
*Department of Psychiatry, Tohoku University School of Medicine***

Introduction

The subchronic administration of methamphetamine (MAP) or amphetamine (AMP) to experimental animals produces progressive and enduring augmentation of hyper locomotion and stereotyped behavior[1,2]. The precise neurochemical mechanism underlying this phenomenon, referred to as behavioral sensitization or reverse tolerance, is not completely understood. Although various mechanisms have been proposed to explain the expression of MAP- or AMP-induced behavioral sensitization, little attention has been paid to the pharmacokinetic change. We have previously studied the pharmacokinetic change of MAP in the brain following repeated MAP administration and reported the significant increase in [^{11}C]MAP uptake in the MAP-sensitized mouse brain[3] and [^{14}C]MAP uptake in the MAP-sensitized rat brain[4]. In addition, we reported that the maximum accumulation level of [^{11}C]MAP in the MAP-sensitized dog brain was 1.4 times higher than that in the control[5]. In order to confirm these facts in detail, we investigated positron emission tomographic (PET) study using rhesus monkeys and found anesthetics changed kinetics of [^{11}C]MAP in monkey brain. This effect of anesthesia is an important problem of the MAP-kinetic study. We report here an investigation of kinetics of [^{11}C]MAP in monkey brain under the different general anesthesia (halothane anesthesia and pentobarbital anesthesia).

Materials and Methods

SYNTHESIS OF [^{11}C]MAP

The synthesis of [^{11}C]MAP was carried out by modifying the on-line [^{11}C]methylation method[6] as previously reported[7]. The mass spectra, HPLC and TLC of this material were identical to authentic material. The specific activity was about 48.1

GBq/μmol at the time of supply. The radiochemical purity of [^{11}C]MAP was determined to be more than 99 %.

PET STUDY IN MONKEY

Four experiments were performed on two male rhesus monkeys weighing 5.8 and 7.5 kg. Monkeys were initially anesthetized with ketamine (10 mg/kg, i.m.). In case of intravenous anesthesia, they were maintained under pentobarbital (25 mg/kg) anesthesia. In case of inhalation anesthesia, they were maintained under halothane (0.5-1.0 %, H_2O 2.5 L/min and O_2 2.5 L/min) anesthesia. Catheters were inserted into the femoral artery for blood sampling and into the brachial vein for administration of [^{11}C]MAP. Vital signs (blood pressure, pulse rate, blood pH, pO_2, pCO_2 and body temperature), monitored and recorded throughout the PET study, were kept within a physiological range. After an intravenous injection of [^{11}C]MAP (159-218 MBq) into the animal, dynamic scan was carried out parallel to the orbitomeatal (OM) line using PET scanner (PT931, CIT Inc., Knoxville USA at the Cyclotron and Radioisotope Center, Tohoku University, Sendai, Japan) for 60 min. The following regions of interest (ROI) were selected : parietal cortex, occipital cortex, temporal cortex, frontal cortex, striatum, thalamus and cerebellum. Tissue concentration of [^{11}C]MAP was measured using a ROI program. These animal experiments were approved by the Tohoku University Animal Care Committee.

Results and Discussion

Figure 1 shows the influence of pentobarbital and halothane anesthesia on brain distribution and kinetics of [^{11}C]MAP in two monkeys (A and B). The brain uptake of [^{11}C]MAP in the monkey anesthetized with halothane was more rapid than that with pentobarbital. Moreover, the maximal level of [^{11}C]MAP accumulation under halothane anesthesia was significantly higher than that under pentobarbital anesthesia. Thus it becomes clear that pharmacokinetic changes of [^{11}C]MAP take place under the different anesthesia.

In general, all volatile anesthetics are considered potent cerebral vasodilators and to increase cerebral blood flow (CFB). In recent human study using the transcranial Doppler, the CBF increased by 23 % with inhalation of halothane at 1.0 minimum alveolar concentration (MAC)[8]. On the other hand, it was reported that pentobarbital anesthesia (40 mg/kg) resulted in a 50 % decrease in CFB of the rat brain[9]. Therefore, we considered that the variations of kinetics of [^{11}C]MAP might have been caused by the changes of CBF produced by anesthetics. However, we cannot definitely determine this reason, because we did not directly measure CBF and the depth of anesthesia is unclear. Further studies are necessary to determine the influence of general anesthesia.

Acknowledgments

We are grateful to the PET staffs of the Cyclotron and Radioisotope Center, Tohoku University, for their cooperation. A part of this research was supported by a scientific research fund from the Ministry of Welfare of the Japanese Government.

References

1) Seagal D. S. and Mandell A. J., Pharmacol. Biochem. Behav. **2** (1974) 249.
2) Nishikawa T., Mataga N., Takashima M., et al., Eur. J. Pharmacol. **88** (1983) 190.
3) Mizugaki M., Hishinuma T., Nakamura H., et al., Nucl. Med. Biol. **20** (1993) 487.
4) Numachi Y., Yoshida S., Inosaka T., et al., Ann. N. Y. Acad. Sci. **654** (1992) 153.
5) Mizugaki M., Nakamura H., Hishinuma T., et al., Nucl. Med. Biol. **22** (1995) 803.
6) Iwata R., Pasucali C., Yuasa M., et al., Appl. Radiat. Isot. **43** (1992) 1083.
7) Mizugaki M., Nakamura H., Hishinuma T., et al., CYRIC Annual Report 1993 (1994) 93.
8) Matsumoto S., Nishii T., Arai T., et al., J. Clin. Anesth. (Jpn.) **19** (1995) 1134.
9) Gjedde A. and Rasmussen M., J. Neurochem. **35** (1980) 1382.

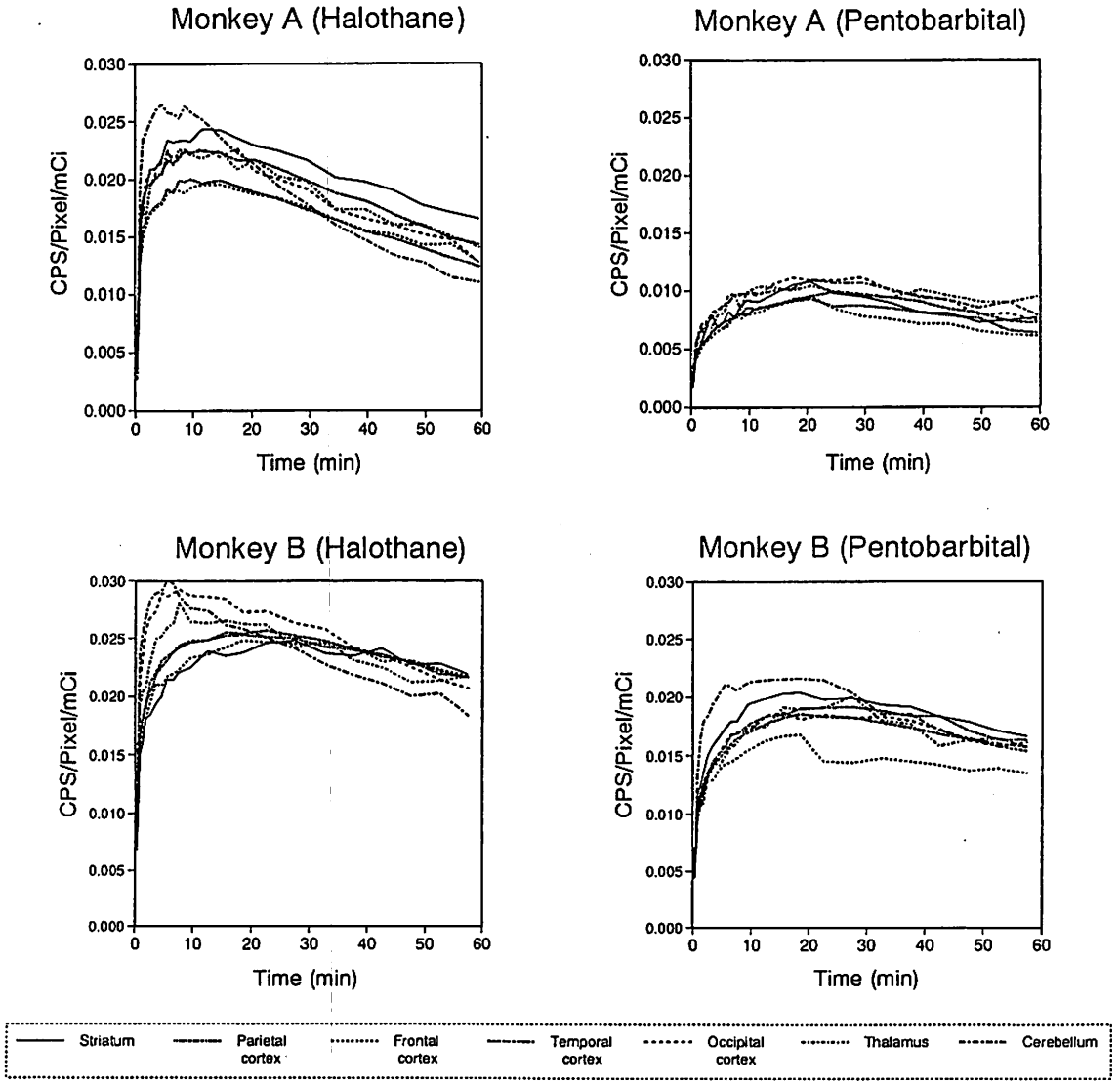

Fig. 1 The influence of general anesthesia on brain distribution and kinetics of [^{11}C]methamphetamine in monkey.

IV. BIOLOGY AND MEDICINE (Clinical)

IV. 1. Radiation Absorbed Dose Estimation of 2-[F-18]Fluoro-2-Deoxy-D-Glucose Using Whole Body PET and Measured Organ Volume from MRI

Deloar H. M., Shidahara M., Fujiwara T., Nakamura T., Miyake M., Watanuki S., Watabe H, Narita M., and Itoh M.

Cyclotron and Radioisotope Center, Tohoku University

Introduction

To assess the radiation risk of administered radiopharmaceutical in PET study, two important parts are concerned; one is the total cumulated radioactivity in an organ and another is the absorbed dose estimation in the organ[1]. In both cases biokinetic information with human organ volumes and masses are essential. To estimate the cumulated activity and internal absorbed dose, the organ volumes from the MIRD phantom[2] for the Caucasian reference men and an another phantom for the Asian/Japanese reference men[3] are usually used[4]. Whatever the phantom is, in practice the deviation of organ size from the phantom may introduce an error in the cumulated activity and in the absorbed dose as well. Hence by using actual organ volumes of the individual in the whole body PET, a quantitative analysis of the organ cumulated activity and absorbed dose may give more accurate results than those with the MIRD phantom[2] and the Japanese reference man[3].

The purpose of this study was to establish an accurate measurement method of cumulated activity and absorbed dose of organs by using the whole body PET and MRI for the intake of 2-[F-18]Fluoro-2-Deoxy-D-Glucose (FDG). The following measurements has been done in this study:

1. Measurement of organ volumes as well as masses (source and target organs) of the individual by using whole body MR images.
2. Measurement of activity concentration of all source organs from the whole body PET image and estimation of total and cumulated activities of the source organs for the measured organ volumes.
3. Absorbed dose estimates of the individuals by using the measured target organ masses.
4. A comparison of the cumulated activities and internal absorbed doses by using individual organ information (volumes and masses) with MIRD phantom and Japanese reference man[2,3,4].

Materials and methods

The study consisted of 6 normal volunteers. All subjects gave their written consent and the study protocol was approved by the Ethics Committee for Clinical Research of Tohoku University. On each volunteer MRI and PET scans were performed[5] to measure the organ volumes and organ activity concentration.

The PET studies were done with a whole body PET scanner at CYRIC, Tohoku University.

The polynomial ROIs of each source organ on the transaxial PET images were defined by referring the MR image and the average activity concentration of an organ was measured[5].

All the data were corrected for physical decay. Cumulated activities of the source organs were calculated from the time activity curves[5]. To investigate the discrepancies of actual individual results against the phantom results, cumulated activities were also calculated with the MIRD phantom[2] and the Japanese reference man[3] by the following equation:

$$\tilde{A}_P = \tilde{A}_{MR} \times \frac{V_P}{V_{MR}} \qquad (1)$$

where $\tilde{A}_{MR}$ is the cumulated activity of the source organs using the measured individual volume V_{MR}, the cumulated activity $\tilde{A}_P$ is for the organ volume V_P, obtained either from the MIRD phantom (2) or from the Japanese reference man[3].

Absorbed Dose and Effective Dose Equivalent Calculations:

In the MIRD method (1) the mean absorbed dose to the k-th target organ is defined as:

$$D(r_k) = \sum_h \tilde{A}_h \, S(r_k \leftarrow r_h) \qquad (2)$$

where $S(r_k \leftarrow r_h)$ is the absorbed dose in the k-th target organ per unit cumulated activity of the h-th source organ, i.e. S-value, and $\tilde{A}_h$ the cumulated activity of the h-th source organ.

The absorbed doses in the 27 target organs were calculated for the three different sets of cumulated activities with the IDES code[6] based on the MIRD method[1]. A transformation method[7] was applied to the MIRD S-Tables[2] to obtain the S values of the measured individual organ weights and organ weights for the Japanese reference man[3]. In the case of major airway and nasal cavity wall, the S-values calculated by Deloar et al.[8] were used.

The effective dose equivalent of the target organs were calculated from the following relations:

$$H_E = \sum_h W_i H_i = \sum_h W_i D_i \quad Q = \sum_h W_i D_i \qquad (3)$$

where H_i is the dose equivalent of the i-th target organ, D_i is the absorbed dose of i-th target organ, Q is the quality factor (=1 for b and g-rays) and w_i tissue weighting factor given in ICRP 60[9].

Results and Discussion

The organs having the weighting factors according to the ICRP 60[9], were considered as the source organs and the volume of those organs were measured by MRI. The organ volumes of each individual were reported[5] with the organ volumes of MIRD phantom[10]. To obtain target organ masses from their volumes, the corresponding densities of those tissues in the MIRD phantom[10] were used[5].

The cumulated activities of 18 source organs for three sets of organ volumes were calculated[5]. Those mean cumulated activities are shown in Table 1 with the standard deviations and compared with the other result[4]. Among the cumulated activities of the source organs in our study, the brain, bladder and liver showed the highest values in this descending order. The results except for bladder, lung, liver and pancreas showed good agreement among these three calculations. The discrepancies of the results for those organs are due to the differences of organ volumes in between measurements and in the MIRD phantom and Japanese reference man[2,3]. The cumulated activity of the bladder for measured volume is very close to the result of Mejia et al.[4], but differences arise in phantom studies[2,3] due to the assumption of constant bladder volume. The cumulated activity of the kidney in this study was around 7 times higher than the result of Mejia et al.[4]. This large values with wide dispersion may be due to the difference of the renal function of the individuals and in this study all the subjects were relatively younger (average age 30 yrs) than the Mejia et al.[4]. The cumulated activities of the liver and pancreas are very close to those of Mejia et al[4], but those in the lung shows 4 times difference. The brain cumulated activities under this work are consistent among these three cases but 4 times differ from the result of Mejia et al. [4]. The heart cumulated activity is around a factor 2 times lower than the result of Mejia et al. [4]. In the remainder of the body, variation of cumulated activities among three cases is due to the difference of organ sizes in individual measurement and two phantoms[2,3]. The cumulated activity in the remainder of the body calculated by Mejia et al. [4], 1964 kBq-h/MBq, which is around 14% higher than this study. The reason is, in the study of Mejia et al. only seven source organs are considered and other organs were the part of the remainder body.

The mean absorbed doses of 27 target organs with their standard deviations for three different types of cumulated activities are summarized in Table 2 and compared with the other result[4].

The mean absorbed doses in Table 2 show good agreement among three cases (for individual, MIRD phantom and Japanese reference man) except the doses of bladder wall, stomach wall, colon (LLI+ULI) and testes due to the difference of volumes, which affected the cumulated activities of those organs. Although the mean effective dose equivalent calculated from Eq. 3, for the measured organ volumes of average body weight 64 kg and the MIRD phantom of 70 kg body weight are almost equal together, the effective dose equivalent for the Japanese reference man of 60 kg is 25% lower than the former two results. In the comparative study with other results[4] in Table 2, the absorbed doses in bladder for measured

mass and MIRD phantom[2] are 4 times and those in lung and brain are around 2.5 times higher than other results[4].

In conclusion, a coupled use of the whole body PET for the organ activity concentration measurement and MRI for the organ volume measurement can greatly improve the accuracy of the cumulated activities and absorbed doses of the organs.

References

1) Loevinger R.et al. The Society of Nuclear Medicine, Inc., New York. 1988.
2) Cristy M. et al. OAK RIDGE NATIONAL LABORATORY, Oak Ridge, Tennessee 37831.
3) Tanaka G. Nippon Act Radiol 1988; 48: 509-513.
4) Mejia AA. et al. J Nucl Med 1991; 32: 699-709.
5) Deloar HM et al. submitted to J. Nucl. Med.
6) Hongo S. et al. Japan Health Physics Society; 1992:17-27.
7) Yamaguchi Y. Phys Med Bio 1975; 20: 593-601.
8) Deloar HM. et al. J Nucl Med, Schedule. 1997; July.
9) Annals of the ICRP, ICRP publication 60, , Vol. 21 No. 1-3; 1991.

Table 1. Comparison of Average Cumulated Activity (kBq-h/MBq) (mean ± standard deviation) of the Source Organs Using the organ volumes from the Measurment (MRI), MIRD Phantom (2), Japanees reference man (3) and Other Result.

Source Organs	This Work			
	Average Cumulated Activity Using the Measured Volume by MRI	Average Cumulated Activity Using MIRD Phantom (2)	Average Cumulated Activity Using the Organs Volume of the Japaness reference man (3)	Cumulated Activity by Mejia et.al. (4)
Adrenal	1.1 ± 0.6	1.4 ± 0.6	1.1 ± 0.5	
Major Airway (Wall)	4.2 ± 1.6	5.3 ± 3.0	4.9 ± 2.3	
Nasal Cavity (Wall)	3.7 ± 1.6	5.1 ± 3.5	4.3 ± 2.8	
Bladder Content	176.4 ± 122.2	262.5 ± 228.9	86.7 ± 76.8	162
Stomach Content	15.8 ± 9.1	11.7 ± 6.2	6.4 ± 3.2	
Small Intestine	52.1 ± 30.0	68.8 ± 41.4	55.8 ± 34.2	
ULI Content	19.0 ± 11.9	14.6 ± 6.9	13.0 ± 6.2	
LLI Content	13.3 ± 5.4	10.3 ± 5.7	9.2 ± 5.2	
Kidney	57.5 ± 26.0	58.2 ± 26.1	61.8 ± 20.8	8.1
Liver	132.4 ± 25.1	189.0 ± 48.0	158.3 ± 40.2	112
Left Lung	44.2 ± 13.6	70.8 ± 18.3	71.5 ± 18.9	*23.2
Right Lung	45.8 ± 12.4	54.2 ± 7.5	63.5 ± 10.1	
Pancreas	6.2 ± 3.3	15.3 ± 19.7	21.2 ± 3.3	10.3
Spleen	13.2 ± 3.8	12.8 ± 4.3	10.0 ± 3.3	34.1
Testes	4.0 ± 1.6	2.5 ± 0.9	2.3 ± 0.8	
Thymus	4.5 ± 10.2	4.7 ± 7.7	5.9 ± 13.7	
Thyroid	1.1 ± 0.8	1.5 ± 0.7	1.3 ± 0.6	
Brain	444.3 ± 73.8	414.0 ± 56.8	428.0 ± 62.8	178
Heart (Left Ventricle)	41.6 ± 14.7	29.7 ± 18.1	31.9 ± 11.6	85.1
Remainder Body	1559.7 ± 157.6	1407.6 ± 263. 9	1603.0 ± 151.6	1964.2

* Both Left and Right Lung

Table 2. Average Absorbed Dose Estimates (mGy/MBq) (mean ± standard deviation) to the Target Organs in This work and Comaprision with Other Results.

Target Organs	This work			Mejia et al. (4)
	Absorbed dose for measured mass (by MRI) of 64 kg average body weight	Absorbed dose for MIRD Phantom (2) of 70 kg body weight	Absorbed dose for Japanees reference man (3) of 60 kg body weight	
Adrenal	2.1E-02 ± 4.5E-03	2.1E-02 ± 5.3E-03	2.4E-02 ± 6.0E-03	1.8E-02
Major Airway (Wall)	2.5E-02 ± 4.1E-03	2.3E-02 ± 6.8E-03	2.9E-02 ± 7.3E-03	
Nasal Cavity (Wall)	3.1E-02 ± 5.0E-03	2.7E-02 ± 3.6E-03	3.4E-02 ± 4.6E-03	
Bladder wall	4.0E-01 ± 3.2E-01	4.1E-01 ± 3.4E-02	1.8E-01 ± 1.5E-01	1.2E-01
Stomach wall	1.4E-02 ± 1.5E-03	1.4E-02 ± 3.3E-03	1.4E-02 ± 2.2E-03	1.5E-02
Small Intestine	1.6E-02 ± 2.8E-03	1.6E-02 ± 4.0E-03	1.8E-02 ± 4.1E-03	1.7E-02
ULI wall	1.7E-02 ± 3.4E-03	1.6E-02 ± 3.9E-03	1.9E-02 ± 4.3E-03	1.7E-02
LLI wall	1.5E-02 ± 2.7E-03	1.5E-02 ± 3.2E-03	1.7E-02 ± 3.6E-03	1.8E-02
Kidney	4.0E-02 ± 1.4E-03	4.1E-02 ± 1.6E-02	4.6E-02 ± 1.8E-02	3.0E-02
Liver	2.6E-02 ± 6.7E-03	2.7E-02 ± 5.6E-03	2.8E-02 ± 5.7E-03	2.3E-02
Lung	2.6E-02 ± 2.8E-03	2.6E-02 ± 4.1E-03	3.1E-02 ± 4.4E-03	1.1E-02
Ovary	1.5E-02 ± 1.9E-03	1.4E-02 ± 1.9E-03	1.5E-02 ± 1.2E-03	
Pancreas	3.3E-02 ± 2.1E-03	3.6E-02 ± 3.4E-02	3.7E-02 ± 3.5E-03	2.0E-02
Spleen	2.0E-02 ± 3.6E-03	1.9E-02 ± 4.6E-03	2.1E-02 ± 4.9E-03	2.2E-02
Testes	1.8E-02 ± 2.9E-03	1.7E-02 ± 3.7E-03	1.7E-02 ± 3.6E-03	1.5E-02
Thymus	1.1E-02 ± 1.5E-03	9.5E-03 ± 1.4E-03	1.3E-02 ± 8.0E-04	
Thyroid	1.8E-02 ± 4.8E-03	1.7E-02 ± 5.2E-03	1.9E-02 ± 5.0E-03	1.3E-02
Uterus	1.8E-02 ± 2.6E-03	1.8E-02 ± 5.5E-03	1.7E-02 ± 2.3E-03	1.9E-02
Breast	8.7E-03 ± 1.1E-03	7.6E-03 ± 1.1E-03	1.0E-02 ± 7.0E-03	1.0E-02
Ribs	9.7E-03 ± 1.2E-03	8.6E-03 ± 1.1E-03	1.2E-02 ± 6.0E-04	
Skull	3.0E-02 ± 6.3E-03	2.4E-02 ± 2.0E-03	3.1E-02 ± 2.4E-03	
Spine	1.3E-02 ± 1.6E-03	1.1E-02 ± 1.3E-03	1.5E-02 ± 7.0E-04	
Pelvis	1.2E-02 ± 1.4E-03	1.1E-02 ± 5.0E-03	1.3E-02 ± 6.0E-04	
Brain	6.9E-02 ± 6.9E-03	6.8E-02 ± 6.7E-03	9.0E-02 ± 8.9E-03	2.9E-02
Heart Wall	2.3E-02 ± 1.0E-02	2.3E-02 ± 9.9E-03	3.1E-02 ± 1.3E-02	3.0E-02
Red Marrow	7.2E-03 ± 1.2E-03	6.1E-03 ± 4.0E-04	7.7E-03 ± 3.0E-03	1.2E-02
Bone Surface	8.7E-03 ± 1.3E-03	7.4E-03 ± 6.0E-04	9.5E-03 ± 0.0003	1.5E-02
Effective Dose Equivalent (mSv/MBq)	3.6E-02 ± 1.6E-02	3.6E-02 ± 1.8E-03	2.7E-02 ±7.3E-03	2.4E-02

IV. 2. Decreased Striatal Dopa Uptake Correlated with Fronto-Temporal Glucose Utilization in Alzheimer's Disease

Meguro K., Yamaguchi S., Itoh M., Fujiwara T.*, and Yamadori A.*

Section of Neuropsychology, Division of Disability Science,
Tohoku University Graduate School of Medicine
**Cyclotron and Radioisotope Center, Tohoku University*

Previously we used [^{18}F]6-fluoro-L-dopa (FDOPA) and PET (positron emission tomography) and found that FDOPA uptake into the striatum (the Ki value) in Alzheimer's disease (AD) correlated with cognitive function. Decreased cerebral glucose utilization (CMRglc) in the parietal and temporo-parieto-occipital region were well-known PET finding in AD. We investigated the relationship between the Ki value and regional CMRglc (rCMRglc), with reference to cognitive impairment and wandering behavior. Ten AD with moderate severity of dementia were studied. Using PET and FDOPA and [^{18}F]-fluoro-deoxyglucose techniques, the Ki value and rCMRglc in the frontal, temporal, parietal, temporo-parietal, and occipital lobes were measured. There were significant Spearman correlation between the Ki value and mean cortical CMRglc. For rCMRglc, those of the frontal and temporal lobe significantly correlated with the Ki value. There could be a functional neural network between the striatum and the frontal and temporal lobes in AD.

Introduction

There were many neuroimaging studies using [^{18}F]6-fluoro-L-dopa (FDOPA)[1] as a presynaptic indicator of dopaminergic neurons in the striatum of Parkinson disease[2]. For Alzheimer's disease (AD), we noted[3] that the rate of FDOPA uptake into the striatum (the Ki value) correlated with cognitive function as shown by MMS (Mini-Mental State[4]). Using an antagonist to D_2 receptor, we reported[5] an intercorrelation between level of dopa uptake and D_2 receptor level: the data variability could support heterogeneity of AD, and that the PET-assessment of dopamine function could predict outcome of neuroleptic treatments for dementia symptoms. Subsequently we noted[6] that psychiatric wandering behavior of AD correlated with increased D_2 receptors.

On the other hand, decreased regional CMRglc in the temporal, parietal, and temporo-parieto-occipital (TPO) region in its early stage, and that in the frontal lobe in its late stage, were well-known PET finding in AD[7-9]. In this study, we investigated the relationship

between the Ki value and rCMRglc, with reference to their cognitive impairment as well as an abnormal psychiatric wandering behavior.

Methods

Patients

Ten probable AD patients with moderate severity of dementia with the NINCDS-ADRDA criteria[10] were studied. All were within 5 years of onset. All received MMS and WAIS-R[11] for their cognitive assessment.

MRI

MRI used was a 0.5T MRVectra (GE-YMS, Japan). An axial T_1-weighted MRI (TR/TE 300/15) parallel to the OM (orbito-meatal) line was examined at the same head position as in the PET study, and an axial T_2-weighted (TR/TE 2000/100) MRI was performed to exclude patietns with infarctions out of the subjects. Using the OM +40, 50, 60, 70 mm T_1-weighted planes, the % brain volume to the cranial cavity was calculated. Also, using the OM + 40 mm T_1-weighted plane, the striatum was outlined to calculate the volume by a digitizer system[12].

CMRglc Measurement

The PET study was performed with a model PT-931 scanner (CTI Inc., USA), according to the [^{18}F]-fluoro-deoxyglucose (FDG) method[13,14]. A short cannula was placed in a radial artery for blood sampling. A cross of light was projected onto marks on the subject's head, which were set at the standard points of 30 and 77 mm above and parallel to the OM line. A 20-min transmission scan using a ^{68}Ge/^{68}Ga external ring source was performed. Thirty to 45 min after the 5-12 mCi FDG injection, a series of two emission scans was performed. Twenty blood samples were collected. The plasma glucose were measured every 10 min. The analysis for CMRglc was the same as previously[12]. The rCMRGlc in the following regions were measured: upper frontal, anterior frontal, inferior frontal, primary auditory, temporal, parietal, TPO, primary visual, occipital, basal ganglia.

FDOPA Uptake Measurement

General condition including the transmission scan was the same as the FDG study. Dynamic data acquisition was performed after i.v. administration of the ligand: 6 scans of 60 sec., 8 scans of 3 min., 6 scans of 5 min., and 3 scans of 10 min. Tissue time-activity curves of the bilateral striatum were obtained using the OM +40 mm plane or the adjacent plane which had suitable striatum images. The elliptical regions of interest (ROIs) of the bilateral striatum (3.6±0.6 cm^2) were set. The measurement of the Ki value was the same as previously described[3].

Statistical Analysis

We used each unilateral value of the Ki (i.e., two values for each subject) as well as rCMRglc (i.e., two values for the same ROI for each subject, 10 values for the same ROI for each group). Spearman rank correlation coefficients were calculated between the Ki value and rCMRglc in each ROI. After finding significant correlations, the effects of age, duration of the disease, and educational level were patialled out by covariance.

Results

There was no significant relationship between the Ki value and the % brain volume nor did the striatum measured by MRI (data not shown), indicating that the results described below was not due to an effect of atrophy. The Ki value and mean cortical CMRglc were significantly correlated ($p<0.01$). For rCMRglc, those in the frontal (anterior and inferior) and in the temporal (upper and lower) lobes were significantly ($p<0.01$) correlated with the Ki value.. The rCMRglc in the basal ganglia region was mildly correlated ($p<0.05$).

Discussion

We found that the striatal dopa uptake correlated with fronto-temporal glucose utilization in AD. Although the Ki value mildly correlated with rCMRglc in the basal ganglia, there was no correlation between rCMRglc in the region and those in the frontal, temporal, or parietal lobe. It meant that the finding of the Ki value - rCMRglc relation was not due to the relationship between rCMRglc in both areas. Also, since there was no significant relationship between the Ki value and the % brain or the striatum volume, the results was not due to an atrophy. The AD-pathologic changes are evident in the hippocampal area and the association neocortices[15,16]. And hippocampal atrophy and decreased rCMRglc in the parietal lobe or TPO region are well-known neuroimaging findings. We think there is a functional neural network between the striatum and the fronto-temporal lobe. It is important in AD, not only the neural network between the hippocampus and the temporo-parietal cortex[12] related to cognitive function, but also a possible network between the striatum and the fronto-temporal lobes.

References

1) Garnett E. S., Firnau G., Nahmias C., Nature 1983;**305**:137-138.
2) Leenders K. L., Palmer A. J., Quinn N., et al., JNNP 1986;**49**:853-860.
3) Itoh M., Meguro K., Fujiwara T., et al., Ann. Nucl. Med. 1994; **8**(4):245-251.
4) Folstein M. S., Folstein S. F., McHugh P. R., J. Psychiat Res. 1975;**12**:189-198.
5) Itoh M., Yamaguchi S., Meguro K., et al., Elsvier Science B. V. Brain, heart and tumor imaging. Updated PET and MRI, 1995; Ochi H. et al., editors.
6) Meguro K., Itoh M., Yanai K., et al., Eur. J. Neurol. 1997, in press.
7) Chase T. N., Foster N. L., Fedio P., et al., Ann. Neurol. 1984;**15**(Suppl):S170-S174.

8) Cutler N. R., Haxby J. V., Duara R., et al. Ann. Neurol. 1985;**18**:298-309.
9) Foster N. L., Chase T. N., Patronas N. J., et al., Ann. Neurol. 1986;**19**:139-143.
10) McKhann G., Drachman D., Folstein M., et al., Neurology 1984;**34**:939-944.
11) Wechsler Adult Intelligence Scale - Revised, Japanese version, The Psychological Co., Tokyo;1990
12) Yamaguchi S., Meguro K., Itoh M., et al., JNNP 1997; in press.
13) Phelps M. E., Huang S. C., Hoffman E. J., et al., Ann. Neurol. 1979;**6**:371-388.
14) Reivich M., Kuhl D., Wolf A. P. et al., Circ. Res. 1979;**44**:127-137.
15) Ball M. J., Acta Neuropath 1977;37:111-118.
16) Pandya D. N., Seltzer B., Trends Neurosci. 1982;5386-5390.

IV. 3. Clinical Value of ^{11}C-MET PET and ^{201}Tl SPECT for Differentiation of Recurrent Glioma from Radiation Necrosis

Sonoda Y., Kumabe T., Takahashi T., Shirane R., and Yoshimoto T.

Department of Neurosurgery, Tohoku University School of Medicine

Introduction

Computerized tomography (CT) and magnetic resonance (MR) imaging are essential for the evaluation of gliomas. However, tumor recurrence is often difficult to distinguish from cerebral necrosis after radiochemotherapy by these methods[1,2]. Positron emission tomography (PET) is effective for differentiating recurrent glioma from radiation-induced changes using the metabolic tracer [^{18}F]fluorodeoxyglucose ([^{18}F]FDG) and carbon-11-labeled amino acids such as L-methyl-^{11}C-methionine (^{11}C-MET)[3-9]. [^{18}F]FDG PET is useful for the diagnosis of malignant transformation of tumor, and ^{11}C-MET PET can provide early detection of tumor recurrence[7-9]. Recently, thallium-201 single photon emission computerized tomography (^{201}Tl SPECT) has been used to predict the degree of malignancy and differentiate glioma recurrence from radiation necrosis[10-14].

This study evaluated the clinical usefulness of ^{11}C-MET PET and ^{201}Tl SPECT for the differentiation of tumor recurrence from radiation necrosis, and the delineation of the extent of tumor recurrence.

Clinical Material and Methods

This study included nine patients with lesions highly suggestive of recurrent glioma on MR imaging. The patients had previously received radiochemotherapy for histologically confirmed glioma. The histological diagnosis was based on CT-guided stereotaxic biopsy (Table 1, patient 9) or surgically resected specimens (patients 1-8). The malignancy of the gliomas was assessed using the new WHO classification system (3 grade IV, 1 grade III, and 5 grade II gliomas)[15]. All patients underwent ^{11}C-MET PET and ^{201}Tl SPECT studies. One patient (Table 1, patient 2) was examined twice, so a total of 10 studies were performed.

PET studies using ^{11}C-MET used a PT-931 (CTI, Knoxville, Tenn., U.S.A.) with a spatial resolution of 8 mm (full width half maximum) and a slice thickness of 7 mm. Thirty minutes after injection of 3-15 mCi of tracer, a scan of 10 minutes duration was performed. The circular ROIs with a 2 cm diameter were the site of the tumor (including the pixel with the highest accumulation) and the homologous contralateral region of the gray matter.

The PET scans were evaluated qualitatively by visual inspection as follows: hotter uptake, normal uptake, and colder uptake, compared with the homologous contralateral gray matter. Quantitatively, the differential absorption ratio (DAR) was calculated from the mean values as follows: DAR = Ci x BW / dose (where Ci is the tissue radioactivity obtained by the PET, BW is the patient body weight, and dose is the radioactivity of the injected tracer). We also calculated the T/N ratio defined as the ratio of DAR of tumor tissue to that of the homologous contralateral gray matter[16].

The patients were injected with 3 mCi of ^{201}Tl and ^{201}Tl SPECT brain scans were obtained with a Siemens MULTI SPECT 3 hours after injection. A 64 × 64 matrix with a Butterworth filter was used and scans were constructed in the transverse plane to facilitate comparison with MR images. The regions of interest (ROIs) were drawn on the slice with the tumor activity.

The ^{201}Tl SPECT scans were evaluated both qualitatively by visual inspection and quantitatively by ^{201}Tl indices. The regions of tumors were classified as hot or cold by visual inspection. The ^{201}Tl index was calculated as the ratio of average counts per pixel in the tumor to average counts per pixel in the contralateral homologous region[12].

Diagnosis of the recurrent lesion was based on CT-guided stereotaxic biopsy in two patients (Table 1, patients 2 and 9) and surgical resection of the lesion within 4 weeks after scintigraphic examinations in 2 patients (patients 6 and 7). Histological examination showed viable tumor cells with necrosis in two patients (patients 6 and 9), and necrosis without viable tumor cells in the other two patients (patients 2 and 7). The diagnoses were made without histological verification in the other 5 patients. The lesions were considered to be radiation necrosis if the clinical presentation was characterized by relatively stable neurological symptoms and no signs of massive enlargement and/or dissemination of the lesion on follow-up MR images. However, the lesion was finally diagnosed as tumor recurrence in patient 2, as will be described below. As a result, the final clinical diagnoses in the 9 patients were 5 recurrent gliomas and 4 radiation necrosis.

Statistical analysis used the unpaired t-test.

Results

The results are summarized in Table 1. Qualitative analysis of the PET studies showed 6 hot and 4 normal uptake lesions. Four tumors with normal uptake were diagnosed as radiation necrosis, but only one hot lesion was also diagnosed as radiation necrosis. The T/N ratio of DAR ranged from 1.07 to 2.70 (1.49 ± 0.69) in radiation necrosis and from 1.71 to 5.30 (3.10 ± 1.40) in tumor recurrence. The difference between radiation necrosis and tumor recurrence was statistically significant ($p < 0.05$). Qualitative visual analysis of the ^{201}Tl SPECT images revealed 8 hot and 2 cold lesions. Both cold lesions were clinically diagnosed as radiation necrosis, but 3 of 8 hot lesions were also diagnosed as radiation

necrosis. Quantitatively, the ^{201}Tl indices ranged from 1.31 to 3.33 (mean ± SD of 1.92 ± 0.82) in radiation necrosis and from 1.99 to 7.44 (3.76 ± 2.22) in tumor recurrence. There was no significant difference between the two groups.

Representative Cases

Case 1: Patient 2 had been treated for left frontal glioblastoma multiforme by subtotal resection followed by radiochemotherapy. Six months after the tumor resection, follow-up MR imaging revealed an enlarging enhanced lesion around the left anterior horn of the lateral ventricle. ^{201}Tl SPECT showed this lesion as a high uptake area. The lesion was classified as a recurrent tumor. She was treated with γ-knife irradiation. After four months, MR imaging showed the enhanced mass remained (Fig. 1, left), but ^{201}Tl SPECT showed decreased accumulation of ^{201}Tl and ^{11}C-MET PET revealed a normal uptake, suggesting the lesion was radiation necrosis (Fig. 1, middle and right). After five months, MR imaging showed extensive enhanced lesions involving the corpus callosum and left cingulate gyrus (Fig. 2, left). ^{201}Tl SPECT showed the lesion as a high uptake area (Fig. 2, middle). However, ^{11}C-MET PET revealed a smaller hot lesion compared with that on the ^{201}Tl SPECT scan (Fig. 2, right). The patient was readmitted and CT-guided stereotaxic biopsy was performed. Serial specimens were obtained at 5 mm intervals from the target Histological examination of the specimens revealed areas of necrosis of the tumor cells and radiation changes, but no evidence of tumor recurrence (Fig. 3). However, the lesion showed progressive growth in size, and a new enhanced lesion in the left hippocampus was detected by MR imaging. Therefore, these lesions were identified as recurrence.

Case 2: Patient 7 had been treated for a low grade cerebellar astrocytoma by resection and postoperative radiochemotherapy. Six months after the tumor resection, MR imaging revealed a small enhanced mass at the cerebellar vermis. One month later, another enhanced lesion was confirmed. She underwent γ-knife irradiation. However, these lesions continued to enlarge (Fig. 4, left). Both ^{11}C-MET PET and ^{201}Tl SPECT demonstrated hot lesions suggesting tumor recurrence fourteen months after tumor resection (Fig. 4, middle and right). The patient underwent total resection of the cerebellar mass. Histological examination of the resected tissue revealed radiation-induced changes without any evidence of tumor recurrence (Fig. 5).

Discussion

The mechanisms by which ^{201}Tl and ^{11}C-MET are accumulated remain unclear. ^{201}Tl chloride is a potassium analogue with high affinity for the Na^+-K^+-adenosine triphosphatase pump and does not cross the normal blood-brain barrier (BBB)[17, 18]. Uptake of ^{201}Tl on early images is believed to depend on BBB dysfunction and increased regional blood flow, whereas ^{201}Tl uptake on the delayed images may depend on active transport by the membrane

pump[19]. Uptake of ^{11}C-MET is related to active carrier-mediated transport across the cell membrane and disruption of BBB[20-22]. However, disruption of the BBB is not necessary for increased ^{11}C-MET uptake, because high uptake of ^{11}C-MET is observed in low grade glioma in which the BBB is intact[21].

^{201}Tl SPECT is reported to be as effective as PET for distinguishing radiation necrosis from brain tumor recurrence[23-26]. However, increased uptake of ^{201}Tl has been observed in radiation necrosis and inflammatory-infectious processes[27]. In our study, ^{201}Tl SPECT images tended to show both radiation necrosis and tumor recurrence as hot lesions. The selectivity for tumor recurrence was only 63% (5/8 cases). In contrast, the results of the ^{11}C-MET PET studies matched the clinical diagnoses, with a false positive result in only one case. The selectivity for tumor recurrence was 83% (5/6 cases). The T/N ratio of DAR of recurrent glioma was statistically different from that of radiation necrosis. Although the quantitative analysis was not generalized for evaluation of recurrent tumor in both ^{11}C-MET PET and ^{201}Tl SPECT, our quantitative analysis agreed with the qualitative analysis. We also found the hot lesions on ^{201}Tl SPECT images were larger than those on ^{11}C-MET PET images in patients 2 and 6. In patient 6, comparison of the PET and SPECT studies with the histological examination of the surgical specimens shows that ^{11}C-MET PET was superior to ^{201}Tl SPECT for delineating the extent of the tumor. The clinical diagnosis in patient 2 suggests sampling error possibly occurred in the stereotaxic biopsy. The ^{11}C-MET PET image, which showed a small hot lesion, might have detected the tumor recurrence in the radiation necrosis within the enhanced lesion. Both ^{11}C-MET PET and ^{201}Tl SPECT images showed radiation necrosis as a hot lesion in patient 7. The ^{11}C-MET PET and ^{201}Tl SPECT scans might be false positive, because sampling error rarely occurs in a histological study using a surgical specimen. The cause of this contradiction is not yet clear. However, the partial volume effect influences both PET and SPECT studies[12, 16]. If the tumor recurrence is very small or the tumor has a metabolically inactive large area such as a necrotic core, false negative results could be obtained in both studies.

In conclusion, ^{11}C-MET PET is helpful for differentiating tumor recurrence from radiation necrosis, and for estimating the extent of recurrent tumor in the enhanced lesion on MR imaging. However, further investigation concerning the pathophysiology of radiation necrosis is necessary.

References

1) Lilja A., Spannare B., Olson Y., J. Comput. Assist. Tomogr. **5** (1984) 625-634.
2) Dooms G. C., Hecht S., Brant-Zawadzki M., et al., Radiology **158** (1986) 149-155.
3) Patronas N. J., Di Chiro G., Brooks R. A., et al., Radiology **144** (1982) 885-889.
4) Di Chiro G., Oldfield E., Wright D. C., et al., AJR. **150** (1988) 189-197.
5) Di Chiro G., DeLaPaz R. L., Brooks R. A., et al., Neurology. **8** (1986) 1323-1329.
6) Valk P. E., Budinger T. F., Levin V. A., et al., J. Neurosurg. **69** (1988) 830-838.
7) Francavilla T., Miletich R. S., Di Chilo., et al., Neurosurg **24** (1989) 1-5.
8) Lilja A., Lundqvist H., Olsen Y., et al., Acta Radiol. **30** (1989) 121-128.
9) Ogawa T., Kanno I., Shishido F., et al., Acta Radiol. **32** (1991) 197-202.
10) Mountz J. M., Stafford-Schuck K., Mckeever P. E., et al., J. Neurosurg. **68** (1988) 705-709.
11) Black K. L., Hawkins R. A., Kim K. T et al., J. Neurosurg. **71** (1989) 342-346.
12) Kim KT., Black KL., Marciano D., et al., J. Nucl. Med. **31** (1990) 965-969.
13) Carvalho P. A., Schwartz R. B., Alexander E., et al., J. Neurosurg. **77** (1992) 565-570.
14) Yoshii Y., Satou M., Yamada Y., et al., Eur. J. Nucl. Med. **20** (1992) 39-45.
15) Kleihues P., Burger P. C., Scheithauer B. W., World Health Organization International Histlogical Classification of Tumours, Kleihues P. ed. Berlin Heidelberg: Springer-Verlag; (1993).
16) Kameyama M., Shirane R., Itoh J., et al. Acta Neurochir. **104** (1990) 8-12.
17) Atkins H. L., Budinger T. F., Lebowitz E., et al. J. Nucl. Med. **18** (1977) 133-140.
18) Ancri D., Basset J. Y., Lonchampt M. F., et al. Radiology **128** (1978) 417-422.
19) Ueda T., Kaji Y., Wakisaka S., et al. Eur. J. Nucl. Med. **20** (1993) 138-145.
20) Bergström M., Ericson K., Hagenfeldt L., et al. J. Comput. Assist. Tomogr. **11** (1987) 208-312.
21) Derlon J. M., Bourdet C., Bustany P., et al. Neurosurgery **25** (1989) 720-728.
22) Sato K., Kameyama m., Ishiwata K., et al. Eur. J. Nucl. Med. **19** (1992) 426-430
24) Hoh C. K., Khanna S., Harris G. C., et al. J. Nucl. Med. **33** (1992) 867.
25) Black K. L., Emerick T., Hoh C., et al., Nerol. Res. **16** (1994) 93-96.
26) Kahn D., Follett K. A., Bushnell D. L., et al., A. J. R. **163** (1994) 1459-1465.
27) Buchpiguel C. A., Alavi J. B., Alavi A., et al., J. Nucl. Med. **36** (1995) 159-164.
28) Schwartz R. B., Carvalho P. A., Alexander III E., et al. A. J. R. **12** (1992) 399-403.

TABLE 1: Results of Tl-201 SPECT and C-11-MET PET Examinations, Compared With Histological and Clinical Diagnosis

Patient No.	Age/ Sex	WHO Grade	Tl-201 SPECT		C-11-MET PET		Histological Diagnosis	Clinical Diagnosis
			Visual inspection	Index	Visual inspection	T / N		
1	24/M	IV	Hot	3.33	Normal	1.32	ND	RN
2a	31/F	IV	Cold	1.37	Normal	1.07	ND	RN
2b	31/F	IV	Hot	1.99	Hot	1.71	RN	TR
3	57/F	IV	Hot	7.44	Hot	2.08	ND	TR
4	36/M	III	Cold	1.31	Normal	1.22	ND	RN
5	36/F	II	Hot	1.80	Normal	1.12	ND	RN
6	56/M	II	Hot	4.21	Hot	5.30	TR	TR
7	21/F	II	Hot	1.80	Hot	2.70	RN	RN
8	55/M	II	Hot	2.60	Hot	3.32	ND	TR
9	68/M	II	Hot	2.54	Hot	3.10	TR	TR

Note. SPECT = single photon emission computerized tomography, MET = methionine, index = average counts per pixel in the tumor / average counts per pixel in the contralateral homologous region, PET = positron emission tomography, T/N = ratio of differential absorption ratio of tumor tissue to that of the homologous contralateral gray matter, TR = tumor recurrence, RN = radiation necrosis, ND = not done.

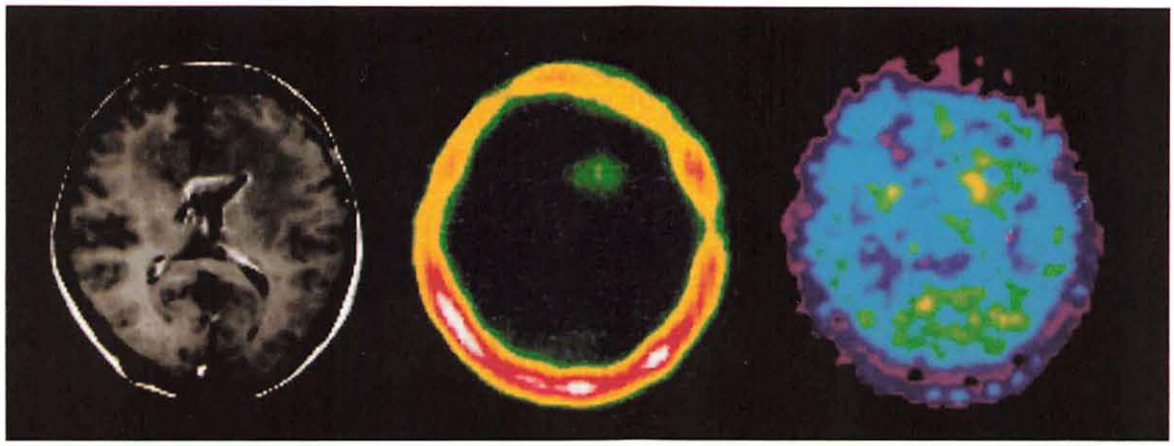

Fig. 1. A 31-year-old female (patient 2a) had received γ-knife irradiation for a recurrent glioblastoma multiforme five months previously. Left, Contrast-enhanced T1-weighted MR image showing enhanced abnormality around the left anterior horn of the lateral ventricle. Middle, ^{201}Tl SPECT transaxial slice scan at the same level as the MR image showing decreased activity compared to the previous ^{201}Tl study (data not shown). Right, ^{11}C-MET PET scan at the same level showing normal uptake in the same lesion.

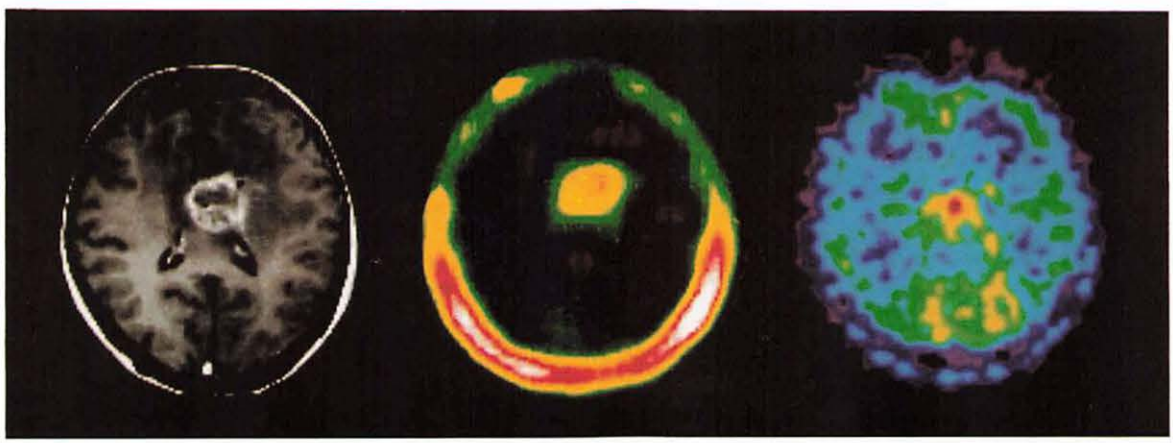

Fig. 2. Patient 2b underwent scintigraphy studies again four months later. Left, Contrast-enhanced T1-weighted MR image showing enhanced abnormalities in the corpus callosum. Middle, ^{201}Tl SPECT transaxial slice scan at the same level as the MR image showing increased activity. Right, ^{11}C-MET PET scan at the same level showing increased uptake which was quite limited compared with the enhanced lesion on the MR image and the hot lesion on the ^{201}Tl SPECT scan.

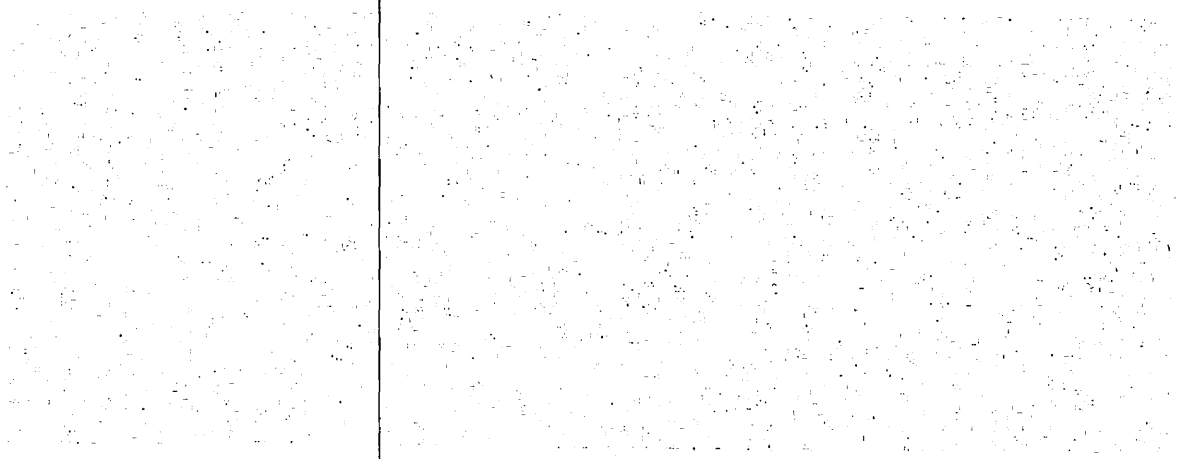

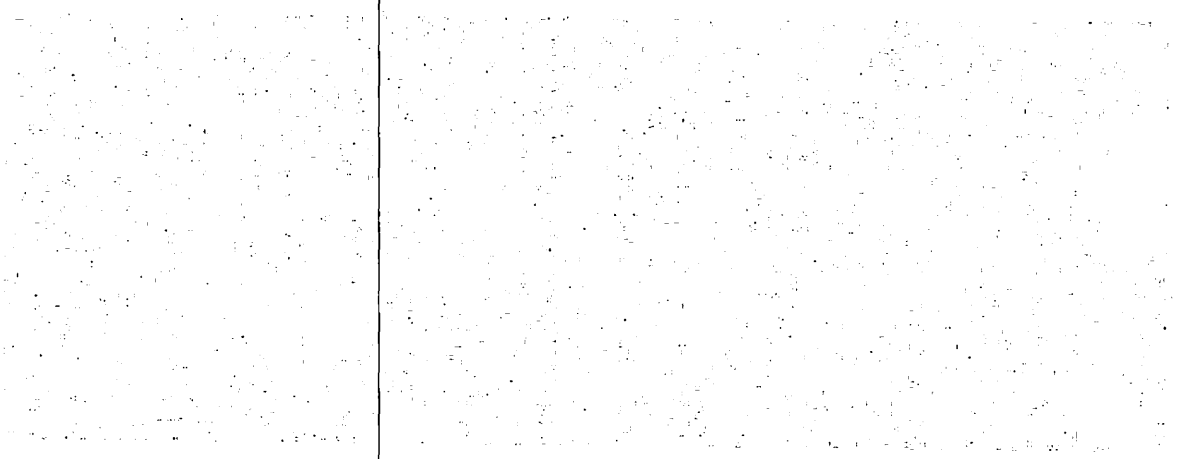

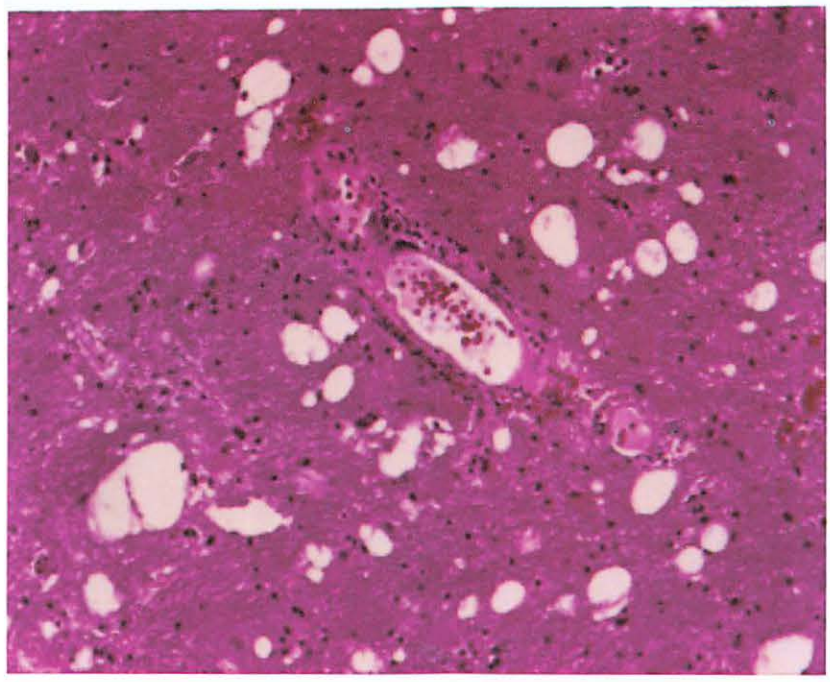

Fig. 3. Patient 2b underwent CT-guided biopsy with serial specimens obtained at 5 mm intervals from the target. Photomicrograph showing necrosis of the tumor cells (Hematoxylin & eosin staining, original magnification × 100).

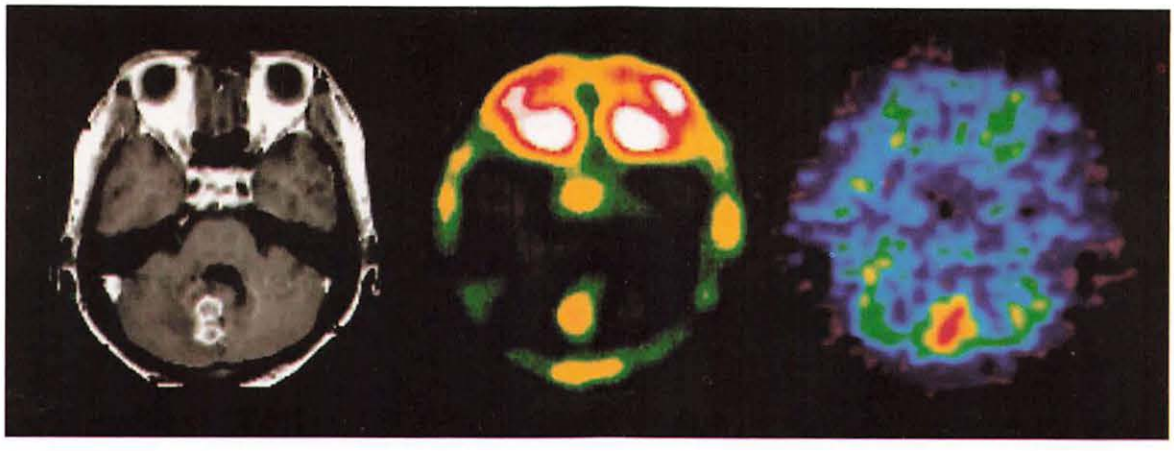

Fig. 4. A 21-year-old female (patient 7) had undergone resection of a cerebellar astrocytoma followed by radiation therapy 14 months previously, and booster γ-knife irradiation 6 months previously. Left, Contrast-enhanced T1-weighted MR image showing enhanced abnormalities in the cerebellar vermis. Middle, ^{201}Tl SPECT transaxial slice scan at the same level as the MR image showing increased activity corresponding to the enhanced lesions on the MR image. Right, ^{11}C-MET PET scan at the same level showing increased activities in the same lesions.

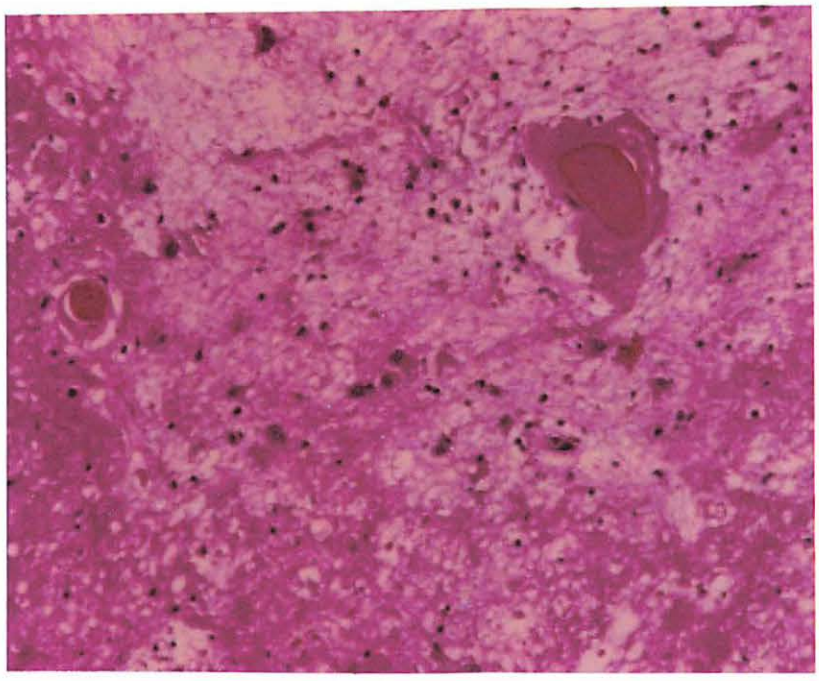

Fig. 5. Patient 7 underwent total resection of the cerebellar mass. Photomicrograph of the surgical specimen showing coagulation necrosis, extensive demyelination of white matter, and degenerating vascular alteration, such as hyalinization and mineralization in the vessel walls (Hematoxylin & eosin staining, original magnification × 100).

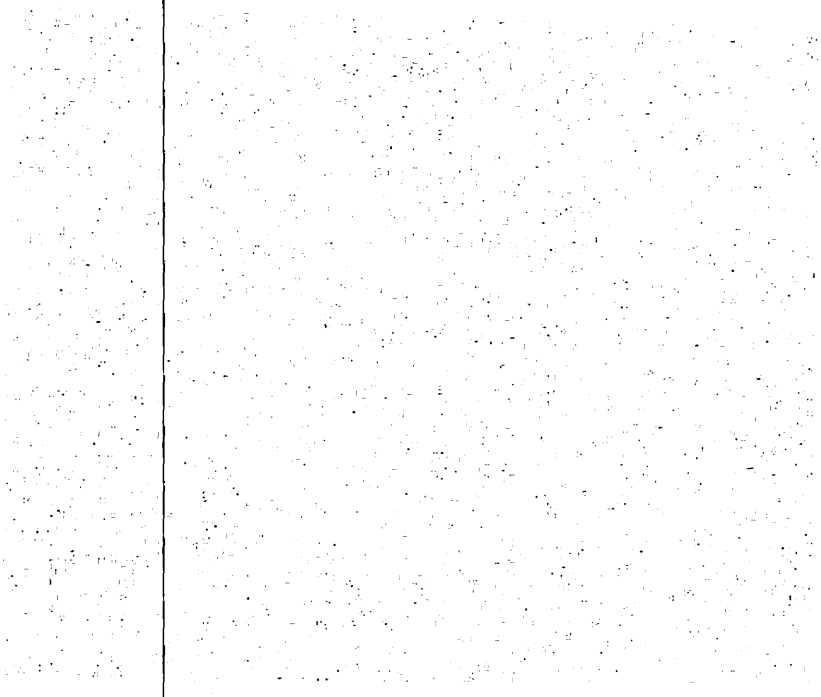

IV. 4. Mapping of Energy Consumption in Masticatory and Tongue Muscles during Gum Chewing by Using Positron Emission Tomography and ^{18}F-fluorodeoxyglucose

Rikimaru H., Kikuchi M., Tashiro M., Itoh M.*, Ido T.*, Watanabe M.*

Department of Geriatric Dentistry, Tohoku University School of Dentistry
*Cyclotron and Radioisotope Center, Tohoku University**

Introduction

Masticatory and tongue muscles play an important role in stomatognathic function. These muscles have anatomically complex structures different from limb and trunk muscles, and this characteristic enables complex functional partitioning. The muscles do not work as a whole but partitions of the muscles produce a vector of task forces that is appropriate for particular action. The masticatory and tongue muscle cooperation has not been fully investigated because of in methodological difficulties. The electromyography (EMG) is insufficient to record activity of deeply situated masticatory muscles.

The investigations of energy metabolism in masticatory muscles using ^{31}PNMR are useful for evaluation of skeletal muscle function[1, 2]. Positron emission tomography (PET) which offers unique possibility of quantitative imaging of muscular activity has recently been applied for the estimation of tissue metabolism *in vivo*, with ^{18}F-fluoro-deoxy-glucose (FDG) used as a tracer. Its uptake is closely related to tissue energy consumption in brain and muscles. The outstanding advantage of using FDG and PET to evaluate muscle activity is that subjects are scanned while lying, after exercise. Fujimoto et al.[3] demonstrated that PET clearly identifies muscles involved in physical activities.

Recently, three-dimensional whole-body PET (3D-PET) has become available as a diagnostic tool sensitive enough to reduce radiation exposure.

In this study, activities of the masseter, temporal, lateral pterygoid, medial pterygoid and tongue muscles associated with gum chewing were measured using FDG and 3D-PET.

Materials and Methods

Four patients (3 males and 1 female) aged from 32 to 61 years and suffering from a malignant neoplasm other than head and neck tumor collaborated in the study. None had diabetes. They all gave informed consent, and prior approval of this experiment was granted by the Clinical Committee for Radiopharmaceutical Use of Tohoku University.

The subject were each intravenously injected with approximately 75MBq of FDG when they started to chew two sheets of gum (Ezaki Glico Co., Japan) for 30 min. After additional 30 min during which subjects sat in a comfortable chair, they were positioned on a PET couch and PET scan of 50 min duration was started. The tissue attenuation correction was carried out using a rotating ^{68}Ge/Ga line source in the post-injection transmission mode. A whole-body PET (SET 2400W, Shimadzu Co. & Inc., Japan) was used in a 3D mode. The axial resolution and an in-plane resolution were 4.5 mm and 3.9 mm respectively at the center of the field of view.

Acquired PET images were then transferred to a workstation for data analysis (TITAN2, Kubota Computer Co., Japan) and visual identification of areas with increased FDG uptake in the muscles was performed. The images were also processed by means of the Application Visualization System (AVS, Advanced Visual System Inc., USA) in order to obtain volume-rendered images. 3D-surface emission images of the head were constructed based on the surface rendering of the transmission images. Additionally, the regions of interest (ROI) were defined for the muscles by referring corresponding magnetic resonance image (MRI). The total counts for each masticatory or tongue muscle were summed up. The uptake was normalized for injected activity and subject's body weight to give the standardized uptake values (SUV) according to the following formula:

$$SUV = (\text{ROI count} \times \text{calibration factor}) / (\text{injected dose} / \text{body weight})$$

Results

Transverse images of the upper neck and face during gum chewing in one subject are shown in Figure 1. An enlarged image extracted from these serial images is shown in Figure 2. The degree of accumulation of FDG was represented by different colors as shown in the color scale, e.g., moderately activated area is shown in yellow, and red shows highly activated area. Intramuscular activities in the masticatory muscles, especially in the masseter muscles, were found to be spatially heterogeneous. Activities of the lateral and medial pterygoid muscles were also clearly visible in these figures. The most prominent accumulation of FDG was observed in the intrinsic tongue muscle. On the whole, 3D-volume-rendered images (Figure 3) accelerated identification of the muscles involved in gum chewing.

SUV in each muscle for all subjects are summarized in Figure 4. The accumulation in the tongue muscles was higher than that in any of masticatory muscles, except in the subject D, in whom accumulation in the intrinsic tongue muscle was higher than that in the masseter, temporal, and medial pterygoid muscles but the highest accumulation was found in the lateral pterygoid muscles.

Discussion

Heterogeneous activities of masticatory and tongue muscles were observed in the PET images as suggested by previous EMG studies[4,5]. The level of activity for the corresponding muscles in the right and left side was different (Figure 2) showing that the regional activities of the masticatory and tongue muscles dependent on the chewing manner that includes the predominant side of chewing, as well as chewing habits.

In general the activities of tongue muscles were found to be higher compared to those of masticatory muscles. This may indicate that the tongue plays the most important role in chewing although workforce of the masticatory muscles is indispensable. However, in one subject, the activities of lateral pterygoid muscles was the highest among the muscles investigated. This variation may depend on the subject's dental condition such as the number and distribution of missing teeth, and on chewing habit. Because oral examination was not performed in this particular subjects, additional experiments have to clarify this point.

In the previous EMG studies, the medial pterygoid muscle, lateral pterygoid muscle and tongue muscles have not been fully explored because of their complex anatomy and technical difficulty. PET offers an advantage of simultaneous measurement of activities of all masticatory and tongue muscles. Another advantage of PET is to visualize whole muscle activities as images in situ in physiological conditions, while subjects masticate without installation of any instruments. Since all the masticatory muscles are visualized quantitatively, cooperative muscular movements in the particular action of mastication may be investigated further. Low resolutions of PET, not only spatial but also temporal, can be partly compensated for by applying MRI and/or EMG. We propose to use FDG-PET for the analysis of stomatognathic functions.

References

1) Plesh O., Meyerhoff D. J., Weiner M. W., J. Dent. Res. **70** (1991) 428.
2) Lam E. W. N., Hannam A. G., Archs. oral Biol. **37**, **1** (1992) 49-56.
3) Fujimoto T., Itoh M., Kumano H., et al., THE LANCET **348** (1996) 266.
4) Van Eijden T. M. G. J., Brugman P., Wejis W. A., et al., J. Biomechanics **23**, **5** (1990) 475-485.
5) Blanksma N. G., Van Eijden T. M. G. J., J. Dent Res **69**, **10** (1990) 1686-1690.

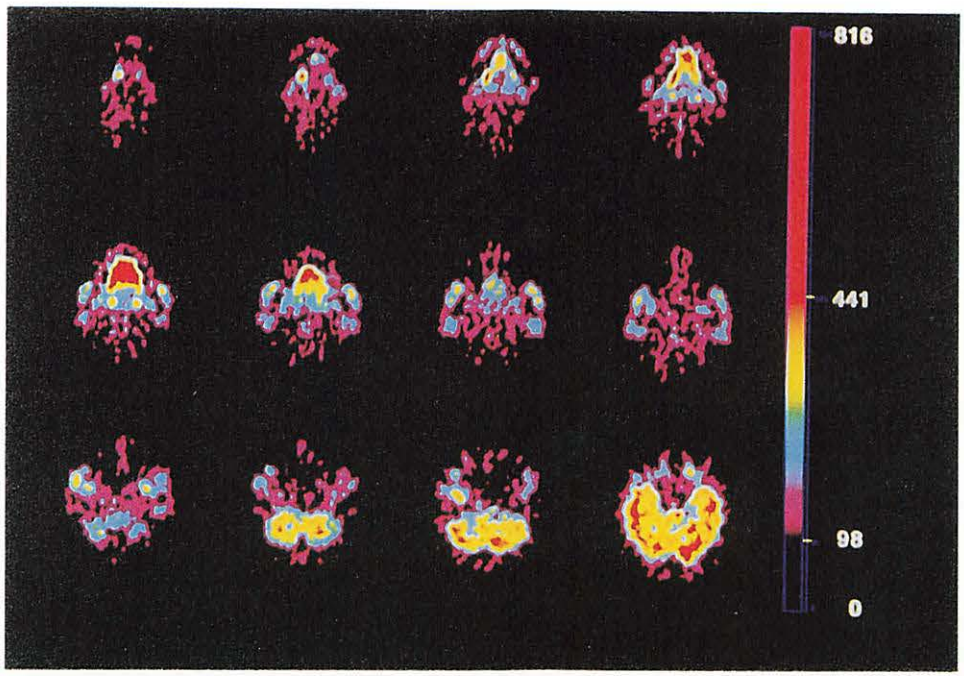

Fig. 1 FDG-PET scan of the head. High uptake of FDG is seen in masticatory and tongue muscles.

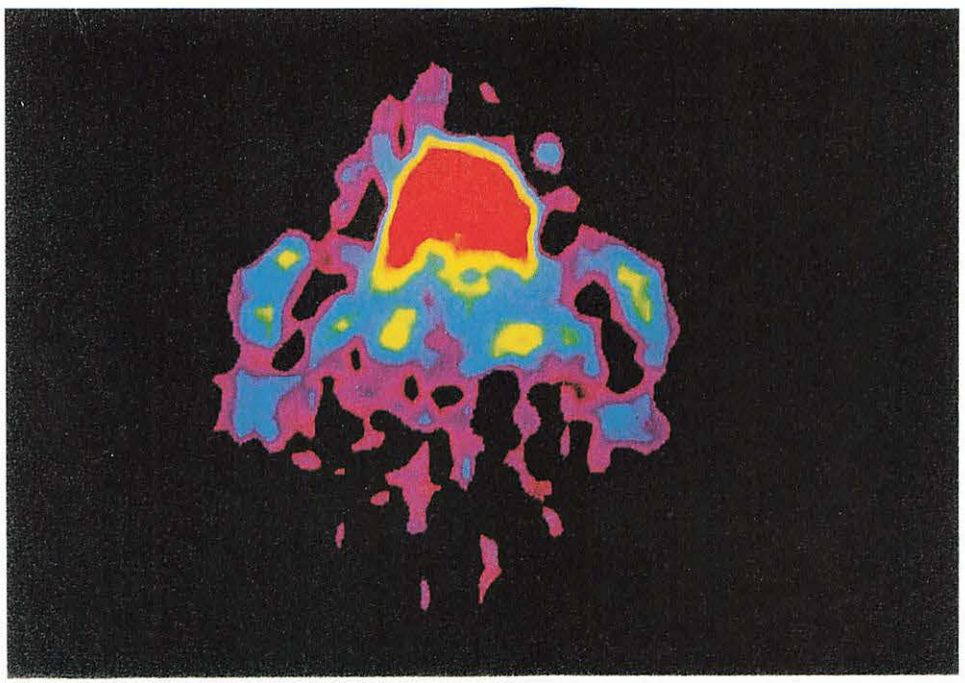

Fig. 2 Enlargement from Figure 1. Heterogeneous uptake is seen in masticatory, especially masseter muscles.

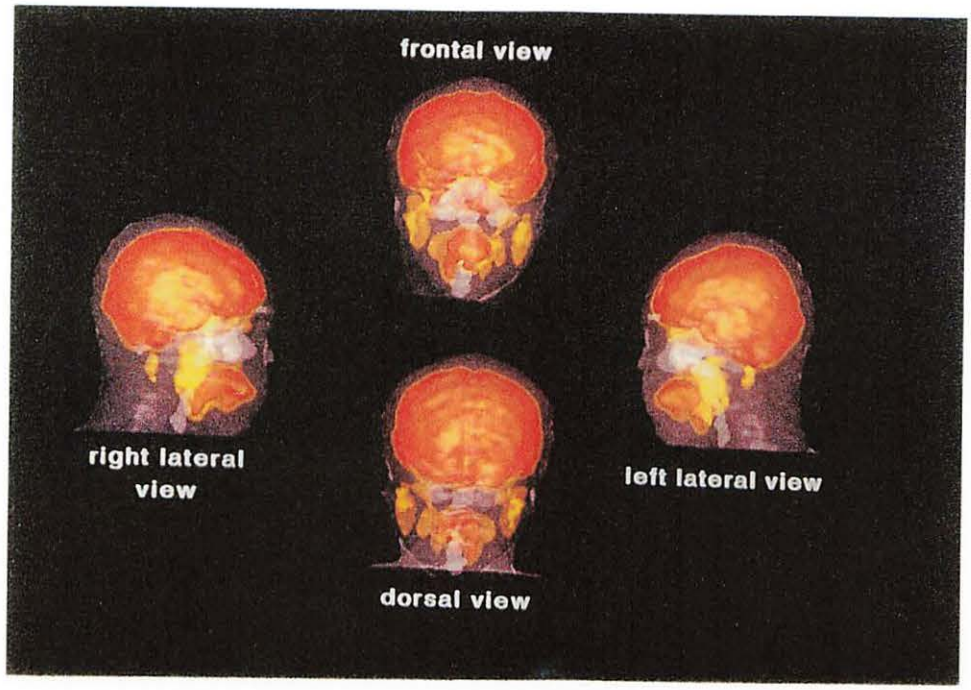

Fig. 3 3D-volume-rendered images. Area of moderate activation associated with gum chewing is shown in yellow, and red shows highly activated area.

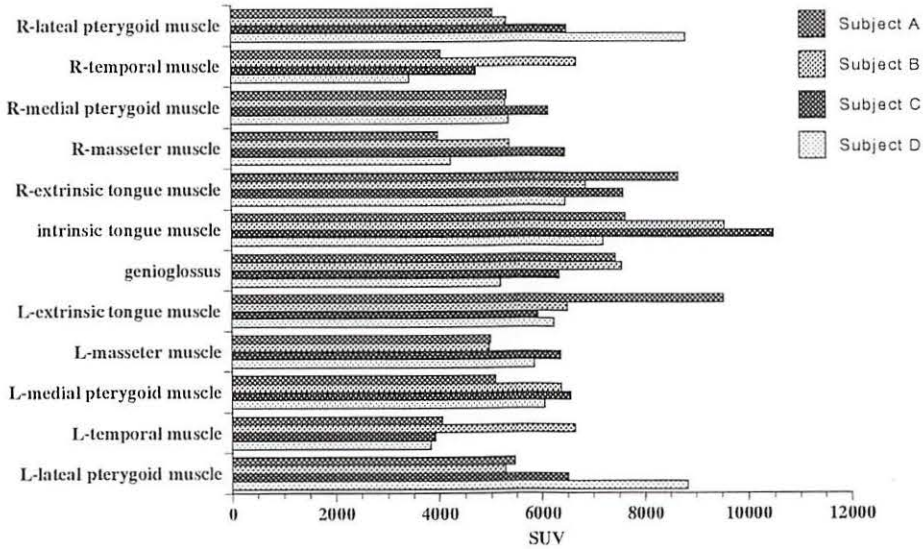

Figure 4. SUV in each muscles

Fig. 4 Standardized Uptake Value in each muscle of every subject investigated.

IV. 5. Whole-Body Mapping of Muscular Activity During Field Running Using ^{18}F-FDG and PET

Tashiro M., Fujimoto T., Miyake M., Itoh M., Ido T.***

*Divisions of Nuclear Medicine and Nuclear Pharmacology**, Cyclotron Radioisotope Center*
*Dept. of Medicine and Science in Sports and Exercise, Tohoku University School of Medicine**

Introduction

Running is one of common habitual actions in our life. Anatomy describes the function of each muscle based on its location and attachment to bones, though understanding by this approach has been limited within the knowledge of general movement of muscles. Individual differences in muscle usage among subjects during particular movements can only be explored by observation of muscles in ongoing actions.

Skeletal muscle activities during exercise have been studied using electromyography (EMG), which has high time-resolution to specify every muscle contraction at any moment during a certain phase of a running stride[1]. However, because of its low spatial resolution, EMG is not suitable for investigation of muscle activities as a whole.

Nuclear medicine has been another choice for research in sports medicine. ^{201}Tl which behaves like potassium was successfully used in imaging of muscle activities using gamma camera, though it merely gave information regarding blood flow increases, an indirect index of activity[2]. Another approach is to use PET with ^{18}F-fluorodeoxiglucose (^{18}F-FDG), an analogue of glucose that can be used as an index of energy consumption. The advantage of the FDG method lies in "metabolic trapping", which allowed us to have subjects run after injection until the scan start time[3]. Additionally, 3D data acquisition is able to reduce radiation exposure to subjects down to 1/5 or 1/10 of those by 2D data acquisition.

Subjects and Method

Subjects consisted of eight healthy male volunteers aged from 19 to 23 years (average of 20.7±1.6). They were requested to run for a total of 45 minutes, with 15 minutes before and 20 minutes after intravenous injection of FDG (1.9±0.4mCi on average). A set of 3D-whole body emission scan was performed for 30 minutes, followed by the post-injection transmission for 30 minutes, using a 32 ring-PET (SET-2400W, Shimadzu Inc, Japan). All subjects were discouraged from eating and drinking for at least three hours before the study and were requested to urinate just before the emission scan. Their running pace was maintained so as to keep their heart rates at 140-150 beats per minute. Two male subjects

(age 22 and 24 years) identically examined at rest were included as a control. The graphical data of whole-body emission and transmission scans were additionally processed into "the volume rendering images" by a software package AVS Medical Viewer, presented by AVS (Application Visualization System).

We manually drawn ROIs (regions of interest) at lower extremities including bilateral soles, legs and thighs. The legs were studied more precisely as anterior (tibialis anterior and extensor digitorum longus muscles, etc) and posterior (gastrocnemius, soleus, posterior tibialis muscles, etc) compartments of legs were analyzed separately and lateral compartment was omitted. The standardized uptake ratio (SUR) were calculated to represent FDG uptake of muscles per unit volume according to the following equation:

$$\text{SUR} = \text{mean ROI count (cps/mL)} \times \text{body weight (kg)} / \text{injected dose (mCi)} / \text{calibration factor (cps/}\mu\text{Ci)}.$$

Total amount of FDG uptake by each muscle bulk was evaluated by defining the total radioactivity distribution (TRD), which is expressed by the following:

TRD = total organ count (cps) × standard weight (60kg) / injected dose (mCi) / subject's weight(kg) / calibration factor .

Results

Fig. 1 depicts volume-rendered images of the legs and soles which are superimposed on the surface contour defined by the corresponding transmission image. The posterior compartments of the legs are more activated than the anterior (Fig.1). The TRD and SUR for each part of the lower limbs are shown in Tables 1 and 2, in which the averaged values of TRD for soles, legs and thighs in runners were 0.50, 6.81 and 6.53, and those for soles, legs and thighs in controls were 0.34, 1.34 and 3.21, respectively. TRD for all parts showed increased in runners. Especially, legs showed significant increase in TRD in runners.

In Table 2, standardized uptake ratios (SUR), which reflect energy consumption per volume, for each part of the lower limbs are shown. SUR of soles, legs and thighs were 1.10, 1.40 and 0.57 in runners and 0.18, 0.25 and 0.25 in controls, respectively. SUR of the soles in runners were extremely high compared with that among controls. Contrarily, SUR of thighs were not so high compared with that among controls, representing that activity of the thighs per volume is relatively low. And the averaged SUR of the posterior compartment of the legs were about 1.5 times as high as that of the anterior.

Discussions

The skeletal muscle requires much energy when in action. A high energy source stored in muscle tissue, the creatinine-6-phosphate, is exhausted almost in seconds. Contribution of Carbohydrate as an energy source is around between 70 and 80% at initial

stage of running and drops to 50-55% at the point of fatigue. Lipid contribution is initially at 20-30% and rises to 45-50% at the point of fatigue[4]. Therefore, the energy source during the early phase of exercises is mainly glucose and glycogen. Therefore, FDG accumulation in the muscle roughly reflects the intensity of its activity. Quantification of glucose metabolic rate was technically impractical especially during running in the field. Difficulty in obtaining arterial input functions of FDG confined us in qualitative analysis. However, as shown in our results, functional imaging of qualitative muscular activity surely help us understand coordination of muscles engaged in particular exercise.

SUR represents the energy production in unit volume of muscle. TRD represents the total energy production in respective muscles. Our results demonstrated the posterior compartments are more involved in running activity. This agrees with our daily experiences that the contraction of these muscle groups produce power for the forward movement of the body. Based on the previous study using EMG, these muscles became active for longer period in one stride cycle of running than in that of walking[8]. The role of the anterior compartments of the legs is in general to get dorsal flexion while a runner swings the lower limb forward. This functional difference may explain the in dominance of the postrior compartments in SUR.

The role of thighs is basically to stabilize the pelvic girdle as well as to lift the lower limbs forward. But at the sustained running as in this study, the latter function can be achieved by only inertia. This may be the reason that SUR is relatively low parts in spite of high TRD, as well as relatively large muscle bulk which lower the contribution of individual muscle bundles in each muscle.

The sole muscles were also involved in action. Their role is to maintain the arch structure of the feet which is very suitable for upright standing[5]. The ground reaction force, which our lower limbs must face while standing or running, should be low enough (similar amount caused by the body weight) for tendons and aponeurosis to bear upon, not requiring contribution of foot base muscles. The arch structure and foot base muscles work for this purpose just like a mechanical spring. When the ground reaction force increases in accordance with increase in running speed, strong contraction of foot base muscles should occur. For example, at the speed of 14 kilometer per hour the ground reaction force is about 2.7 times as strong as the body weight of runners, requiring continuous contraction of foot base muscles[6]. This fact may be the reason for the relatively high SUR in the sole muscles.

Generally, the individual patterns of muscle usage during running were almost similar across subjects. However, the relative strength of each muscle showed some variations. FDG mapping of muscular activity may be clinically applicable in sports-science and medicine. This can provide an index for proper training of particular muscles that fits for particular sport.

References

1) Suzuki R., J. Jpn. Orthop. Assoc. **61** (1987) 75.
2) Seto H., Kageyama M., et al., Nuc. Med. Commun., **16** (1995) 661.
3) Fujimoto T., Itoh M., Kumano H., et al., The Lancet, **348** (1996) 266
4) Morton Callow A., and Guppy M., Eur. J. Appl. Physiol. **55** (1986) 654.
5) Bateman J. E. et al. The Foot and Ankle, Thieme, New York, 1980.
6) Cavanagh P. R. and Lafortune M. A., J. Biomechanics **13** (1980) 397.

Table 1. Normalized Total Radioactivity Distribution (TRDn) of the Lower Limb Parts

subjects	soles	legs	thighs	TOTAL	posterior	anterior	P/A
A	0.10	5.02	3.94	9.07	3.89	0.25	15.56
B	0.37	5.88	11.51	17.76	4.80	0.80	6.00
C	0.97	8.88	7.17	17.01	5.67	1.09	5.20
D	0.40	5.46	3.52	9.39	3.60	0.64	5.63
E	0.51	7.60	5.43	13.54	5.17	0.38	13.61
F	0.23	3.01	3.79	7.03	2.37	0.50	4.74
G	0.95	11.85	10.36	23.17	1.55	0.53	2.92
mean	0.50	6.81	6.53	13.85	3.86	0.60	7.67
SD	0.34	2.91	3.28	5.79	1.50	0.28	4.86
control1	0.12	0.90	1.47	2.48	0.60	0.20	0.59
control2	0.55	1.78	4.94	7.27	1.09	0.48	0.68
mean	0.34	1.34	3.21	4.88	0.85	0.34	0.64
SD	0.30	0.62	2.45	3.39	0.35	0.20	0.06

Table 2. Standardized Uptake Ratio (SUR) of the Lower Limb Parts

subjects	soles	legs	thighs	TOTAL	posterior	anterior	P/A
A	1.04	1.27	0.34	0.57	1.59	1.04	1.53
B	0.83	1.56	0.70	0.86	1.48	0.90	1.64
C	0.97	1.45	0.62	0.90	1.80	1.09	1.65
D	0.88	1.00	0.36	0.60	1.64	1.01	1.62
E	2.12	1.81	0.71	1.12	2.42	0.98	2.47
F	0.38	0.54	0.31	0.38	0.63	0.52	1.21
G	1.46	2.15	0.93	1.33	2.53	2.46	1.03
mean	1.10	1.40	0.57	0.82	1.73	1.14	1.59
SD	0.55	0.53	0.24	0.33	0.64	0.61	0.46
control1	0.16	0.18	0.19	0.18	0.19	0.19	1.00
control2	0.20	0.32	0.30	0.29	0.36	0.35	1.03
mean	0.18	0.25	0.25	0.24	0.28	0.27	1.01
SD	0.03	0.10	0.08	0.08	0.12	0.11	0.02

Fig. 1 volume-rendered images of the legs and soles superimposed on the surface contour defined by the transmission image

IV. 6. Whole Body Metabolic Map with Positron Emission Tomography of a Man after Running

Fujimoto T., Itoh M., Kumano H., Tashiro M.* and Ido T.**

Department of Medicine, Tohoku University
*Cyclotron and Radioisotope Center, Tohoku University**

Positron emission tomography (PET) is a tool used to visualize tissue metabolism in-vivo in humans. ^{18}F-fluoro-deoxy-glucose (FDG)[1] has been used to measure regional function of organs such as the brain or heart as an index of tissue energy consumption. Tumor uptake of this tracer was shown to be closely related to the level of cellular proliferation and grades of malignancy[2]. Recent technological advances have opened a new era in this field: i.e., a whole-body, three dimensional (3D) data acquisition[3]. Electronic coincidence detections between all the opposing photon-sensitive crystals are extended from 2D plane to 3D volume, thus yielding higher sensitivity (around 5 fold for detectors with 15 cm axial-length and around 10 fold for those with 20 cm length as in our case). While some difficulties in absolute quantification of isotope distribution due to scatter events in the body are an issue, the high sensitivity should compensate for this problem. Decreases in exposure to radiation and increases in image quality are major benefits[4]. Whole-body imaging is now possible by injection of only 40~75 Mbq (one or two mCi) or less of ^{18}F-FDG. We propose applications of 3D-FDG-PET technique for sports medicine as a tool for non-invasive mapping of working strength of all the muscles in the body.

The subject was a healthy male volunteer, aged 22, 75 MBq of ^{18}F-FDG was injected during running, i.e., an injection was given at 15 minutes after the start of running of total 35 minutes. Running intensity was maintained at the level with heart rates of between 140 and 150 beats per minute, as measured by a wrist pulse monitor. PET measurements were started at 40 minutes after injection using a whole body tomograph, SET2400W (Shimadzu Co, Japan), with an intrinsic spatial resolution of 3.9 mm. The tomograph has 32 rings of BGO crystals separated 3.15 mm in axial dimension covering 20 cm of axial field. The figure shows PET images of the subject lying supine measured by the 3D data acquisition mode. Correction of tissue attenuation was made after the emission acquisition (Post injection transmission) using a needle ^{68}Ge/Ga source.

We found that ^{18}F-FDG uptake increased remarkably in the soleus and gastrocemius muscle, those muscles most suitable for endurance running. Accumulations of ^{18}F-FDG in other muscles including thighs were also noted. The results indicate that PET can specify the

muscles used in any physical activity via markers of whole body energy consumption. The amount of radioactivity required for imaging can probably be reduced to less than 40 MBq. This corresponds to a whole body radiation dose which is around 0.5 mSv equivalent to one half exposure of usual abdominal x-ray examination[5]. PET mapping of muscle activity may provide additional data not only for sports medicine but also for rehabilitation medicine.

References

1) Ido T., Wan C.-N., Casella V. et al., J. Labelled Compounds Radiopharm **14** (1978) 175-183.
2) Chiro G. D., Hatazawa J, Katz D. A. et al., Radiology **164** (1987) 521-526.
3) Bailey D. L., Zito F., Gilardi M. -C. et al., Eur. J. Nucl. Med. **21** (1994) 381-387.
4) Jones T., Eur. J. Nucl. Med. **23** (1996) 207-211.
5) Maccia C., Benedittini M., Lefaure C., et al., Health Physics **4** (1988) 397-408.

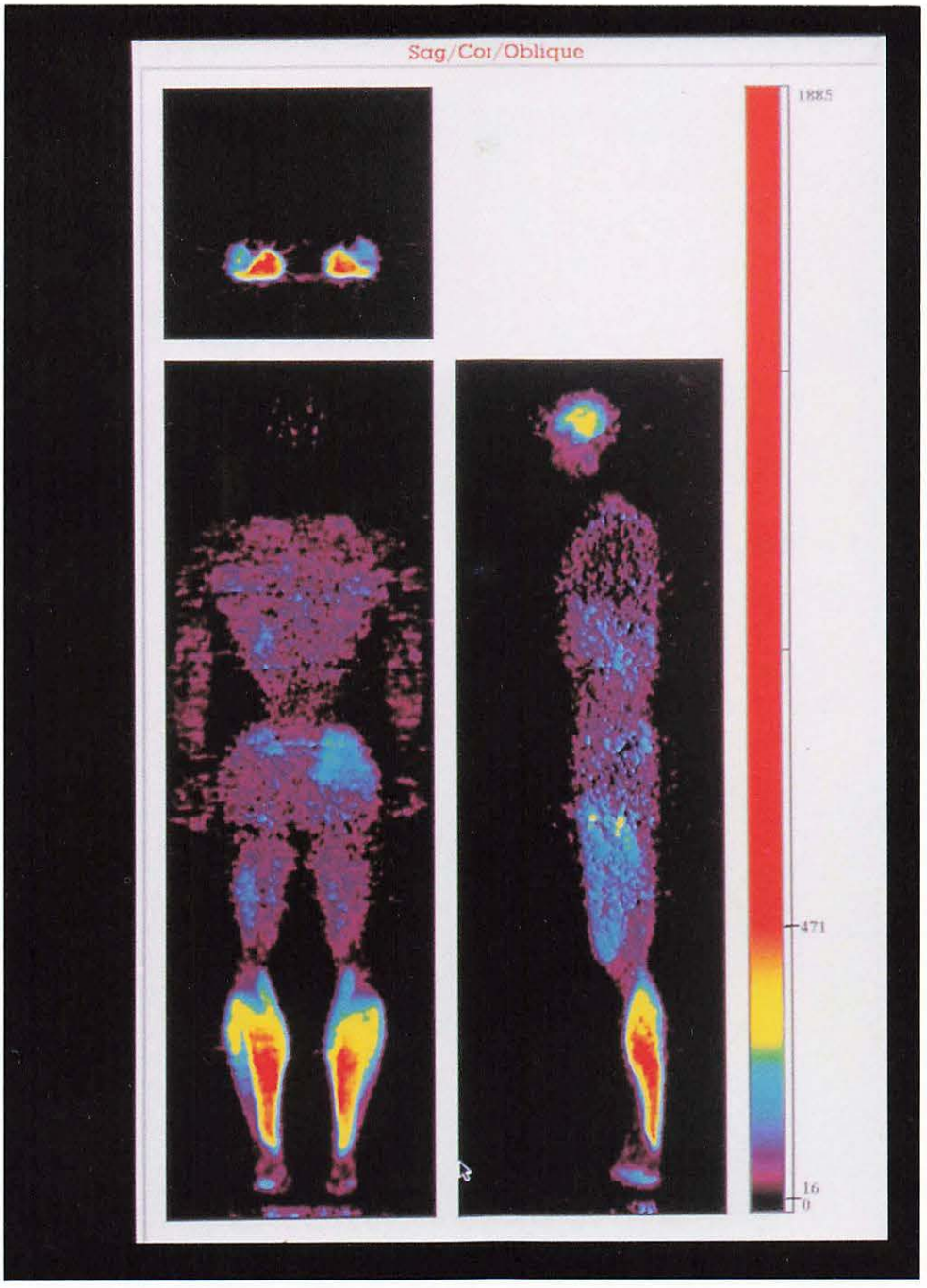

Fig. 1. Whole body PET image of a man lying supine after running.

IV. 7. Functional Mapping of the Brain during Running in the Field Using ^{18}F-FDG PET

Ota H., Tashiro M., Itoh M., Ido T, Fujimoto T***

Divisions of Nuclear Medicine and Nuclear Pharmacology, Cyclotron and Radioisotope Center*
*Department of Medicine and Science in Sports and Exercise, School of Medicine**,*
Tohoku University.

Introduction

Exercise is not only a matter of muscle training but also involves mental effort. Our knowledge of the latter has so far been very limited. Positron emission tomography (PET) has therefore been used to visualize regional brain activation in man as induced by physical exercise.

[^{15}O] labeled water or butanol are the markers of choice in brain activation measurements because the half life of ^{15}O is as short as 2.1 minutes. However, so short a half life can be disadvantageous when investigating subjects engaged in ordinary actions, e.g. running. The functional MRI is also unsuitable for investigating this type of higher brain functions. Using the tracers such as [^{18}F] fluorodeoxyglucose for PET and [^{123}I] iodoamphetamine or [99m] Tc-labled compounds for single photon detection seems to be the only choice at present.

Recently, PET technology has been greatly improved by adopting the three dimensional (3D) data acquisition systems with wide axial field of view. This increases sensitivity of detection by a factor of ten or, inversely, radiation exposure to subjects is reduced to 1/5 or 1/10. 3D data acquisition also shortens the examination time so that the whole body imaging of man has become possible.

In order to test the performance of 3D data acquisition system, we started whole body mapping of energy consumption during running[1]. Here, we report on regional activation of the brain which accompanies field running. The regional cerebral glucose utilization in man is investigated upon exercise using FDG-PET, while taking advantage of the useful property of fluorodeoxyglucose known as metabolic trapping. This method enables observation of the activated regions of the brain during ongoing exercise, which has so far evaded quantification. The method makes the regional neuronal activity visible as the relative strength of averaged activity in a specific span of time. It is suitable for observation of performance in sports and daily life, and may become a new tool of research on "vivid brain imaging" or "brain imaging in life". It departs from an orthodox approach in which a

"pure" condition is investigated with subjects immobile except for specific motion of a particular part of the body.

Materials and Methods

Subjects were eight healthy male Japanese volunteers, aged from 19 to 40 years (average of 24.5±7.3 years). They were requested to run for a total of 35 minutes, with 15 minutes before and 20 minutes after intravenous injection of FDG (1.8±0.4mCi on average). A set of 3D-whole body emission scan was performed for 30 minutes, followed by the post-injection transmission for 30 minutes, using a PET (SET-2400W, Shimadzu Inc, Japan). All subjects were discouraged from eating and drinking for at least three hours before the study and were requested to urinate just before the emission scan. Their running pace was maintained so as to keep their heart rates at 140-150 beats per minute. Seven subjects identically examined at rest (5 males / 2 females, average age 35.9±12.6 years) were included as a control.

The graphical data of brain images were extracted from the whole body data of both experimental and control groups, then realigned and standardized according to Friston et al. using SPM96 (Statistical Parametrical Mapping) software package. The threshold of statistical significance of activation or deactivation between running and control groups was defined at 3.5 in the Z score for the local peak activations.

Results

The results of statistical analyses by SPM showed activation of certain brain regions during running as compared to the control subjects (Fig.1 and Table 1). Activated areas included the occipital and posterior parietal cortices, precentral area and cerebellum on both sides. According to Talirach's atlas, the peaks of activation in the occipital cortex corresponded to the primary visual area (Brodmann's area 17) and the visual association area (areas 18 and 19), those in the posterior parietal cortex to the somatosensory association area (areas 5 and 7), and those in the precentral area to the primary motor area (area 4). The occipital cortex was activated widely and Z score reached 4.53 to 5.61, the value much higher than in any other area. The posterior parietal cortex showed slightly higher statistical significance than that of the precentral area. The precentral area was activated in a relatively small region. Its location corresponded to the area that sends the efferent inputs to contralateral lower extremity and trunk. The activation in the cerebellum was mainly found in the anterior lobe, including the vermis and the intermediate parts of bilateral hemispheres.

Discussion

Unlike fMRI and ^{15}O-water brain activation techniques, the present method requires longer time of measurement. Brain function during the roughly 30 minutes is quantified as FDG uptake reflecting regional energy consumption. To quantify glucose metabolic rate, a

constant steady-state of plasma glucose level is required. Because it is impossible to obtain arterial level of FDG during running, our study has been confined to semiquantitative analysis.

Our results revealed significant activation mainly in the primary and association areas of svisual informantion. The somatosensory association and primary motor areas were also activated, although to a lesser extent. The primary visual area contains neurons which receive visual input from the retinas and have projects to the occipital association areas, in which visual information is processed into its characteritics, e.g. motion, color and shape. The high activation of primary visual and visual association areas suggests that processing of visual information is very important during running, possibly serving the second-to-second renewal of spatial maps of extracorporal space.

The posterior parietal cortex has been reported to be activated by such tasks as mapping of direction in space required for a hand and arm movements[2]. This area may be involved in the execution of movement which is guided by an internal spatial map in the body-oriented coordinates. Single neuron study in monkeys showed that parietal cortex uses information on intended eye movement[3]. The posterior parietal cortex has also been reported to be activated by somatosensory information including proprioceptive inputs and nociceptive or heat stimuli[4]. The present study suggests that the constant changes in the retinal images during running require recalibrations or updates of spacial information and therefore leads to pronounced continuous activation in the posterior parietal cortex.

As to the function of the motor cortex, many reports have been accumulated. The motor function is performed by the coordination of several areas including the primary and supplementary motor areas and premotor area. The supplementary motor and premotor areas are reported to be activated by many different types of motion such as temporal sequencing of multiple movements besides simple motor task. Primary motor area is mostly involved in the execution of motor tasks[5]. A previous study using rCBF measurement in human brain showed increased blood flow in the frontal lobe which may correspond to supplementary motor and premotor area, but no significant change in the precentral area containing primary motor area during exercise on a bicycle ergometer[6]. However, little was known about local cerebral metabolism of glucose in human brain during exercise.

In the cerebellum, the vermis and the intermediate part of the hemisphere together form the spinocerebellum, related to motor control, especially that of ongoing execution of movement. Anterior part of the spinocerebellum (anterior lobe) contains a somatotopic map of the entire body surface and also receives various sensory inputs. The activation of the anterior lobe is compatible with the known physiological data.

We expected that the frontal motor areas associated with execution of movements would be most activated during running. However, our results clearly revealed that it is the occipital brain that is activated, suggesting that abundant visual information from the surroundings is received by, and processed in, the brain.

References

1) Fujimoto T., Itoh M., Kumano H., et al., The Lancet **348** (1996) 266.
2) Kawashima R., Roland Per E., et al., Cerebral Cortex **2** (1995) 111.
3) Duhamel J. R., Colby C. L. and Goldberg M. E., Science **255** (1991) 90.
4) MacKay W. A. and Crammond D. J., Behavioural Brain Research **24** (1987) 167.
5) Tanji J. and Mushiake H., Cognitive Brain Research **3** (1996) 143.
6) Herholz K., Buskies W., et al., Journal of Neurology **234** (1987) 9.

Table. 1 The areas of statistical significance are shown below. (The threshold of statistical significance; Z>3.50)

Region	Brodmann's area	Talairach Coordinates of peak activation			Z score of peak activation
		x	y	z	
primary occipital area	17	10	-76	12	4.81
	17	6	-80	6	4.76
occipital association area	18	-10	-78	4	5.61
	18	14	-80	-2	4.53
posterior parietal area	7	-18	-44	60	3.65
	5-7	14	-42	78	3.94
primary motor area	4	-16	-36	50	3.50
cerebellum (vermis)		-10	-44	-10	3.53
(left hemisphere)		-14	-54	-6	3.51

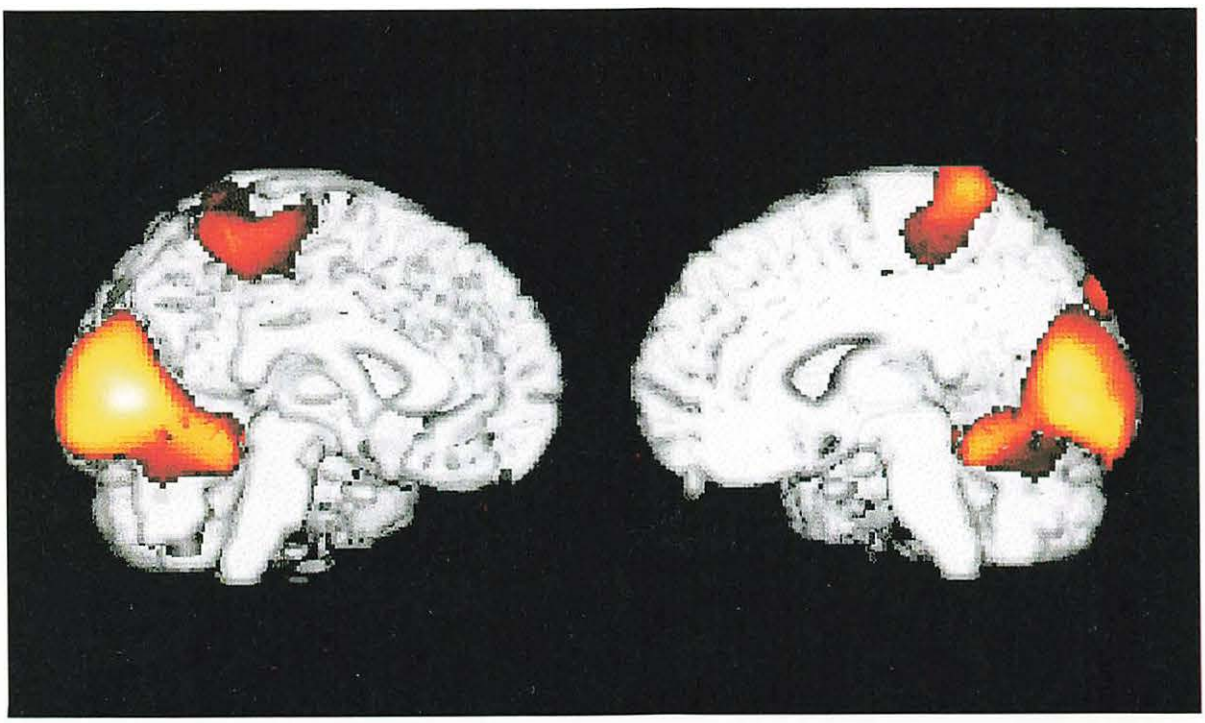

Fig. 1 The graphical display of brain activation (volume rendering). Colored regions represent the areas of statistically significant rise in FDG uptake in runners, with yellow denoting higher significance than red.

IV. 8. A PET Study of Divided Auditory Attention

Goto R., Kawashima R., Satoh K., Ono S. and Fukuda H.

Department of Nuclear Medicine and Radiology, Division of Brain Sciences, Institute of Development, Aging and Cancer (IDAC), Tohoku University

Functional anatomy of auditory attention were investigated in responding vowel targets under presence of distractors and condition of divided attention.

Methods:

The regional cerebral blood flow (rCBF) was measured in 7 right-handed normal healthy male volunteers using positron emission tomography (PET). The subjects wore earphones lying supine with their eyes closed in the PET system. Auditory inputs consisted of random series of five vowels (a,e,i,o,u) with or without coupling of six consonants (h, k, m, n, s, t), namely 35 discriminative monosyllables (for example; a, ki, u, me, ho, tu, i, se, ...). For each subject, two vowels out of five vowels were allocated as auditory targets. The task design was as follows ; Right attention task: Inputs from bilateral ears were different random series of monosyllables and subjects were asked to respond to right side stimuli. Left attention task: Inputs were same as Right attention task, but subjects were asked to respond to left side stimuli. In both cases subjects had to lift their right thumb when they hear any monosyllables containing the allocated two vowels. Divided attention task: Inputs were same as in the Right or Left attention task, but subjects must respond to one of two vowels on one side and another vowel on the other side. All rCBF images were anatomically standardized[1)], then descriptive t-images were calculated to find significant changes between tasks.

Results:

The figure represents commonly activated areas both in Divided attention minus Right attention and Divided attention minus Left attention images. Activations were located in the left lingual gyrus, the right lingual gyrus, the right pulvinar, the left inferior frontal gyrus, the right medial frontal gyrus and the left cingulate gyrus, shown in the figure from left to right.

Conclusions:

In the Divided attention task, regions demonstrated here were Broca's area, thalamus, paralimbic and its adjacent structures. Previous divided attention study on visual discriminations

indicated activations in nonstriated areas as shown here[2]. Various studies recently demonstrated the importance of the cingulate gyrus in attention. The lingual and parahippocampal gyri were involved in human memory function. The pulvinar was supposed to participate in focal attention combined with scrutinizing. In conclusion, our result suggests that between areas disposing sensory input and involving attention and memory subsist the areas collating these informations.

References

1) Roland P.E. et al. Hum. Brain Map. 1994, 2:1.
2) Corbetta M. et al. The Journal of Neuroscience, August 1991, *11* (8): 2383.

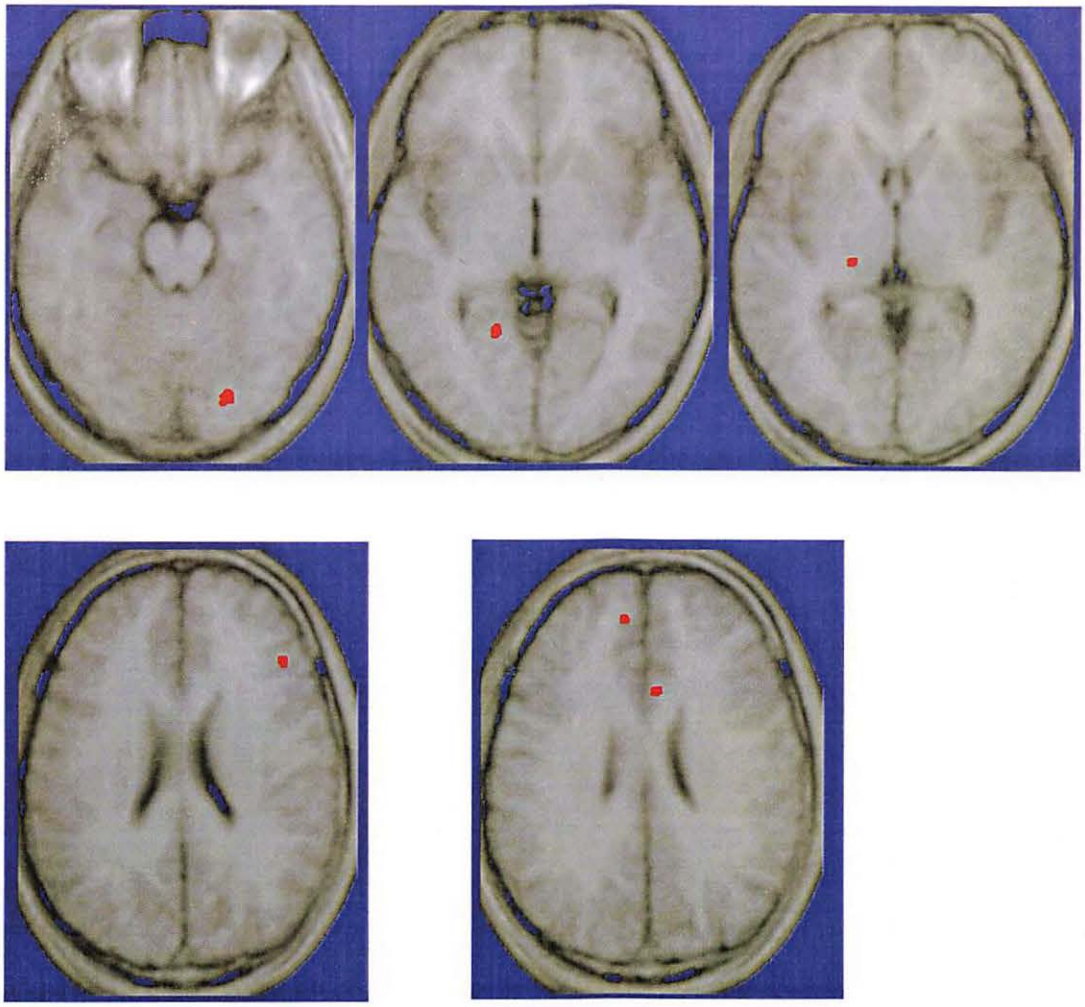

Fig. 1. The location of the specific activation areas supposed to be relevant to divided attention. Sections are -18, -1, 3, 22 and 25 mm above AC-PC line from the left side to the right side of the figure. The regions are the left lingual gyrus, the right lingual gyrus and the right pulvinar (upper column) ; the left inferior frontal gyrus, the right medial frontal gyrus and the left cingulate gyrus (lower column), pointed from the left side to the right side of the figure.

IV. 9. A PET Study of Memory for Future Plan

Okuda J., Fujii T., Yamadori A., Kawashima R., Fukatsu R.**, Suzuki K., Tsukiura T., Motooka N., Ito M.*** and Fukuda H.**

Graduate School of Medicine, Tohoku University
*Institute of Development, Aging & Cancer (IDAC), Tohoku University**
*Department of Neurology, Miyagi National Hospital, Miyagi, Japan***
*Cyclotron and Radioisotope Center, Tohoku University****

Introduction

A number of neuroimaging studies on memory systems in humans have revealed that specific regions are associated with encoding or retrieving experienced episodes, i.e., events of the past[1-5]. There may be another type of memory which we need in everyday life. This is called prospective memory and is defined as an ability to remember future plans[6]. This ability of not forgetting to do a necessary task at a certein time in the future has been suggested to be associated with activities of the frontal lobes[7-9]. The aim of this study is to investigate possible neural basis involved in prospective memory using the neuroimaging technology of PET.

Methods

Subjects

Six healthy young male volunteers participated. All subjects were right handed. A written informed consent was obtained from each subject.

Task design

Subjects performed two tasks, i.e., a control task and an experimental task, which were arranged to be preceded by a pre-scan learning period and to be followed by a post-scan recall period. The subjects repeated both tasks in random order. In a learning period, the subjects were auditorily presented with the lists of 10 stimuli of Japanese noun words three times in a row and were required to retain these words as target stimuli throughout the PET scan. In a recall period immediately after the PET scan, the subjects were asked to recall the 10 stimuli. In a scan period, the subjects heard a set of 5 stimuli of Japanese noun words from a tape recorder through a pair of earphones in the rate of one word per second and were required to repeat orally the set of stimuli within a blank duration of 7 seconds. The subjects repeated this sequence 10 times during the scan. Further, only in the experimental task, list of

stimuli was set to include the target stimuli with very low frequency (2 or 3 times during whole list) and the subjects were instructed to notice if one of them appeared or not. If it appeared, the subjects had to tap their left hand while repeating it orally.

Scanning Methods and Regional Analysis

Regional cerebral blood flow (rCBF) was measured using PET (SET2400W, Shimadzu) and ^{15}O labeled water (approximately 35 mCi for each injection). Subjects had a catheter placed into the right brachial vein for tracer administration, closed their eyes, and wore an individual stereotaxic fixation helmet. Each PET data acquisition started at the time of bolus injection and the start of word repetition task, and lasted 120 sec. All rCBF images were transformed into the standard anatomical format using Human Brain Atlas System[10] and each subject's MRI. Then all standardized rCBF images were smoothed with a three dimensional Gaussian filter 10mm in wide and normalized for global cerebral blood flow of 50 ml per 100 g per min[11-12]. The comparison between the control task and the experimental task was performed by 2 way analysis of variance (ANOVA, two tasks and six subjects as factors). Namely, image of F- values for differences between tasks was calculated on a voxel by voxel basis and voxels with F-values >11.8 ($p<0.005$) were considered to represent regions of significantly increased rCBF. Each activation was superimposed onto the average reformatted MRI of the six subjects. Finally, anatomical localization of areas of activation was estimated in relation to this MRI.

Results

Behaviorally, the mean rate of the subjects' averaged performance of repetition of words in the experimental task was 0.77 and one in the control task was 0.81. The mean rate of successful execution of tapping the left hand during the experimental task was 0.63.

When compared with the control task, regions with significantly increased rCBF during the experimental task were as follows (Table 1, Fig. 1); the left superior frontal gyrus (Brodmann Area, BA 10), anterior cingulate gyrus (BA 24), parahippocampal gyrus (BA 28), the right inferior frontal gyrus (BA 47), middle frontal gyrus (BA 8, 9) and medial frontal lobe (BA 8).

Discussion

Our results provide an evidence that frontal lobe is related to processes involved in prospective memory. The activations of the prefrontal and hippocampal areas may reflect mental processes of memory for the future plan, i.e., tapping the left hand in response to the target item memorized before, during the routine task of word repetition. We suppose that the results may mainly be associated with a process of retention of the encoded behavioral plan, because retrieval and execution of the plan rarely occurred during the task.

In preceding neuroimaging studies, the lateral frontal lobes were activated in relation with encoding and retrieval of episodic/semantic memory[13], and with working memory paradigm[14-15]. Our experimental design seems similar to dual task paradigm of working memory. The lateral frontal activation might be related to the temporary retention and reference of primarily stored information.

On the other hand, activations of the medial frontal region were reported during attention shifting task like Stroop test[16-17]. Frequent checking whether a presented item is the target or not requires frequent shift of attention, which might have caused the medial frontal lobe activation in the present study.

Another important finding in the results is the left hippocampal activation. In our preceding PET study, we reported that activation of the left parahippocampal region was associated with non-matching to sample strategy of verbal recognition[18]. In connection with this result, neurophysiological study also showed that the hippocampal regions were involved in novelty detection of non-verbal materials[19]. We suppose that the same mechanism underlies the left hippocampal activation in the present study, because our experimental task clearly involved a number of non-matching to sample operations (i.e., novelty detection) than matching operation.

Acknowledgment

This work was supported by a Grant-in Aid(08279103) for scientific research from the Ministry of Education, Science and Culture, Japan.

References

1) Buckner, R.L., Petersen, S. E., Ojemann, J. G., et al., J. Neurosci. **15** (1995) 12.
2) Grasby, P. M., Frith, C. D., Friston, K.J., et al., Brain **116** (1993) 1.
3) Kapur, S., Craik, F. I. M., Tulving, E., et al., Proc. Natl. Acad. Sci. USA **91** (1994) 2008.
4) Shallice, T., Fletcher, P., Frith, C.D., et al., Nature **368** (1994) 633.
5) Tulving, E., Kapur, S., Markowitsch, H.J., et al., Proc. Natl. Acad. Sci. USA **91** (1994) 2012.
6) Meacham, J.A. & Leiman, B., In: Neisser U., ed. Memory observed: Remembering in natural contexts. San Francisco: Freeman, (1982) 327.
7) Cockburn, J., Cortex **31** (1995) 87.
8) Cockburn, J., J. Clin. Exp. Neuropsychol. **18** (1996) 304.
9) Maylor, E.A., Neurocase **1** (1995) 285.
10) Roland, P., Graufelds, C. J., Wahlin, J., et al., Hum. Brain Map. **1** (1994) 173.
11) Herscovitch, P., Markham, J. & Raichle, M. E., J. Nucl. Med. **24** (1983) 782.
12) Raichle, M. E., Martin, W. R. W., Herscovitch, P., et al., J. Nucl. Med. **24** (1983) 790.
13) Tulving, E., Kapur, S., Craik, F. I. M., et al., Proc. Natl. Acad. Sci. USA **91** (1994) 2016.
14) Petrides, M., Alibisatos, B., Evans, A. C. et al., Proc. Natl. Acad. Sci. USA **90** (1993) 873.
15) Petrides, M., Alibisatos, B., Meyer, E., et al., Proc. Natl. Acad. Sci. USA **90** (1993) 878.
16) Bench, C. J., Frith, C. D., Grasby, P. M., et al. Neuropsychologia **31** (1993) 907.
17) Pardo, J. V., Pardo, P. J., Janer, K.W., et al., Proc. Natl. Acad. Sci. USA **87** (1990) 256.
18) Fujii, T., Okuda, J., Kawashima, R., et al. NeuroReport **8** (1997) 1113.
19) Knight, R. T. Nature **383** (1996) 256.
20) Talairach, J. & Tournoux, P. Co-Planar Stereotactic Atlas of the Human Brain. Stuttgart: Thieme (1988).

Table 1. Activation foci during the experimental task.

	Anatomical structures	Talairach coordinates x	y	z	peak F-value
Left	Anterior cingulate gyrus (24)	-10	32	8	26.3
	Superior frontal gyrus (10)	-11	66	14	33.9
	Parahippocampal gyrus (28)	-20	-16	-9	19.9
Right	Inferior frontal gyrus (47)	34	18	-16	62.1
	Middle frontal gyrus (9)	35	26	38	13.5
	Middle frontal gyrus (8)	31	12	51	20.0
	Medial frontal lobe (8)	0	40	41	19.1

Regions with significantly increased rCBF during the experimental task compared with the control task. Stereotaxic coordinates refer to the maximal activation indicated by the highest F-values in a particular cerebral structure. Distances refer to the stereotactic space defined by Talairach and Tournoux[20]. Numbers in parenthesis refer to Brodmann areas.

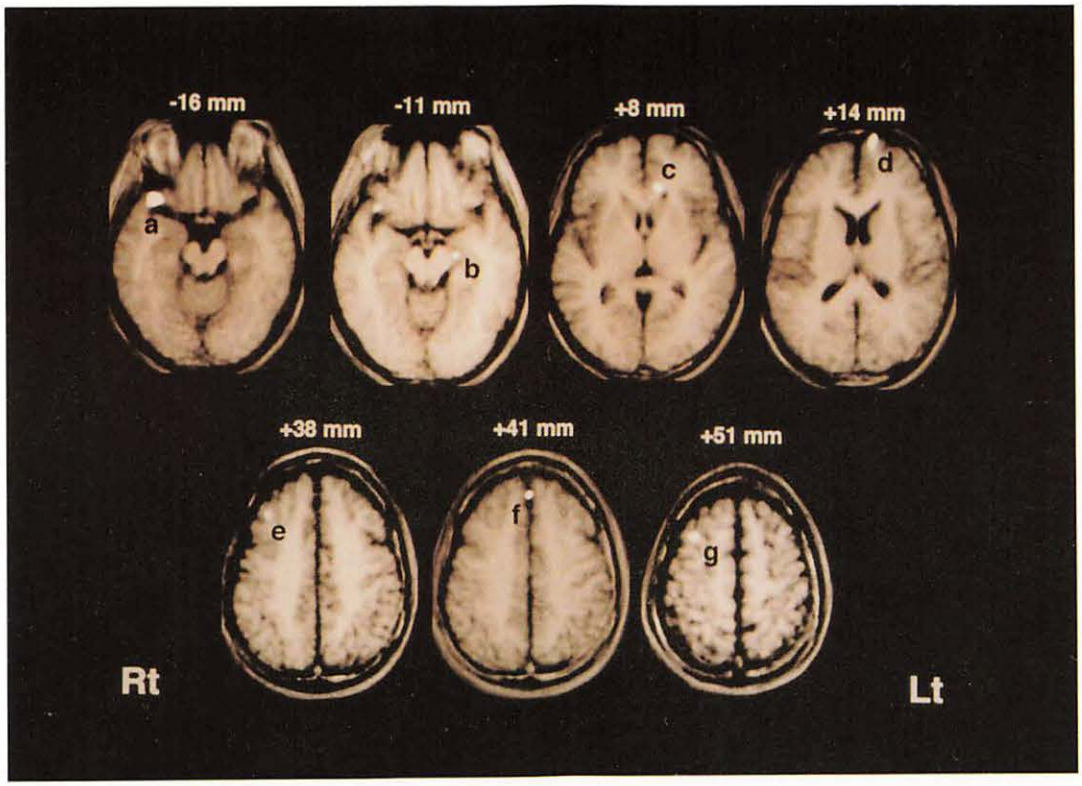

Figure 1. Significantly activated areas (F>11.8, p<0.005) during the experimental task superimposed onto axial sections of averaged MRI of the subjects. Each section's distance from AC-PC line was noted above each section. The left side of the section refers to the right side of the brain. a) The right inferior frontal gyrus (BA 47), b) the left parahippocampal gyrus (BA 28), c) the anterior cingulate gyrus (BA 24) and part of the corpus callosum, d) the superior frontal gyrus (BA 10), e) the right middle frontal gyrus (BA 9), f) the medial frontal lobe (BA 8), g) the right middle frontal gyrus (BA 8).

IV. 10. A PET study of Pointing with Visual Feedback of Moving Hands

Inoue K., Kawashima R., Satoh K., Kinomura S., Itoh M., and Fukuda H.*

Department of Nuclear Medicine and Radiology, IDAC, Tohoku University
*Cyclotron and Radioisotope Center, Tohoku University**

Introduction

To make accurate reaching movements with the arm, complex neural transformations from visual and somatosensory inputs through to motor outputs are required. It is widely believed that several brain areas are involved in these neural operations. Recent positron emission tomography (PET) studies of humans performing visually guided finger or hand movement revealed many areas to demonstrate significant increases in regional cerebral blood flow (rCBF), including the primary motor area, the premotor area, the supplementary motor area, the superior parietal lobule, the cingulate cortex, the occipital areas, the superior frontal area, the basal ganglia, the thalamus and the cerebellum[1-2, 6-8]. Nevertheless, none of the previous PET studies has specifically attempted to relate rCBF changes to the neural operations which use visual information on hand movement to execute accurate reaching movements.

The present study was therefore designed to examine where in the human brain visual feedback of hand movements is processed and utilized to allow accurate pointing. To do this, we measured changes in rCBF using ^{15}O-labeled water ($H_2{}^{15}O$) and PET during performance of pointing tasks with and without visual feedback of moving hand.

Methods

Subjects

Nine right-handed normal male volunteers (aged 19-26 years) participated in this study. Handedness was assessed by the H.N.Handedness Inventory[3]. Written informed consent was obtained from each subject in accordance with the guideline approved by Tohoku University and the Declaration of Human Rights, Helsinki, 1975. A high resolution MRI scan (0.5T) was also performed on a separate occasion.

Task Procedure

Each subject wore an individual stereotaxic fixation helmet and a head mounted display (i-glass; Virtual I/O, USA) (HMD) during the PET measurements. A black board bearing six red light emitting diodes (LEDs) aligned on a circle with a10cm radius 10cm apart

from neighboring LEDs with a green LED at the center was set at a distance about 50cm in front of the subjects. A CCD camera (XC-999; SONY, Japan) was fixed on the helmet so that the LEDs could be captured at the center of its field of view. These LEDs and the subject's hand movements were monitored using the CCD camera (Figure 1). In all tasks, the center green LED and one of the target six red LEDs were alternately switched on and off. Visual stimuli were presented to the subjects on the HMD.

Each subject performed the following three tasks during PET measurement: (1) a control task, (2) a reaching with visual feedback (R-with-F) task and (3) a reaching without visual feedback (R-without-F) task. In the control task, subjects were asked to hold their right hand on their chests in a pointing shape and to simply look at each LED as it was illuminated. In the R-with-F task, the subjects were instructed to point to the lit target LED with the right index finger with a natural pointing hand shape, and to return the hand to a resting position on the chest after each trial. In this task, the view of LEDs and subject's moving hand near the target were presented to the subject through the HMD. In the R-without-F task, the subjects were instructed as for the R-with-F task, but they couldn't monitor their hands. In this task, the sequence of LED lighting previously recorded on a videotape was presented on the HMD.

The performance of each subject was recorded with a videorecorder (30frames/sec.). The number of movements, reaction time (duration from the target LED lighting to the beginning of movement), movement time (duration from the beginning of movement to the pointing to the target), pointing error (the distance from the position of the finger tip to the target position) and the finger tip trajectories for each reaching task were determined by frame by frame analysis of video recordings.

PET *measurements*

Each subject was placed comfortably in a supine position on a PET scanner (Shimadzu SET2400W, FWHM 4.0mm)[5]. A transmission data of the subject in the same position by the use of a ^{68}Ge source was used to correct for attenuation. The rCBF was measured after administration of a bolus injection of approximately 30mCi (1110MBq) $H_2{}^{15}O$. The control task and the R-without-F task were started 30sec prior to the bolus injection. The R-with-F task was started 3 min prior to the bolus injection to allow the subjects to become accustomed to make reaching movements with the HMD monitoring. Each PET measurement was commenced immediately after radioactive counts were monitored on the PET camera and was continued for a period of 60 secs. PET scans were converted to relative rCBF images using a modified autoradiographic method[4,9]. All PET images were smoothed with a three dimensional Gaussian filter of 10 mm wide, then normalized for global cerebral blood flow of 50ml/100g/min.

In the present study, standard anatomical structures of a human brain atlas (HBA) system[10] were fitted interactively to each subject's MRI using both linear and nonlinear parameters. These parameters were subsequently applied to transform normalized rCBF PET

images into the standard brain anatomy. After the anatomical standardization of the rCBF images, we made voxel-by-voxel subtraction pictures of the R-without-F from R-with-F images as well as the control from each reaching task images for each subject. Then, mean and variance pictures and descriptive Student's t-pictures for each subtraction were calculated. In the present study, voxels with t-values > 3.355 ($p<0.005$, without correction for multiple comparisons) were considered to represent regions of significantly changed rCBF in each reaching task minus control task image. The voxels showing statistically significantly increases in rCBF not only in the R-with-F minus control image but also in the R-with-F minus R-without-F image were considered to represent the specific activation fields related to the visual perception of the moving hand and the pointing position, the information processing to make motor commands to correct movements based on the visual feedback and the execution of corrective movements per se.

Finally, each activation was then superimposed onto the average reformatted MRI of the same 9 subjects involved in this study. Anatomical localization of areas of activation in each subtraction was made in relation to the mean reformatted MRI.

Results and discussion

The mean (SD) number of reaching movements during PET measurment in the R-with-F task and the R-without-F task were 19.6 (0.7) and 19.3 (0.3), respectively. The mean (SD) reaction time for reaching movements during PET measurement in the R-with-F and the R-without-F tasks were 0.31 (0.05) sec and 0.31 (0.05) sec, and the mean (SD) movement time were 0.49 (0.16)sec and 0.49 (0.13)sec, respectively. The mean (SD) pointing error in the two cases were 1.6 (1.1) cm and 5.4 (3.5) cm, respectively, the difference being statistically significant ($P<0.0001$, two sample t-test)

Table 1 summarizes the data on anatomical structures, Talairach coordinates[11] and t-values of peak activation in the R-with-F task minus control and R-without-F task minus control images. Among them, six fields showed significant activation not only in the R-with-F task minus control images but also in the R-with-F task minus the R-without-F task images (Figure 2). In the parietal cortex, there was one in the supramarginal gyrus of the left hemisphere. In the frontal cortex, a field was found in the dorsal part of the premotor cortex of the left hemisphere. The orbito-frontal cortex of right hemisphere was also activated. Another field was located in the ventral lip of the posterior part of cingulate sulcus of the left hemisphere. The other three fields were located in the caudate head, the lateral part of thalamus of the right hemisphere and the vermis.

In this study, we demonstrated fields of activation related to reaching with and without the visual feedback of hand movements. The principal finding was that the fields of activation were identified in the supramarginal gyrus, the posterior part of the cingulate cortex and the dorsal premotor cortex in the left hemisphere specific to the R-with-F tasks. The results may

indicate that these areas may play important roles in integrating visual feedback from hand movements and movement execution with right hand.

References

1) Grafton S. T., Mazziotta J. C., Woods R. P. et al., Brain **115** (1992) 565.
2) Grafton S. T., Fagg A. H., Woods R. P. et al., Cereb. Cortex **6** (1996) 226.
3) Hatta, T. and Nakatsuka, Z. Handedness Inventry. In: Papers on Celebrating 63rd Birthday of Prof. Ohnishi, edited by Ohno, D., Osaka: Osaka City University, (1975) 224.
4) Herscovitch P., Markham J., and Raichle M. E. J. Nucl. Med. **24** (1983) 782.
5) Iida, H., Miura, S., Kanno, I., et al. A new PET camera for noninvasive quantification of physiological functional parametric image Headtome-V-Dual. In: Quantification of Brain Function., edited by Uemura, K., Lassen, N. A., Jones, T., and Kanno, I., New York: Academic Press, (1996) 57.
6) Kawashima R., Roland P. E., and O'Sullivan B. T. J. Neurosci. **14** (1994) 3462.
7) Kawashima R., Roland P. E., and O'Sullivan B. T. Cereb. Cortex **2** (1995) 111.
8) Matsumura M., Kawashima R., Naito E., et al. Neuroreport **7** (1996) 749.
9) Raichle M. E., Martin W. R. W., Herscovitch P., et al. J. Nucl. Med. **24** (1983) 790.
10) Roland P. E., Grafelds C. J., Wahlin J., et al., Hum. Brain Map. **2** (1994) 1.
11) Talairach, J. and Tournoux, P. Co-planar stereotaxic atlas of the brain., New York: Thieme. (1988).

Table 1. Fields demonstrating statistically sigificantly activation specific to the R-with-F task.

Table 1. Fields of significant activation. (P<0.005, without correction for multiple comparison)

Anatomical structures	Talairach coordinates and t-values of peak activation			
	x	y	z	t
Right hemisphere				
Thalamus	-17	-23	1	7.8
Caudate	-12	22	3	7.7
Cerebell.~vermis	-24	-64	-45	10.7
Vermis	-1	-53	-42	7
Left hemisphere				
Supramarginal	48	-38	22	6.1
Premotor	12	-7	47	7.5
Posterior cingulate	20	-40	39	5.2

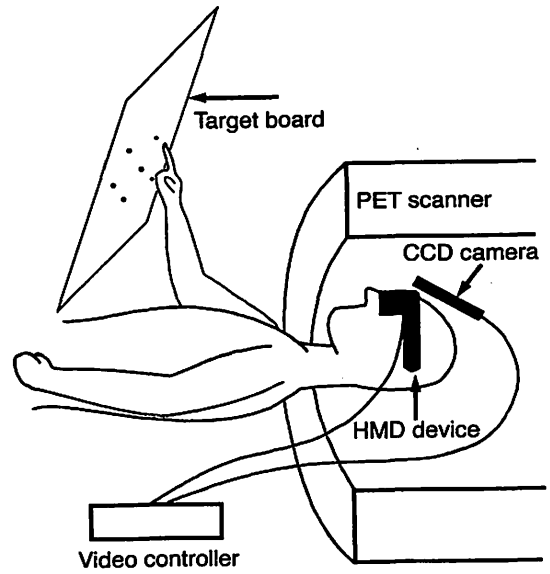

Fig. 1. Experimental setup. The subject was placed in a supine position on the PET scanner wearing the HMD over the fixation helmet (not shown). The CCD camera was fixed on the helmet. The subject was instructed to point at a lit target LED on the target board in front of him with or without being able to monitor the hand movement.

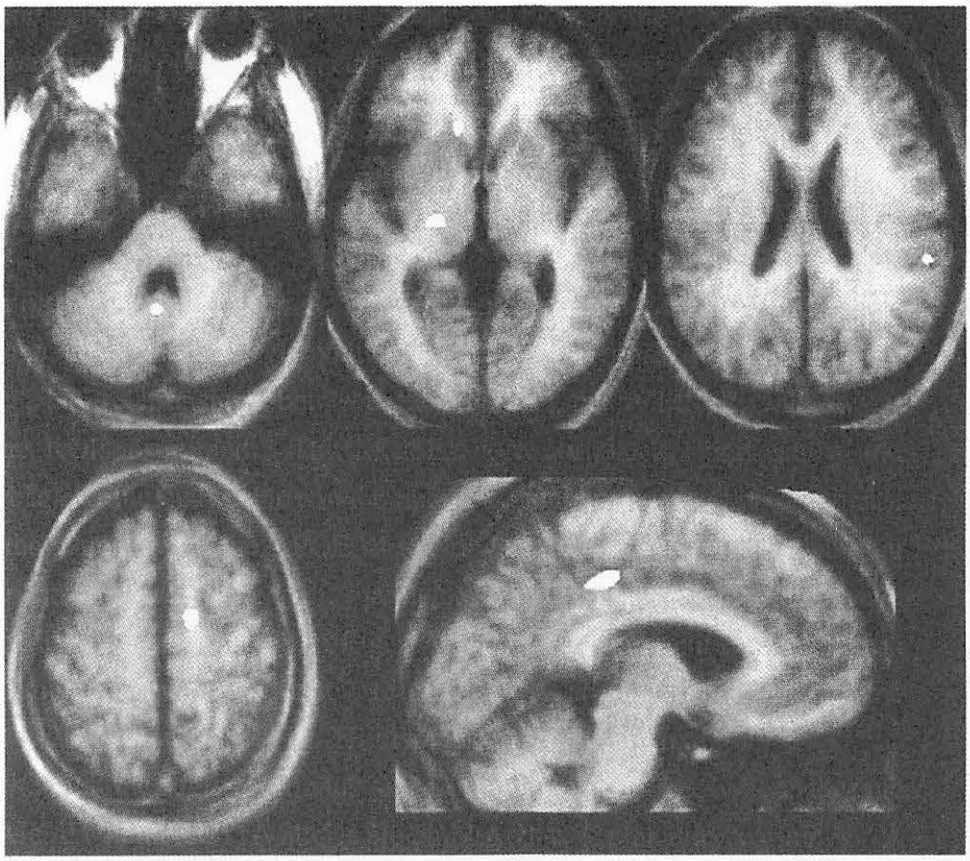

Fig. 2. Statistically significant fields of activation specific to the R-with-F task are shown in white, superimposed on the normalized mean MRI image. The four axial sections (upper row and lower left) are -32, 1, 22, and 51mm above the anterior- posterior commissural line. The anatomic right is on the left side of the figure. The sagital section (lower right) is 6mm left to the midline.

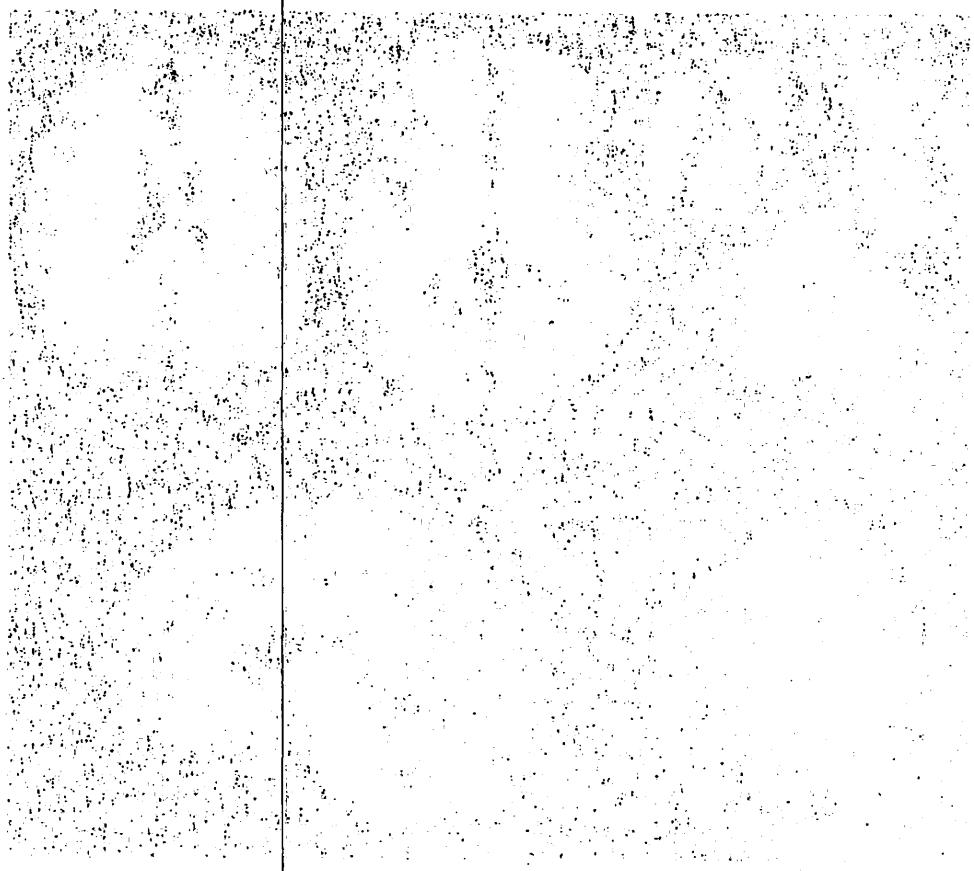

IV. 11. Influences of Apolipoprotein E and α_1-Antichymotrypsin Genotypes on Regional Cerebral Glucose Metabolism in Alzheimer's Disease

Miyama N., Higuchi M., Arai H.*, Itoh M., Nakagawa T.*, Kosaka Y.*, Matsui T.*, and Sasaki H.**

Cyclotron and Radioisotope Center, Tohoku University
*Department of Geriatric Medicine, Tohoku University School of Medicine**

Introduction

Alzheimer's disease (AD) is a neurodegenerative disorder that results in a progressive loss of intellectual functions. The aplolipoprotein E (APOE) ε4 allele has been demonstrated to have a strong association with late-onset familial and sporadic AD as a major susceptibility or risk factor gene[1]. Further, the α_1-antichymotrypsin (ACT) type A allele (ACT*A) also has been indicated to be a risk factor for AD[2,3]. However, the roles played by these risk factors in the functional impairment or death of neurons in specific groups during the AD process are still enigmatic.

The present study was aimed to elucidate the effects of the APOE and ACT genotypes on the neuronal functions in specific populations, examining cerebral glucose metabolism by using positron emission tomography (PET) and ^{18}F-2-fluoro-2-deoxy-D-glucose (FDG) for AD patients with defined APOE and ACT genotypes.

Subjects and methods

Twenty patients with sporadic AD (7 males and 13 females, mean age ±SD: 67.6 ±8.2 years, range 49 to 82 years) were examined. The profiles of these patients including the severity and progression of dementia assessed by Mini-Mental State Examination (MMSE) are summarized in Table 1.

Genomic DNA was extracted from peripheral leukocytes, and allelic polymorphisms of the APOE and ACT genes were determined as described elsewhere[2-4].

A PET scan with FDG and ECAT PT931 (CTI Inc, Knoxville, TN, USA) scanner was performed for each patient under a resting condition. Parametric images of the regional cerebral metabolic rate of glucose (rCMRglc) were constructed by means of the autoradiograpic method described by Hutchins et al.[5] Twenty-three regions of interest (ROIs) were placed on these calculated images by referring to the individual magnetic resonance (MR) images, and the rCMRglc values in these ROIs were determined.

A simple linear regression approach was employed for analyzing the correlations of the age, MMSE score and gene doses of the APOE ε4 and ACT*A with the rCMRglc value in each ROI. These relationships also were examined by a multiple regression analysis.

Results

The list of the APOE and ACT genotypes for the patients examined in this study is shown in Table 1.

The coefficients of correlation of the age, MMSE score and gene doses of the APOE ε4 and ACT*A with the absolute rCMRglc value by the simple regression analysis are contained in Table 2A. No relationships between the age and the rCMRglc value were observed in any of the ROIs examined. The MMSE score correlated significantly and positively with the rCMRglc value, particularly in the middle frontal areas ($p < 0.01$ by t-test). The rCMRglc value in the patients with the APOE ε4 allele was significantly higher than that in the non-APOE ε4 carriers in a dose-dependent manner, especially in the frontal areas ($p < 0.05$ by t-test). A typical example is depicted in Fig. 1A. There was a significant reduction of the rCMRglc with an increasing gene dose of the ACT*A allele, particularly in the temporo-parietal areas ($p < 0.05$ by t-test). Fig. 1B displays a typical example.

The results of the multiple regression analysis are shown in Fig. 2B, where the age and gene doses of the APOE ε4 and ACT*A alleles are employed as explanatory variables. A strong and positive correlation between the gene dose of the APOE ε4 allele was found, especially in the frontal and temporal areas ($p < 0.01$ or $p < 0.05$ by t-test). On the other hand, the gene dose of the ACT*A allele correlated strongly and negatively with the rCMRglc value in the temporal and parietal areas ($p < 0.01$ or $p < 0.05$ by t-test).

Little correlation between the gene doses of each allele and the rCMRglc value was observed in the paracentral and primary visual cortices, thalamus, striatum, pons and cerebellum in the simple and multiple regression analyses.

Discussion

Recent PET studies have indicated that the changes in cerebral glucose metabolism frequently present an anterior-posterior heterogeneity in AD patients[6]. Moreover, this heterogeneous pattern has been demonstrated to be associated with the clinical heterogeneity in AD, and to show no change with the progression of AD, suggesting that some 'stable' factors such as genetic factors may play a role in forming these functional and clinical heterogeneities[6].

The rCMRglc in the fronto-temporal areas were found to be preserved in the AD patients with the APOE ε4 allele. This suggests that the APOE gene alone does not affect the progression of AD adversely, once the disease is triggered. No or rather 'protecting' effect of APOE ε4 allele on the progression of AD also has been indicated in recent studies for evaluating the clinical correlates of this allele[7,8].

There was a significant reduction of the cerebral glucose metabolism in the patients carrying the ACT*A allele, especially in the areas typically involved in AD. Although the ACT protein consistently co-localizes with Aβ in senile plaques, the association of the ACT genotype with AD remains unsettled[9]. Further investigations for seeking pathological and / or clinical correlates of the ACT polymorphism are required.

The present study employed analyses with multiple ROIs, and there may be a problem of an excessive multiple comparison that produces a possibility of a spurious significance. The areas with a significant correlation, however, were spatially adjacent to form large areas, suggesting a biological meaningfulness of our results.

References

1) Strittmatter W. J., Saunders A. M., Schmechel D., et al. Proc. Natl. Acad. Sci. U. S. A. **90** (1993) 1977.
2) Kamboh M. I., Sanghera D. K., Ferrell R. E., et al. Nature Genetics **10** (1995) 486.
3) Muramatsu T., Matsushita S., Arai H., et al. J. Neural Transm. **103** (1996) 1205.
4) Wenham P. R., Price W. H., Blundell G., et al. Lancet **337** (1991) 1158.
5) Hutchins G. D., Holden J. E., Koeppe R. A., et al. J. Cereb. Blood Flow Metab. **4** (1984) 35.
6) Haxby J. V., Grady C. L., Koss E., et al. Neurology **38** (1988) 1853.
7) Frisoni G. B., Govoni S., Geroldi C., et al. Ann. Neurol. **37** (1995) 596.
8) Growdon J. H., Locascio J. J., Corkin S., et al. Neurology **47** (1996) 444.
9) Haines J. L., Pritchard M. L., Saunders A. M., et al. Genomics **33** (1996) 53.

Table 1. Summary of the patients' profile examined here.

Patient No.	Age (years)	Sex	MMSE (/30points)	Genotypes	
				APOE	ACT
1	49	F	18	4/3	-
2	56	M	25	4/3	A/A
3	59	M	26	3/3	A/T
4	62	F	18	4/3	A/A
5	62	M	6	3/2	-
6	64	F	22	3/3	T/T
7	66	F	21	4/4	T/T
8	66	M	20	3/3	A/A
9	67	F	17	4/3	-
10	67	F	21	4/3	A/T
11	67	F	26	4/3	-
12	67	M	24	4/3	A/T
13	68	F	20	4/3	T/T
14	70	F	23	4/4	T/T
15	70	F	24.5	4/4	T/T
16	71	F	14.5	4/3	T/T
17	79	F	11	4/3	A/T
18	79	F	5	4/4	A/T
19	80	M	17	3/3	-
20	82	F	24	3/3	-
mean	67.6		19.2		
S. D.	8.21		6.10		

- : Data not available

Table 2. 2A) Simple correlation coefficients of rCMRglc to the age, the MMSE score and the gene doses of APOE ε4 and ACT*A. Significance of each coefficient is tested by t- statistic.
2B) Partial correlation coefficients and determination coefficients calculated by multiple regression analysis for rCMRglc values. R^2 means coefficient of determination. The age and the gene doses of APOE ε4 and ACT*A are used as predictor variables without selection.

2A

ROI	Age	APOE ε4	ACT*A	MMSE
Upper lateral frontal	0.126	0.472 *	-0.545 *	0.508 *
Middle lateral frontal	0.099	0.482 *	-0.389	0.597 **
Lower lateral frontal	0.046	0.511 *	-0.368	0.492 *
Upper medial frontal	0.134	0.486 *	-0.498	0.517 *
Middel medial frontal	0.096	0.535 *	-0.515	0.565 **
Lower medial frontal	0.016	0.534 *	-0.500	0.530 *
Upper lateral temporal	0.029	0.282	-0.517	0.404
Middle lateral temporal	0.015	0.300	-0.492	0.455 *
Lower lateral temporal	0.044	0.372	-0.601 *	0.428
Medial temporal	-0.048	0.400	-0.563 *	0.401
Upper lateral parietal	0.188	0.263	-0.802 **	0.316
Lower lateral parietal	0.166	0.238	-0.708 **	0.462 *
Temporo-parietal junction	0.143	0.223	-0.727 **	0.407
Upper medial parietal	0.119	0.243	-0.675 **	0.242
Lower medial parietal	0.157	0.216	-0.557 *	0.349
Lateral occipital	0.240	0.205	-0.646 *	0.279
Medial occipital	0.094	0.308	-0.481	0.377

2B

ROI	Age	APOE ε4	ACT*A	R^2
Upper lateral frontal	-0.6495 *	0.6908 *	-0.6275 *	0.6781 **
Middle lateral frontal	-0.6416 *	0.7161 **	-0.4314	0.6271 *
Lower lateral frontal	-0.4960	0.6850 *	-0.3206	0.5528 *
Upper medial frontal	-0.5745	0.6344 *	-0.5390	0.5922 *
Middel medial frontal	-0.8373 **	0.8617 **	-0.7333 **	0.8460 **
Lower medial frontal	-0.6851 *	0.7383 **	-0.5955 *	0.7010 **
Upper lateral temporal	-0.5982 *	0.6146 *	-0.5774 *	0.6011 *
Middle lateral temporal	-0.6560 *	0.7109 **	-0.5696	0.6684 **
Lower lateral temporal	-0.5572	0.6828 *	-0.6435 *	0.6783 **
Medial temporal	-0.5962 *	0.7017 *	-0.6174 *	0.6781 **
Upper lateral parietal	-0.3502	0.6129 *	-0.8102 **	0.7781 **
Lower lateral parietal	-0.4962	0.5620	-0.7347 **	0.6825 **
Temporo-parietal junction	-0.4306	0.4365	-0.7379 **	0.6459 *
Upper medial parietal	-0.2468	0.3678	-0.6426 *	0.5346 *
Lower medial parietal	-0.2124	0.2715	-0.5189	0.3695
Lateral occipital	-0.2220	0.3352	-0.6070 *	0.4868
Medial occipital	-0.3581	0.5355	-0.4366	0.4600

*$p < 0.05$, **$p < 0.01$ by t-test (for each parameter) or by ANOVA (for R^2).

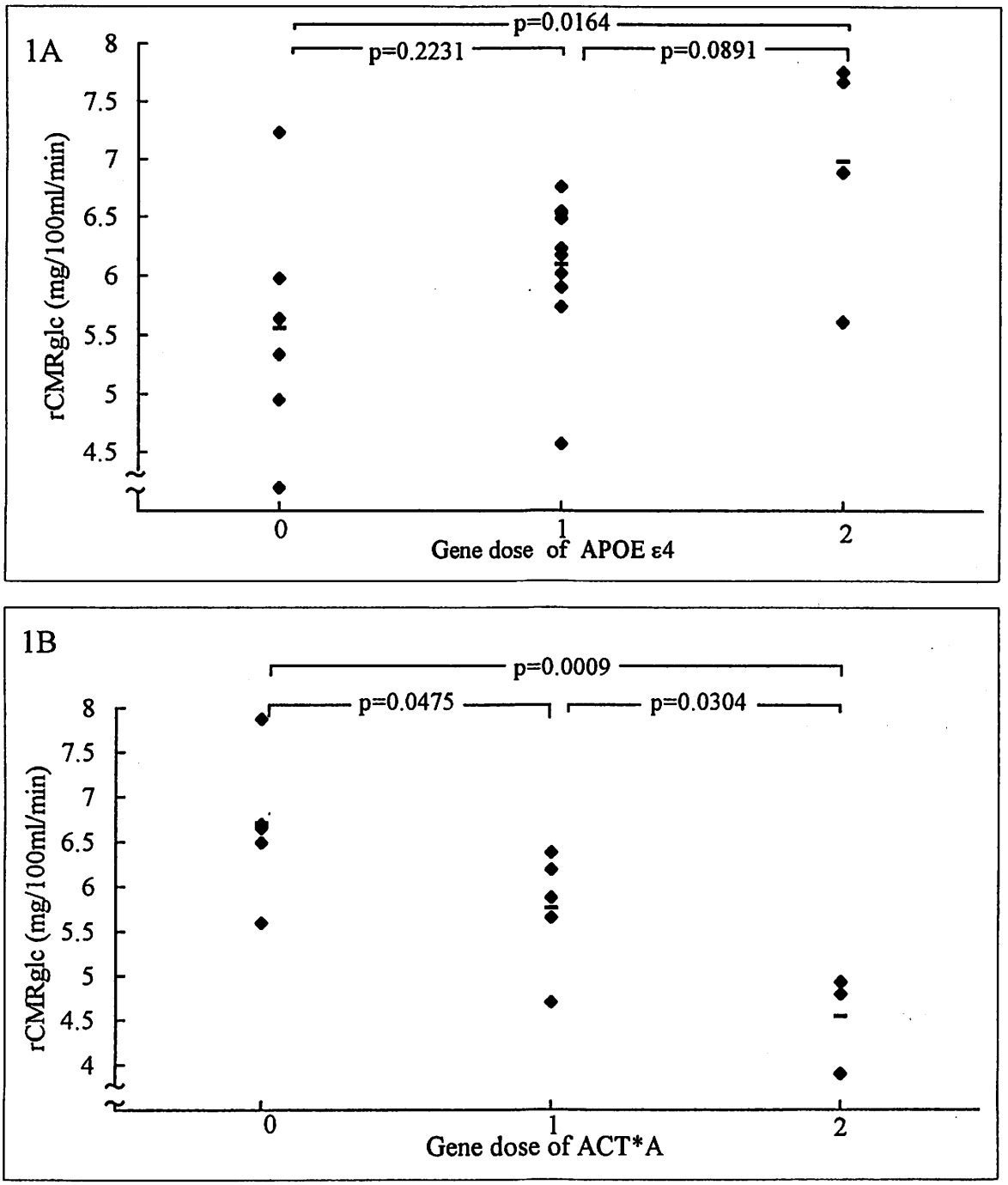

Fig. 1. Values of rCMRglc in the middle medial frontal area as a function of the dosage of APOE ε4 allele (1A, $R = 0.535$, $p < 0.05$) and in the upper lateral parietal area as a function of the dosage of ACT*A allele (1B, $R = -0.802$, $p < 0.01$). Horizontal bars represent mean values for the discrete conditions. Significance of difference is examined by analysis of variance (ANOVA).

IV. 12. Quantification of Striatal Dopamine D_2 Receptors in Normal Aging and Dementia Using PET and [^{11}C]YM-09151-2

Higuchi M., Itoh M., Okamura N., Tashiro M.*, Arai H., Fujiwara T, Ido T.*, and Sasaki H.*

Department of Geriatric Medicine, Tohoku University School of Medicine
*Cyclotron and Radioisotope Center, Tohoku University**

Introduction

Recent positron emission tomographic (PET) investigations have reported modifications of the striatal dopamine D_2 receptor binding during normal aging[1-3]. Most of the studies with PET and a radioligand for D_2 receptors such as [^{11}C]N-methylspiperone[1,2] or [^{11}C]raclopride[3] have noted that there is an age-related reduction of the D_2 receptor binding. However, the results of the quantification are influenced by which model for describing the tracer kinetics is employed. A reliable analytical method to quantify the tracer kinetics is required for a particular ligand-receptor system.

Multiple types of neurotransmissions in the brain have been demonstrated to alter in various dementing illnesses including Alzheimer's disease (AD) and vascular dementia (VD). Nevertheless, the state of the striatal dopaminergic transmission in living patients with these dementia remains unsettled.

The primary goal of the present study was to apply new analytical methods to PET measurement of the changes in the striatal dopamine D_2 receptor binding during normal aging and in dementia. These methods allow estimation of the kinetic parameters without arterial blood sampling and enable consideration of the nonspecific processes in the tracer kinetics including regional differences in the tracer delivery and nonspecific binding of the tracer.

Methods

Subjects

Thirty-seven subjects consisting of 13 normal volunteers (11 males and 2 females, mean age ±SD: 48.2 ±24.0 years), 16 AD patients (5 males and 11 females, mean age ±SD: 69.2 ±8.1 years) and 8 VD patients (5 males and 3 females, mean age ±SD: 76.5 ±5.8 years) were studied. Six normal subjects were selected as age-matched normal controls (4 males and 2 females, mean age ±SD: 70.7 ±8.2 years) from the group of normal subjects. The severity and progression of dementia in patients with AD or VD were evaluated using Mini-Mental State Examination (MMSE). The MMSE scores of the AD and VD patients ranged from 7 /

30 to 29 / 30 points (mean ±SD: 18.7 ±7.2 points), and from 17 / 30 to 27 / 30 points (mean ±SD: 21.5 ±4.5 points), respectively.

Informed consent was obtained from all the subjects or their families.

PET measurement and image analysis

The subjects underwent a PET study using ECAT PT931 (CTI Inc, Knoxville, TN, U.S.A.) positron emission tomograph. [^{11}C]YM-09151-2 was prepared as described elsewhere[4], and was injected intravenously, following a ^{68}Ge / Ga transmission scan. A dynamic PET scan of 90 min was performed post tracer injection.

Regions of interest (ROIs) were placed bilaterally on the striatum (i. e. specific region) and occipital cortex (i. e. reference region) of the reconstructed PET images, and time-radioactivity curves for these regions were obtained. The kinetic parameters estimated in the present analysis includes k_3 (a rate constant for association with D_2 receptors), k_4 (a rate constant for dissociation from D_2 receptors), k_5 (a rate constant for association with nonspecific binding sites), k_6 (a rate constant for dissociation from nonspecific binding sites), binding potential (BP, determined as k_3 / k_4) and R_0 (a ratio of the rate constant for the tracer delivery between the specific and reference region). These parameters were determined by using novel analytical methods ('linearized', 'nonlinearized' and 'progressional' methods) that was developed from the methods in the previous study[5]. These methods enable a parameter estimation without individual plasma data, when a priori information of the rate constants for the tracer delivery (K_1 and K_1 / k_2) and the standard plasma time-radioactivity curve are provided. We used the standard values of K_1 (= 0.25 ml min^{-1} ml^{-1}) and K_1 / k_2 (= 7) and the standard plasma curve obtained previously.

The correlation of each kinetic parameter with the age or MMSE score was examined by t-test. The significance of difference in each kinetic parameter between the normal subjects and patients with AD or VD was assessed by using Student's t-test.

Results

The relationship between the age and the BP value in the normal subjects is depicted in Fig. 1. The three analytical methods produced similar values of BP, and there was a decline of the BP closely related to the age. A close and negative associations of the k_3 and k_5 with the age also were observed in the normal subjects ($p < 0.01$ by t-test, data not shown), while no significant correlations of the k_4, k_6 and R_0 with the age were found ($p > 0.05$ by t-test, data not shown).

The BP values in the age-matched normal subjects and patients with AD and VD are compared as shown in Fig. 2. The BP value in the VD patients increased significantly compared with those in the normal subjects or AD patients ($p < 0.01$ by Student's t-test), whereas no significant difference in the BP was found between the normal subjects and AD

patients. The k_3 value in the VD patients were higher than that in the normal subjects but the difference did not achieve a statistical significance ($p > 0.05$ by Student's t-test, data not shown). The k_4 value in the VD patients decreased significantly compared with that in the normal subjects ($p < 0.05$ by Student's t-test, data not shown). No significant differences in the k_3 and k_4 values were observed between the normal subjects and AD patients ($p > 0.05$ by Student's t-test, data not shown).

There was no relationship between the BP value and the age in the AD (C. C. = -0.263, $p > 0.05$ by t-test) and VD (C. C. = - 0.176, $p > 0.05$ by t-test) patients. On the other hand, the BP value correlated significantly and negatively with the MMSE score in the AD and VD patients as shown in Fig. 3.

Discussion

The three analytical methods similarly detected an age-related decline of the dopamine D_2 receptor binding. The k_3 value decreased with aging, while the k_4 value remained unchanged, and it is thus probable that not the affinity for the receptors but the number of the receptors decreases with an increasing age. These results are in agreement with the findings in the previous PET studies with other radioligands[1-3, 6], though the rate of BP decline in this study was greater than that in the previous studies. The decline rate was larger due to the consideration of the nonspecific binding as an independent compartment, because the nonspecific binding in the younger subjects was larger in the elder subjects.

The patients with VD had higher values of BP especially in the early stage of dementia. Therefore, the measurement of D_2 receptor binding by using the present techniques is indicated to be a sensitive means for detecting early VD, and may enable a differential diagnosis between AD and VD in the early dementia. It is likely that an up-regulation of D_2 receptors occurs in early VD as observed in Parkinson's disease[7].

This study demonstrated a reduction of the D_2 receptor binding with the progression of dementia. According to the regression lines in Fig. 3, the BP value is estimated to be below the normal range in severely demented patients. It is difficult to confirm the decreased receptor binding in patients with severe AD and VD by performing a PET measurement. However, it is likely that a disturbance of the dopaminergic neurotransmission in the striatum causes motor impairments, a high incidence of misswallowing and consequent aspiration pneumonia in the advanced stage of AD and VD, since a reduction of the striatal dopamine metabolism with the progression of dementia has also been demonstrated[8]. Further assessments for severely demented patients will be requested to elucidate relationships between the disturbance of the striatal dopaminergic function and the prognosis of life in AD and VD.

References

1) Wong D. F., Wagner H. N. Jr., Dannals R. F., et al. Science **226** (1984) 1393.
2) Wong D. F., Broussolle E. P., Wand G., et al. Ann. N. Y. Acad. Sci. **515** (1988) 203.
3) Rinne J. O., Hietala J., Ruotsalainen U., et al. J. Cereb. Blood Flow Metab. **13** (1993) 310.
4) Hatano K., Ishiwata K., Kawashima K., et al. J. Nuc. Med. **30** (1989) 515.
5) Watabe H., Hatazawa J., Ishiwata K., et al. IEEE Trans. Med. Imag. **14** (1995) 688.
6) Baron J. C., Maziere B., Loc'h C., et al. J. Cereb. Blood Flow Metab. **6** (1986) 131.
7) Sawle G. V., Playford E. D., Brooks D. J., et al. Brain **116** (1993) 853.
8) Itoh M., Meguro K., Fujiwara T., et al. Ann. Nucl. Med. **8** (1994) 245.

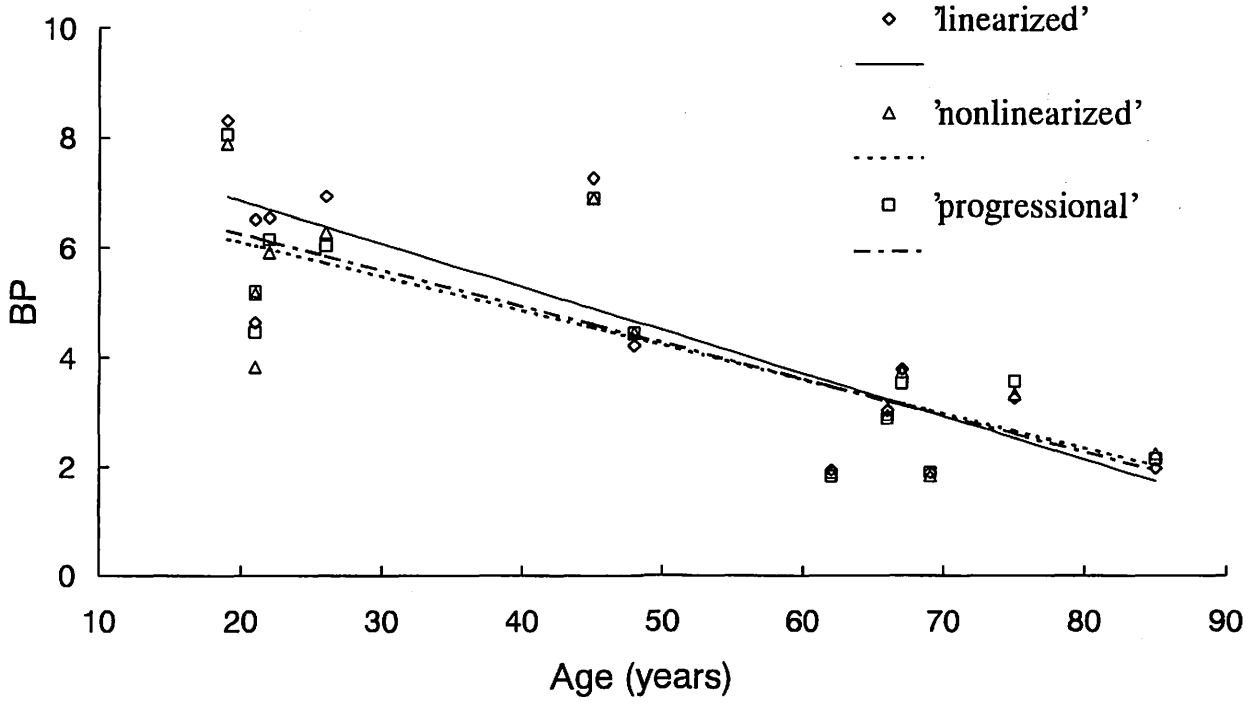

Fig. 1. Relationship between the age and the binding potential (BP) value for the striatal dopamine D_2 receptors estimated by the three types of methods in normal subjects. Straight lines represent the regressions. The coefficients of correlation are -0.841**, -0.763** and -0.796** for the 'linearized', 'nonlinearized' and 'progressional' methods, respectively.
**$p < 0.01$ by t-test.

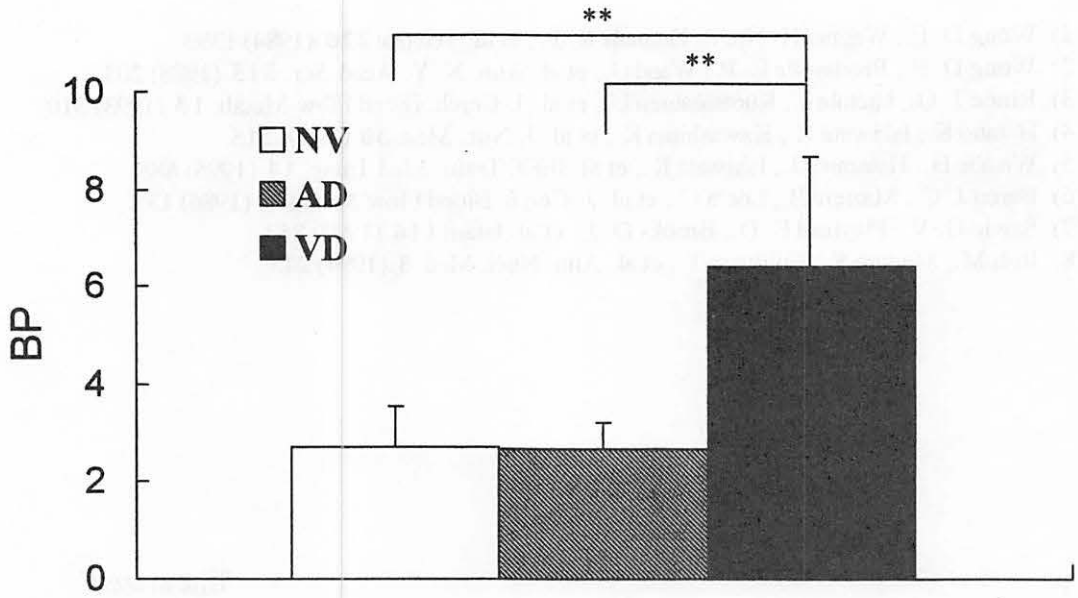

**p < 0.01 by Student's t-test.

Fig. 2. Comparison of the binding potential (BP) values for the striatal D_2 receptors in age-matched normal controls (NV) and patients with AD (AD) and VD (VD) estimated by the 'linearized', 'nonlinearized' and 'progressional' methods. Vertical lines on the bars represent SD values.

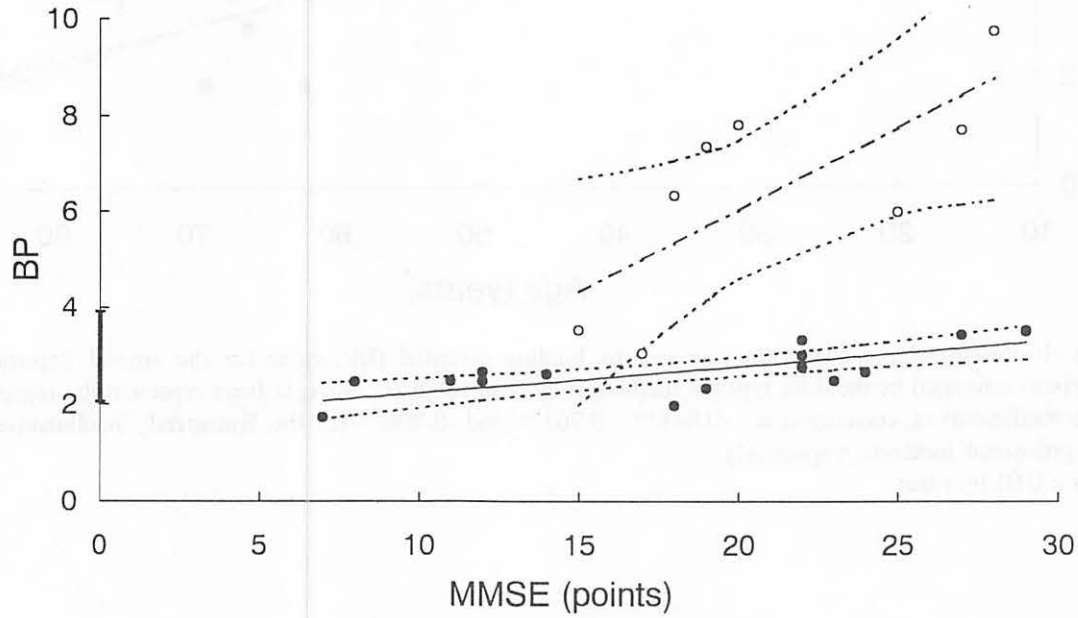

Fig. 3. Plot of BP estimated by the the 'linearized', 'nonlinearized' and 'progressional' methods versus MMSE score in patients with AD (●) or VD (O). Regression lines with 95% confidence limits (broken lines) for AD (solid line) and VD (dash-dotted line) are displayed according to BP = 0.0549 (MMSE + 1.679 and BP = 0.3424 (MMSE - 0.8038, respectively. Vertical line on y-axis represents range of BP values in age-matched normal subjects. The coefficients of correlation between the BP value and the MMSE score in the patients with AD and VD is 0.752** (AD) and 0.727* (VD).
*p < 0.05, **p < 0.01 by t test.

IV. 13. Cerebral Muscarinic Acetylcholine Receptor Binding is Associated with the Severity of Dementia: A [^{11}C]benztropine-PET Study in Alzheimer's Disease

Tokunaga T., Higuchi M., Arai H.*, Itoh M., Fujiwara T., Ono S.**, Fukuda H.**, and Sasaki H.**

Cyclotron and Radioisotope Center, Tohoku University
*Department of Geriatric Medicine, Tohoku University School of Medicine**
*Department of Nuclear Medicine and Radiology, Institute of Development, Aging and Cancer, Tohoku University***

Introduction

Alzheimer's disease (AD) is the most common form of dementia in elderly. Alterations of the neocortical and hippocampal acetylcholine receptors in AD brains have been demonstrated, reflecting abnormalities of the central cholinergic system in AD. Accumulating in vitro evidences have shown reductions in the high-affinity binding of nicotine in the neocortex and hippocampal formation[1-3]. In respect of the muscarinic acetylcholine receptors, the findings in neurochemical studies have generally indicated that the muscarinic M_1 receptors remains unchanged in the cortical and hippocampal areas of AD brains[4-6], whereas no consistent results have been obtained for the changes in the muscarinic M_2 receptors of AD[4-6]. The association between the M_1 or M_2 receptor binding and the severity of AD also remained unsettled.

The present study was aimed to investigate the alterations of the central muscarinic acetylcholine receptor binding in living AD patients with different levels of disease severity by using positron emission tomography (PET) and [^{11}C]benztropine, a specific radioligand for the muscarinic M_1 and M_2 receptors.

Methods

Thirteen patients diagnosed as probable AD (6 males and 7 females, mean age ±SD: 71.0 ±9.3 years, range 56 to 86 years) were studied. The severity and progression of dementia in these patients were evaluated with Mini-Mental State Examination (MMSE). The MMSE scores ranged from 5 / 30 to 29 / 30 points (mean ±SD: 18.7 ±7.2 points). Informed consent was obtained from all the subjects or their families.

The patients underwent a PET scan with ECAT PT931 / 04-12 scanner (CTI Inc, Knoxville, TN, USA). [^{11}C]benztropine was synthesized as described elsewhere[7], and was injected intravenously, followed by 70-min dynamic PET scans. An arterial blood sampling

was performed during the emission scans, and the radioactivity in arterial plasma was measured. The percentages of unmetabolized tracer in plasma at selected time points were determined as described elsewhere[7].

The dynamic PET images and the plasma time-radioactivity curve corrected for metabolites were used for generating parametric images of the irreversible disposal rate constant (i. e. 'Patlak slope') by means of Patlak's analysis[8], assuming an irreversibility of the tracer binding. The parametric images describing the approximate tracer delivery to the brain tissue were constructed by averaging the dynamic PET images from 1 to 15 min. Pixel values of these 'delivery' images were divided by the value of the injected tracer dose for each subject.

The 'Patlak slope' and 'delivery' images were analyzed statistically on a voxel-by-voxel basis by using Statistical Parametric Mapping (SPM96) software[9]. A spatial transformation was used to match these images to a template that conforms to the standard anatomical space[10], and the following analyses were performed using t-statistic:

1) The correlation between the age and tracer binding ('Patlak slope').
2) The correlation between the severity of dementia (MMSE score) and tracer binding ('Patlak slope').
3) The correlation between the severity of dementia (MMSE score) and tracer 'delivery'.

The analyses 1) and 2) were performed without any method for a global normalization. The analysis of covariance (ANCOVA) correction for the global value was employed for the analysis 3). The SPM{t} was transformed to a SPM{Z}, and the distribution of Z values was evaluated.

Results

In the patients studied here, there were little relationships between the age and the 'Patlak slope' value in any of the voxels ($p > 0.05$, data not shown).

Fig. 1 shows the distribution of the Z values for the correlation between the MMSE score and the 'Patlak slope' value. The SPM{Z} map is thresholded at $p = 0.01$ and $p = 0.001$ (uncorrected) in Figs. 1A and 1B, respectively. As shown in Fig. 1A, a significant and positive correlation between the MMSE score and the 'Patlak slope' value was found in most of the voxels examined here. An especially close correlation was observed in the bilateral lower temporal and right lower frontal areas as shown in Fig. 1B. The structures showing a close correlation are listed in Table 2, and are rendered on the magnetic resonance imaging (MRI) template as displayed in Fig. 2. The bilateral middle temporal gyri, the right fusiform gyrus, the right hippocampus, the right amygdaloid nucleus, and the right inferior frontal gyrus were included in the regional maxima of the Z value. There were no voxels presenting a significant negative correlation between the MMSE score and the 'Patlak slope' value in the entire area examined here ($p > 0.05$, data not shown).

The association of the MMSE score with the 'delivery' value is depicted in Fig. 3. The variance of the global 'delivery' value was removed by ANCOVA. The SPM{Z} map was thresholded at $p = 0.05$ (uncorrected). A close correlation was observed in the left frontal region, where the regional tracer delivery showed a decline with decreasing MMSE score. No structures were found to be highlighted in both SPM{Z} maps for the associations of the MMSE score with the 'Patlak slope' and 'delivery' values.

Discussion

The assessment of the central acetylcholine neurotransmission in AD has two major aspects: 1) the participation of the cholinergic deficit in the pathogenesis of AD, 2) the potential of treatments for AD patients by agents stimulating the cholinergic system. The present approach is not only helpful to obtain a biological information for development of AD, but also to examine if the efficacy of a cholinergic agent for each AD patient is predictable from his or her severity of dementia.

Since the highlighted regions were different between the SPM analyses for the correlations of the MMSE score with the 'Patlak slope' and 'delivery' values, these regional effects of the MMSE score are not apparent by the morphological atrophy during the AD progression. There would have been identical structures between the two analyses if an obvious partial volume effect by the cortical atrophy had affected the apparent changes in the 'Patlak slope' and 'delivery' values. Further, the significant reductions of the 'Patlak slope' values can be considered as reductions of the receptor binding rather than decreased levels of the regional cerebral blood flow (rCBF), for the 'delivery' value that reflects the rCBF was strongly associated with the MMSE score in a different area.

The decrease of the muscarinic receptor binding correlated strongly to the decreasing MMSE score in the basal forebrain and the temporal areas including the hippocampus, suggesting that the cholinergic deficit plays an important role in a cognitive decline during the AD progression. Moreover, the response to a drug inhibiting cholinesterase such as tacrine may be smaller in patients with severe dementia than in mildly demented patients. Actually, the effect of tacrine was reported to be obvious, exclusively in patients with mild AD[11]. The present results also indicate a need of therapeutic intervention from the early stage of AD.

References

1) Flynn D. D. and Mash D. D. J. Neurochem. **47** (1986) 1948.
2) Whitehouse P. J., Martino A. M., Wagster M. V., et al. Neurology **38** (1988) 720.
3) Perry E. K. Morris C. M. Court J. A., et al. Neuroscience **64** (1995) 385.
4) Mash D. C., Flynn D. D., and Potter L. T. Science **228** (1985) 1115.
5) Araujo D. M., Lapchak P. A., Robitaille Y., et al. J. Neurochem. **50** (1988) 1914.
6) Rinne J. O., Lonnberg P., Marjamaki P., et al. Brain Res. **483** (1989) 402.
7) Dewey S. L., MacGregor R. R., Brodie J. D., et al. Synapse **5** (1990) 213.
8) Patlak C. S., Blasberg R. C., and Fenstermacher J. D. J. Cereb. Blood Flow Metab. **3** (1983) 1.
9) Friston K. J. Ashburner J., Poline J. B., et al. Human Brain Mapping **3** (1995) 165.

10) Talairach J. and Tournoux P. A Co-planar Stereotaxic Atlas of a Human Brain (1988) Stuttgart, Thieme.
11) Nordberg A., Lilja A., Lundqvist H., et al. Neurobiol. Aging **13** (1992) 747.

Table 1. The locations of maxima included within the regions highlighted in Fig. 1B.

Coordinates (x,y,z mm)	Structure	Brodmann's area	Patlak slope value ($\times 10^{-3}$ ml /g /min)	Correlation with MMSE score
40, -8, -4	GTm right	21	8.12 ± 2.61	0.874
38, -28, -24	GF right	20	6.93 ± 1.92	0.846
26, 16, -16	GFi right	47	7.72 ± 2.61	0.844
26, -28, -6	Hi right	-	7.18 ± 2.21	0.834
54, 26, -4	GFi right	47	6.07 ± 2.00	0.816
26, -2, -20	NA right	-	6.42 ± 2.51	0.816
-38, -24, -4	GTm left	21	7.12 ± 2.31	0.870

The final column is the correlation between the MMSE score and the Patlak slope value. Coordinates x, y and z are the lateral distance from the midline (positive = right), the anterior-posterior distance from the anterior commissure and the height above the intercommissural line, respectively. GTm = middle temporal gyrus; GF = fusiform gyrus; GFi = inferior frontal gyrus; Hi = hippocampus; NA = amygdaloid nucleus. The 'Patlak slope' values are expressed as mean ±SD.

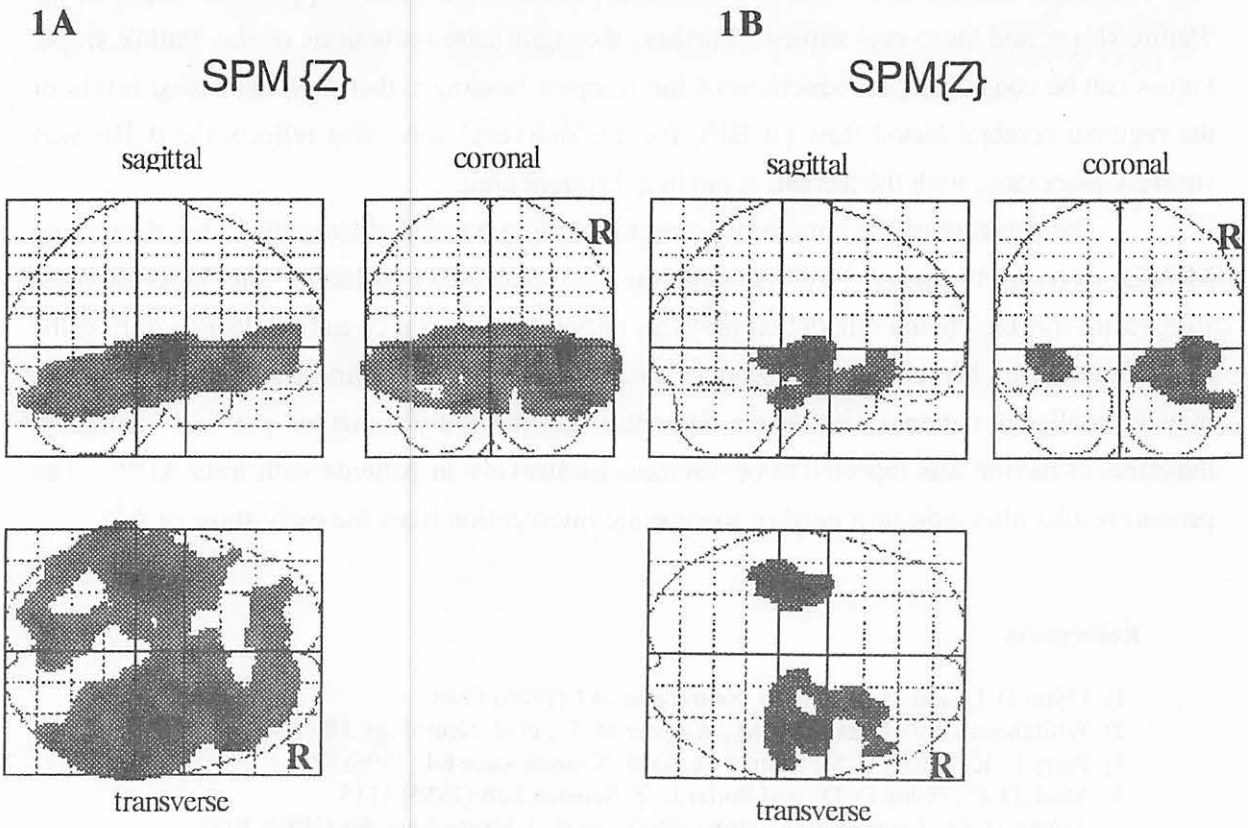

Fig. 1. SPM{Z} maps for the positive correlation between the MMSE score and the 'Patlak slope' value. The maps are thresholded at p = 0.01 (1A) or p = 0.001 (1B) (uncorrected), and are displayed as orthogonal projections.

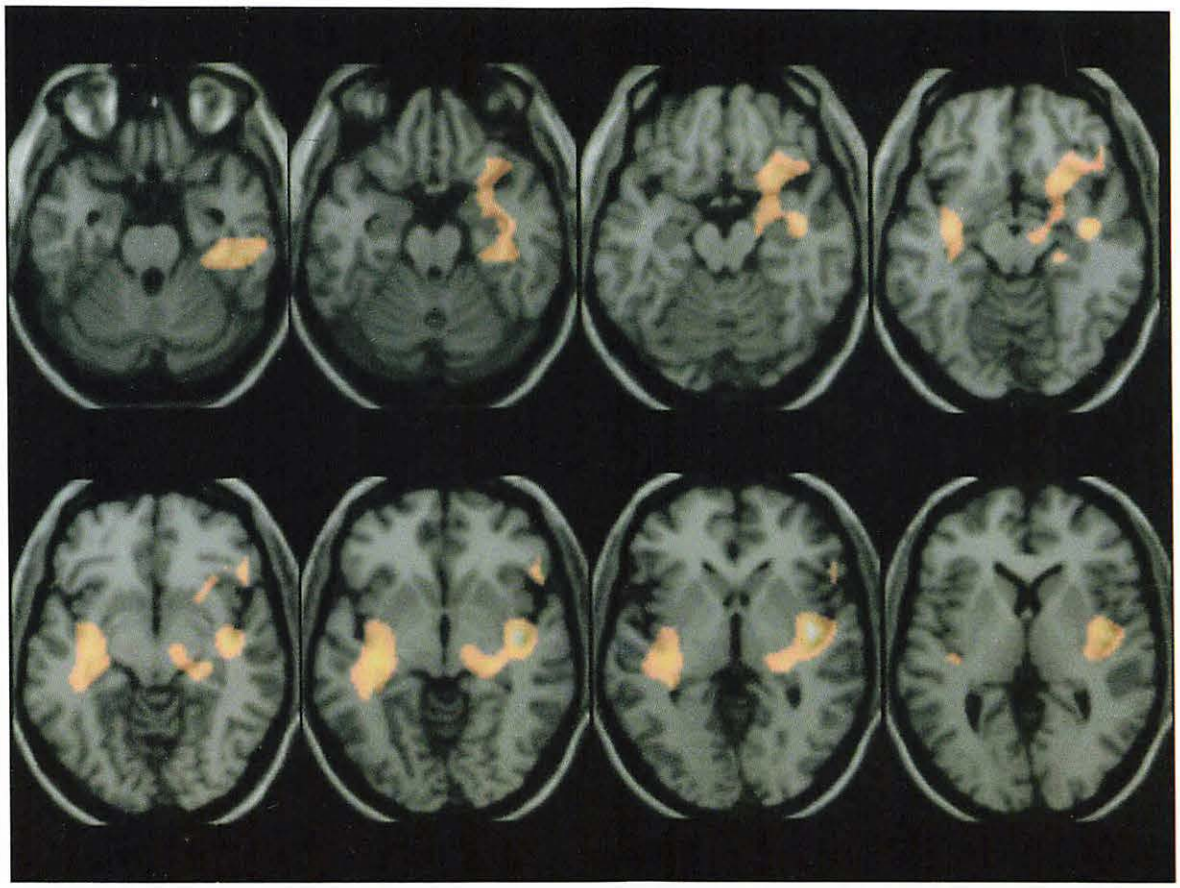

Fig. 2. SPM{Z} map for the positive correlation between the MMSE score and the 'Patlak slope' value. The map is thresholded at p = 0.001 (uncorrected), and are rendered on the MRI template which conforms to the standard anatomical space.

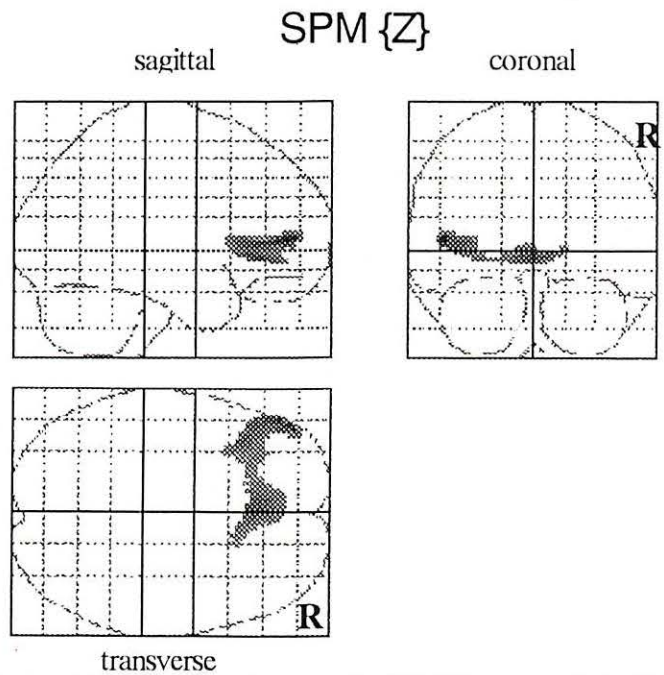

Fig. 3. SPM{Z} map for the positive correlation between the MMSE score and the 'delivery' value. The maps are thresholded at p = 0.05 (uncorrected), and are displayed as orthogonal projections. The effect of global variance is removed by ANCOVA.

V. RADIATION PROTECTION AND TRAINING OF SAFE HANDLING

V. 1. Detector for High Energy Neutron Spectrometry

Nakao M., Sasaki M., Nakamura T. Nakao N., and Shibata T.**

Cyclotron and Radioisotope Center, Tohoku University
*Institute for Nuclear Study, University of Tokyo**

Introduction

With increasing use of high energy accelerator, the detection of secondary produced high energy neutrons having strong penetrability becomes more and more important for radiation shielding and safety.

But, there has been no available neutron spectrometer to detect neutrons of energies higher than about 100MeV, except the TOF(Time of Flight) method which can only be used in the limited field.

We therefore developed a self-TOF detector to obtain neutron spectrum of energy above 100MeV.

Materials and Methods

A self-TOF detector consists of an assemby of radiator, start and stop detectors. We assembled 20 sets of 10cm × 10cm and 6mm thick NE102A plastic scintillator as radiator, 10cm × 10cm and 5mm thick NE102A as a start detector, and nine sets of 20cm × 20cm and 2cm thick NE102A as stop detctors, in this order to the incident neutron beam.

Fig. 1 shows a schematic view of the detector's assembly. Nine stop detectors are set on a plane perpendiculer to the neutron beam and at 1m behind a start detector. When neutrons are incident on the radiator array, recoiled protons are produced by the H(n,n) reaction from a certain radiator. Output pulses from each radiator are counted separately with the photomultiplier coupled to each radiator, which gives the position of proton production and its energy loss, ΔE, in the radiator array. The energy of the recoil protons incident on the start detector E_p is determined by the TOF method between the start and stop detectors. Neutron energy is then determined by relativestic kinematics using induced proton energy corresponding to $E_p + \Delta E$.

Experiment

Experiment of CYRIC, Tohoku University

As the first experiment for this detector performance, we measured the spectrum of neutrons produced from the 1mm thick ^{7}Li target bombarded by 65MeV ^{3}He ions by using the AVF cyclotron of Cyclotron and Radioisotope Center (CYRIC). Fig. 2 shows the experimental geometry. The proton beam was inclined at 10Åãto the horizontal line with a beam swinger in order to shield neutrons producecd from the Faraday cup. The neutrons emerging from the Li target at 10° were then formed into a beam by the double collimators and transported down to the TOF extention room. In this experiment we used the detector assembly consisting of three radiators, one start and three stop detectors. Fig. 3 shows light output of the radator, start, and stop detectors. We can find the plateau peak of recoil protons at high energy end corresponding to the monoenergetic peak neutrons, especially in the stop detector.

Experiment of RIKEN

We secondly measured the spectrum of neutrons produced from the 10mm thick ^{7}Li target bombarded by 210MeV protons which were extracted from the separate-sector cyclotron of Institute of Physical and chemical Research (RIKEN). Fig.4 shows the experimental geometry. The charged particles which penetrated the thin target or produced in the target were transported to the beam dump by the dipole bending magnet. The neutrons emitted in the forward direction were measured with the detector through the collimator of 22cm × 22cm aperture and 120cm length. In this experiment we used the detector assembly consisting of six radiators and one start and three stop detectors.

Raw data and analysis

The measured light output data were analyzed as follows,

(1) Select only the proton event from the two dimensional (2D) distribution of stop detector's light output and recoil proton TOF spectra.
(2) Separate proton TOF spectrum by each radiator.
(3) Convert TOF spectrum into proton energy spectrum.
(4) Correct proton energy loss through the radiator.
(5) Change proton spectrum to neutron spetctrum with dividing by the efficiency.

Fig. 5 (a)(b) shows the 2D distribution of TOF(X-axis) and stop detector's light output (Y-axis) and that selected only recoil proton events(Fig. 5(b)) which were obtained at the CYRIC experiment. The 1D distributions projected on the X-axis, that is, the proton TOF spectra are also shown in Fig. 5(c)(d). The 2D distribution gives two gamma-ray peaks, proton and deutron events. The right peak was caused by gamma rays which were produced in the start detector and reached the stop detector, and the left peak was vice versa. Proton

events were produced by the relevant H(n, n) reaction and deutron events by the C(n,d) reaction.

Fig. 6 shows the 2D distribution of TOF and stop detector's light output which were obtained at the RIKEN experiment. In this higher neutron energy experiment, the proton and deuteron events overlapped each other as seen in Fig. 6(b), because proton and deutron did not fully loss their energy, but escaped from the stop detector.

To avoid the pile up of proton and deuteron light outputs, we placed 10cm × 10cm and 2.5cm thick brass bar between radiator and start detector to absorbe deuteron pulses. This results are also shown in Fig. 6(a). The deuteron pulses are fully absorbed in brass bar, but proton pulses are also absorbed especially in lower energy region at the same time.

Results and discussions

The neutron energy spectrum obtained at the CYRIC experiment is shown in Fig. 7(a) after the analysis desecribed in Sec. 4. The results is relatively compared with the neutron spectrum simultaneously obtained by the neutron TOF method with the 12.7cm-diam by 12.7cm long NE213 detector, since the efficiency of the self-TOF detector has not yet been calculated. Both spectra show rather good agreement in shape, but the energy resolution of the self-TOF detector is poor.

Fig. 8 gives the preliminary results of neutron energy spectrum obtained at the RIKEN experiment. Since we used the brass absober as described before, only high energy neutron components around 200MeV can be seen due to the absorption of lower energy protons.

To improve the discrimination level of proton and deuteron light output we will do experiment by the two ways as follows

(1) adding lead glass and plastic scintillator BC400 to stop detectors

(2) using the organic liquid scintillator NE213 as the stop detector instead of NE102A

Acknowledgments

We are deeply grateful to cyclotron operators at CYRIC and RIKEN. This work has been done as a Reseach Project with Heavy Ions at NIRS-HIMAC (National Institute of Radiological Sciences).

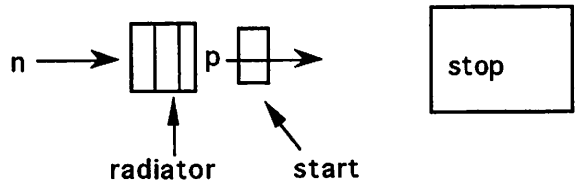

Fig. 1. Geometry of the Self-TOF detector.

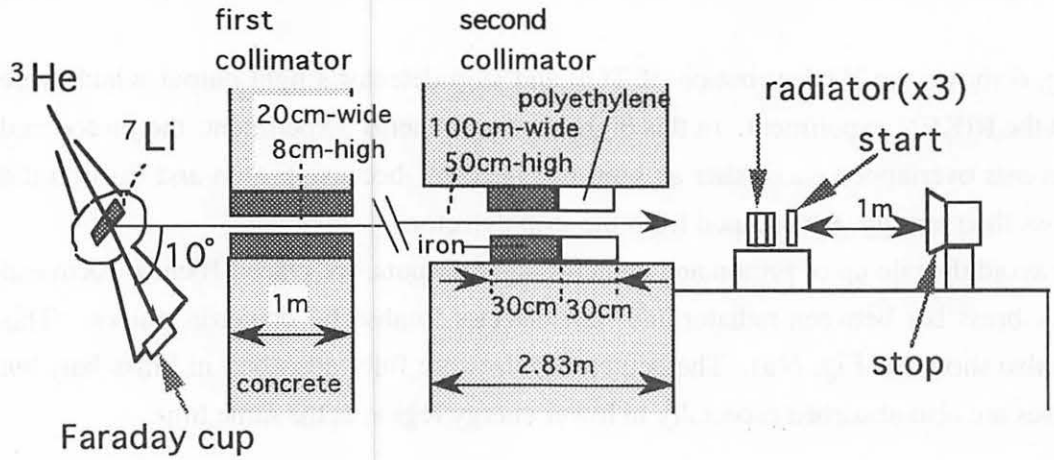

Fig. 2. Experimental setup at CYRIC.

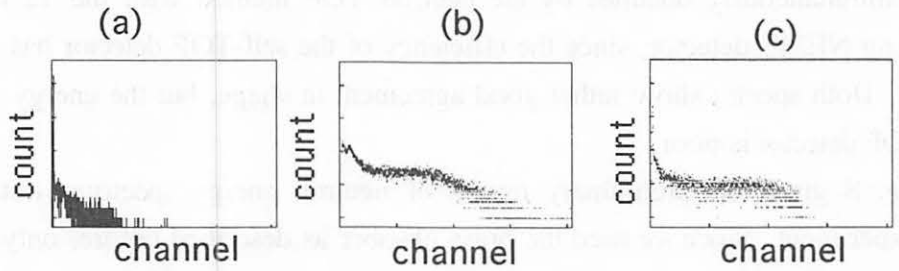

Fig. 3. Pulse height distribution of scintillation light output from (a)the first radiator, (b)the start detector, (c)the stop detector.

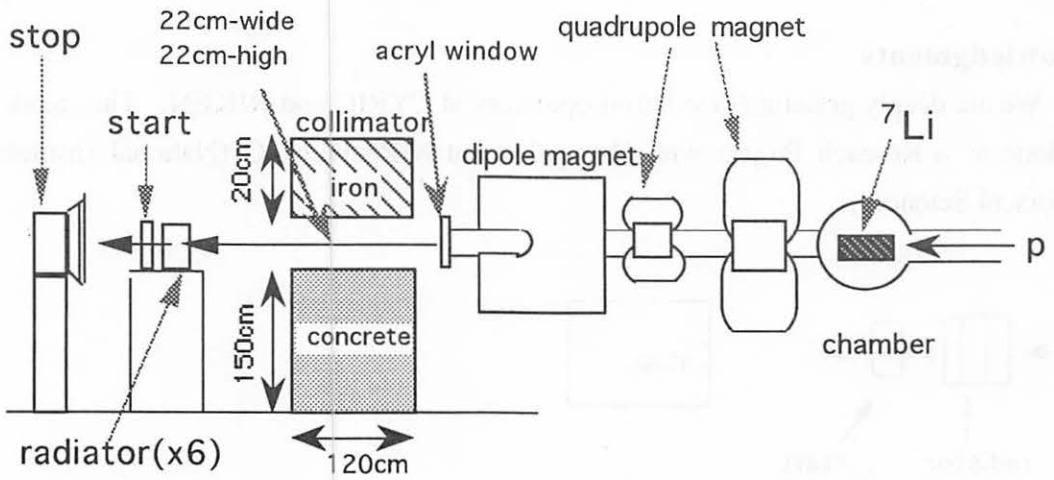

Fig. 4. Experimental setup at RIKEN.

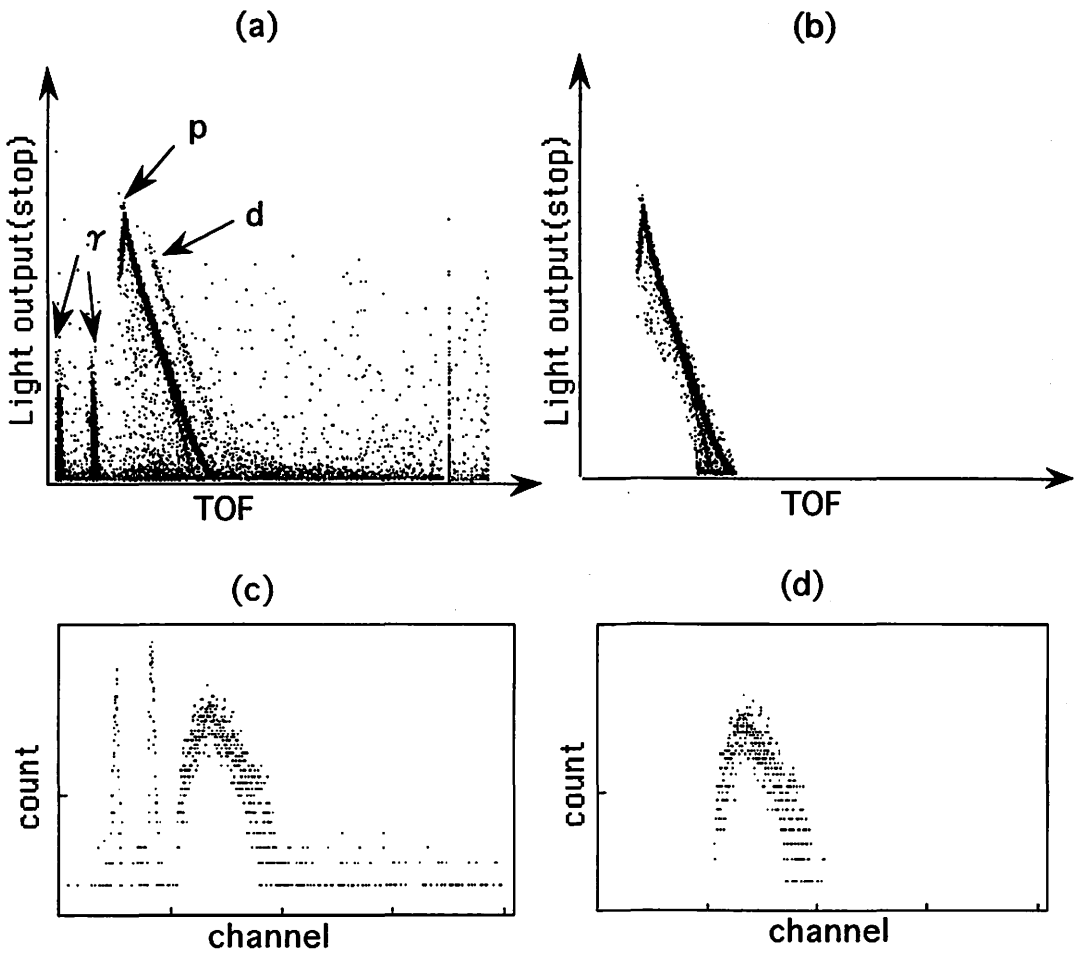

Fig. 5. Two dimensional plots of TOF and stop detector's light output (a) without selection, (b) after selection of proton events. The TOF spectrum (c) without selection, (d) after selection of proton events.

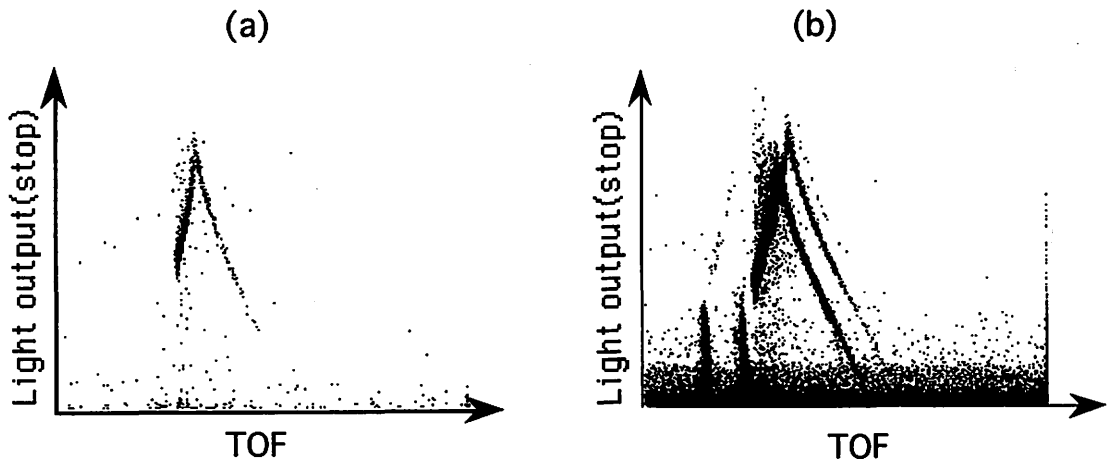

Fig. 6. Two dimensional plots of TOF and stop detector's light output (a)with brass absober, (b)without brass absober.

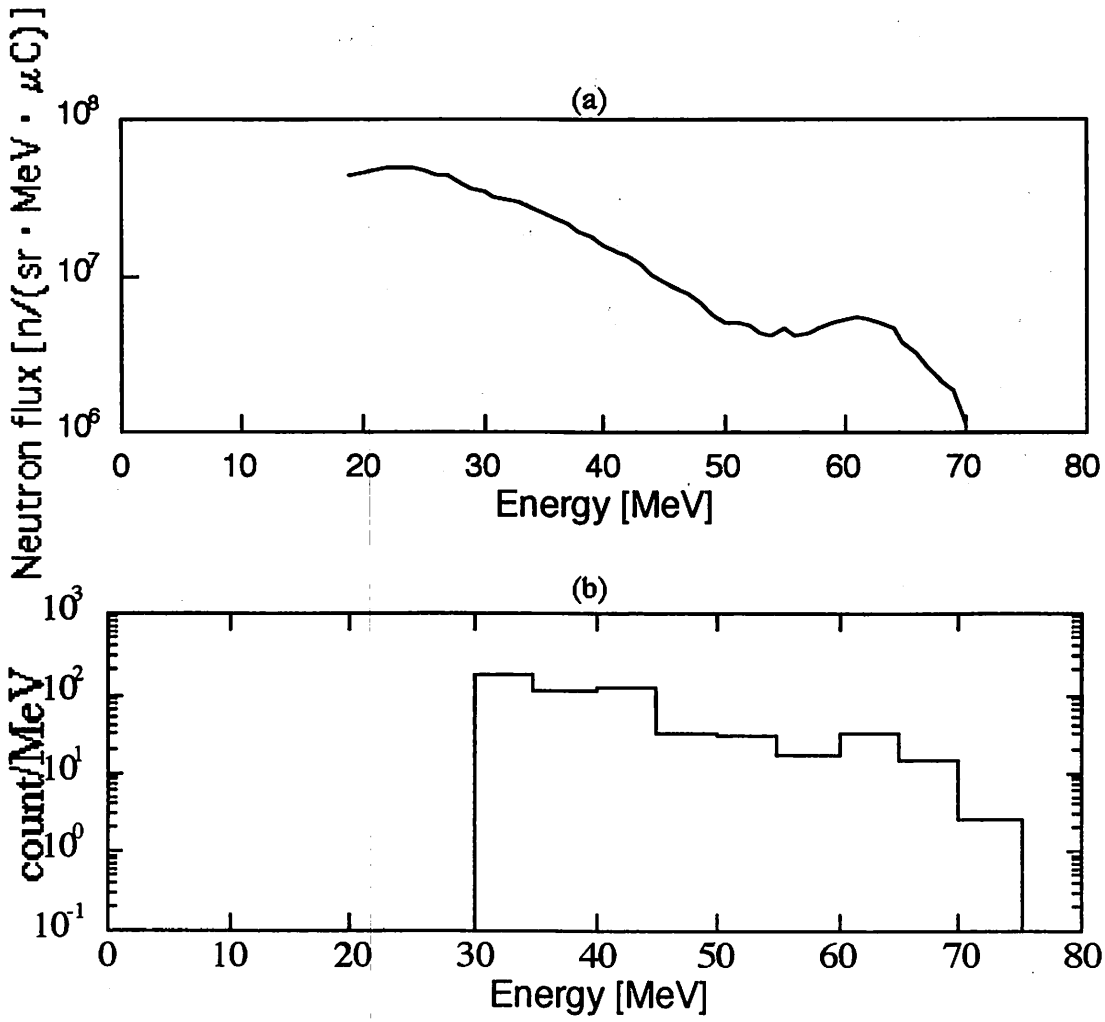

Fig. 7. Neutron energy spectra produced from ^{7}Li bombarded by 65MeV ^{3}He beams (a)obtained by self-TOF detector, (b)obtained by 12.7cm-diam by 12.7cm long NE213 detector with the neutron TOF method.

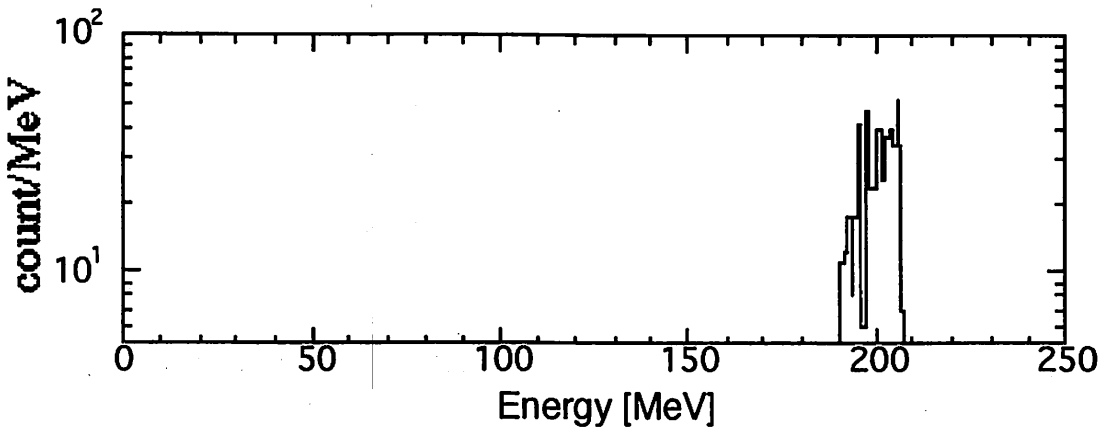

Fig. 8. Preliminary result of neutron energy spectrum produced from ^{7}Li bombarded by 210MeV protons which were obtained by self-TOF detector.

V. 2. Fast Neutron Profiling with Imazing Plate

Saito K., Baba M., Sanami T., Ibara Y., Hirakawa N., Yamadera A., Taniguchi S*., and Nakamura T.**

School of Quantum Science and Energy Engineeing, Tohoku University
*Cyclotron and Radioisotope Center, Tohoku University**

Introduction

Measurement of neutron spatial distributions (neutron profiling) is an important technique in many fields. Several devices have been developed for thermal neutron profiling such as a film method, a television method and so on. The Imaging Plate (IP) was successfully applied to thermal neutrons too[1]. However, there are few reports of application of IP to fast neutrons probably because of low sensitivity to them and high sensitivity to background gamma-rays.

We developed a method of neutron profiling with IP by use of a polyethylene converter in front of IP to increase the sensitivity and to discriminate events by gamma-ray backgrounds. In this method, we obtain a fast neutron profile by detecting recoil protons from the converter with IP, and gamma-ray backgrounds could be eliminated by taking difference between measurements with and without the converter, because gamma-ray sensitivity of IP is nearly independent of such a the thin polyethylene converter.

In this study, we obtained a profile of 14.1MeV neutrons after a 20cm-long copper collimator, and the response of IP coupled with a polyethylene converter at several neutron energies. Besides we tried fast neutron radiography of a simple step-shaped acrylic sample.

Conical Collimator Image

Experiment

Experiments were carried out at Fast Neutron Laboratory in Tohoku University using a 4.5 MV Dynamitron accelerator.

Figure 1 shows an experimental setup to measure a 14.1 MeV neutron profile after a conical collimator. Neutrons were obtained by the T(d,n) reaction and collimated by a Cu collimator, 20 cm-long. They bombarded a 0.5mm thick polyethylene converter set on the surface of IP, 12.5 x 12.5cm^2. We used IP for X-rays manufactured by Fuji Film Co. Ltd. An NE213 scintillation counter was employed as a neutron monitor for normalization between measurements with and without the converter. The number of neutrons on IP was about 2.4 x 10^8 /cm^2. About 1 hour after the exposure, we scanned IP and analyzed the photo-

stimulated-luminescence (PSL) distribution. Scanning and analyzing were performed by the BAS system (Fuji Film Co. Ltd.) at the Cyclotron-Radioisotope-Center of Tohoku University.

Result

Figure 3 shows the PSL distribution of IP with the converter. In this figure, the outer rectangular area corresponds to the area covered with the converter, and the circular area at the center shows the area bombarded by direct neutrons through the collimator hole. We set a ROI (Region of Interest) in a long rectangular region "A" , and deduced a one-dimensional distributions in fig.3. In the figure, the solid and broken lines show the distributions with and without the converter, respectively. The central peak value with the converter is about 6 times as large as that without the converter. This fact indicates that the polyethylene sheet acts as an effective converter. Besides, the net neutron profile could be obtained by subtracting the result without a converter from the one with a converter. The events at both wings of center peak are due to neutrons scattered at the floor.

Application to Fast Neutron Radiography

Experiment

Figure 4 illustrates an experimental setup and a detailed view of the sample for a step sample radiography. Incident neutrons of 1, 2, 5 and 15 MeV produced via the T(p,n), the D(d,n) and the T(d,n) reaction, respectively, were used in the experiment. The distance between the target and IP was fixed for 100 cm and the thickness of the polyethylene converter was 0.5cm for all measurements. To reduce background neutros, the target was shielded with a water tank. The sample for radiography was composed of 1cm-thick acrylic steps and, 5 and 3.5 cm-thick Fe slabs as shown in fig.4. The exposure time for all neutron energy was about 2 hours with a 4mA direct beam current. We scanned IP and analyzed PSL distribution about 1 hour after the exposure.

Result

Figure 5 shows a typical image for the step sample. The numbers of 1, 2, 3 ,4 indicates the regions with converter alone; (1), 3.5cm thick Fe slab (2), 5cm Fe slab (3) and the acrylic step (4), respectively.

Figures 6 to 9 show PSL distributions in "A" region in fig.5. From this results, we can clearly distinguish the acrylic region from the Fe slab region. The images for 5 and 15 MeV neutrons are good enough to distinguish the acrylic steps, but not in 1 and 2 MeV results. It is noted that the edges of the steps are imaged to be round shapes in whole region in all results because of point neutron source.

We deduced PSL values for regions with and without a converter to evaluate converter efficiency. Table 1 summarizes the PSL values, S/N values and efficiencies of proton

emission calculated with an effective thickness of the converter and evaluated cross section from JENDL.3. The effective thickness is determined from the maximum proton range which depends on the neutron energy or the thickness of the converter. This table indicates that the PSL(n) of 1 and 2 MeV neutrons are smaller than that for 5 and 15 MeV because of a smaller converter efficiency. The inferior image quality for 1 and 2 MeV neutrons can be understood by the low efficiency of the converter.

Therefore, neutron energies providing high conversion efficiency are appropriate to obtain fast neutron radiography by this method.

Summary

To obtain fast neutron profiles, we developed a method using IP combined with a polyethylene converter. This method can eliminate gamma-ray contaminations from neutron images and provides results within a short expose time. It was possible to inspect neutron collimation and to distinguish acrylic steps from Fe ones by the method. Therefore, it is promising as the method of fast neutron imaging.

References

1) Niimura N. et al., Nucl. Instrm. And Meth., **A349** (1994) 521.

Table 1. Parameters for step radiography experiment. Neutron flux was based on ref.1. The (n,p) cross section was taken from JENDL-3.2.

		Foreground	Background	FG-BG	(FG-BG)/BG		
En(MeV)	neutron flux(#/cm2)	with converter(PSL)	without(PSL)	PSLn	S/N	PSLn/flux	Ef(%)
1	2.65E+06	46.9	40.5	6.4	0.2	2.42E-04	0.05
2	5.02E+06	160	124	36	0.3	7.18E-04	0.224
5	3.17E+07	242	69.8	172	2.5	5.43E-04	4.5
15	1.67E+07	295	166	129	0.8	7.73E-04	2.3

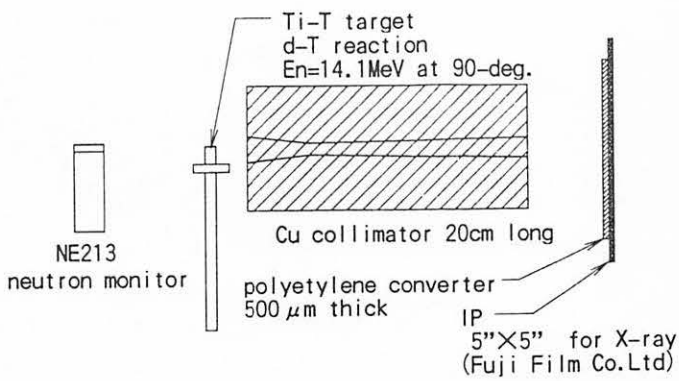

Fig. 1. Experimental setup of conical collimator image for 14.1 MeV neutrons. The 14.1 MeV neutrons were obtained at 90-deg via the T(d,n) reaction.

Fig. 2. Scanned image of IP with a 0.5mm 0.5mm thickness polyethylene converter.

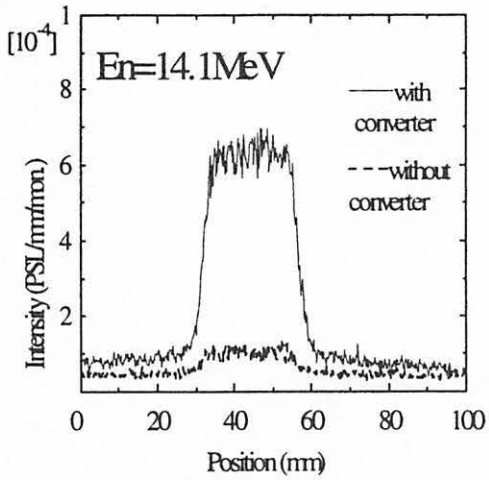

Fig. 3. PSL distributions of the conical corresponds to the collimator experiment, the solid line without converter.

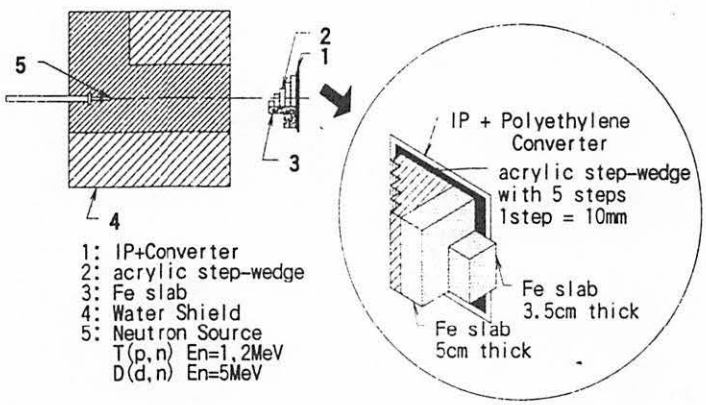

Fig. 4. Experimental setup for the radiography of astep shaped sample. Target to sample distance is 100 cm, step width of sample is 1 cm, and thickness of convertor are fixed for 0.5. neutron energies were 1, 2, 5, 15 MeV.

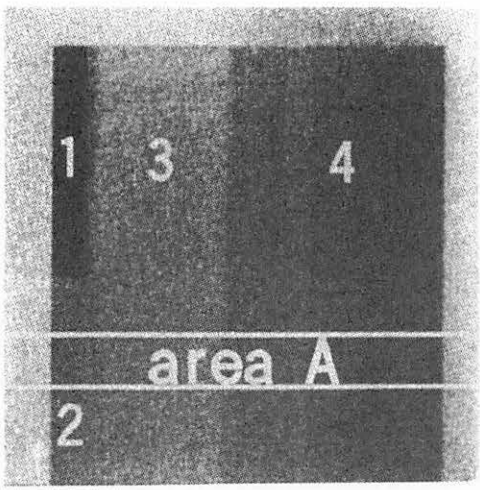

Fig. 5. Typical scanned image of IP for a step sample. Neutron energy is 5 MeV.

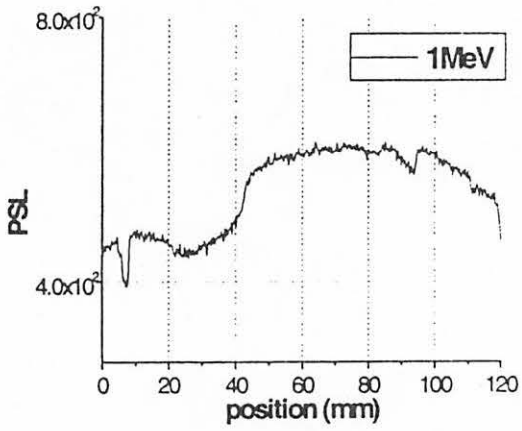

Fig. 6. Profiling result of a step sample for sample. Neutron energy is 5 MeV.

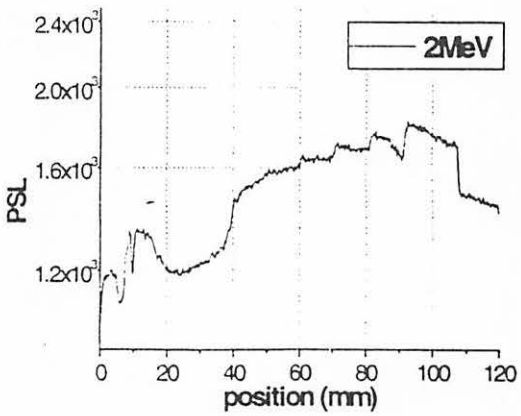

Fig. 7. Profiling result of a step sample for 2 MeV neutrons.

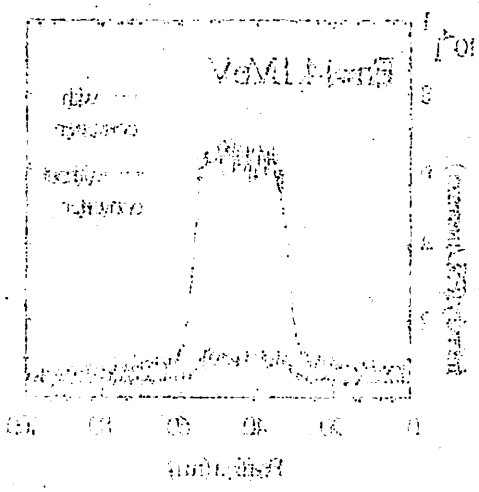

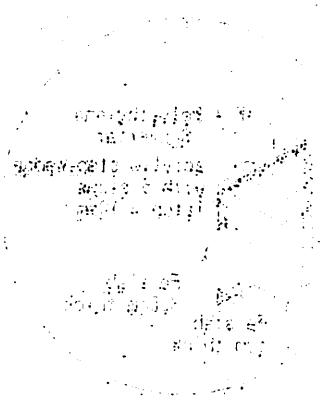

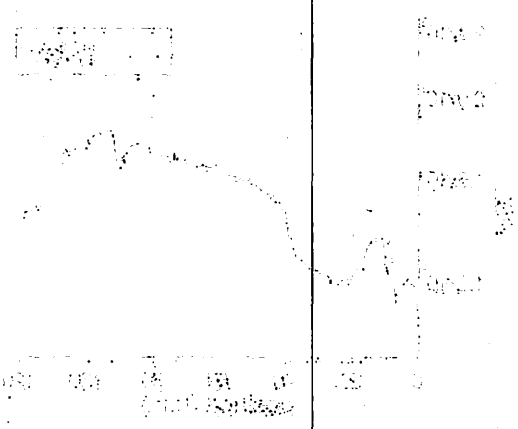

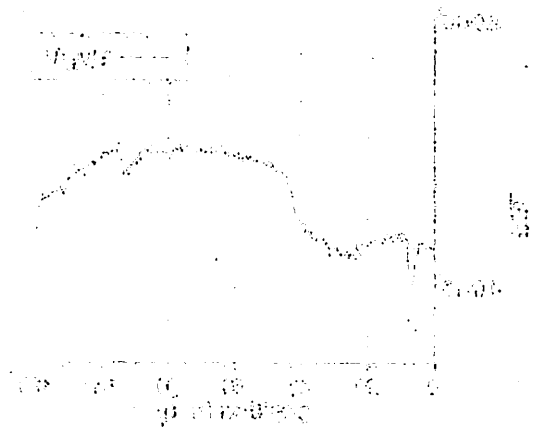

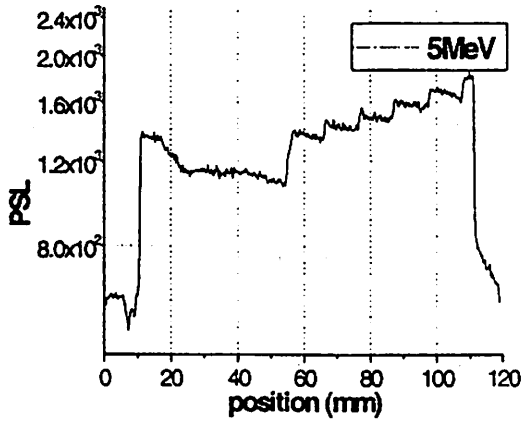

Fig. 8. Profiling result of a step sample for 5 MeV neutrons.

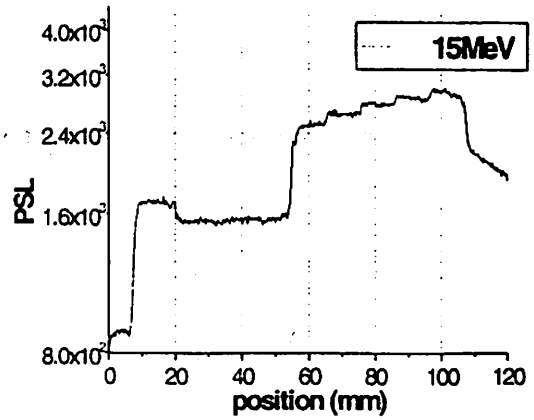

Fig. 9. Profiling result of a step sample for 15 MeV neutrons.

V. 3. Measurement of Radiation Tracks by Using Imaging Plate

*Taniguchi S., Yamadera A., Nakamura T., and Fukumura A.**

Cyclotron and Radioisotope Center, Tohoku University
**National Institute of Radiological Sciences Chiba 263, Japan*

Introduction

Imaging Plate(IP) was originally developed for diagnostic radiography and subsequently for autoradiography by Fuji Film Co. Ltd. Since IP has several advantages such as high sensitivity, high spatial resolution, digital data-taking, etc, it is extensively used in various fields: electron microscope, X-ray diffraction, neutron-radiography, radioactivity measurement, dosimetry, etc. Recently, identification of particles and their energies incident on IP has been tried by reading the photo-stimulated luminescence(PSL) at two different light wave lengths[1].

In this study we developed a new type track counting method using IPs for more distinct particle identification. We irradiated IP with protons with various energies and measured the distributions of energies deposited by these particles. This study can lead to the estimation of IP sensitivity for these various particles with energies in wide range and clarify the energy distributions deposited by projectiles. Nuclear emulsion film and polycarbonate film such as CR-39 are widely used for counting high-energy particle tracks. But, for obtaining accurate track information, IP has great advantages of no need for development or etching and of much higher (about 100 times) sensitivity and wider view range.

Experiment

Irradiation Experiments

At CYRIC we irradiated IP with 6, 9 and 12 MeV protons. Fig. 1 shows the experimental setup at CYRIC. We irradiated BAS-UR type IP with protons of 6, 9 and 12 MeV energies. The protons which were scattered in the direction of 90 deg by thin gold foil were irradiated on IP through the vaccum window of 3 mm thick Mylar foil. We changed the distance between the window and IP to change the proton energy incident on IP. The incident energy was changed in the range from 3 MeV to 12 MeV due to air absorption. The energy was estimated from the range-energy table in ICRU-49[2]. The number of protons which hit on IP was obtained from the beam current at Faraday cup which was placed behind the gold foil. The current at the Faraday cup was calibrated to the counts of ZnS(Ag) scintillation

survey meter fixed just outside the window, which is equal to the number of injected protons. The irradiation density was about 50 particle/cm^2 and the window size was 0.8 cm^2. To check the reproducibility we repeated the experiments by exposing about 40 particles on IP and read out the latent figure of IP about one hour after the irradiation by the BAS-3000 scanner system.

Analysis of Experimental Results

We measured the photo-stimulated luminescence (PSL) of each track by setting ROI(Region of Interest) in manual to cover each track. The PSLs were counted for about 300 tracks for each IP irradiated with different projectile energies and we obtained average values and standard deviations of these PSLs.

Calculation of Stopping Power and Residual Energy

We calculated the proton energy loss in IP with the SPAR code[3] which is based on the Bethe formula. In this calculation we assumed two different compositions for IP as listed in Table 1, because the precise composition of IP is not announced by Fuji Film Co. Ltd. The composition of No. 1 was obtained assuming that the IP was composed only of fluorine, bromine and barium, and No.2 that the IP was composed of fluorine, bromine, barium, hydrogen and oxygen. Hydrogen and oxygen are the elements of the binder of crystals.

Results and discussion

Fig. 2 shows the distributions of PSL per track for 6 and 9 MeV protons. The PSL distributions for both energies are similar and their peaks are at 0.1 PSL, but the ditribution for 9 MeV proton is shifted to the side of higher PSL compared with that for 6 MeV proton.

Fig. 3 shows the dependence of PSL/track for protons as a function of proton energy. The figure also shows proton energy loss calculated for IP with the compositions of No. 1 (solid line) and No.2 (dotted line), which are shown in Table 2. The energy of a proton whose range is equal to the thickness of sensitive layer of BAS-UR type IP(150 mm) is 3 MeV. Consequently, protons with energies lower than 3 MeV are fully stopped in the sensitive layer and deposit their whole energy in IP, and protons with energy higher than 3 MeV penetrate the sensitive layer and deposit only a part of their energy. This is the reason why the calculated results (solid and dotted lines) increase with the proton enegy up to 3 MeV then decrease thereafter. The observed PSL (black and white circles with error bars) has a tendency different from this. It decreases in the energy range from 3 to 6 MeV similarly as the calculated results, but increases in the range above 6 MeV.

Coclusion

We have developed a new type of track counting method by using IP. We measured distributions of PSL per track on IP irradiated with proton. They were compared with theoretical values of energy loss.

References

1) Takebe M., Abe K., Soda M. et al.: "A Particle Energy Determination with an Imaging Plate", Nucl. Instr. Methods **A359** (1995) 625-627.
2) International Commission on Radiation Units and Measurements: "Stopping Powers and Ranges for Protons and Alpha Particles", ICRU-49 (1993).
3) Armstrong T. W. and Chandler K. C: "SPAR, a FORTRAN Program for Computing Stopping Powers and Ranges for Muons, Charged Pions, Protons, and Heavy Ions", ORNL - 4869 (1973), Oak Ridge National Laboratory.

Table 1. IP composition.

No. 1		No. 2	
Element	Atomic Density [x 10^{21} atoms/cm^3]	Element	Atomic Density [x 10^{21} atoms/cm^3]
F	6.37	H	4.30
Br	6.37	C	2.20
Ba	6.37	F	6.37
-	-	Br	6.37
-	-	Ba	6.37

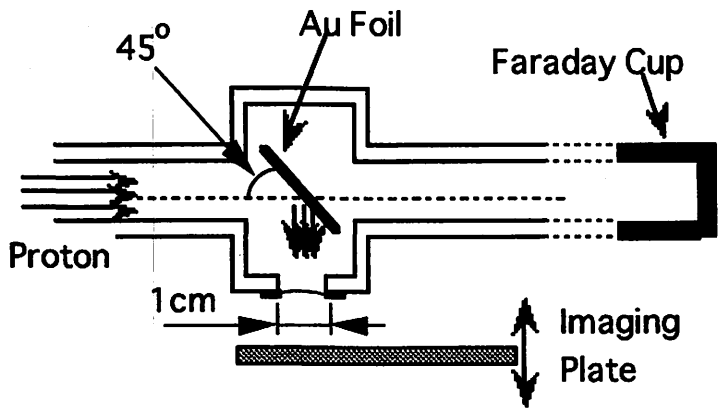

Fig. 1. Experimental setup at CYRIC.

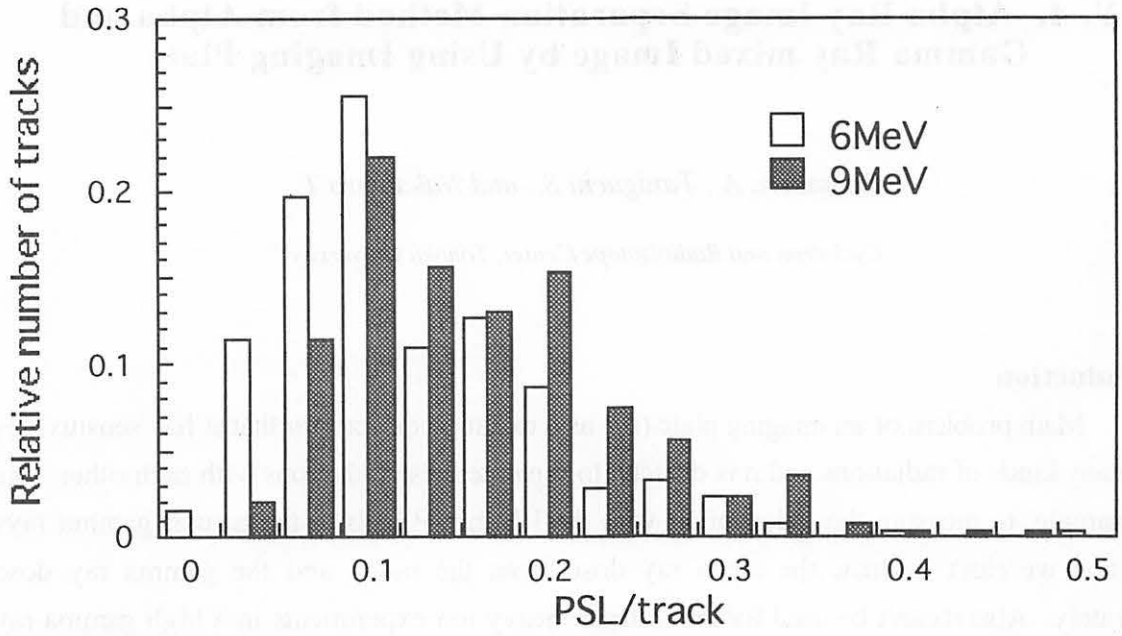

Fig. 2. Distribution of PSL/track of 6 and 9 MeV protons.

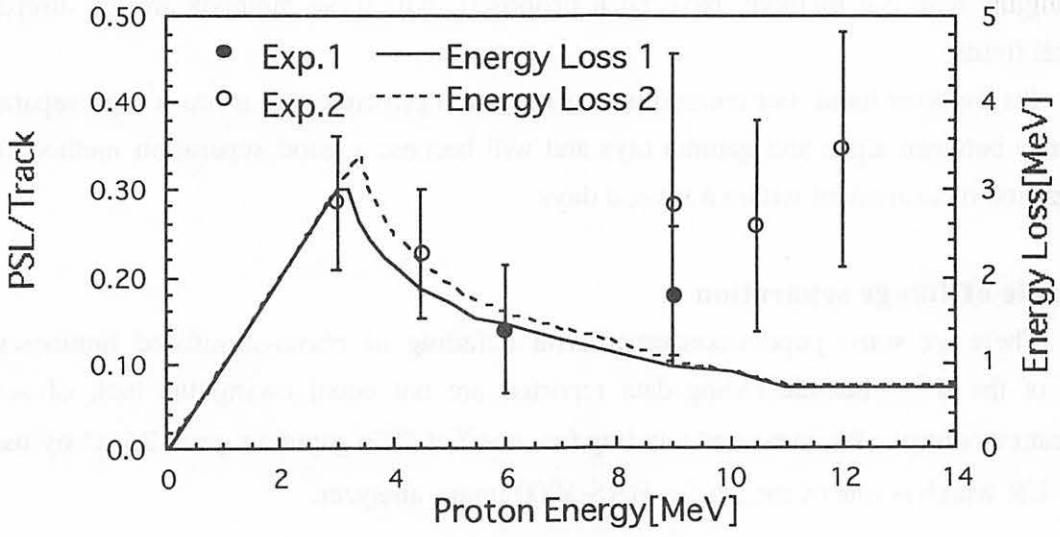

Fig. 3. Relation of PSL/track of protons with proton energy.

V. 4. Alpha Ray Image Separation Method from Alpha and Gamma Ray mixed Image by Using Imaging Plate

Yamadera A., Taniguchi S., and Nakamura T.

Cyclotron and Radioisotope Center, Tohoku University

Introduction

Main problem of an imaging plate (IP) as a radiation detector is that it has sensitivities for many kinds of radiations and it is difficult to separate these radiations with each other. As an example, to measure the radon in air with the IP, the IP feels to the natural gamma rays too, and we can't evaluate the alpha ray dose from the radon and the gamma ray dose separately. Also it can't be used for the in-beam heavy ion experiments in a high gamma ray field such as an irradiation vault. The largest defect of the IP is that the radiated memory in it fades according with elapsed time, which can not be neglected for using the IP as an integral type detector. To use the IP as a radiation detector, this defect must be overcome.

By using this fading phenomenon of the IP, we succeeded to separate an alpha ray image and a gamma ray image from an alpha and gamma ray mixed image.

As a separation method of mixed images, a plural times read out method[1] and a two wavelengths read out method[2] have been proposed, but, these methods are not useful in practical fields.

On the other hand, our method is very easy in a principle and it has a high separation efficiency between alpha and gamma rays and will become a good separation method for a short period measurement within a several days.

Principle of image separation

There are some papers concerned with a fading of photo-stimulated luminescence (PSL) of the IP[3,4], but the fading data reported are not equal owing the luck of severe temperature control. We measured a fading function[5] of ^{60}Co gamma rays at 25°C by use of BAS - UR which is one of the IPs for BAS-3000 image analyzer.

$$F(t) = 0.537\, e^{-0.693 \times t / 2.29} + 0.463\, e^{-0.693 \times t / 24.27}$$

Here, t is elapsed time(days). There are two fading components, one component of 53.7% fades with half life of 2.29 days and the other one of 46.3% fades with half life of 24.27

days. The component ratio changes depending on the kinds of radiation. For ^{60}Co gamma rays, it is 1.16 and for alpha rays it becomes more larger.

The speed of fading is changed largely depending on the temperature and the kinds of radiation; it is not so large at 0°C, but it becomes larger remarkably at 50°C. Here, we call the fading at 50°C as "annealing". By using annealing phenomena we could separate alpha ray and gamma ray images.

The method is very simple; we read out the first image from the IP which has irradiated with alpha and gamma rays, it is annealed for 2 hours in a constant temperature convection oven which is kept at 50°C, and finally the second image is read out from the annealed IP.

An alpha ray image is obtained by subtracting the second image from the first image as following ways. Here we call this method as " Annealing-Ratio Subtract Method (ARS method) ".

On every pixel in the IP image, PSL value irradiated with unit dose equivalent of gamma rays stands for f(t) and that of alpha rays stand for g(t) as a function of annealing time (t). Here, we assume that annealing temperature is constant and fading at room temperature is negligible small.

Before the irradiation of the IP with alpha and gamma rays, one part of the IP is covered with a thin polyethylene film, not to be irradiated with alpha rays and to be irradiated only with gamma rays. The PSL density of the area irradiated by the only gamma ray is shown as follows.

$$P_\gamma(t) = R \times f(t), \qquad (1)$$

where, R is the dose equivalent of the IP irradiated by gamma rays.
The PSL density irradiated by gamma and alpha rays is shown as follows;

$$P_{mix}(t) = a \times f(t) + b \times g(t) \qquad (2)$$

Here, a and b are the dose equivalents due to gamma rays and alpha rays, respectively.
Now, we subtract an annealed image from a first measured image as follows;

$$\Delta P = P_{mix}(0) - K \times P_{mix}(t)$$

$$= R\{ f(0) - K \times f(t) \} + a\{f(0) - K \times f(t) \} + b\{ g(0) - K \times g(t) \}. \qquad (3)$$

Here, $P_{mix}(0)$ is the first measured PSL density of the irradiated IP. We put it in a fixed temperature oven for t hours. $P_{mix}(t)$ is the second measured PSL density of it. K is a constant.

In equation (3), the first part shows the PSL component irradiated by the gamma rays, the second part shows the PSL component irradiated by gamma rays which are emitted

accompanied with alpha decay and the third part shows the PSL component irradiated by alpha rays.

Now, we set K = f(0) / f(t), the first and second parts are canceled and the equation is simply expressed as follows.

$$\Delta P = b\{ g(0) - K \times g(t) \}. \quad (4)$$

Here, K is the annealing coefficient which means the reversed function of annealing ratio (= f(t) / f(0)) of gamma ray component. Therefore, we can easily calculate K from measured f(t) and f(0) values of the region of interest (ROI) area which is irradiated with only gamma rays and not irradiated with alpha rays. We call K as an annealing coefficient (AC).

By using the equation (4), we can obtain a pure alpha ray image which will be used for qualitative image analysis. But, this equation does not show an absolute PSL distribution, because ΔP is changed by experimental conditions such as an annealing temperature and an elapsed time.

For obtaining an absolute PSL image, we must calculate the AC of alpha ray component. But, we can not calculate it from the usual IP image, because the IP which is irradiated with alpha rays is usually irradiated with beta and gamma rays too. It is calculated by measuring a PSL value of every alpha particle track of the first and the second images.

$$L = g(0) / g(t). \quad (5)$$

Here, L means the AC of the PSL component irradiated by alpha rays.
From equation (4) and (5), an absolute alpha ray image is shown as follows;

$$b \times g(0) = \Delta P / (1 - (K / L)). \quad (6)$$

By using equation (6), we can compare the alpha images which are measured on the different conditions.

Experiment

We used an image analyzing system (Fuji Photo Film Co.,Ltd) which is composed of an image reader (BAS-1000), an analyzer (MacBAS), an image printer (PICTROGRAPHY3000), MO disc drive (Panasonic LF-3200) and printer (Laser Jet4). The type of the IP is BAS-1000III s, of which size is 20 × 40 cm and pixel size is 100μm. The time for image reading per an IP is about 3.5 minutes.

We used a ^{60}Co gamma ray source from which dose was 0.12 mGy at 1m and a ^{238}U alpha source of which size was 5 cm in diameter and its activity density was 10.8 Bq/cm^2. The alpha source is in radioactive equilibrium between ^{238}U and ^{234}U.

The IP is irradiated with a ^{60}Co gamma ray source at 2 meter for 30 minutes. In front of the IP, three lead absorbers are set and the absorber thickness are 5, 10 and 15mm. Next,

the IP is irradiated with alpha ray source which is put on the IP directly for 15 ~ 45 minutes. After the IP is cooled for 30 minutes waiting for the disappearance of short life fading component, the first reading is carried out.

After the first reading, the IP was annealed for 2 hours in a convection oven which is kept at 50 ± 0.5 °C and the second reading is carried out.

Result

Measurement of annealing coefficient

On ARS method, it is important to obtain an accurate annealing coefficient.

Figure 1 shows the first IP image which is irradiated with radiations from ^{60}Co and ^{238}U sources. In the Fig. 1, A is the area where ^{238}U is set and C, D and E are the shadows of the lead absorbers of which thickness are 5, 10 and 15 mm, respectively.

Figure 2 shows the PSL/mm^2 distribution on the line of a –a' in Fig. 1. The open circles are the first measurement and the crosses are the second measurement. On comparing the first and second curves, the distance of peak area where is irradiated with ^{238}U source is larger than the other gamma ray irradiated areas.

Table 1 shows the AC obtained in every ROI area. The AC of area A is 2.12 and 1.2 times greater than the other areas. The AC of them show almost same value 1.74 and their standard deviation is calculated to be ± 0.02. It is clear that the AC of gamma ray irradiated areas are not changed even if absorber thickness are changed and that of the alpha ray irradiated area is annealed faster than gamma irradiated areas.

In Fig. 2 , the differences of the open circles and 1.7 times of the crosses are the black circles. The alpha ray irradiated area is emphasized and gamma ray shadows are disappeared.

Separation of images

An operation between image data are carried out by using "LPprocess" which is a image reconstructing software developed by Fuji Photo Film Co., Ltd.

By using LPprocess, We tried to separate an alpha ray irradiated image from a alpha and gamma ray mixed image.

Figure 3 shows the first measured raw image. The IP was irradiated with the same condition as Fig.1, and the area F and G were irradiated with alpha particles from the ^{238}U source for 45 minutes and 15 minutes, respectively. After annealing treatment, the IP was set to the image reader.

Figure 4 is an image subtracted with the second image by a factor 1.7 from the first image. In Fig. 4, the shadows of lead absorbers are almost cleared but many black points (pixels) are remained. This is explained as that two images are not measured at the same position within the length of one pixel and the statistical error due to subtraction are emphasized in view. Before the image subtraction, we smoothed the first and second images

by using LPprocess and subtracted the two images with above mentioned method. Figure 5 shows the subtracted image. The gamma background is clearly eliminated and alpha irradiated areas are remained.

The PSL densities of A, F and G are 18.8, 24.0 and 8.8 PSL/mm^2, respectively, and these values are roughly proportional to the irradiation time 30, 45 and 15 minutes, respectively.

Conclution

We have developed a separation method of an alpha ray image and a gamma ray image by using an IP. The IP which has been read out the first image by the image reader is annealed at 50°C for 2 hours in a convection oven and is read once more by the image reader. Subtracting K times of the second image from the first image, we can get the alpha ray image. Here, K is the annealing coefficient which is defined as the PSL density of gamma ray irradiated area of the first measurement to the one of the second measurement area.

References

1) Chizuo M., Matumura A., Suzuki T. et al., Nucl. Instr. And Meth., **A339** (1994) 278.
2) Takebe M., Abe K., Souda M. et al., Nucl. Instr. and Meth., **A359**.(1995).625.
3) Shindo D., Taniyama A., Hiraga K. and Oikawa T., Sixth Asia-Pacific Conference On Electron Microscopy, (Hong Kong, 1996).
4) Mori C. and Matsumura A., Nul. Instr. and Meth., **A312** (1992) 40.
5) Yamadera A., Kim E., Miyata T. and Nakamura T., RADIOISOTOPES, **42** (1993) 676.

Table 2. Annealing coefficient of the area indicated in Fig. 1.

area	AC	radiation, absorber
A	2.12	gamma + alpha
B	1.73	gamma
C	1.76	gamma, lead 5mm
D	1.71	gamma, lead 10mm
E	1.75	gamma, lead 15mm

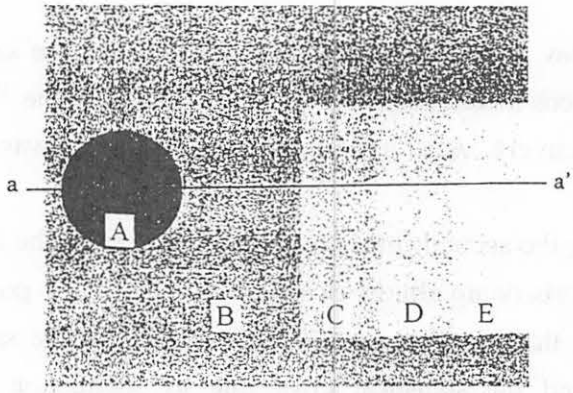

Fig. 1. The first measured image irradiated with ^{60}Co and ^{238}U sources. Circle shows the place irradiated with Uranium source and three rectangles at right side are the shadows of Lead filters (thickness : 5, 10, 15 mm).

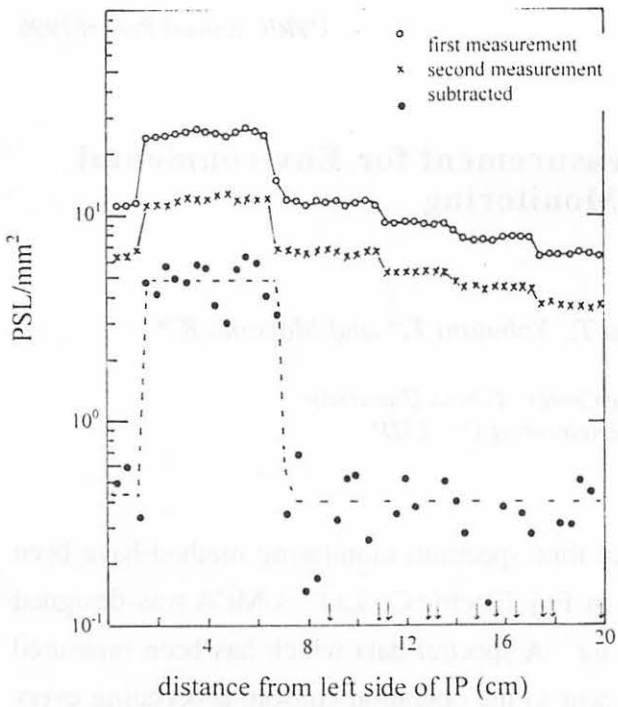

Fig. 2. PSL distribution of the first measurement, the second measurement and subtracted values.

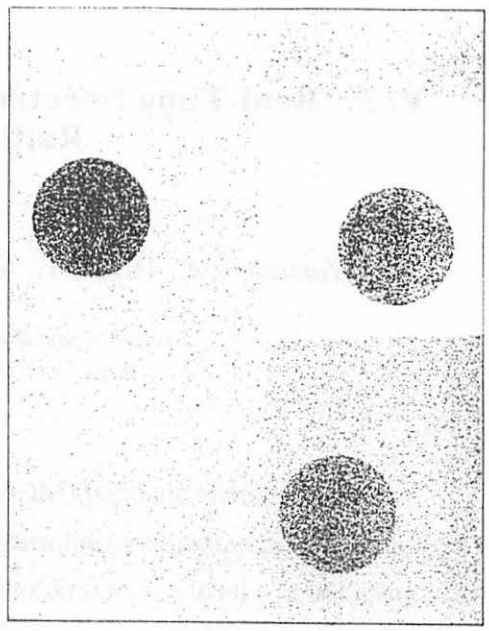

Fig. 3. The first measured image irradiated with ^{60}Co and ^{238}U. Three circles belong to Uranium sources.

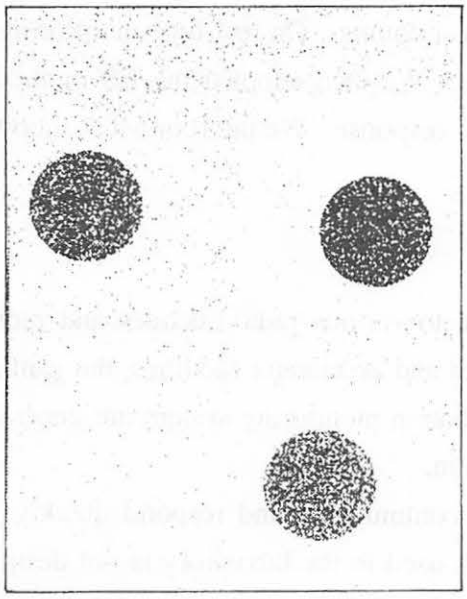

Fig. 4. Subtracted alpha ray image. (no smoothing).

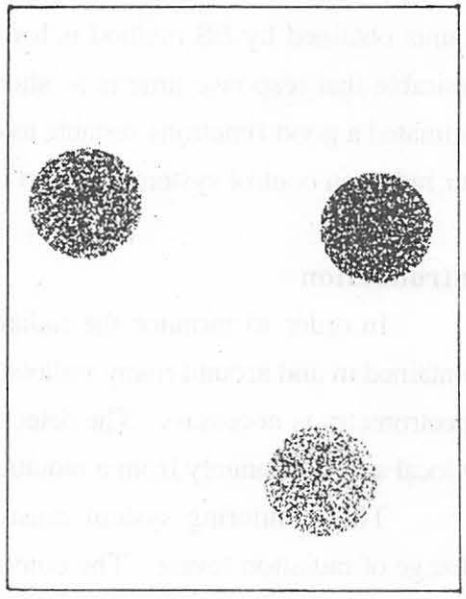

Fig. 5. Smoothed and subtracted alpha ray image.

V. 5. Real Time Spectrum Measurement for Environmental Radiation Monitoring

Yamadera A., Miyata T., Nakamura T., Yabutani T. and Matsuno K.**

Cyclotron and Radioisotope Center , Tohoku University
*Fuji Electric Techno-Engineering Co., LTD**

A multichannel analyzer (MCA) and real time spectrum monitoring method have been developed for the radiation monitoring system by Fuji Electric Co.Ltd. A MCA was designed to be installed at a local site of a radiation detector. A spectral data which has been measured and collected in the MCA in every 1 minute is sent to the operation console proceeding every measured data. Because of poor count rate, the raw data measured in 1 minute have large statistical error and do not form a clear energy spectrum. For obtaining clear spectrum, we compared the "running average (RA) method" and the "exponential smoothing (ES) method". The response of the ES method is initially faster than that of the RA method, but the total counts obtained by ES method is lower than the real counts. On real time monitoring, it is desirable that response time is as short as possible. We then adopted the ES method, and estimated a good functions suitable to obtain the fast response. We put four MCA monitors in our radiation control system and start operation.

Introduction

In order to monitor the radiation level due to various radio-nuclides and radiations contained in and around many radioisotope facilities and accelerator facilities, the gamma ray spectrometry is necessary. The detectors of the radiation monitoring system are generally set at local sites, separately from a radiation control room.

The monitoring system must be operated continuously and respond quickly to the change of radiation levels. The conventional MCA used in the laboratory is not designed to measure continuously for varying radiation with quick response and is also expensive.

For these reasons, spectrum measurement has not been applied to radiation monitors. Only the total count rates have been measured by using single channel analyzers.

We have developed a local setting MCA which is installed at monitoring station housing with radiation detectors and data reduction methods with a real time response to be used in radiation monitors.

Method of real time spectrum measurement

Table 1 shows the specification of the MCA. The MCA contains an amplifier, a high voltage power supply, a temperature sensor and optical interface for data transmission to the central console. Detector bias voltage, amplifier gain and measuring period are adjustable from the central console. The MCA is used together with a 5.08 cm diameter by 5.08 cm long NaI(Tl) detector.

A spectra measurement is repeated for 1 minute and, after each measurement, spectrum data are transmitted from the MCA to the operation console via an optical fiber cable. The personal computer in the operation console stores every 1 minute spectrum for long time interval.

We applied two computing method. Both methods have been utilized in digital count rate meters. One method is the "running average (RA) method".

Each spectral data transmitted from the preamplifier is stored in a rotating 10 stage memory stack. The most recent datum replaces the oldest one cyclically. Thus, the spectrum of the RA method shows simply the mean value of 10 minutes and its response is delayed depending on the radiation level.

The other method is the "exponential smoothing (ES) method", which responds exponentially to the change of radiation level.

$$N_i = R_i^{-1} \left[N_{in} + (R_i - 1) N_{i(n-1)} \right], \quad (1)$$

$$\tau_i = (R_i - 0.5) \Delta t, \quad (2)$$

$$P = \left[2 \tau_i N_{i(n-1)} \right]^{-1/2} \times 100, \quad (3)$$

where

N_i = counts of i-channel after refreshment,

Ri = Exponential smoothing coefficient,

N_{in} = Counts of i-channel transmitted,

$N_{i(n-1)}$ = Counts of i-channel before refreshment,

τ_i = Time constant of i-channel, and

P = Relative standard deviation which is common to the whole channel.

The exponential smoothing coefficient R_i is derived from Eqs. (1), (2) and (3).

$$R_i = \left[2 N_{i(n-1)} \Delta t \right]^{-1} (100/P)^2 + 0.5 \quad (4)$$

By setting the value of Δt(now, Δt = 1 minute) and P before hand, R_i is calculated with $N_{i(n-1)}$. Then, the count numbers of each channel are exponentially smoothed.

The time constant for each channel changes according to the count of each channel. As a result, relative standard deviations of the whole channel have the same value in the range of τ_i from 1 to 10 minutes.

Experiments of real spectrum

We put ^{137}Cs and ^{60}Co radiation sources which intensities were about 300kBq on the surface of the gaseous effluent detector and after about 15 minutes we removed the both sources.

Fig. 1 shows the change of the spectrum for every 1 minute analyzed by the RA method and Fig. 2 shows the change in the gross count rates of the photo peak area of ^{137}Cs 662keV gamma rays. The count rates lineally increase and decrease symmetrically.

Fig. 3 shows the change of the spectrum for every 1 minute analyzed by the ES method when the relative standard deviation is set to 5%. Fig. 4 shows the changes in the gross count rates of the ^{137}Cs gamma ray peak area when the standard deviation is set to 5%, 10% and 20%. With increase of standard deviation, the count rates rise up rapidly and rise down rapidly and the plateau peak range becomes wide, which indicates the quicker response. For obtaining real time response, it is therefore desirable to select large standard deviation, but data fluctuation become large.

Application to radiation monitors

We applied this real time spectrum measurement system in the radiation monitoring system at Cyclotron and Radioisotope Center of Tohoku university. Two area monitors were set at the boundary and two gaseous effluent monitors were set on two air stack of our facility.

We have a AVF cyclotron and the positron emitting nuclides of ^{18}F, ^{15}O and ^{11}C are produced routinely every week for radiopharmaceutical production for positron emission tomography study and also many kinds of radioisotopes which have brought in the facility are used.

Considering radioisotope releasing for short period from an air stack, we injected 1 ml of $^{11}CO_2$ gas of 500kBq to an input tube of the monitors. Fig. 5 shows the activity change. A solid line is the real activity change detected with the NaI(Tl) detector directly and a dotted and a broken lines are thoes analyzed with the ES and RA methods, respectively. The change of the ES method shows the similar shape of the real activity curve except for slower attenuation. But, the distribution of the RA method shows a quite different shape and a peak position of the RA method appears 10 minute later than real discharge time. By using the RA method, we can not decide the discharge time of radioisotope on time. Fig. 6 shows the spectra of area monitor set on the boundary of our facility. The peak of 1.46MeV is the gamma rays of ^{40}K and the peak of near 0.55MeV is the mixed gamma rays of ^{208}Tl and ^{214}Bi. These are all natural isotopes and artificial isotope is not recognized.

Summary

We have developed an MCA and two real time spectrum monitoring methods for use in the radiation monitors. The "running average method" cannot keep up with radiation changes. The "exponential smoothing method" has a fast response because of an automatically variable time constant. The latter method is preferable for area monitors and gaseous effluent monitors.

Table 1. Specifications of the MCA.

Bias voltage supply	600 - 1,200 V
Amplifier gain	1.1 V/pc ×1,2,3
ADC conversion gain	512 ch
Counts per channel	$2^{16}-1$
Integral non-linearity	± 0.5 %
Differential non-linearity	± 2 %
Operating condition	0-45 ℃, 95 %RH

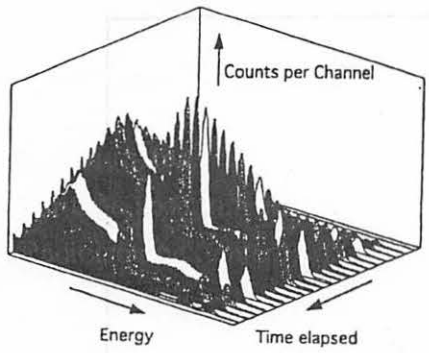

Fig.1 Changes in spectra analyzed with running averaging method.

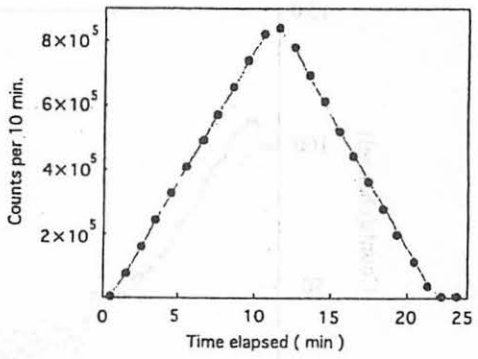

Fig.2 Changes in gross counts of ^{137}Cs with running averaging method.

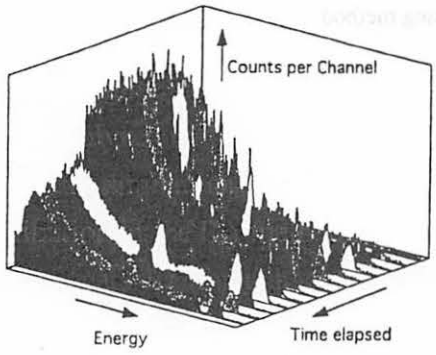

Fig.3 Changes in spectra analyzed with exponential smoothing method.

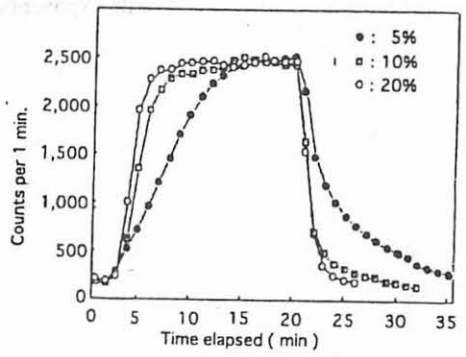

Fig.4 Changes in gross counts of ^{137}Cs with exponential smoothing method.

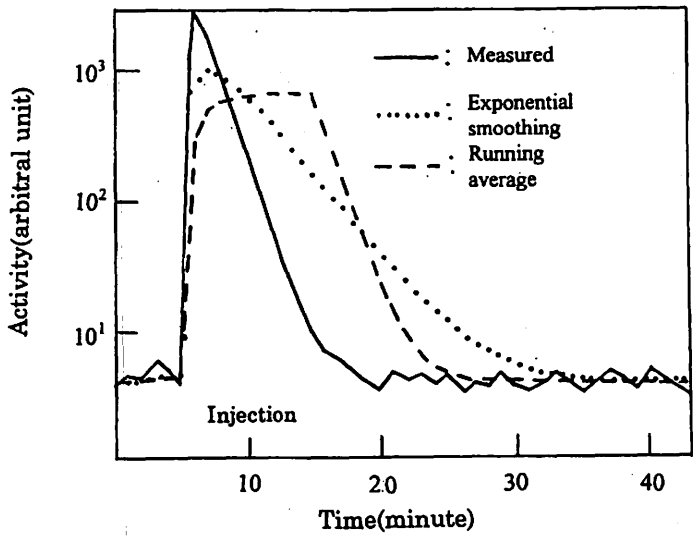

Fig. 5 Comparison of running averaging method and exponential smoothing method with use of active gas $^{11}CO_2$

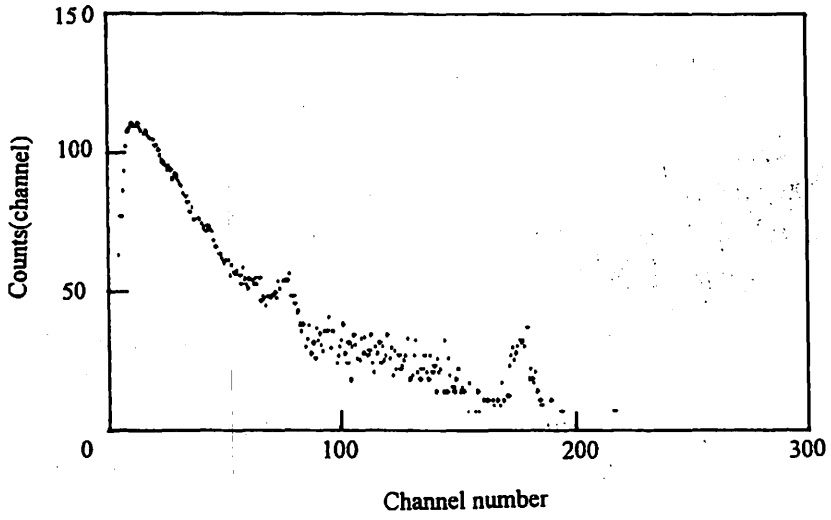

Fig.6 Spectra measured at monitoring post and analyzed with exponential smoothing method.

V. 6. Study on the Radiation Shielding Performance of an Assembly of Concrete Blocks

Sasaki M., Hoshi K., Yamadera A., Nakamura T.
Terai M., Odagawa M.*, and Mikami H.**

Cyclotron and Radioisotope Center, Tohoku University
*Takenaka Civil Engineering Co. Ltd.**

Introduction

An assembly of concrete blocks has widely been used to make a wall for radiation shielding because of easy dismantling and restoration when needed. But some attention must be paid to the radiation leakage through the air gaps between the blocks. Recently, concrete blocks having the smallest air gaps when assembled them have been specially fabricated by Takenaka Civil Eng. Co.Ltd. and other companies, and used in nuclear power plant. This study was done to measure the performance of radiation shielding against neutrons and photons of an assembly of concrete blocks by changing the thickness of concrete blocks. In order to clarify the effect of air gaps between concrete blocks, we also changed the width of air gaps. The experimental results were compared with the calculated results obtained from the MCNP Monte Carlo Code[1].

Experiment

In this study, we used a ^{252}Cf (0.92mCi) neutron source with polyethylene collimator and ^{60}Co gamma-ray source (11mCi) with lead collimator. The schematic views of experimental arrangement and collimators are shown in Fig. 1. Polyethylene collimator is a sphere of 35cm diameter having a collimator hole of 5.1cm diameter by 15cm length and lead collimator is a cylinder of 10cm diameter by 10cm height having a tapered collimator hole of 30cm outer diameter by 3.5cm length. For neutron detection, we used dose equivalent surveymeter, rem counter, NSN1, fabricated by Fuji Electric Co. Ltd. and Bonner sphere spectrometer loading ^{3}He proportional counter[2] , and for photon detection, we used NaI(Tl) scintillation surveymeter, TCS-161, fabricated by ALOKA Co.Ltd. and NaI(Tl) scintillation spectrometer of 7.62cm diameter by 7.62cm length. The concrete blocks were assembled to have a concrete wall of 130cm height and 145cm width and the wall thickness was changed as 50, 60, 80, and 100cm. The collimator exit of neutron or photon source was fixed to be 10cm distant from the concrete wall surface and the collimator hole was kept for collimated

neutron and photon beams to be normally incident on the wall surface. The detectors were placed in contact with the rear surface of the concrete wall.

The experiment was done in the room of 6.05m × 9.92m × 4.58m and to estimate the contribution of room-scattered radiation, we repeated twice the measurements with and without the shadow bar of the collimator. By subtracting these two measured results, we approximately excluded the room-scattered radiation. Both the sources and detectors were placed at a few positions faced on the flat block surface and on the gap of two blocks as shown in Fig.1. For further investigation of air gap leakage effect, both at 50 and 80cm wall thicknesses, we inserted metal washers with 1mm or 3mm thickness between the blocks to enlarge the air gaps as also indicated in Fig. 1.

The counts measured with Bonner ball were converted to the neutron energy spectra using the SAND-2 code[3] with an initial guess based on the MCNP calculation and the calculated response functions[2] and the neutron dose equivalent values were obtained from these-obtained spectra and the dose conversion factor given by ICRP-51[4].

The pulse height distribution measured with NaI(Tl) were also converted to the photon energy spectra using the FERDO-U code[5] and the calculated response function[6], and the dose equivalent values were also directly obtained from the pulse height distributions using the G(E) function[7], which includes the dose conversion factor.

Calculation

To compare with the experimental data, we calculated the neutron and photon energy spectra and dose equivalents penetrated through concrete shields with the MCNP Monte Carlo code[2]. In this calculation, the cross section data library, ENDF/B-IV was used. The atomic composition of the concrete used in the calculation is listed in Table 1. The density of the concrete blocks was determined as 2.15 g/cm^3.

Results and discussion

Figs. 2 and 3 show the calculated and measured neutron energy spectra, respectively. Although the units of spectra are different in both figures, the spectral shapes are in good agreement between calculation and experiment.

Figs. 4 and 5 show the measured and calculated attenuation curves of neutron and photon dose equivalent rates as a function of the concrete thickness, respectively. Since the source-to-detector distance was changed at different wall thickness, the dose values were normalized at the distance of 1m. In these figures, 'pos.a-b' indicates that the source position is 'a' and the detection position is 'b', where 'pos.1-1' faces to the flat concrete surface with no air gaps, while 'pos.2-2' and 'pos.2-3' face just at air gaps as seen in Fig. 1. There can be seen no noticeable difference between two experimental results at 'pos.1-1' and 'pos.2-2'/ 'pos.2-3', which means that the leakage effect of neutrons and photons through air gaps between concrete blocks are negligibly small for this specially-designed blocks.

The agreement between experimental and calculated dose equivalent data is rather good for photons, but some discrepancy can be seen for neutrons. This discrepancy may be caused by the difference of actual water content (not available in this concrete blocks) and that used in the calculation, because the neutron attenuation through concrete is strongly influenced by water content, especially hydrogen content. Figs.6 and 7 shows the variation of measured neutron and photon dose equivalent rates with the slit width inserted between concrete blocks at t (shield thickness) = 50 and 80cm. At t = 50cm, slight increase of neutron and photon dose equivalent rates can be seen with slit width (about 40% up to 3mm slit width) but at t = 80cm, there can be seen no increase of dose rates with slit width. The leakage effect through air gaps of slits may be canceled out with decreasing the direct radiation components.

Conclusion

It can be clarified from this study that an assembly of specially-designed concrete blocks has enough shielding performance compared with normal(slab) concrete wall.

References

1) Kosako K. et al : MCNP-A General Monte Carlo Code for Neutron and Photon Transport, *JAERI-memo* 05-145 (1993).
2) Uwamino Y., Nakamura T., Hara A.: Two Types of Multi-moderator Neutron Spectrometers, Nucl.Instr.Methods. **A239** (1985) 299-309.
3) McEloy W. N., Berg S., Crockett T., Hawkins R. G.: AFWL-TR-67-41, *Air Force Weapons Laboratory* (1967).
4) Annals of ICRP, *ICRP publication 5 1*(1987).
5) Uwamino Y., Shin K., Fujii M., and Nakamura T., Nucl.Instr.Methods. **204** (1982) 179-189.
6) Berger M. J., and Seltzer S. M., Nucl. Instr.Methods. **104** (1972) 317-332.
7) Moriuchi S., A New Method of Dose evaluation by spectrum-Dose Conversion Operator and Determination of the Operator (1970).

Table 1. Concrete data used in the MCNP Monte Calro Code.

Element	Atomic Density
H	7.1929-3
O	4.0323-2
Mg	1.2782-4
Al	2.1883-3
Si	1.4556-2
Ca	2.6683-3
Fe	2.8282-4
Na	9.6302-4
K	6.3578-4

unit (10^{24}/cm^3)

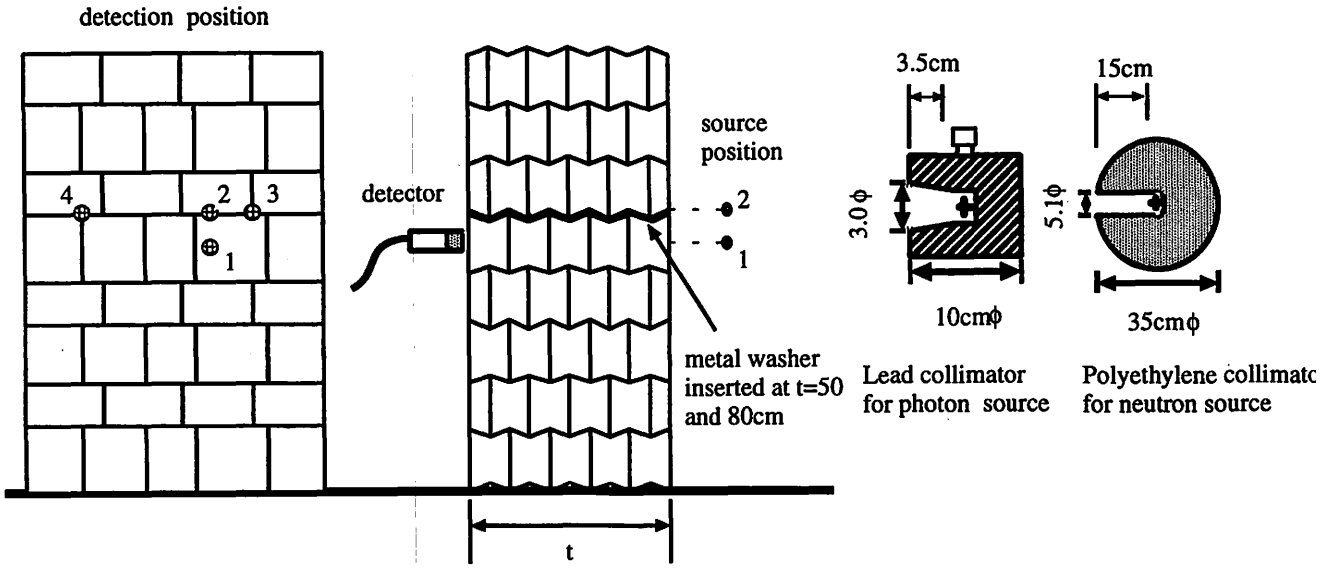

Fig. 1. Schematic view of experimental arrangement and radiation source.

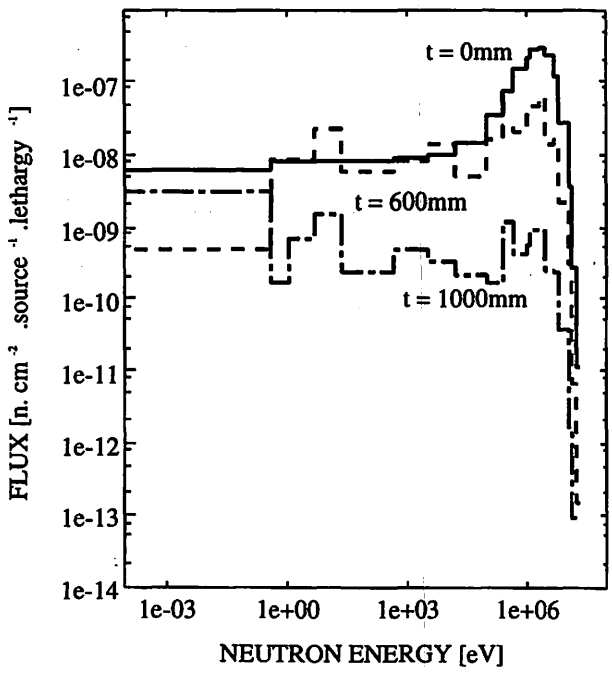

Fig. 2. Calculated neutron spectra at each concrete thickness.

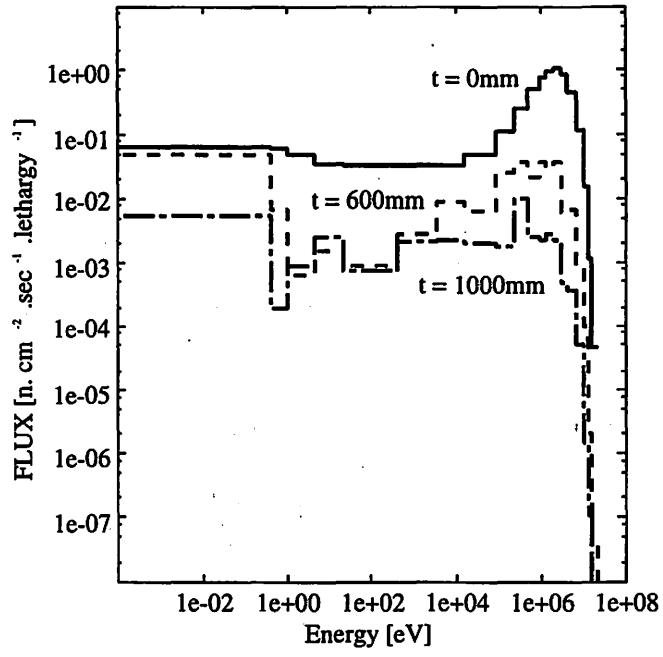

Fig. 3. Measured neutron spectra at each concrete thickness.

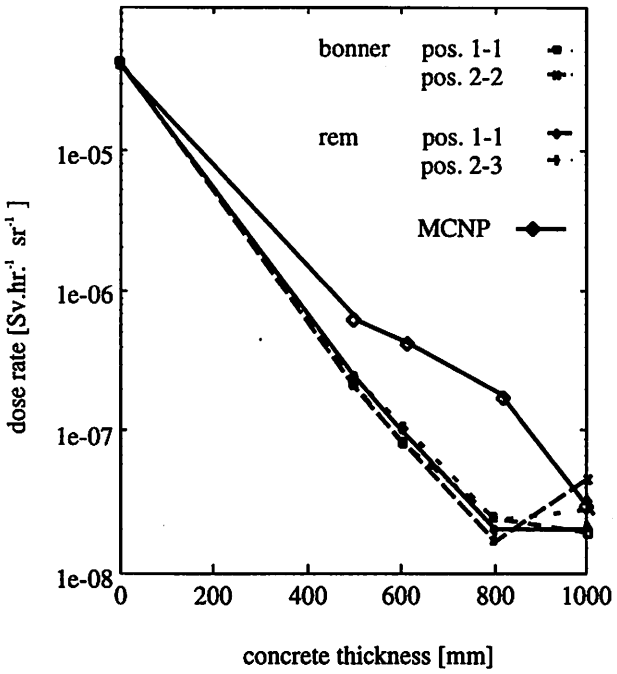

Fig. 4. Attenuation of neutron dose equivalent rate as a function of the concrete thickness.

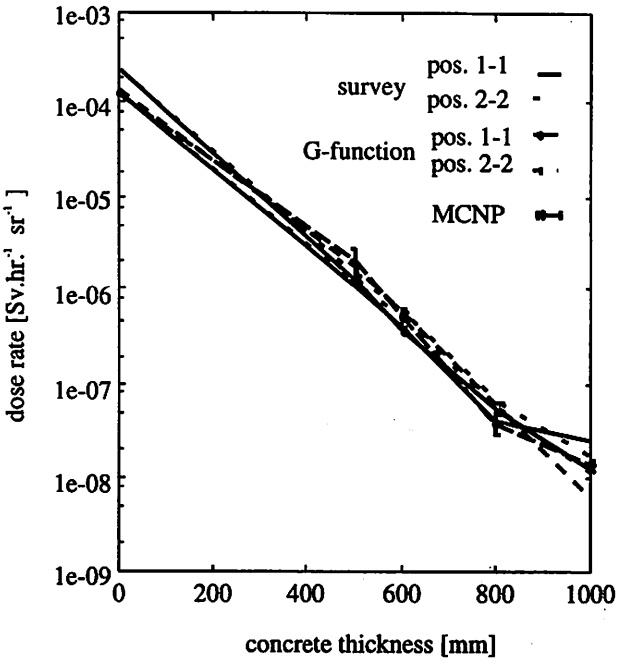

Fig. 5. Attenuation of photon dose equlvalent rate as a function of the concrete

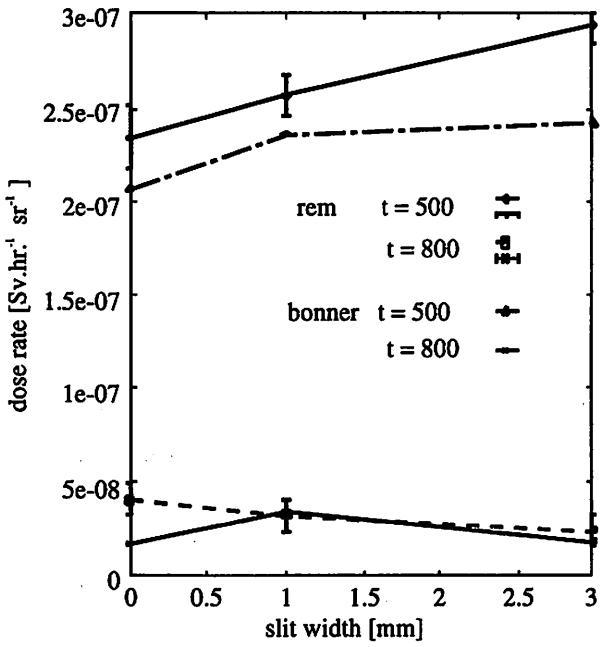

Fig. 6. Dependence of neutron dose equlvalent rate on the slit width.

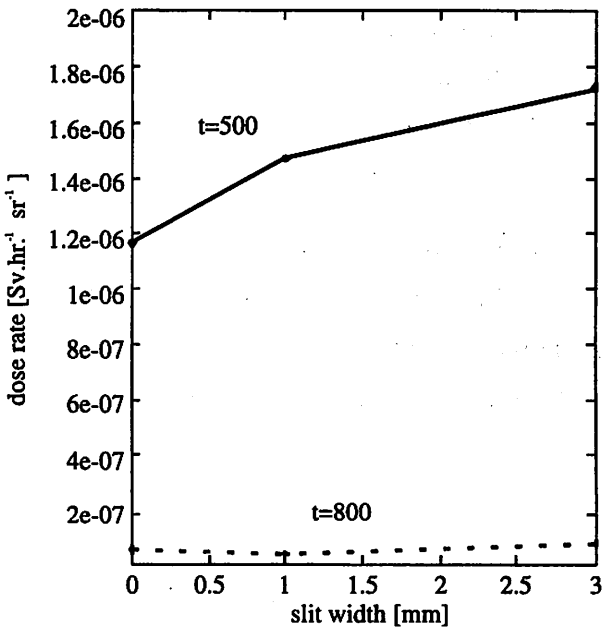

Fig. 7. Dependence of photon dose equivalent rate on the slit width.

V. 7. Radiation Protection and Management

*Miyata T., Yamadera A., Nakamura T. and Watanabe N.**

Cyclotron and Radioisotope Center, Tohoku University
*Japan Radiation Protection Co., Ltd.**

(1) Unsealed radionuclides used in the center

The kinds and activities of unsealed radionuclides handled in the center in 1996 are shown in Table 1. The table includes the isotopes produced by the cyclotron, purchased from the Japan Isotope Association and took over from another RI institutes.

(2) Individual monitoring

The exposure doses of the workers in the center in 1996 is given in Table 2. They were less than the permissible doses.

(3) Monitoring of the workplace

Radiation dose rates inside and outside of the controlled areas were monitored periodically and as needed. They were below the legal permissible levels. Surface contamination levels of the floors inside the controlled areas were measured by smear method and with survey meters periodically and as needed. They also cleared under the legal regulation levels.

(4) Wastes management

The radioactive wastes delivered to the Japan Radioisotope Association in 1996 are shown in Table 3. The concentration of radioisotopes in the air released after filtration from the stack was monitored with stack gas monitors. The levels were less than the legal regulation levels. The radioactive water was storaged at the tanks at least for 3 days and then released to the sewerage after confirming that the concentration was less than permissible levels.

The treated volume of radioactive waste of organic scintillator was 1901 ℓ by the incinerator made by Fujikogyo Co., Ltd.

Table 1. Unsealed radionuclides used in the center in 1996.

(a)Cyclotron Building (kBq)		(b) RI Building (kBq)			
group 3		group 1		^{123}I	673,400.000
^{11}C	282,354,400.000	^{90}Sr	397.500	^{131}I	116,815.700
^{15}O	28,971,005.000				
^{28}Mg	1,850.000	total	397.500	total	4,838,707.291
^{111}In	2,376,370.000	group 2		group 4	
		^{45}Ca	134,857.346	^{3}H	706,726.463
total	313,703,625.000	^{60}Co	1,504.840	^{14}C	25,069.976
group 4		^{65}Zn	3,060.600	^{18}F	165,784,310.000
^{18}F	387,160,600.000	^{68}Ge	379,116.000	^{201}Tl	139,390.000
		^{85}Sr	26,849.000		
total	700,864,225.000	^{99}Tc	2,500.000	total	166,655,496.439
		^{125}I	929,629.663		
(c)Research Building (kBq)		^{137}Cs	15,263.343		
group 3					
^{11}C	3,196,800.000	total	1,492,780.792		
^{15}O	29,785,000.000	group 3			
		^{11}C	1,232,100.000		
total	32,981,800.000	^{28}Mg	1,517.000		
group 4		^{32}P	1,238,512.721		
^{18}F	3,367,000.000	^{35}S	15,361.870		
		^{99}Mo	705,000.000		
total	3,367,000.000	^{99m}Tc	853,000.000		

Table 2. Occupational radiation exposures at the center in 1996.

Dose range (mSv)	Number ofindividuals
No measurable exposure	37
Measurable exposure less than 1.0	4
1.0 to 2.5	5
Total persons monitored	46

Table 3. Radioactive wastes delivered to the Japan Radioisotope Association in 1996.

Wastes	Container	Number
solids		
Combustible Type I	50 ℓ drum	29
Combustible Type II	50 ℓ drum	17
Incombustibles	50 ℓ drum	6
Annimal carcasses	50 ℓ drum	11
Filters	50 ℓ /unity	53
liquids		
inorganic liquids	25 ℓ PE bottle	14

Type I:Cloth and Paper made of natural cellulose.

Type II:Combustible Plastics such as Polyethylene and Polypropylene.

V. 8. Training for Safehandling of Radiation and Radioisotopes and X-Ray Machines for Beginners in Tohoku University

Nakamura T., Yamadera A. and Miyata T.

Cyclotron and Radioisotope Center, Tohoku University

Training for safehandling of radiation and radioisotopes for beginners has been conducted twice a year from 1977 in Tohoku University. The contents of lectures and practices are shown in Table 1. In 1996 the training was performed for 511 persons. The departments to which they belong are given in Table 2.

Training for safehandling of X-ray machines and electron microscopes began from the end of 1983. The training is scheduled to be held twice a year at the same time as the safehandling of radiation and radioisotopes. Only lectures are given and not practices. The contents of the lectures and the distributions of trainees are shown in Tables 3 and 4, respectively.

Training for safehandling of synchrotron radiation began from the end of 1995. The contents of the lectures are the same as safehandling of radiation and radioisotopes for beginners and not practices. In 1996 the training was performed for 36 persons.

Table 1. Contents of lectures and practices for safehandling of radiation and radioisotopes in 1996.

Lectures (one day)	
Radiation physics and measurements	1.5 (hours)
Chemistry of radioisotopes	1.0
Radiological protection ordinance	1.5
Effects of radiation on man	1.0
Safehandling of radioisotopes	1.5

Practices (one day)	
Treatment of unsealed radioactive solution	4.0 (hours)
Measurements of surface contamination and decontaminatio	1.0
Measurements of gamma rays and beta rays	2.0

Table 2. Distribution of trainees for safehandling of radiation and radioisotopes in 1996.

Department	Staff	Student	Total
Faculties	0	0	0
Medicine	41	87	128
Dentistry	1	6	7
Pharmacy	4	59	63
Science	2	77	79
Engineering	3	64	67
Agriculture	2	82	84
Research Institutes	9	66	75
The others	2	5	8
Total	64	447	511

Table 3. Contents of lectures for safehandling of X-ray machines and electron microscopes in 1996.

Safehandling of X-ray machines	1.5 (hours)
Radiological protection ordinance	1.0
VTR for safehandling of radiation and radioisotopes	1.0

Table 4. Distribution of trainees for safehandling of X-ray machines and electron microscopes in 1996.

Department	Staff	Student	Total
Faculties	0	0	0
Medicine	0	0	0
Science	2	23	25
Engineering	7	85	92
Agriculture	0	0	0
Research Institutes	15	87	102
Total	24	195	219

Table 5. Distribution of trainees for synchrotron radiation in 1996.

Department	Staff	Student	Total
Faculties	0	0	0
Science	1	16	17
Pharmacy	0	0	0
Engineering	0	2	2
Agriculture	0	0	0
Research Institutes	4	13	17
Total	5	31	36

VI. PUBLICATIONS

VI. PUBLICATIONS

(January 1996 ~ December 1996)

A

1. High energy g-ray production from Be, C, and Al targets with 65 MeV ^{3}He bombardment
   M. Hosaka, K. Ishii, M. Ohura, A. Terakawa, S. Miyamoto, Z. Guan and H. Orihara
   PHYSICAL REVIEW C NUCLEAR PHYSICS, Vol. 54, No. 5, pp. 2429-2434, (1996)

2. Noninvasive Quantification of rCBF Using Positron Emission Tomography
   H. Watabe, M. Itoh, V. Cunningham, A. A. Lammertsma, P. Bloomfield, M. Mejia, T. Fujiwara, A. K. P. Jonse, T. Jones, and Nakamura
   Journal of Cerebral Blood Flow and Metabolism, Vol. 16, No. 2, pp. 311-319, (1996)

3. Analysis of Plasma Metabolites during Human PET Studies with Three Receptor Ligands,[^{11}C] YM-09151-2, [^{11}C]doxepin and [^{11}C] pyrilamine
   KIICHI ISHIWATA, KAZUHIKO YANAI, REN IWATA, TOSHIHIRO TAKAHASHI, JUN HATAZAWA, MASATOSHI ITOH, KOJI WATANABE, and TATSUO IDO
   Tohoku J. Exp. Med., Vol. 178, pp. 129-136, (1996)

4. Characterization of 22 and 33 MeV quasi-monoenergetic neutron fields for detectorcalibration at CYRIC
   Masashi Takada, Takashi Nakamura, Mamoru Baba, Tomohiko Iwasaki, Takehide Kiyosumi
   NUCLEAR INSTRUMENTS & METHODS IN PHYSICS RESEARCH Section A, Vol. 372, pp. 253-261, (1996)

5. Measurement of the Neutron Activation Cross Sections of ^{12}C, ^{30}Si, ^{47}Ti, ^{48}Ti, ^{52}Cr, ^{59}Co, and ^{58}Ni Between 15 and 40 MeV
   Yoshitomo Uno, Yoshitomo Uwamino, and Titik S. Soewarsono and Takashi Nakamura
   NUCLEAR SCIENCE AND ENGINEERING, Vol. 122, pp. 247-257, (1996)

6. A performance study on a phoswich detector consisting of an inner NE213 scintillator and an CaF_2(Eu) crystal wall
   Masashi Takada, Tokushi Shibata, Yoshitomo Uwamino, Tskashi Nakamura
   NUCLEAR INSTRUMENTS & METHODS IN PHYSICS RESEARCH Section A, Vol. 379, pp. 293-306, (1996)

B

7. Space charge effects in thin rectangular proportional counter
Kosuke Kageyama, Masahiro Fujita, Eiji Tanaka, Manabu Fujioka
NUCLEAR INSTRUMENTS & METHODS IN PHYSICS RESEARCH Section A, Vol. 369, pp. 151-156, (1996)

8. Feasibilty of Fluorine-18-Fluophenylalanine for Tumor Imaging Compared with Carbon-11-L-Methionine
Kazuo Kubota, Kiichi Ishiwata, Roko Kubota, Susumu Yamada, Joutaro Takahashi, Yoshinao Abe, Hiroshi Fukuda and Tatsuo Ido
THE JOURNAL OF NUCLEAR MEDICINE, Vol. 37, No. 2, pp320-325, (1996)

9. PET imaging of primary mediastinal tumours
K. Kubota, S. Yamada, T. Kondo, K. Yamada, H. Fukuda, T. Fujiwara, M. Ito and T. Ido
British Journal of Cancer, Vol. 73, pp. 882-886, (1996)

10. The peak time difference of time-density curve in intravenous digital subtraction angiography correlates to an asymmetric cerebral blood flow as determined by positron emission tomography
T. Imamura, H. Nagasawa, M. Itoh, and K, Tsuburaya
European Journal of Neurology, Vol. 3, pp. 227-231, (1996)

11. A Concise One-pot Synthesis of [18F] Fluoromisonidazole from (2R)-(-)-Glycidyl Tosylate
Masao Tada, Ren Iwata, Hiroshi Sugiyama, Kazunori Sato, Kazuo Kubota, Roko Kubota, Hiromu Takahashi, Hiroshi Fukuda, and Tatsuo Ido
Journal of Labelled Compounds and Radiopharmaceuticals, Vol. 38 No. 8, pp. 771-774, (1996)

12. PET study of cerebral glucose metabolism and fluorodopa uptake in patients with corticobasal degeneration
Haruo Nagasawa, Hiroaki Tanji, Hiroshi Nomura, Hiroshi Saito, Yasuto Itoyama, Itaru Kimura, Shoji Tuji, Takehiko Fujiwara, Ren Iwata, Masatoshi Itoh, Tatsuo Ido
Journal of the Neurological Sciences, Vol. 139, pp. 210-217, (1996)

13. Different age-related changes in NMDA and glycine receptors in the rat brain
Tsutomu Araki, Hiroyuki Kato, Katsuro Shuto, Takehiko Fujiwara, Yasuto Itoyama
Environmental Toxicology and Pharmacology, Vol. 1, pp. 103-107, (1996)

14. Effects of cerebral ischemia on dopamine receptors in the gerbil striatum
Tsutomu Araki, Hiroyuki Kato, Katsuro Shuto, Takehiko Fujiwara, Kyuya Kogure, Yasuto Itoyama
European Journal of Pharmacology, Vol. 306, pp. 73-79, (1996)

15. Regional age-related alterations in cholinergic and GABAergic receptors in the rat brain
Tsutomu. Araki, Hiroyuki Kato, Takehiko Fujiwara, Yasuto Itouyama
Mechanisms of Ageing and Development, Vol. 88, pp. 49-60, (1996)

16. Re-Evaluation of Myocardial FDG Uptake in Hyperglycemia
Kazuo Kubota, Roko Kubota, Susumu Yamada, Masao Tada, Toshihiro Takahasi and Ren Iwata
The Journal of Nuclear Medicine, Vol. 37, No. 10, pp. 1713-1717, (1996)

17. Effects of vinconate on neurotransmitter receptor systems in aged rat brain
Tutomu Araki, Hiroyuki Kato, Katsuro Shuto, Takehiko Fujiwara, Yasuto Itoyama
Environmental Toxicology and Pharmacology, Vol. 2, pp. 343-349, (1996)

18. Brain 6-[^{18}F]fluorodopa metabolism in early and late onset of Parkinson's disease studied by positron emission tomography
Haruo Nagasawa, Hiroaki Tanji, Yasuto Itoyama, Hiroshi Saito, Itaru Kimura, Takehiko Fujiwara, Ren Iwata, Masatoshi Itoh, Tatsuo Ido
Journal of the Neurological Sciences, Vol. 144, pp. 70-76, (1996)

19. PET study in a patient with spinocerebellar degeneration before and after long-term administration of thyrotropin releasing hormone
H. Tanji, H. Nagasawa, T. Hayashi, H. Onodera, T. Fujiwara, M. Itoh, T. Ido and Y. Itoyama
Behavioural Neurology, Vol. 9, pp. 171-175, (1196)

17. [illegible] of vibrations on postprandial glycemia in aged rat brain
Tsuboi, Atsuki, Ikeda, Ryo, Kimura, Shinji, Takeshita, Fumiya, Yasuo, Ito
Comprehensive Psychology and Neuroimaging, Vol. 2, pp. 143–154 (1990)

18. Brain c-[illegible]-immunoreactivity in early and late preterm Parkinson's disease
studied by proteomic microarray
Hiroto, Shimizu, Kazuo, Tsuji, Yuko, Nakamura, Hiroshi, Sato, Eiichi, Ogawa
Toxicology Mechanisms, Part B, Pharmacology, Vol. 7, No. 1, pp. 77–83 (1990)

19. [illegible] study in rodent with spontaneous degeneration before and after long-term
administration of thyroxine in drinking water
K. Tang, M. Nakamura, T. Hayashi, A. Okada, S. Ishiwata, M. Lee, T. Ueno, and
Y. Toyama
Behavioral Neurology, Vol. 9, pp. 111–123 (1990)

VII. MEMBERS OF COMMITTEES

VII. Members of Committees (as of Jan. 1, 1997)

General

(Chairman)	Hikonojo	Orihara	(CYRIC)
	Osamu	Hashimoto	(Faculty of Science)
	Hiroshi	Kudo	(Faculty of Science)
	Takashi	Yoshimoto	(School of Medicine)
	Tadashi	Yamada	(School of Dentistry)
	Akira	Naganuma	(Faculty of Pharmaceutical Sciences)
	Katsunori	Abe	(Faculty of Engineering)
	Reimon	Hanada	(Institute for Materials Research)
	Ken-ichi	Akiba	(Research Institute for Mineral Dressing and Metallurgy)
	Hiroshi	Fukuda	(Institute for Development, Aging and Cancer)
	Syogo	Yamada	(School of Medicine)
	Masumi	Sugawara	(Faculty of Science)
	Manabu	Fujioka	(CYRIC)
	Tatsuo	Ido	(CYRIC)
	Takashi	Nakamura	(CYRIC)
	Masatoshi	Itoh	(CYRIC)
	Ren	Iwata	(CYRIC)
	Akira	Yamadera	(CYRIC)
	Keizo	Ishii	(Faculty of Engineering)
	Takeo	Fujino	(Research Institute for Mineral Dressing Dressing and Metallurgy)
	Yoshiyuki	Kamio	(Faculty of Agriculture)
	Tadao	Saitou	(Faculty of Agriculture)

Research Program

(Chairman)	Takashi	Nakamura	(CYRIC)
	Takemi	Nakagawa	(Faculty of Science)
	Takashi	Yamaya	(Faculty of Science)
	Tsutomu	Sekine	(Faculty of Science)
	Kazuyoshi	Masumoto	(Faculty of Science)
	Mieko	Kawamura	(Faculty of Agriculture)
	Takashi	Yoshimoto	(School of Medicine)
	Hidetada	Sasaki	(School of Medicine)
	Katsunori	Abe	(Faculty of Engineering)
	Keizo	Ishii	(Faculty of Engineering)
	Reimon	Hanada	(Institute for Materials Research)
	Hiroshi	Fukuda	(Institute for Development, Aging and Cancer)
	Manabu	Fujioka	(CYRIC)
	Tatsuo	Ido	(CYRIC)
	Masatoshi	Itoh	(CYRIC)

Cyclotron

(Chairman)	Manabu	Fujioka	(CYRIC)
	Osamu	Hashimoto	(Faculty of Science)
	Takemi	Nakagawa	(Faculty of Science)
	Kazushige	Maeda	(Faculty of Science)
	Satoru	Kunii	(Faculty of Science)
	Tsutomu	Sekine	(Faculty of Science)
	Takashi	Yamaya	(Faculty of Science)
	Kyuya	Kodajima	(Faculty of Engineering)
	Ken	Abe	(Faculty of Engineering)
	Keizo	Ishii	(Faculty of Engineering)
	Akira	Hasegawa	(Faculty of Engineering)
	Reimon	Hanada	(Institute for Materials Research)
	Ken-ichi	Akiba	(Research Institute for Mineral Dressing and Metallurgy)
	Tatsuo	Ido	(CYRIC)
	Takashi	Nakamura	(CYRIC)
	Masatoshi	Itoh	(CYRIC)
	Ren	Iwata	(CYRIC)

	Tsutomu	Shinozuka	(CYRIC)
	Astuki	Terakawa	(CYRIC)

Radiation Protection and Training of Safe Handling

(Chairman)	Tadashi	Yamada	(School of Dentistry)
	Yoshiaki	Fujii	(Faculty of Science)
	Hiroshi	Kudo	(Faculty of Science)
	Tetsuya	Ono	(School of Medicine)
	Kazuo	Ouchi	(Faculty of Pharmaceutical Sciences)
	Naohiro	Hirakawa	(Faculty of Engineering)
	Toshiyasu	Yamaguchi	(Faculty of Agriculture)
	Akira	Nagamuma	(Faculty of Pharmaceutical Sciences)
	Masayuki	Hasegawa	(Institute for Materials Research)
	Hiroshi	Fukuda	(Inute for Dstitevelopment, Aging and Cancer)
	Manabu	Fujioka	(CYRIC)
	Takashi	Nakamura	(CYRIC)
	Akira	Yamadera	(CYRIC)

Life Science

(Chairman)	Tatsuo	Ido	(CYRIC)
	Kazuo	Yamamoto	(Faculty of Science)
	Yasuhito	Itoyama	(School of Medicine)
	Reizo	Shirane	(School of Medicine)
	Masahiko	Yamamoto	(School of Medicine)
	Kazuie	Iinuma	(School of Medicine)
	Michinao	Mizugaki	(University Hospital)
	Shin	Maruoka	(University Hospital)
	Kazuo	Ouchi	(Faculty of Pharmaceutical Sciences)
	Keizo	Ishii	(Faculty of Engineering)
	Mieko	Kawamura	(Faculty of Agriculture)
	Hiroshi	Fukuda	(Institute for Development, Aging and Cancer)
	Kazuo	Kubota	(Institute for Development, Aging and Cancer)
	Manabu	Fujioka	(CYRIC)

	Takashi	Nakamura	(CYRIC)
	Masatoshi	Itoh	(CYRIC)
	Takehiko	Fujiwara	(CYRIC)
	Yoshihito	Funaki	(CYRIC)

Prevention of Radiation Hazards

(Chairman)	Takashi	Nakamura	(CYRIC)
	Takemi	Nakagawa	(Faculty of Science)
	Tsutomu	Sekine	(Faculty of Science)
	Ken	Abe	(Faculty of Engineering)
	Manabu	Fujioka	(CYRIC)
	Tatsuo	Ido	(CYRIC)
	Akira	Yamadera	(CYRIC)
	Takehiko	Fujiwara	(CYRIC)
	Muneo	Aoyama	(CYRIC)
	Takamoto	Miyata	(CYRIC)

VIII. PERSONNEL

VIII. Personnel (as of Jan. 1, 1997)

Director Hikonojo Orihara

Division of Accelerator

Manabu	Fujioka
Takashi	Yamaya[1)]
Tsutomu	Shinozuka
Minoru	Tanigaki
Shizuo	Kan[6)]
Shizuo	Chiba[6)]
Naoto	Takahashi[6)]
Yasuaki	Omiya[6)]

Division of Instrumentations

Hikonojo	Orihara
Keizo	Ishii[2)]
Astuki	Terakawa
Yasuhisa	Tajima
Sho-ichi	Watanuki
Tsutomu	Ichikawa

Division of Radiopharmaceutical Chemistry

Tatsuo	Ido
Ren	Iwata
Yoshihito	Funaki
Masaaki	Okazaki
Hideo	Takahashi
Yo-ichi	Ishikawa[7)]

Division of Cyclotron Nuclear Medicine

Masatoshi Itoh
Takehiko Fujiwara
Kazuhiko Yanai[4)]
Masayasu Miyake

Division of Radiation Protection and Safety Control

Takashi Nakamura
Akira Yamadera
Takamoto Miyata
Noboru Watanabe[7)]

Graduate Student and Researcher

Masahiro Fujita (Graduate School, Division of Science)
Yasumori Kanai (Graduate School, Division of Science)
Toshio Kouda (Graduate School, Division of Science)
Guan Zhong (Graduate School, Division of Science)
Kazuya Itoh (Graduate School, Division of Science)
Chong-Cheoul Yun (Graduate School, Division of Science)
Asaki Yamamoto (Graduate School, Division of Science)
Naoto Matsumura (Grduate School, Division of Science)
Kenji Kawami (Grduate School, Division of Science)
Hiroshi Suzuki (Grduate School, Division of Science)
Kaori Suzuki (Graduate School, Division of Pharmaceutical Sciences)
Shinji Nagata (Graduate School, Division of Pharmaceutical Sciences)
Hiroyuki Nagao (Graduate School, Division of Pharmaceutical Sciences)
Minoru Hatushika (Graduate School, Division of Pharmaceutical Sciences)
Yoshikazu Morita (Graduate School, Division of Pharmaceutical Sciences)
Masato Higuchi (Graduate School, Division of Medicine)
Marko Mejia (Graduate School, Division of Medicine)
Nobuyuki Okamura (Graduate School, Division of Medicine)

Manabu	Tashiro (Graduate School, Division of Medicine)
Yu-ichiro	Narita (Graduate School, Division of Engineering)
Hossain	Deloar (Graduate School, Division of Engineering)
Kim-Eun	Ju (Graduate School, Division of Engineering)
Tadahiro	Kurosawa (Graduate School, Division of Engineering)
Shingo	Taniguchi (Graduate School, Division of Engineering)
Makoto	Nakao (Graduate School, Division of Engineering)
Yasuo	Fusejima (Researcher)
Takashi	Suzuki (Researcher)
Syunji	Takagi (Researcher)
Yasuhiro	Okano (Researcher)

Office Staff

Muneo	Aoyama
Hiroshi	Syoji
Hashime	Wako
Kyoko	Fujisawa
Seiji	Kikkukawa
Keietsu	Aizawa
Fumiko	Mayama
Mitsuko	Endo
Yu-ko	Yamashita
Rie	Yoshida
Yuri	Okumura
Miyuki	Domon
Noriko	Suzuki
Noriko	Fukuda
Toshiyuki	Watanabe[7)]

1) Faculty of Science
2) Faculty of Engineering
3) Institute for Materials Research
4) School of Medecine
5) Institute for Development, Aging and Cancer
6) SUMI-JU Accelerator Service Ltd.
7) Japan Radiation Protection Co., Ltd.

Tuesday	Martedì
Monday	Lunedì
Thursday	Giovedì
Friday	Venerdì
Wednesday	Mercoledì
Saturday	Sabato
Sunday	Domenica

January	Gennaio
February	Febbraio
March	Marzo
April	Aprile
May	Maggio
June	Giugno
July	Luglio
August	Agosto
September	Settembre
October	Ottobre
November	Novembre
December	Dicembre